OXIDATION KINETICS OF 316L STAINLESS STEEL IN THE PRESSURISED WATER REACTOR ENVIRONMENT

A thesis presented for the Degree of

DOCTOR OF PHILOSOPHY

within the Centre of Materials Engineering,
Department of Mechanical Engineering,
Faculty of Engineering and the Built Environment

by

Ryan Paul Matthews

February 2019

1. DECLARATION

1. I know that plagiarism is wrong. Plagiarism is to use another's work and pretend that it is one's own.
2. I have used the Elsevier defined convention for citation and referencing. Each contribution to, and quotation in, this thesis from the work(s) of other people has been attributed, and has been cited and referenced. Any section taken from an internet source has been referenced to that source.
3. This thesis is my own work, and is in my own words (except where I have attributed it to others).
4. I have not allowed, and will not allow, anyone to copy my work with the intention of passing it off as his or her own work.
5. I acknowledge that copying someone else's assignment or essay, or part of it, is wrong, and declare that this is my own work.

Signature Signed by candidate

Abbreviations

BWR	Boiling water reactor
CRDM	Control rod drive mechanism
CERT	Constant extension rate test
dpa	Displacement per atom
EBSD	Electron Backscatter Diffraction
EDF	Électricité de France
EPRI	Electric Power Research Institute
EFTEM	Energy filtered transmission electron microscopy
IGSCC	Intergranular stress corrosion cracking
PWSCC	Primary water stress corrosion cracking
PWR	Pressurised water reactor
SCC	Stress corrosion cracking
SEM	Scanning electron microscopy
TEM	Transmission electron microscopy
TGSCC	Transgranular stress corrosion cracking
ToF SIMS	Time of Flight Secondary Ion Mass Spectroscopy
XRD	X-ray Diffraction

2. Contents

3. ABSTRACT

With a view to improving the prediction of primary water stress corrosion cracking in austenitic stainless steels, this investigation measured the oxide growth kinetics of 316L stainless steel when exposed to a simulated primary water environment of a pressurised water reactor (PWR). It is generally accepted that intergranular oxidation at the surface of a metal forms a preferential site for stress corrosion crack (SCC) initiation; therefore the kinetics of both surface and intergranular oxidation were measured. The influence of temperature, within the range of PWR primary water (290°C, 320°C and 360°C), as well as the influence of starting condition (annealed, 20% elongated, 30% elongated and 20% cold rolled) was investigated.

Samples were prepared with the various starting conditions and exposed to simulated primary water, at the specified temperatures, for various durations from 1 hour through to several thousand hours to plot the oxide growth on a log scale time axis. Subsequent to the exposure tests, the Cr rich inner oxide depth was measured locally at selected locations. The surface and intergranular oxide depth was directly measured from cross-sections either with a transmission electron microscope for short duration exposures or, for longer exposures with deeper oxides, within a scanning electron microscope.

No significant difference was noted on the oxide kinetics between the various starting conditions evaluated. Temperature, however, had a significant influence with oxide growth kinetics decreasing, rather counter-intuitively, as temperature increased through the measured range. In addition a strong dependency on grain orientation was observed.

A modification to the Point Defect Model was proposed to arrive at a quantitative expression to describe surface and intergranular inner oxide growth as a function of temperature in 316L stainless steel, which accommodated the deviation from Arrhenius behaviour through the measured temperature range. Functions for both the rate constant, k_3^0, and the transfer coefficient, α_3, associated with the metal/oxide interface reactions were developed. The resultant model was able to predict, with reasonable accuracy, the growth of the Cr-rich inner oxide over time.

The most consistent explanation for the deviation from Arrhenius behaviour was that the coherency across the metal/oxide interface degraded as the temperature increased through the tested temperature range. This would reduce the potential for ionic transfer across the interface necessary for the interface to migrate and increase the oxide depth.

Since a similar temperature dependence on the growth of intergranular stress corrosion cracking (IGSCC) in the primary water environment has been observed within the same temperature range, it is proposed that the above explanation, observed in the absence of applied stress, extends to explain the behaviour of IGSCC kinetics in austenitic stainless steel.

4. ACKNOWLEDGEMENTS

The initial guidance and encouragement from Prof. Bernard Sonderegger as my initial supervisor is gratefully acknowledged.

Prof. Robert Knutsen, as my subsequent supervisor, has since been very supportive, approachable and has also challenged me, which was necessary to extent the project into areas where the greatest scientific value could be found.

This project could not have been conceived had the Eskom Power Plant Engineering Institute not actively encouraged their engineers and scientists to pursue further studies and funded the various projects. In particular I would like to acknowledge the support provided by Eskom's Physical Metallurgy management of Mr Marthinus Bezuidenhout, Mr Frans Havinga and Mr Kobus Smit in encouraging me to participate in the programme and accommodating the gap left at Koeberg Power Station during my full time study leave.

Doctoral studies can be a lonely experience, in particular nuclear materials research in South Africa. However, I am very grateful to Dr Thierry Couvant who responded to a request to collaborate with enthusiasm, for arranging the exposure tests, as well as the fruitful discussions during the project. The collaborative spirit in which Thierry and his colleagues at the EDF R&D laboratories, France, conduct themselves is both generous and conducive to scientific progress.

Whilst preparing samples for oxide thickness measurements, many hours were spent on the electron microscopes at the Centre of High Resolution Transmission Electron Microscopy (CHRTEM). The patient training provided by Mr Ettienne Minnaar on the FIB-SEM was excellent and I'm grateful for his assistance in achieving a high success rate in sample preparation. I am also grateful for the interest that Dr Johan Westraadt took in the project, his guidance and the meticulous care with which he, together with Dr Jaco Olivier performed TEM microscopy. The centre and its staff provide an excellent facility conducted with professionalism in which it is a pleasure to perform materials research.

I am indebted to my supportive family who have patiently endured the time with an absent father and husband who was working on this project. I thank the good Lord for their love and encouragement and hope I can make it up to them.

5. INTRODUCTION

The most significant materials degradation mechanism affecting light water nuclear reactors today is primary water stress corrosion cracking (PWSCC) [1,2]. Utilities operating light water reactors representing all designs of pressurised water reactors (PWR) and boiling water reactors (BWR) have had to respond to this type of degradation that can challenge the integrity of the primary pressure boundary. They are required to implement integrity management programmes with costly qualified examinations to demonstrate component integrity. Many operators have had to either replace components or face the replacements in the future in order to continue operating. In addition a significant global research effort has been devoted to understanding this mechanism for the benefit of the nuclear power generating industry [1–3]. The large majority of PWSCC cases in PWRs have affected nickel based alloys, however in the frame of many reactors extending their operating licences, this study is focused on austenitic stainless steels in an effort to improve the capacity to predict the time to initiate PWSCC in the latter materials.

PWSCC research can broadly be categorised into either crack initiation or propagation studies. The latter has been studied to inform industry of the mechanisms of propagation and the potential crack propagation rate under a variety of conditions. Propagation models can assist operators to demonstrate through conservative calculation that integrity is assured while continuing to operate while a repair or replacement is prepared. While the former, by determining the conditions necessary to initiate, aims to inform where and when, if ever, PWSCC is likely to occur within the primary system. Initiation studies however have proved to be more challenging and research is continuing in order to create models that can accurately simulate the initiation mechanism and therefore be reliably used for predicting the onset of PWSCC.

There are models currently available which aim to predict the time to initiate detectable PWSCC, however most of these models are empirical in nature. EPRI developed a stress corrosion cracking model for both Ni based alloys and austenitic stainless steels that consider, in particular, the influence of cold work on time to initiate cracks [5,6]. Électricité de France (EDF) also developed a model to assess the risk of crack initiation in Ni based material with an associated minimum time for initiation, which is based on the material properties, temperature and mechanical loading [6,7]. However, the applicability of these empirical type of models to predict the future risk of PWSCC in stainless steels in operating reactors have been questioned since they are derived based on data acquired from the laboratory in accelerated conditions, and validated from past operating experience [8],[9].

Therefore the current emphasis in supporting research is to develop phenomenological models that are based on physical mechanisms, which will have a wider applicability with the potential to be more accurate. This is more of a challenging task considering the complexities involved in describing the number of potential phenomena involved and their interdependence. These can be broadly categorised into: surface reactivity; stress assisted diffusion; segregation ahead of the crack tip, local fracture criteria; and crack propagation that considers local plasticity [10].

This research project aims to contribute towards an overall PWSCC initiation model for austenitic stainless steel by characterising the one component, namely the kinetics of intergranular oxidation as a function of time, temperature and material condition. It is known that oxidation preferentially propagates down grain boundaries of austenitic structural materials when exposed to high temperature primary water [11,12]. Since PWSCC propagates as an intergranular crack, an oxidised grain boundary will form a preferred initiation site for such a crack and therefore it is generally agreed that intergranular oxidation forms a precursor from which PWSCC can initiate [8,11,13–15]. However, to the authors knowledge, there is no quantitative study that has measured the growth of intergranular oxidation in austenitic stainless steel. This type of model will therefore form part of the surface reactivity category described above. While the mechanism of intergranular oxidation may be quite different from stress corrosion cracking it forms a necessary part of the time taken to create the environment necessary for cracking to propagate.

The investigation focused on a single material, 316L austenitic stainless steel, which represents the material often used for the primary piping and other components within PWRs. Stainless steels have generally had a good operating history with relatively few incidents of PWSCC in normal chemistry water when compared to the nickel based alloys. Nevertheless, their long term susceptibility to cracking is still to be established in normal PWR water chemistry. This is currently an important topic for many nuclear reactor operators as they prepare to extend their operating licences beyond the original design life of the plant.

6. LITERATURE REVIEW

Of all the nuclear power plants currently in commercial operation globally, pressurised water reactors (PWR) account for 299, or 66% of a total of 454 reactors [16]. The second most common design is the boiling water reactor, which has a single closed water and steam loop and uses deuterium oxide in the primary water as an efficient neutron moderator; accounting for 16% of the total.

While the application of this investigation is limited to the pressurised water environment, it will remain of interest to the majority of the world's generating nuclear reactors.

6.1. Pressurised Water Reactor Design

This PWR design consists of two closed systems, which are referred to as the primary system, containing the nuclear fuel and reactor coolant, and the secondary system which conveys heat to the turbines using the Carnot steam cycle. A simplified view of the primary and secondary systems together with their main components is given below in Figure 1.

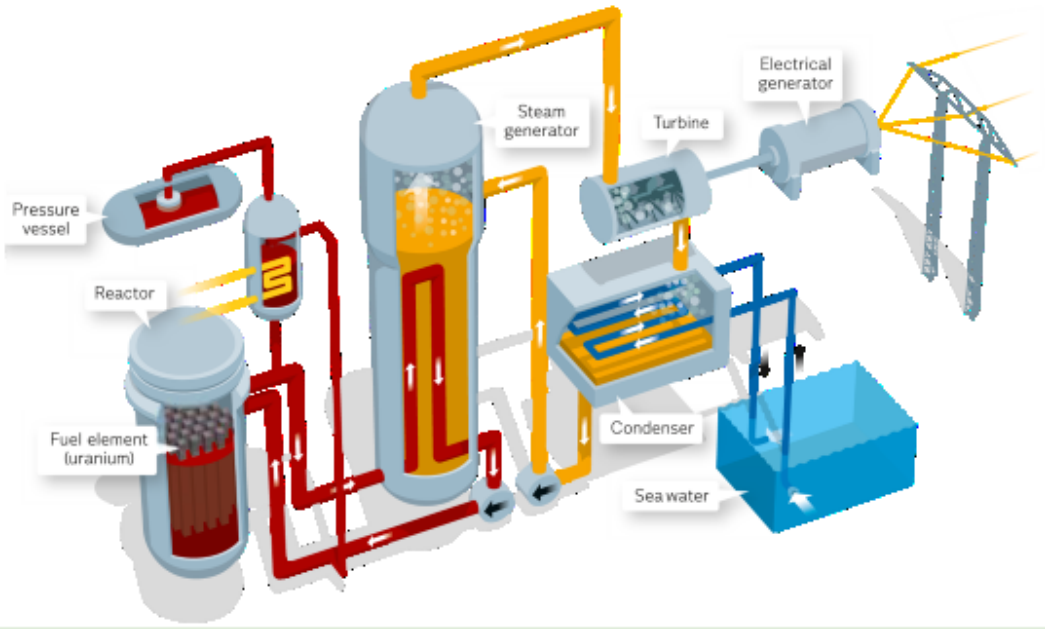

Figure 1. Schematic of the primary (red) and secondary (yellow) systems in a pressurised water reactor [17].

The primary system contains the reactor pressure vessel where nuclear fission produces heat within the fuel rods. This thermal energy is transferred to the primary water through the

fuel cladding. Since the primary water evacuates the heat from the nuclear fuel rods preventing overheating and melting, it is called the reactor coolant. The primary pumps, one per loop, circulate the coolant through the primary system at a significant flow rate of approximately 13,000 kg/s. In order for the coolant to remain water at temperatures of up to 360°C the system pressure is maintained, by the pressuriser, at approximately 15.5 MPa during normal operation. Heat is transferred from the primary system to the secondary system via the steam generators, one per loop. The primary coolant path is split into more than 3000 separate tubes in order to increase the surface area for heat transfer. Pressurised water reactors have been designed to contain up to four loops that circulate the primary water from the central reactor vessel to the steam generators and back via the primary pumps.

The secondary system is maintained at a lower pressure (approx. 6 MPa), therefore steam is produced at approximately 270°C within the steam generators. The steam then conveys the thermal energy to the turbines where the energy is converted into kinetic rotation of the central shaft. On the downstream side of the turbines the pressure within the condenser is reduced and maintained very low largely due to the condensation of the steam. It is this pressure differential across the turbine that drives the flow of steam across the various stages of blades thereby rotating the shaft. Cooling water from the ocean, river or cooling tower is pumped through a multitude of tubes within the condenser on which the steam condenses and falls to the base of the condenser. Thereafter the secondary water is pumped via a train of heaters and multistage pumps back to the steam generators where it enters preheated and at the required pressure.

6.2. Primary Water Environment

In the context of environmentally assisted cracking research it is important to appreciate the unique environment of the pressurised water reactor's primary system. Firstly, the primary system operates at high temperatures typically within the approximate range of 250°C - 350°C, which is pressurised to approximately 15.5 MPa to maintain it within the liquid phase at these temperatures [18]. Secondly, since the primary system is a closed loop, operators have the opportunity to vary the chemistry of the primary water to control the nuclear fission reactivity while also reducing the potential of corrosion of the components exposed to primary water.

6.2.1. Coolant

Probably the most important purpose of the primary water is to conduct heat away from the nuclear fuel and transfer this energy to the secondary system via the steam generator. Should the coolant inventory in the system drop during accident conditions to expose the fuel cladding, also known as the first barrier to fission products, it could fail due to overheating which would cause rapid oxidation and rupture. This would result in a release of highly radioactive material into the primary system.

It is also important that the fuel is submerged by coolant long after the fission reaction has ceased since the residual heat generated by the decaying fission products is sufficient to overheat the cladding. Spent nuclear fuel therefore relies on primary water cooling within a spent nuclear fuel pool for many years before it loses sufficient activity to be stored in a sealed dry cask.

6.2.2. Moderator

The primary water is also used as the moderator in PWRs. The water slows down the fast neutrons released from the fission reaction through a number of elastic collisions to thermal neutrons that can be captured by other U^{235} nuclei for the chain reaction to continue. Boron is added to the primary water as boric acid (H_3BO_3) as a neutron absorber. By manipulating the boron concentration within the primary water, the operators are able to control the reactivity within the reactor pressure vessel.

6.2.3. Corrosion Control

Apart from satisfying the coolant and moderator functions the chemistry of the primary water is managed to reduce the potential for corrosion of the primary system. This not only protects the integrity of the primary system, it also reduces the potential radiological dose that personnel would receive during maintenance operations. If corrosion products become mobile in the primary system they can become activated when passing through the core and if deposited elsewhere in the primary system have the potential to become a local source of high radioactivity.

For this reason the oxygen content of the primary water is maintained at very low concentrations of < 5 ppb to create reducing environment. Corrosion is very sensitive to the presence of dissolved oxidants such as O_2 and H_2O_2. As they bond with free metal ions they will encourage the dissolution of the metal (corrosion). Therefore the presence of these

species will accelerate general corrosion by promoting the cathodic reaction. Figure 2 illustrates how sensitive the electrochemical potential (the potential for corrosion) is to the dissolved oxygen content in the water using 304 stainless steel as an example. The corrosion potential is shown to decrease as the dissolved oxygen content decreases. In the same graph the influence of temperature on the potential is evident particularly at very low oxygen concentrations. From these results the potential at typical operating temperatures can be > 0.7 V lower than the potential at ambient temperatures.

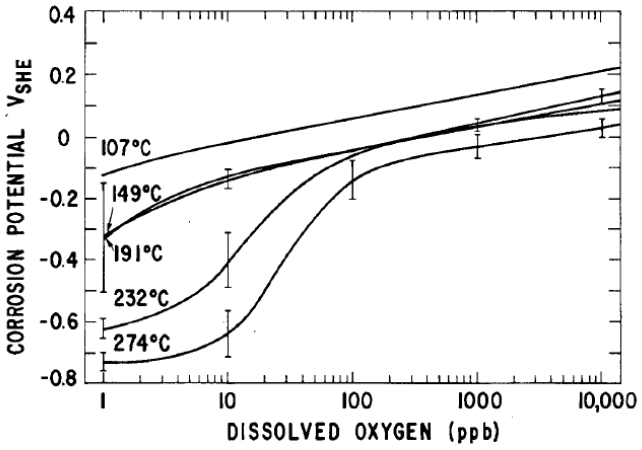

Figure 2. Effect of corrosion potential of 304 stainless steel as a function of dissolved oxygen content and temperature[19].

The importance of maintaining the oxygen concentration at these levels can be appreciated when reviewing the operating experience where a large number of PWSCC incidents were recorded in stainless steels of BWRs whose typical water chemistry has an oxygen concentration of > 15 ppb [3]. In addition most of the PWSCC incidents recorded in PWRs were in cases where the O_2 levels were outside of the specified limits. See section 6.3 for further details.

6.2.4. Radiolysis

When the primary water is exposed to the ionising radiation emitted from the core it can decompose in a process called radiolysis to form a number of possible daughter species. These include the molecular species H_2O_2, O_2 and H_2 as well as radical daughter species H, OH, e^-_{aq} and HO_2. The molecular species however are more stable in solution and would, if left unchecked, increase the potential in the primary system [20]. Therefore to counter the accumulation of radiolysis products, the primary water of PWRs is dosed with H_2 which suppresses the radiolysis. Concentrations of 500 ppb H_2 (5.6 cc/kg) has been found to be adequate but typically PWR primary water chemistry guidelines recommend levels of 25-35 cc/kg [19,21].

6.2.5. pH Control

The last essential addition to the primary water is LiOH, which is added for pH control. If the temperature of water increases it dissociates more readily resulting in a higher concentration of H^+ and OH^- ions and therefore a reduced pH, without changing its neutrality. For example the neutral point of pure water reduces from 7.00 to approximately 5.6 pH at 300°C [19]. This shift in pH due to temperature together with the addition of boric acid (H_3BO_3) requires a pH buffer in the form of LiOH. During the history of PWR operation the general consensus regarding target pH value has varied over time and ranged within 6.9 to 7.4. It has been found that general corrosion rates are higher at the lower end of the range, while at higher pH values the risk of Zircaloy fuel cladding corrosion increased [20,22]. Research has also indicated that the risk of PWSCC initiation, particularly for alloy 600 steam generator tubes, is marginally higher at 7.25 pH but the propagation of the cracks was less sensitive to pH variation [19,23]. Given operating history and research findings most current PWR chemistry regimes operate within the range of 7.0 – 7.2 pH at operating temperatures (≈ 300°C) [8].

6.2.6. Impurities

PWR chemistry guidelines include suggested limits of several impurities that have been found to increase the rate of corrosion and environmentally assisted cracking. The most significant with respect to corrosion are the anions such as chlorides, fluorides and sulphates which have been found to be particularly aggressive in the presence of elevated levels of oxygen but in normal water chemistry have only a marginal affect. Therefore these levels are kept to a minimum with sensitivity measured at levels ≈ 10 ppb [19].

Therefore considering the above factors the following table summarises the recommended guideline for primary water chemistry for PWRs operating at full power.

Table 1. Summary of primary water chemistry control parameters during full power operation [21] .

Parameter/Constituent	Guideline
Boron	Typically 1500 ppm
pH	6.9 – 7.4
Lithium	To achieve target pH, and subject to fuel vendor limits (typically 1.0 – 3.0 ppm)
Hydrogen	25 – 50 cc (STP)/kg
Dissolved oxygen	< 5 ppb
Chloride	< 150 ppb
Fluoride	< 150 ppb
Sulphate	< 150 ppb

6.3. PWSCC Operating Experience of Primary Pressure Boundary Materials

For the purpose of this review only materials of the primary pressure boundary that are exposed to the primary water will be reviewed. The various materials employed for this purpose can broadly be grouped as:

- cladding materials, used as non-structural corrosion protection for the internal surfaces of low alloy steel (LAS) pressure vessels;
- cast austenitic materials, selected for primary piping elbows, primary pump volutes, and other valve bodies;
- welding materials, often used to connect dissimilar metals;
- wrought materials, accounting for the majority of the material used for pressure vessels, primary piping and the steam generator tubes.

No PWSCC has to date been recorded for the stainless steel cladding or cast austenitic stainless steels. However, in the operating history of pressurised water reactors worldwide, both the welding and the wrought materials have provided significant operating experience with respect to PWSCC.

6.3.1. Nickel based material

The vast majority of PWSCC recorded cases have been associated with the wrought steam generator tubes that account for approximately 75% of the total internal surface area of the primary pressure boundary [1]. Most of the early PWR designs selected the nickel based alloy 600 in the mill annealed condition for the tubes. Note that Table 2 provides the compositions of the alloys discussed in this section. This material was initially selected in

preference to stainless steel chiefly due to its corrosion resistance in a chloride environment, which could occur on the secondary side of the tubes if the condenser tubes were to leak sea water into the secondary water [24]. This selection was made despite the caution raised by Coriou et al. in the 1960s, which highlighted the susceptibility of this alloy to SCC in pure high temperature water [25]. After approximately 5 years of service the first intergranular stress corrosion cracks were observed in the steam generators tubes that selected the mill annealed alloy 600 [26]. This material, particularly the mill annealed condition, proved to be unsuitable for this application and PWRs started to replace their steam generators with the preferred alloy 690 thermally treated material. The replacement material is alloyed with significantly more Cr and Mo, and is specified with an extended heat treatment which decorates the grain boundaries with Cr carbides while homogenising the distribution of remaining Cr in solution after precipitating the carbides.

Table 2. Typical compositions of structural materials used in PWR pressure boundary applications (wt %).

			Cr	Ni	Mo	Fe	Co	Cu	C	Mn	Si	P
Ni based	Wrought alloys	Alloy 600	14-17	>72	-	6-10	<1	<0.05	<0.15	<1	<0.5	-
		Alloy 690	27-31	>58	8 – 10	7-11	<0.5	<0.05	<0.05	<0.5	<0.5	<0.015
	Welding alloys	Alloy 182	13-17	Bal.	-	<10	<0.12	<0.05	<0.1	5-9.5	<0.1	<0.03
		Alloy 82	18-22	Bal.	-	<3	<0.10	<0.05	<0.1	2.5-3.5	<0.5	<0.03
		Alloy 152	28-31	Bal.	<0.5	8-12	<0.02	<0.5	<0.045	<5	<0.65	<0.02
		Alloy 52	28-31	Bal.	<0.05	8-12	<0.02	<0.3	<0.040	<1	<0.50	<0.02
Stainless steel	Wrought alloys	AISI 304	18-20	8-10.5	-	Bal.	-	-	<0.08	<2	<1	<0.045
		AISI 304L	18-20	8-12	-	Bal.	-	-	<0.03	<2	<1	<0.045
		AISI 316	17-19	10-13	2-3	Bal.	-	-	<0.08	<2	<1	<0.045
		AISI 316L	17-19	10-13	2-3	Bal.	-	-	<0.03	<2	<1	<0.045
	Welding alloys	308L	19.5-22	9-11	<0.75	Bal.			<0.03	1-2.5	0.3-0.6	<0.045
		309L	23-25	12-14	<0.75	Bal.			<0.03	1-2.5	0.3-0.6	<0.045

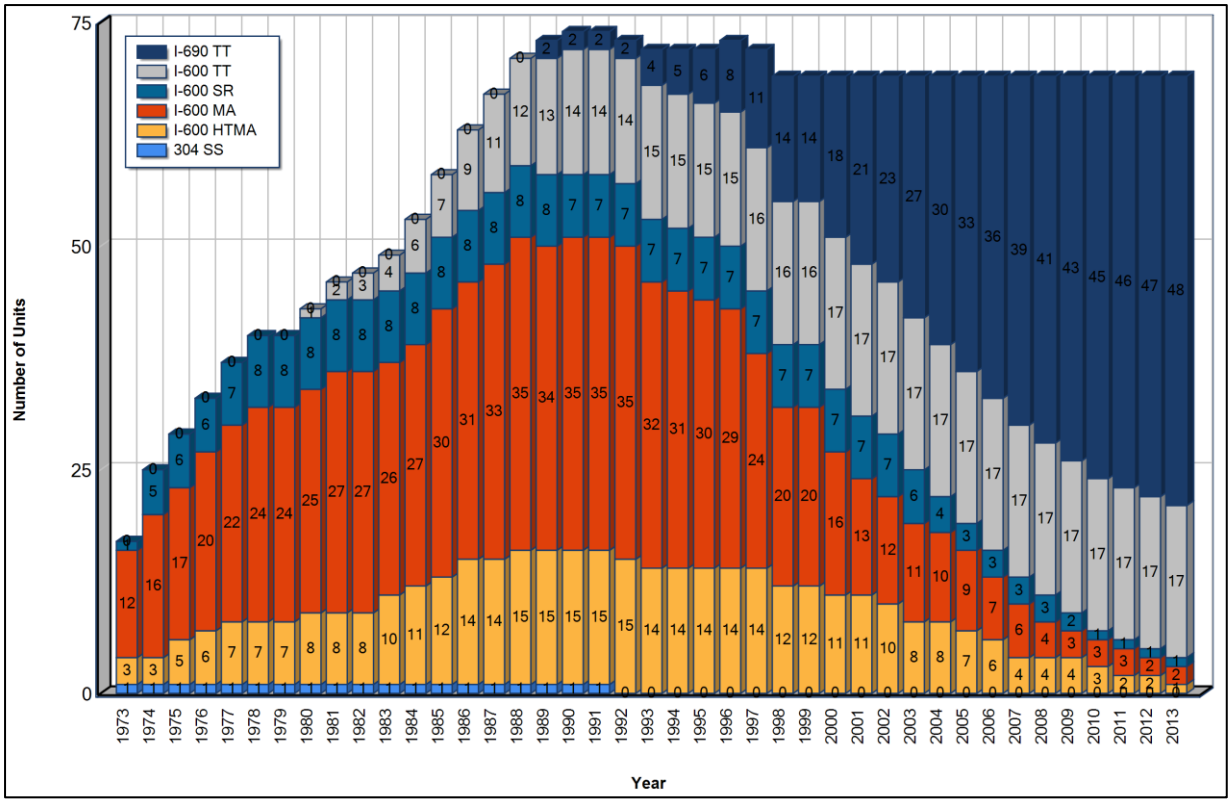

Figure 3. Change in steam generator tube material selected in operating PWR plants in the United States over time. (TT –thermally treated, SR – stress relieved, MA – mill annealed, HTMA – high temperature mill annealed) [27].

The weld filler materials associated with the wrought alloy 600 material are alloy 82 and 182. These weld materials were also found to be susceptible to intergranular stress corrosion cracking (IGSCC) in PWR water chemistry, particularly alloy 182 with lower chromium content, with several locations around the primary system being of concern. Some notable examples include the reactor vessel closure head and bottom penetrations, and dissimilar metal welds. Many control rod drive mechanisms (CRDM) were originally fabricated from roll-expanded alloy 600 penetrations through the vessel head with alloy 182 partial penetration welds, with both the welds and the penetrations proving susceptible to PWSCC, see Figure 4 for a schematic of these penetrations. PWSCC of reactor vessel heads with some significant leaks reported, most notably the experience of Davis Bessie, prompted large scale replacements of reactor pressure vessel heads with alloy 690 material and its associated welding filler materials, alloys 52/152 [28]. Alloys 82 and 182 were often also used as weld filler materials for dissimilar metal welds between the ferritic pressure vessels and the austenitic primary piping since they have a thermal expansion between that of austenitic stainless steel and low alloy carbon steel. However PWSCC initiated in many of these welds [29]. In order to justify continued operation without the loss of pressure boundary integrity, many operators preferred to mitigate the issue with full structural overlays around the nozzle with resistant material (alloy 52). This design took no structural credit for

the original weld and postulated complete through wall cracking of the original nozzle material, but that it would arrest at the alloy 52 material [28].

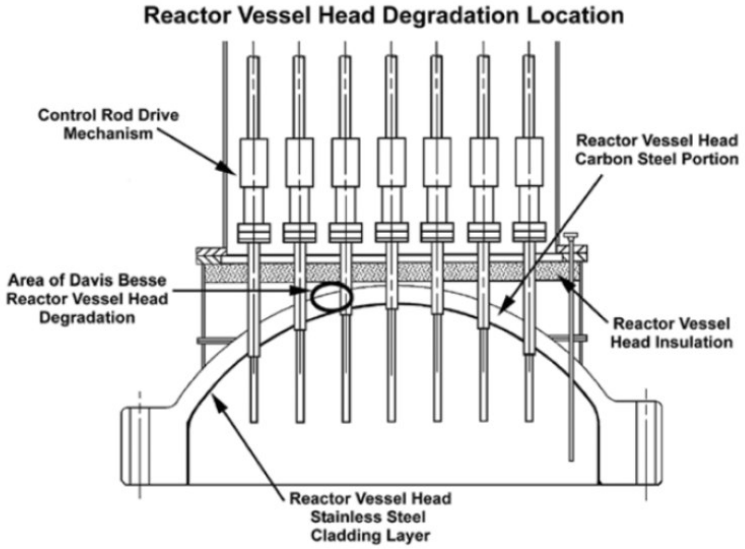

Figure 4. Schematic of a typical reactor vessel closure head showing the alloy 600 penetration nozzles through the head wall which receive a partial penetration seal weld with alloy 182 to the low alloy steel head forging [28].

6.3.2. Austenitic Stainless Steel Material

In contrast to the extensive cracking reported of nickel based alloys, there have been relatively few incidents of PWSCC involving austenitic stainless steel structural materials in PWRs. Nevertheless, they have proven to be susceptible to PWSCC in either off-normal chemistry conditions and/or where the material has had significant cold work introduced, and particularly if the material has been sensitized [2,10]. The Electric Power Research Institute (EPRI) has captured a total of 137 PWSCC events recorded from PWR nuclear operating experience until 2007 as part of their Materials Reliability Programme (MRP-236) [30]. While this may not be an exhaustive summary of all events, since some events are likely to be unreported, it is useful as a summary that highlights conditions that have proved to be susceptible thus far. It is also noted that 11 years of operating experience has accrued since this review was compiled, however the trends are still valid and are supported by more recent publications [31].

Off-normal Chemistry

Off-normal chemistries are typically found in occluded locations of the primary circuit out of the main flow of the primary water e.g. dead legs, within valves or within reactor vessel head penetrations. At these occluded locations the potential for higher oxygen contents exist from

entrapped air during refilling the primary circuit, which would raise the electrochemical potential, see Figure 2. There is also a higher propensity for contaminants (e.g. sulphates, chlorides) to concentrate in occluded areas since they cannot be flushed out and diluted in the general flow. It was been established that oxygenated high temperature water with chloride contaminants, even at low ppm levels, provides for an environment conducive for transgranular stress corrosion cracking (TGSCC) [30–32], see Figure 5. The presence of sulphates have also been found to play a synergistic role with chlorides in aerated environments which would increase the susceptibility to SCC [31]. The sulphates may find their source from the resins used to purify the water in the primary system [2].

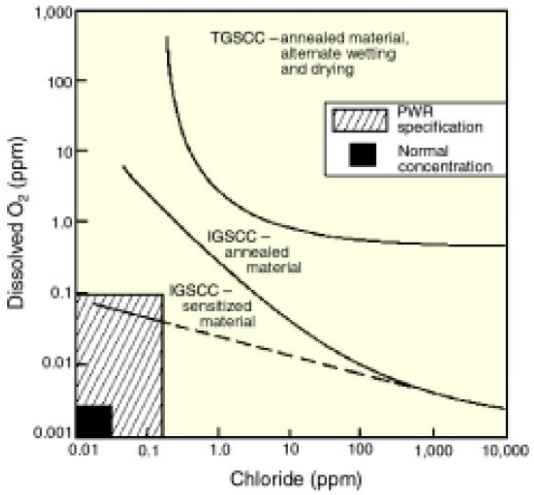

Figure 5. Stress corrosion cracking mode of propagation in relation to chloride and oxygen concentration [2].

Of the 137 PWSCC events recorded, the vast majority of cases are accounted for by events from occluded regions (86%) where off-normal chemistry has occurred. In these areas it is clear that the predominant crack propagation mode has been by TGSCC, see Figure 6 [30]. More than half of the cases (52%) occurred either in the control rod drive mechanism (CRDM) housings, or the canopy seal welds both of which are located on components at the top of the reactor pressure vessel head and are susceptible to high oxygen occluded conditions [30].

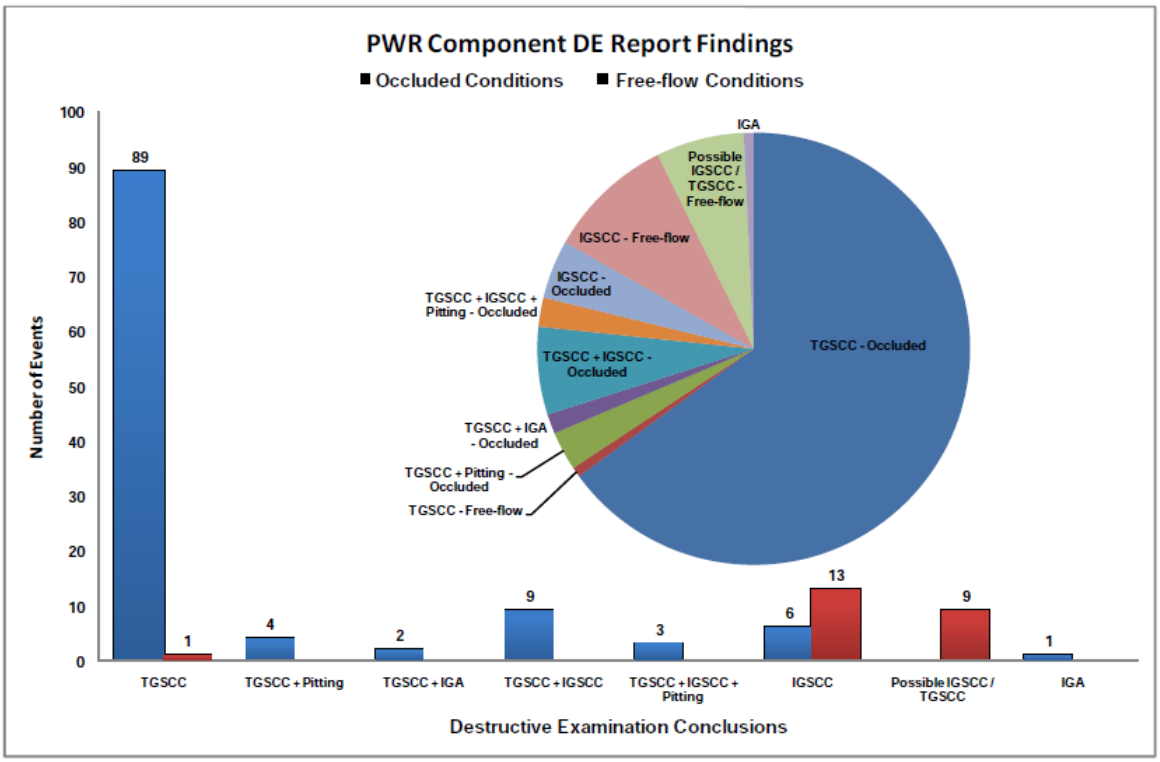

Figure 6. Distribution of 137 PWSCC of stainless steel components events recorded from operating experience. Events are classed with respect to cracking mode and if they occurred in free-flow or occluded locations [30].

It is worth noting that these incidents of SCC where off-normal chemistries are involved are analogous to the numerous events experienced in the boiling water reactors. In the 1970s IGSCC of recirculation systems was recognised as a generic degradation issue for BWR plants, and peaked in 1984 where the averaged capacity loss in the United States reached about 15% [3]. This issue resulted from the combination of sensitised 304 stainless steel adjacent to welds, associated weld residual stress, and an environment of oxygenated (>15ppb) high temperature water, see an example in Figure 7. More recent operating experience, from 2002, highlights that SCC of other non-sensitised materials of type 316 stainless steel have been discovered adjacent to welds in several BWRs [28]. This experience highlights how critical it is to control the oxygen content of high temperature water when trying to avoid an environment conducive for SCC of austenitic stainless steels.

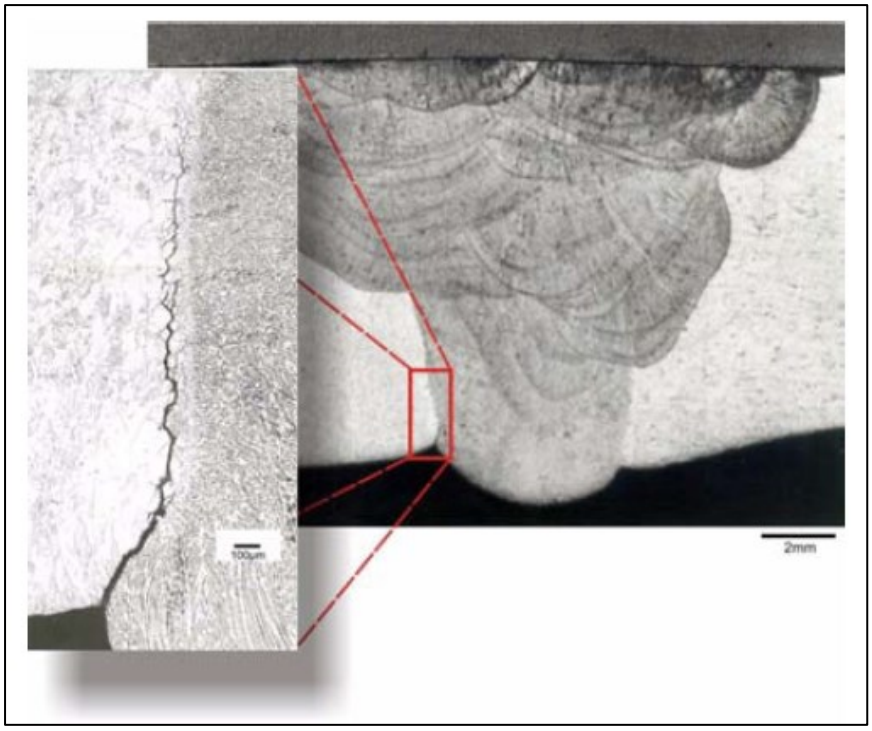

Figure 7. IGSCC adjacent to a weld of a sensitised recirculation piping in a boiling water reactor [28].

Cold Work

While environmental conditions related to PWSCC susceptibility have been discussed, the most significant material related parameter has been the level of cold work introduced. Of the 137 events recorded most were confirmed to have cold work while in many cases (38%) the cold work condition was not reported [30]. Conversely, the occurrences of PWSCC where the material was confirmed not to have significant cold work were very few. In all cases reported in locations exposed to free-flow conditions(16%), where the environment should be normal PWR water chemistry, a high degree of cold work was noted resulting in hardness greater than 300HV [30]. In all of these cases the crack propagation mode was by intergranular stress corrosion cracking (IGSCC).

The time to detect cracking in highly cold worked areas was relatively short, particularly at higher temperatures. For example several pressuriser heater sleeve failures have been recorded where operating temperatures are approximately 360°C. The hardness of cracked sleeves has been measured at ≥400HV, and cracking has been recorded after less than a year's service.

Other locations where PWSCC has been recorded under free-flowing conditions include thermocouple clamping staples, where hardness was measured at 370HV, and tubes within the chemical and volume control system heat exchangers, with hardness greater than 300HV. From a review of the operating history some researchers have suggested that 300HV represents a threshold cold work condition necessary for a material to be susceptible to PWSCC in normal PWR water chemistry conditions (free flow locations) [30]. This hypothesis for austenitic stainless steels has been tested in the laboratory with Tribouilloy et al. finding a crack initiation threshold corresponding to a material hardness of $240HV_{0.1}$, while crack propagation requires a greater hardness of $310HV_{0.1}$ [33].

Subsequent to the EPRI 2007 summary report of PWSCC events, a report from a Japanese PWR, Mihama 2, in 2008 detailed the first case to have initiated on the internal diameter of the primary piping. The report attracted the attention of the global PWR community since the experience raised questions around the possible extent to which austenitic stainless steel is susceptible to PWSCC in free flowing PWR primary water. Before this event only a limited number of components proved to be susceptible; however should the primary piping be included into this group then the scope of susceptible components would be significantly increased.

The cracking at Mihama 2 was located in the heat affected zones (HAZ) on either side of a safe end piece. The safe end is a section of austenitic stainless steel pipe which is welded to the low alloy steel nozzle of the steam generator using a buttered bimetallic weld. In this way the bimetallic weld can be completed at the fabricator in more controlled conditions, leaving the less complex safe end to the primary piping weld, both austenitic materials, to be welded on site. Cracking had initiated within the Ni based bimetallic welds (alloy 82 & 182) prompting the replacement of the nozzle. However, during inspections cracking was also observed in the type 316 stainless steel material adjacent to the welds on either side of the safe end i.e. adjacent to the bimetallic weld and adjacent to the safe end weld, see Figure 8 [34].

Features on the crack surface indicated that crack initiated by IGSCC and continued in this mode to the crack front at a maximum depth of approximately 1.5 mm [34]. Crack initiation was associated with weld residual stresses (measured at 360MPa in longitudinal direction) and a hardened surface layer due to grinding (measured hardness of 280-430 HV) [35]. However this condition may not be uncommon since the internal surface of circumferential weld roots are usually ground after welding. The safe end where cracking was detected was installed in 1994 when the steam generator was replaced, therefore the cracking has been exposed to the primary water for approximately 19 years of operation [35].

This operating experience demonstrates that PWSCC can initiate in austenitic stainless steel, within the primary environment, and with typical stresses associated with welds provided that there is cold work introduced into the material. Therefore at high temperatures and levels of cold work PWSCC can initiate and propagate by IGSCC within a year at normal PWR water chemistries e.g. the pressuriser heaters. At lower temperatures and cold work conditions the cracking can take decades to manifest e.g. Mihama 2 safe end steam generator cracking.

While some laboratory research suggests that there is a threshold cold work condition necessary for initiation and propagation, these tests are conducted under accelerated conditions and therefore may not be adequate to predict behaviours which involve mechanisms with slow kinetics. Some have cautioned the use of thresholds (cold work, stress intensity etc) when defining conditions within which SCC may initiate [19]. Therefore in the context of many PWRs extending their operating lives to 60 years, it is necessary to test these 'thresholds' by observing the kinetics of physically based mechanisms involved in crack initiation and propagation. This approach may find that material below this threshold can, given time, also prove susceptible to PWSCC.

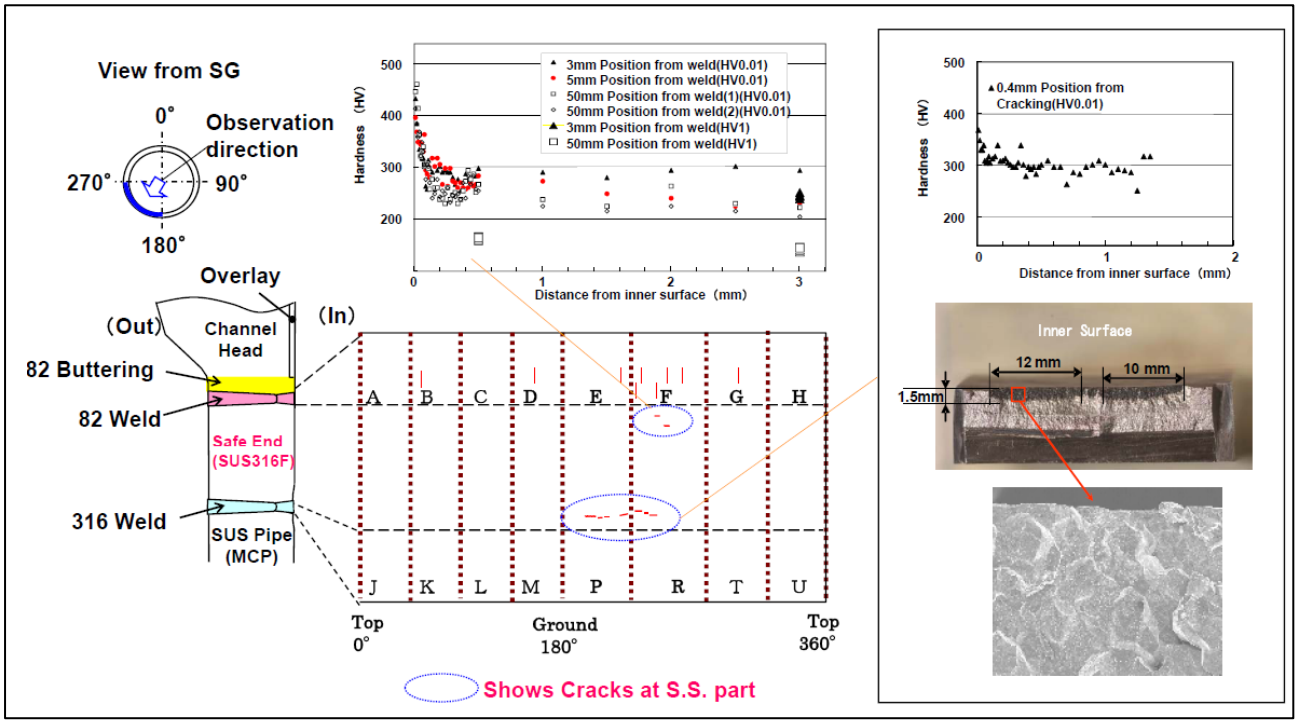

Figure 8. Schematic summarising the detail of IGSCC observed at the Mihama 2 unit. Cracking occurred within the 316L safe end HAZ at the connection between the hot leg primary piping and the inlet nozzle of the steam generator [34].

6.4. Stress Corrosion Cracking Mechanisms

Stress corrosion cracking is a broad type of degradation mechanism that can be activated provided the following criteria are satisfied: i) a susceptible material; ii) the application of tensile stress; and iii) a corrosive environment. Within these conditions several distinct propagation mechanisms are possible and currently there is no universal mechanism that can adequately describe cracking across the spectrum of environments, materials and stress conditions.

There have been many proposed mechanisms to describe environmentally assisted cracking that range from anodic dissolution at the crack front, at low potentials, to hydrogen assisted cracking at higher potentials. However currently there is no consensus on any definitive mechanism that can describe stress corrosion cracking; rather it has been the subject of robust debate between various researchers [36,37]. The mechanisms may vary in applicability depending on the materials, environment and applied stress intensity. Below is an overview of the mechanisms proposed for SCC within the environment of high temperature water.

6.4.1. Slip-Dissolution Mechanism

This proposed SCC propagation mechanism, also referred to as the slip-oxidation model, was advanced by F.P. Ford and P. Andresen into a quantitative model and built upon a number of previous observations where crack propagation rates could be correlated with oxidation current density and the strain conditions at the crack tip [38]. Ford acknowledges that this is not the only mechanism by which stress corrosion cracking can propagate; however, it is argued that it can be reasonably applied to characterise environmentally assisted cracking of austenitic stainless steels in high temperature water typical in light water reactors [39].

The crack is hypothesised to grow periodically as the protective oxide film at the crack tip is repeatedly ruptured under the influence of stress, exposing the metal to the environment where metal dissolution or oxidation occurs, which advances the crack front. Immediately after film rupture the dissolution, or oxidation, rate of the exposed metal is high; however, this rate is retarded as the film grows. The formation of a protective film in the environmental conditions is a necessary component of the mechanism since the unstrained crack sides

must have a significantly lower dissolution rate compared to the crack tip to prevent the crack becoming a blunt notch. Crack progression is therefore a repeated process of film rupture at the crack tip and reformation as illustrated in the Figure 9.

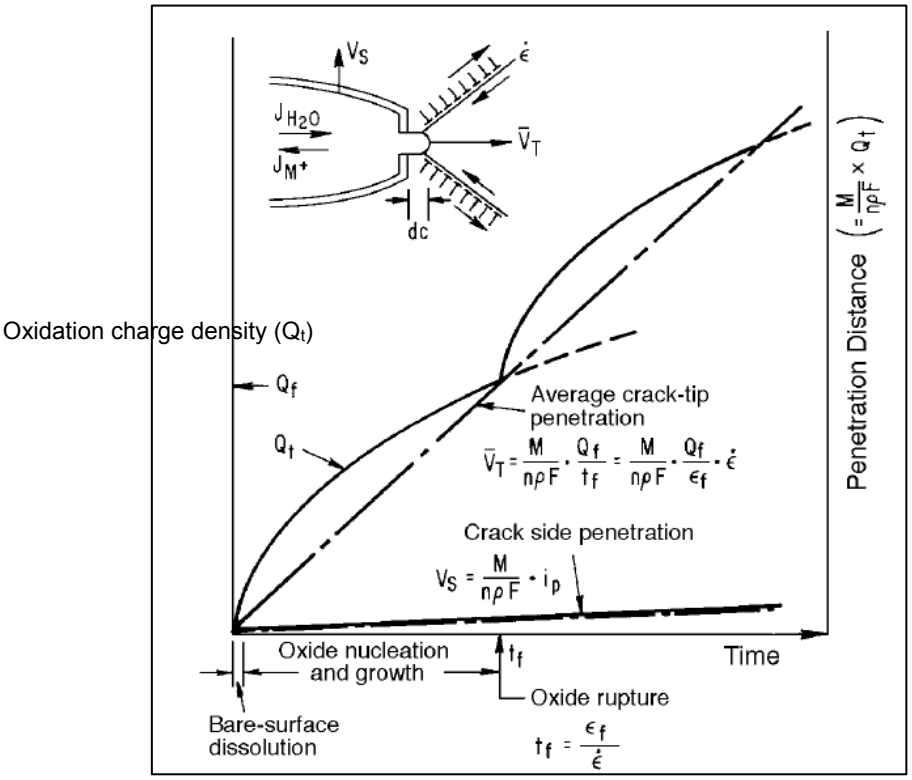

Figure 9. Schematic of the slip dissolution model with oxidation charge density at the crack tip (Q_t), as well as penetration distance plotted during repeated film rupture events. In this plot the above features are compared between the crack tip and crack sides over time [39].

The equation in Figure 9 invokes Faraday's laws of electrolysis to describe the average crack propagation rate in terms of the rate of metal dissolution at the crack tip. For a given material the constants in the expression are M and ρ representing the atomic weight and metal density respectively, n, the number of valence electrons transferred in each metal dissolution ion and F, Faraday's constant. Thereafter Q_f represents the total charge transferred from the metal to the oxide during a single rupture and repassivation event. This factor is dependent on environmental conditions such as crack tip chemistry and temperature. Finally ε_f is the strain required to fracture the film at the crack tip while $\dot{\varepsilon}$ is the strain rate.

The model breaks down the above expression further to express Q_f as an integral of a measureable maximum current, i_0, which decays over the time, defined by the power term, n, for a single rupture and reforming event. The full expression for the rate of crack propagation at the crack tip, $\bar{V}_t$, is given by:

Equation 1 $$\bar{V}_t = \frac{M}{z\rho F} \cdot \frac{i_0 t_o^n}{(1-n)\varepsilon_f^n} \dot{\varepsilon}_{ct}^n$$

with z the number of electrons involved in the oxidation event of a metal atom, i_0 is the initial current density of a bare metal surface for a short time of t_0, n is a constant that will dependent on the material composition and environmental condition at the crack tip, and ε_f is the fracture strain while $\dot{\varepsilon}_{ct}$ is the strain rate at the crack tip.

However the inputs into these expressions are not easily measured and therefore the model is calibrated with measurable inputs for defined conditions. Therefore while the expression appears to be phenomenological it uses empirically measurable parameters to solve the value for, in particular, n. These would include: environmental factors such as oxygen concentration, alloy composition and electrochemical potential; measurable reaction rates at the crack tip; and strain conditions such as stress intensity, K, and loading frequency.

The advantage of this quantitative model is its versatility by predicting crack propagation rates across a spectrum of strain conditions from static loads (stress corrosion), increasing loads (strain-induced cracking) and cyclic loading (corrosion fatigue). This is illustrated in Figure 10 below where the corrosion and mechanical contributions to the total crack propagation rate is given for various strain rates.

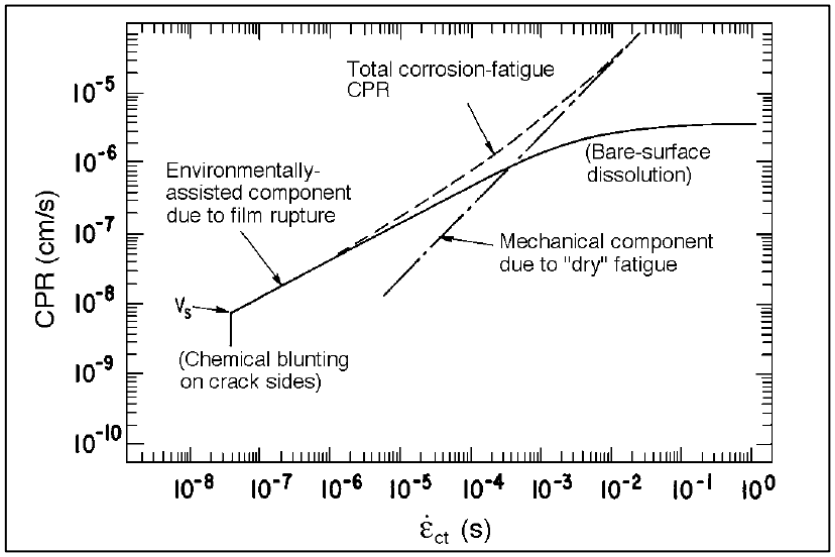

Figure 10. Crack propagation rate (CPR) according to the slip dissolution model as a function of strain rate at the crack tip ($\dot{\varepsilon}_{ct}$), highlighting the dominant crack advancing mechanism in different strain rate regimes [39].

The model has been criticised for, amongst other issues, its reduction of fundamental Faraday's equation to a relation that is empirical in nature [40,41]. Its treatment of a crack progression as an average of many rupture and reforming events along the crack front has also been criticised, where Hall has proposed an alternative differential rate equation to

better describe the phenomenon [41]. Ford concedes that some simplification was necessary for the verification of the model with laboratory data in order facilitate the solving of the computations [39].

There is better agreement between crack velocities and current densities for intergranular cracking than transgranular cracking; the latter appearing to have additional mechanical component to assist the crack propagation rate [42]. Therefore the slip dissolution model is considered suited to predicting IGSCC, and within this type of mode has been successfully correlated with a comprehensive laboratory database of austenitic stainless steel and nickel based materials across a range of conditions, see Figure 11 [39,43]. More recently, other researchers have proposed modifications to the model to better describe the crack tip strain rate with more fundamental and less empirical basis [44]. Therefore it is likely that the model will continue to evolve from empirical towards the more fundamental.

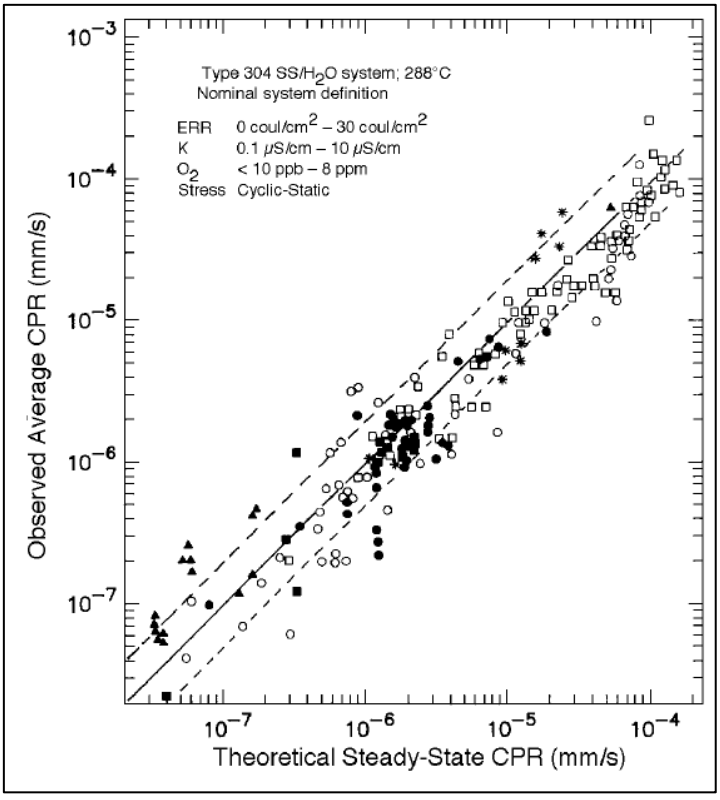

Figure 11. Reasonable correlation between the theoretical predicted crack propagation rates of 304 and 316 stainless steel and an observed laboratory database for a range of environmental and loading conditions [39].

Note that the slip-dissolution mechanism predicts crack propagation rates; however, it does not address crack initiation.

6.4.2. Surface Mobility Mechanism

Galvele has proposed an alternative mechanism to describe environmentally assisted cracking that is related to crack tip dissolution but involves the surface diffusion of vacancies, which is the rate limiting part of the mechanism [45]. This is a generalised mechanism describing stress corrosion cracking not specific to light water environments.

The author is critical of the mechanisms that involve anodic dissolution at the crack tip since the overpotential required to release atoms at the crack tip would be greater than for atoms located on the flat crack surfaces, or other discontinuities where the binding energy is lower. In particular, Galvele does not consider the slip dissolution mechanism to be adequate since the current densities generated by passivation of a surface film in various systems after rupture cannot be reconciled with SCC rates. The position is in disagreement with the findings of Ford and Andresen, although these authors relate crack growth rates to repassivation rates which decrease with time [38].

Essentially the mechanism involves dissolution of metal atoms at favourable locations adjacent to the crack tip. This dissolution would then generate vacancies at the surface of the metal which migrate towards the crack tip where they, under the influence of the tensile stress, are annihilated and in so doing propagate the crack tip forward. The mechanism is described schematically in Figure 12.

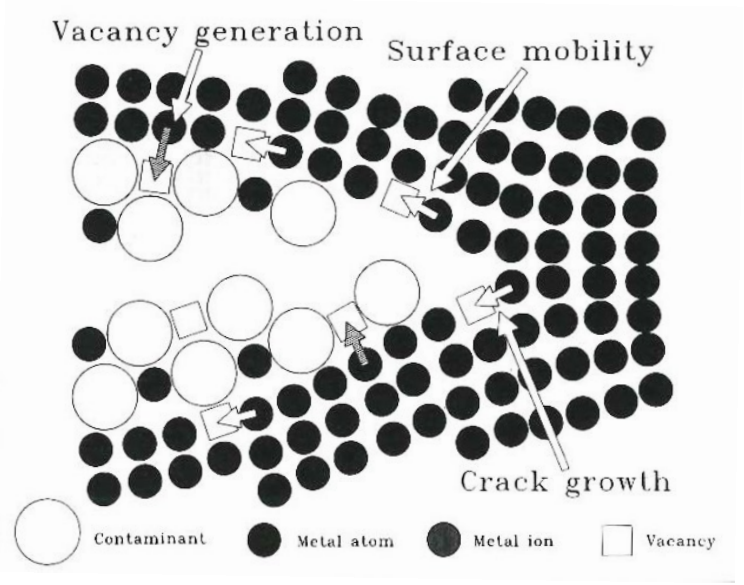

Figure 12. Schematic describing the Surface Mobility Mechanism with an ionic contaminant (oxide) [45].

The mechanism has a quantitative model to describe crack propagation rate which is related to stress, temperature and critically the surface diffusion coefficient and the distance the vacancies travel to the crack tip. Since in this mechanism crack propagation is dependent on vacancy formation and diffusion to the crack tip, the model is derived from equations describing the concentration of vacancies in a metal. With the addition of diffusion coefficients the model of crack propagation rate (CPR) is given by:

Equation 2 $$cpr = \frac{D_S}{L}[e^{\left(\frac{\sigma a^3}{kT}\right)} - 1]$$

D_s is the self diffusion coefficient, L the distance the vacancies diffuse, σ the stress at the crack tip, a is atomic size, k the Boltzmann constant and T the temperature in kelvin. The environment at the crack tip plays a key role in the creation of vacancies, either by encouraging dissolution or by growing surface films with cation vacancies. It also increases the surface diffusivity of the vacancies.

The model has been used by Galvele to predict the SCC propagation rates in several metal/environment combinations. However, the model is reliant largely on knowing the dynamics of surface diffusion in a particular metal/environment combination (D_s and L), to which the author concedes that there is little knowledge regarding the molecular mobility of contaminated metal surfaces [46]. This aspect of the model has been criticised by Gutman who suggests that the model is open to “fitting and manipulations” in order to appear accurate in SCC prediction [37].

Other criticisms of the model include how the vacancy formation was derived from creep processes (Hirth and Nix) which occur within volumes rather than on surfaces[37]. In real cracks, which form a plastic zone around the notch, it has been shown that the tensile stress peaks at the edge of the plastic zone within the volume ahead of the crack tip, see Figure 13 [47]. Therefore this changes the dynamics of the model, which should include bulk diffusion in addition to the accelerated surface diffusion in the presence of contaminants. Indeed this would affect the mechanism itself from purely surface phenomena to one that includes bulk diffusion through the volume.

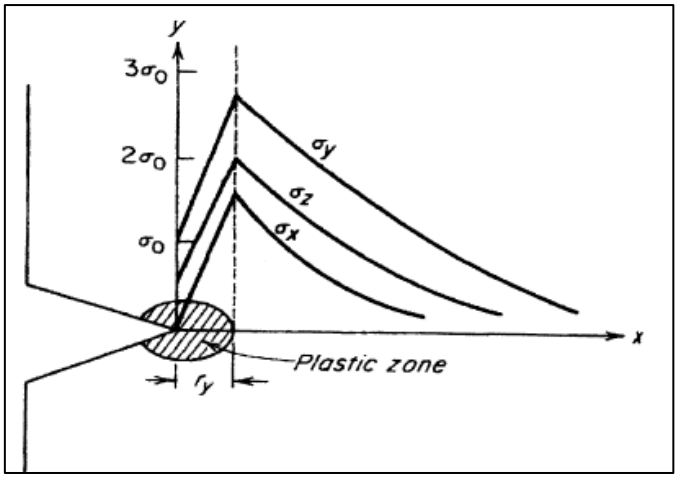

Figure 13. Elastic/plastic stress distribution beneath a notch in plane strain with tensile stresses approaching zero at notch surface and peaking at the edge of the plastic zone, after J.F.Knott [37].

The surface mobility mechanism is presented as a universal mechanism to describe stress corrosion crack propagation applicable in all metal/environments. However, as with the slip dissolution model, it does not describe the initiation process.

6.4.3. Internal Oxidation Mechanism

Scott and Le Calvar initially proposed internal oxidation in 1993 as a mechanism by which stress corrosion cracking can propagate in the context of IGSCC of nickel based alloys in high temperature water [48]. The theory is based on observations from surface oxidation of nickel based alloys when exposed to high temperature (500 - 1200°C). At the lower end of this temperature range intergranular internal oxidation predominates as the mechanism driving the oxide reaction. Similar observations were noted in materials exposed to primary water temperatures (≈300°C) and therefore by extension the authors suggested that IGSCC in light water reactor environments, particularly in relation to alloy 600, is propagated by internal oxidation [49]. This proposed mechanism relates specifically to stress corrosion cracking cases at high temperature.

The mechanism involves the diffusion of atomic oxygen from the metal/oxide interface into the base metal where it oxidises the more reactive constituents of the alloy, e.g. chromium. Since the disorder at grain boundaries is conducive to diffusion kinetics, oxidation is more likely to occur along grain boundaries ahead of the crack tip. Consequently the oxidised grain boundary is embrittled and aids intergranular crack propagation under the application of a tensile stress.

Some high resolution observations have been made to support intergranular oxidation; however, there are no conclusive observations made as yet that unambiguously favour it above any other mechanism [49]. For example, Thomas et al. have observed crack tips exposed to PWR primary water type conditions that resemble those of higher temperature internal oxidation structures, where Cr_2O_3 was observed at the leading edge of the crack with isolated pores immediately ahead of the crack along the grain boundary, see Figure 14 [50].

a) b)

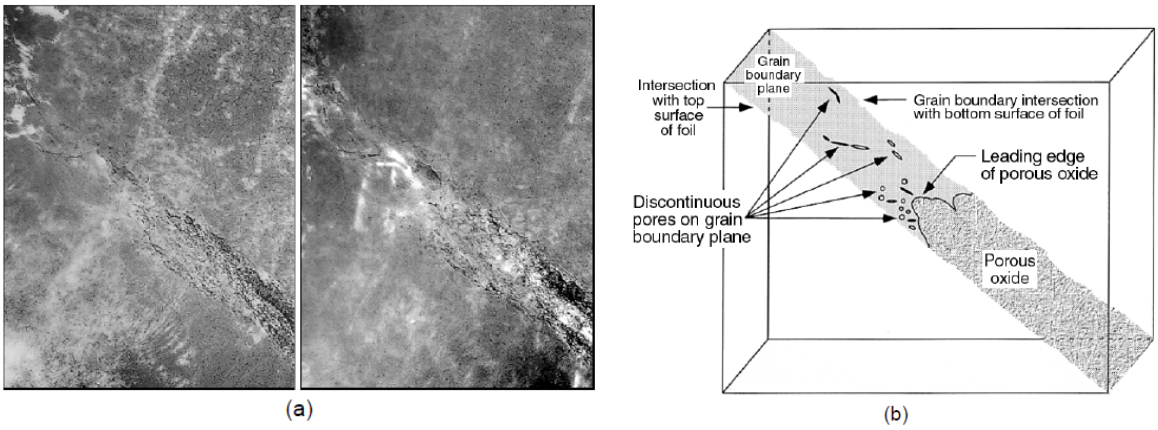

Figure 14. Stereoscopic TEM images are shown in (a) of IGSCC within a sample of alloy 600 that had been exposed to simulated PWR primary water. The structure of a grain boundary plane that included an intergranular crack tip is reconstructed in a schematic (b) indicating discontinuous pores ahead of the continuous oxidised grain boundary [50].

The proposed internal oxidation has been criticised from a few angles. Firstly, Staehle highlights that intergranular oxygen diffusion rates in metals, albeit with limited data available, appear to be too slow by orders of magnitude to account for measured crack growth rates [51]. Secondly, the theoretical activation energy for cracking with a rate determined by oxygen diffusion, is significantly higher than what is measured from Arrhenius type of plots.

Scott responded by acknowledging that there is a large discrepancy between the kinetics of oxygen diffusion in nickel and the associated measured environmentally assisted crack growth rates. However, these rates also cannot explain the rates of oxygen induced intergranular cracking, whose mechanism is not disputed, that are observed at higher temperatures [49]. In Figure 15 the measured rates of oxygen diffusion in nickel are compared with oxygen induced cracking and IGSCC at lower temperatures. It is clear that there are several orders of magnitude difference between crack growth rates and oxygen diffusion rates. In a similar way the activation energies between the two cannot be

reconciled. Therefore Scott argues that one cannot dismiss the internal oxidation mechanism purely based on these findings.

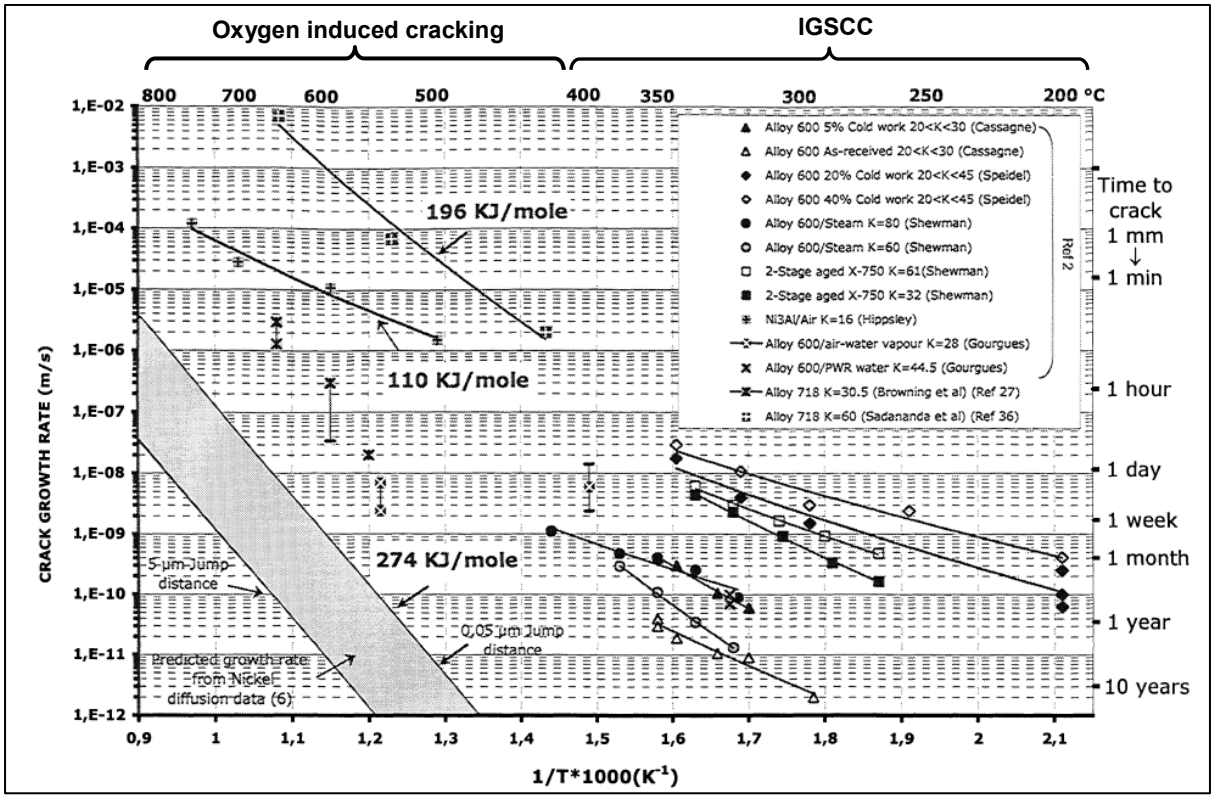

Figure 15. Arrhenius plot of oxygen induced cracking above 425°C and IGSCC below 425°C for various nickel based alloys compared to oxygen diffusion rates data (lower left band) [49].

The influence of stress and crack tip plasticity on the oxygen diffusion rates ahead of the crack tip could offer an explanation to this discrepancy. In creep-fatigue-oxidation studies the accelerated oxygen diffusion rates have been documented for the case of alloy 718; conversely similar acceleration factors could be active in IGSCC [49]. Another possible contributor to increased diffusion rates is the porosity observed in both the intergranular oxide as well as in the grain boundary ahead of the crack tip.

This internal oxidation, or selective oxidation mechanism can be used to describe both initiation as well as propagation of stress corrosion cracking.

6.4.4. Hydrogen embrittlement mechanisms

There are a number of proposed SCC mechanisms where hydrogen is instrumental in crack propagation. Hydrogen, in ionic form, can be adsorbed at the surface and also readily

diffuses into the material ahead of the crack tip where it can concentrate at microstructural features such as dislocations, vacancy clusters, particle matrix interfaces and grain boundaries [52]. Consequently the different ways it interacts with the structure distinguishes the various hydrogen embrittlement mechanisms.

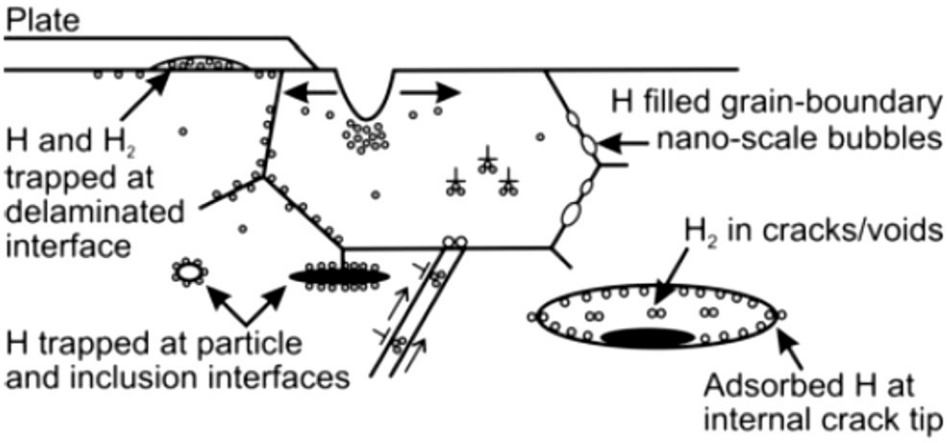

Figure 16. Various microstructural features where hydrogen can concentrate and facilitate crack propagation [52].

The mechanisms, which are dependent on the material/environment system, can be categorised in three distinct types according to the influence of hydrogen: i) where hydrides are stable; ii) enhanced local plasticity mechanisms; and iii) hydrogen induced decohesion mechanisms [53].

In the first category the embrittlement essentially involves hydrogen diffusion ahead of the crack tip into the zone of stress concentration, the formation of brittle hydrides which crack under the applied stress and consequently advances the crack tip [42]. It has been shown that hydrides are stable in alloys containing group Vb metals (V, Nb, Ta) as well as Zr, Ti, Mg and Pd [42]. Since these elements are not included in significant quantities in either 304 or 316 type stainless steels these mechanisms will not be elaborated on in this review.

The second category is hydrogen enhanced local plasticity (HELP) which, as described by Birnbaum, is a mechanism where hydrogen immediately ahead of the crack tip reduces the elastic stress fields and encourages dislocation mobility [53]. Quite counter-intuitively hydrogen in this mechanism promotes plasticity on a localised scale, rather than embrittlement normally associated with hydrogen related degradation of materials. The enhanced plasticity results in crack propagation by ductile flow at the crack tip. Strong laboratory evidence has been found to support the mechanism including in situ TEM observations of crack propagation. This mechanism has been considered as one of the more significant mechanisms for environmentally assisted cracking in high temperature primary water [10,54].

Another mechanism in the same category was proposed by Lynch who described it as the adsorption induced dislocation emission model (AIDE) [52]. Adsorbed hydrogen could facilitate dislocation emission at the crack tip when alternative slip occurs.

However, since slip in both the HELP and AIDE mechanisms are not related to grain boundaries, crack propagation tends to be transgranular in this category. Therefore the enhanced plasticity mechanisms cannot account for the IGSCC normally associated with PWSCC in nickel based alloys and austenitic stainless steels.

The third category, hydrogen enhanced decohesion (HEDE), can promote intergranular crack propagation. It relies on the premise that atomic hydrogen diffuses ahead of the crack tip and reduces the cohesive metallic bonding forces [42,52,53]. In the case of intergranular cracking grain boundaries provide suitable hydrogen traps and consequently lower the energy required to break these intergranular bonds. Direct measurements of the influence of hydrogen, or other species, to cohesive bond strength have, however, been a challenge. Definitive supportive evidence for HEDE has been reported on work conducted using iron-silicon single crystal alloys[42]. This mechanism is considered to be most likely in cases of non-hydriding alloys where intergranular cracks have propagated without any significantly observed slip or deformation adjacent to the crack path[52].

6.4.5. Summary

The review of quantitative and qualitative models described in the preceding sections certainly is not an exhaustive summary of all models, nevertheless, those included are all frequently referred to in the context of stress corrosion cracking in a high temperature water environment. Such a review highlights the diversity in the proposed mechanisms. Assuming that all mechanisms may hold some validity in different conditions, stress corrosion cracking should be considered a broad term representing a group of quite distinct mechanisms. Therefore it may not be feasible to work towards a reliable universal model to describe stress corrosion cracking for all material, environments and stress combinations.

However, the mechanistic model that is most consistent with intergranular stress corrosion cracking observed in typical austenitic stainless steels and nickel based alloys used for pressure boundary materials is the internal oxidation mechanism. In the time since many of these models were first proposed analytical techniques have advanced and allowed detailed crack tip observations to be made. Through such investigations the crack tips appear to lag

behind oxidised grain boundaries [14,15,55,56]. Several studies have also established that the mechanical strength of an oxidised grain boundary is compromised [11,57]. By this understanding the rate at which primary water stress corrosion crack can grow is limited by the rate of intergranular oxidation and, as will be discussed, the time to initiate such cracks is also likely similarly dependent. For this reason the present investigation will focus on the surface and intergranular oxidation kinetics of 316L stainless steel in the primary water environment in the absence of any influence of stress.

On a separate point, the above mechanisms, with the possible exception of the internal oxidation model, describe crack propagation. The calibration of these quantitative models can be performed with relative ease in the laboratory with several laboratory techniques at the researcher's disposal. Experimental techniques such as direct current potential drop (DCPD) monitoring the crack growth of specimens can be monitored in situ. This enables crack growth rate response to be measured while various parameters such as temperature, chemistry, applied loading etc. can be adjusted.

However, the kinetics of crack initiation is a critical element in the overall aim to predict when or whether PWSCC could manifest in the primary circuit of a PWR. The experience of the alloy 600 cracking is a good example where approximately 5 years passed before the first cracks were detected [26]. In contrast to crack propagation modelling, initiation kinetics remains a challenge. Traditional techniques to gauge the SCC susceptibility of materials with U-bend, humped specimens or slow strain rate testing all represent accelerated types of testing but whether data gained from these types of tests can be applied to non-accelerated conditions remains questionable.

6.5. Oxidation

Before the models of oxide growth are discussed it is necessary to provide an overview of the high temperature oxide structure that develops on austenitic stainless steels.

6.5.1. Oxide Structure

It is well known that the original thin Cr_2O_3 oxide that protects stainless steels in ambient air conditions grows and changes its structure when exposed to primary water conditions [19]. This original structure transforms to create dual oxide structure with a porous outer Fe-rich oxide layer that grows on the surface, and an inner Cr-rich oxide that penetrates into the

metal [31,58–60]. The outer layer is porous and is formed by the growth of discreet crystallites on the original surface, while the inner layer is more dense with much finer grained nano-crystalline oxide that acts as the protective passive layer for the alloy, see Figure 17.

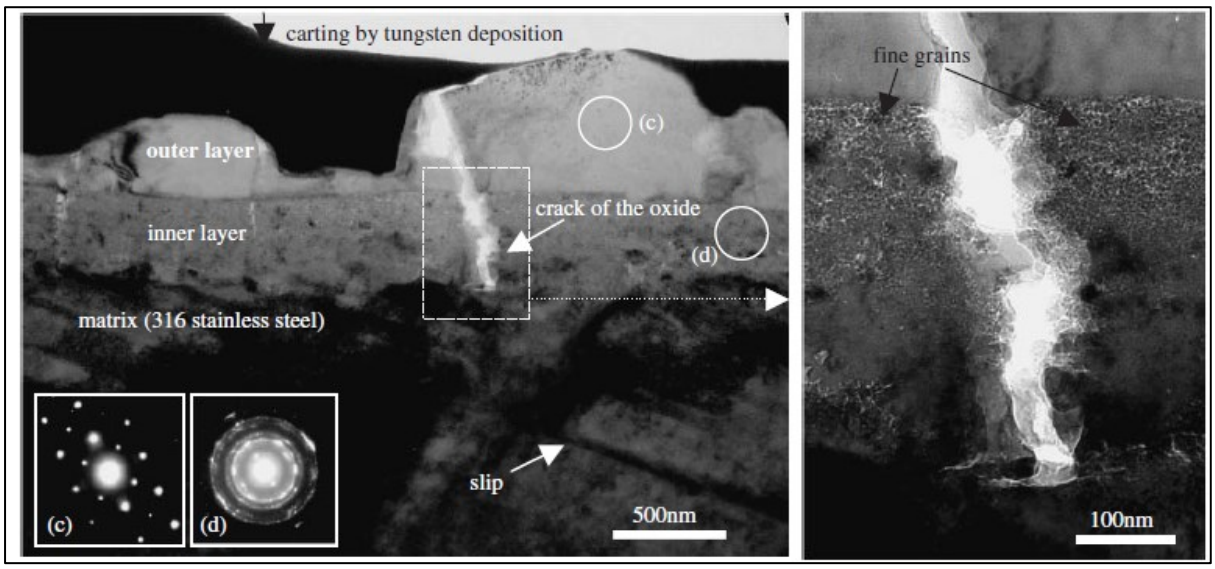

Figure 17. TEM images of oxide formed on cold worked 316 type stainless steel exposed to a simulated PWR primary water for approximately 500 h during a constant extension rate test (CERT). The inserted diffraction patterns from the outer (c) and inner (d) oxide regions are indicative of a crystalline spinel structure and a fine grained nanocrystalline structure respectively [61].

Many publications have characterised the structure of the oxide layers formed on austenitic stainless steels after exposures to high temperature water in the range of 260°C - 360°C. The techniques used to analyse the structures have included grazing incident X-ray diffraction (GIXRD), X-ray photoelectron spectroscopy (XPS), Raman spectroscopy, as well as the analytical microscopy techniques of TEM with diffraction patterns, energy dispersive spectroscopy (EDS) or Auger electron spectroscopy (AES) with depth profiling. The results are largely agreeable with the inner Cr-rich layer being described as an FCC spinel of type $FeCr_2O_4$ albeit with some variation in measured stoichiometry, and traces of Ni also reported [58,59,61–64]. While the outer layer is composed of larger magnetite Fe_3O_4 crystallites, possibly with traces of Ni, deposited on the surface [58,61,62,64,65].

Terachi et al. further substantiated this characterisation by noting the most thermodynamically stable oxide structure. Given that the corrosion potential of 316 stainless steel is reported to be approximately -830 mV in the PWR primary water environment, relevant Pourbaix diagrams indicate that $FeCr_2O_4$ would be the most stable product [61], see Figure 18.

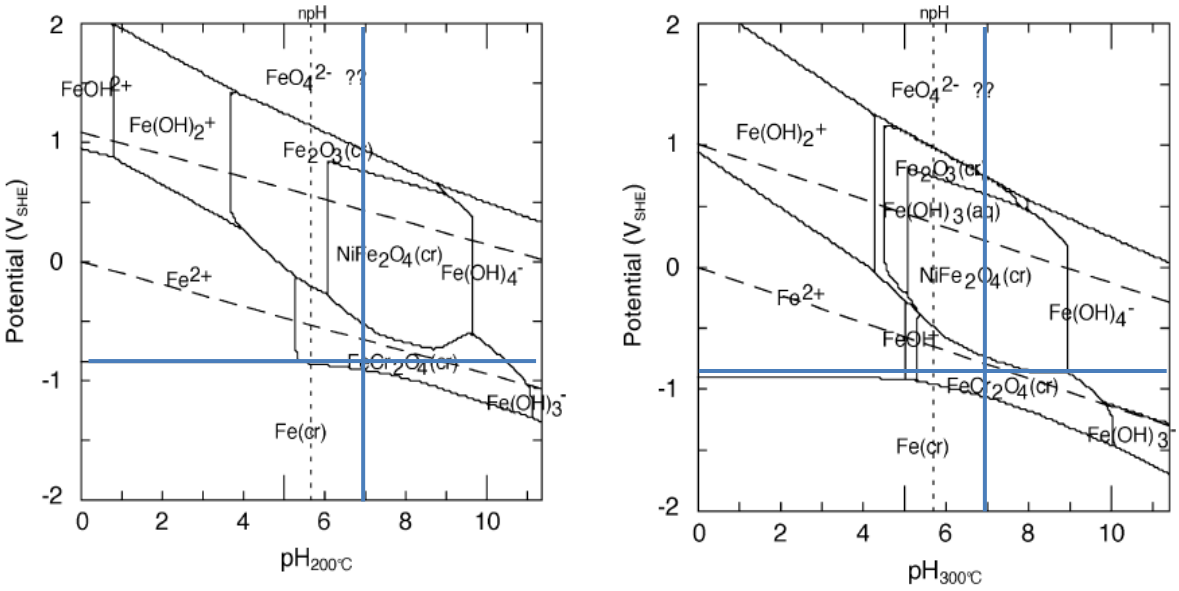

Figure 18. Pourbaix diagram for iron species in the Fe-Cr-Ni ternary system at 200°C and 300°C with dissolved metal concentrations at typical nuclear primary water purity (10^{-8} molal) [66]. Note that the most stable product for 316 SS at pH_T =7 and potential of -830 mV within this temperature range is $FeCr_2O_4$.

Variations in the spinel structure of AB_2O_3 (with Fe, Cr and Ni occupying the A and B sites) have been observed within the oxide of a single sample particularly at high diffusion regions such as grain boundaries. These variances have been attributed to the Fe occupying cation vacancy positions in the oxide while in transit through to the solution interface [59].

Some have differed in their characterization of the Cr-rich spinel from the $FeCr_2O_4$ type oxide observed by those cited above. However these opposing observations were made either after exposures at lower temperature of 250°C, where Cheng observed Cr_2O_3, $Cr(OH)_3$ and CrO_3 present [67], or at higher potentials such as Lu, who reported Cr-rich oxides present as Cr_2O_3 after exposures at 288°C with dissolved oxygen content of 2 ppm [14].

6.5.2. Metal Segregation at Oxide Interface

Whilst studying the oxide structure that develops on austenitic stainless steels exposed to the primary water environment, a number of composition segregation effects have been observed in the alloy adjacent to the oxide interface.

Firstly, immediately ahead of the penetrating inner oxide interface within the stainless steel alloy a Ni enriched zone develops. This enrichment has been observed ahead of the penetration oxide interface from the surface as well as ahead of the oxidised grain

boundaries [14,58,59,63,65,68]. Figure 19 below gives an example that clearly shows the Ni enrichment from energy filtered TEM (EFTEM) elemental maps of a cross section through a 304 stainless steel surface exposed to simulated primary water. In the same figure the atomic concentration profile from atom probe tomography is given, which highlights that together with the Ni enrichment is an associated chromium depletion layer within the metal adjacent to the interface.

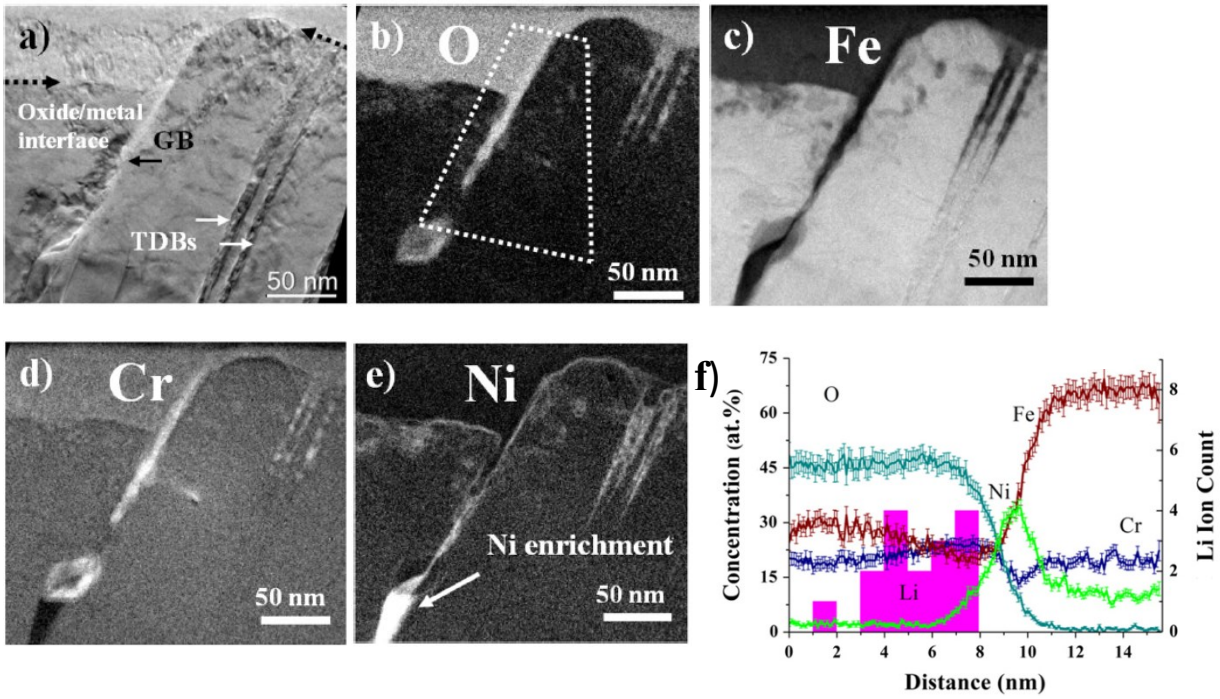

Figure 19. TEM images of a thin film prepared through the surface oxide of a 304 stainless steel sample after 1500 h exposure at 360°C in primary water: a) bright field TEM image of metal/oxide interface including a grain boundary (GB) and twin deformation bands (TBDs); elemental EFTEM maps of b) O, c) Fe, d) Cr and e) Ni showing the preferential oxidation down grain boundaries and slip bands; and f) the atomic concentration profile of each of the elements across the metal/oxide interface (oxide at the left) acquired from atom-probe tomography [59].

This effective segregation of alloy constituents adjacent to the metal/oxide interface is indicative of the relative affinity each has for oxygen available in ionic form within the oxide. Sushko has demonstrated using Density Functional Theory that there is a significantly greater total energy gain with the formation of Cr oxide compared to Ni oxide [69]. The Cr depletion zone in the metal ahead of the advancing interface suggests that it is preferentially leached from the predominantly Fe matrix into the oxide. Whereas the Ni, in comparison to the Cr or Fe, has a lower rate of transfer into the oxide and as a result forms an enrichment zone simply due to the reduction in concentration of the other alloy constituents.

This segregation effect is particularly apparent ahead of the oxide that is advancing down slip bands or grain boundaries. These microstructural features have higher diffusion rates

and therefore the segregation caused by the different rates of transfer into oxide is extended further into the metal along these conduits of greater diffusion. Figure 20 provides an example where Ni enrichment is observed in the metal matrix adjacent to the oxide interface; however, it is particularly evident down the grain boundary ahead of the oxidation [63]. This sample was exposed to an appreciable amount of neutron irradiation known to exacerbate segregation; however, this is consistent with observations from un-irradiated material [59].

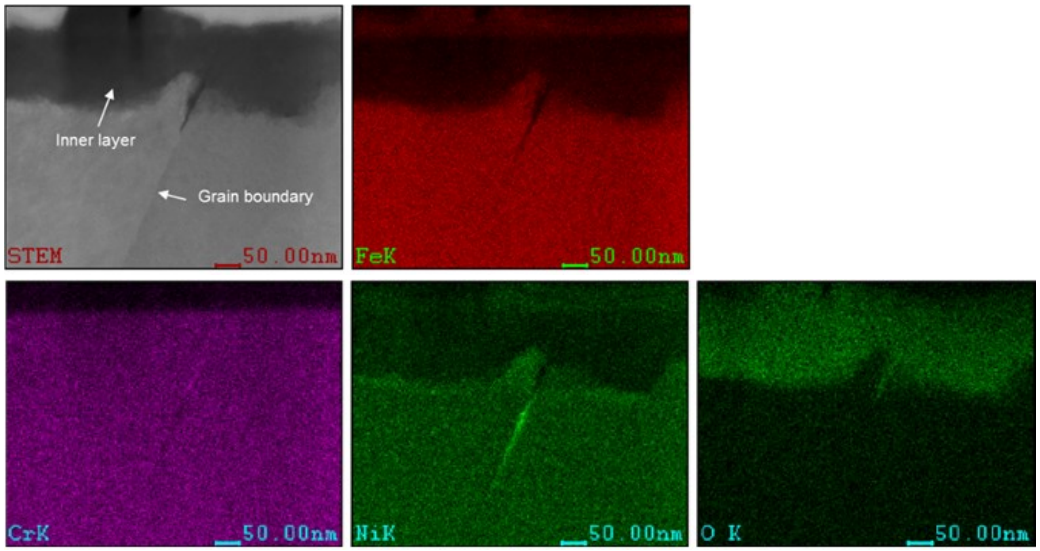

Figure 20. TEM images of a cold worked 316 stainless steel sample of material from a PWR reactor with an irradiation dose of 22 dpa: a) dark field STEM image of FIB section through the surface oxide and EDS elemental maps showing Ni enrichment in the metal ahead of the oxide interface particularly down the grain boundary with associated Cr depletion which is only noticeable in the non-oxidised portion of the grain boundary [63].

6.5.3. Intergranular Oxidation

As discussed in the preceding sections it is evident that the inner Cr-rich layer preferentially penetrates down grain boundaries and deformation bands [59]. This can result in a compromised cohesive strength across the grain boundary[57], and therefore it is generally accepted that oxidised grain boundaries form suitable precursors from which intergranular stress corrosion cracking (IGSCC) could initiate [8,11,13–15].

The advent of the dual beam scanning electron microscope (SEM), combining a focussed ion beam (FIB) together with a conventional electron beam, together with a sample lift-out technique in the late 1990's opened several new sample examination possibilities[70]. One of these being the ability to create polished cross-sections through a surface, at a selected location, in order to examine the surface oxide. This technology offers the advantage of

being able to precisely locate the position of the cross-section on the sample surface, while significantly reducing the time required for sample preparation when considering the alternative of preparing a TEM thin foil specimen using conventional techniques. Therefore researchers have exploited the opportunity to explore how microstructural features like grain boundaries that intersect the surface have influenced the oxidation growth.

By using FIB for the preparation of thin film cross-sections, oxidation propagation was observed to be particularly accelerated down grain boundaries in the Ni based alloys such as alloy 600, previously highlighted to be an alloy particularly susceptible to PWSCC (see section 6.3.1) [13,71–74]. Figure 21 below gives an indication of the intergranular oxide growth possible in two different alloys, with relatively high Ni content, relative to the growth of the oxide at the surface.

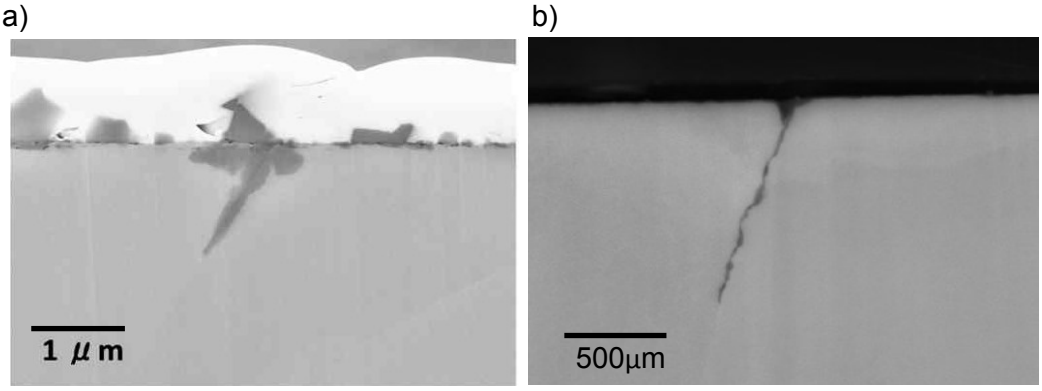

Figure 21. SEM images of FIB prepared cross-sections through the surfaces of Cr-Ni-Fe alloys after exposure to PWR water. Significant intergranular oxidation can be seen in both a) a 32%Ni-16%Cr-Fe alloy[24] and b) a 75%Ni-5%Cr-Fe alloy[73] after exposures to PWR simulated water for approximately 1500 h at 320°C and 360°C respectively.

Kazaki, et al., was able to correlate the rate of intergranular oxidation with the susceptibility to PWSCC in a range of Ni-Cr-Fe alloys [73]. In this study a wide range of alloy compositions were tested for the susceptibility to their potential for intergranular oxidation in the absence of tensile stress and PWSCC susceptibility. It was demonstrated that Ni based alloys with a low Cr content were both susceptible to PWSCC and observed to have high intergranular oxidation rates, while alloys with Cr contents greater than approximately 20 wt% were significantly less susceptible on both accounts. In addition, the Fe based alloys were not susceptible to either PWSCC or significant grain boundary oxidation with Cr contents between 5 – 22 wt%. The austenitic stainless steel alloys of 316, 304, and alloy 800 with nominal Cr contents of 16-23 wt% fall within this composition range and have, thus far, had relatively few PWSCC incidents in service. Figure 22 below provides a summary of the findings from this investigation. Note that the intergranular oxidation measurements

were made using FIB sections from samples exposed to primary water conditions for 1,500 h at 360°C.

a) b)

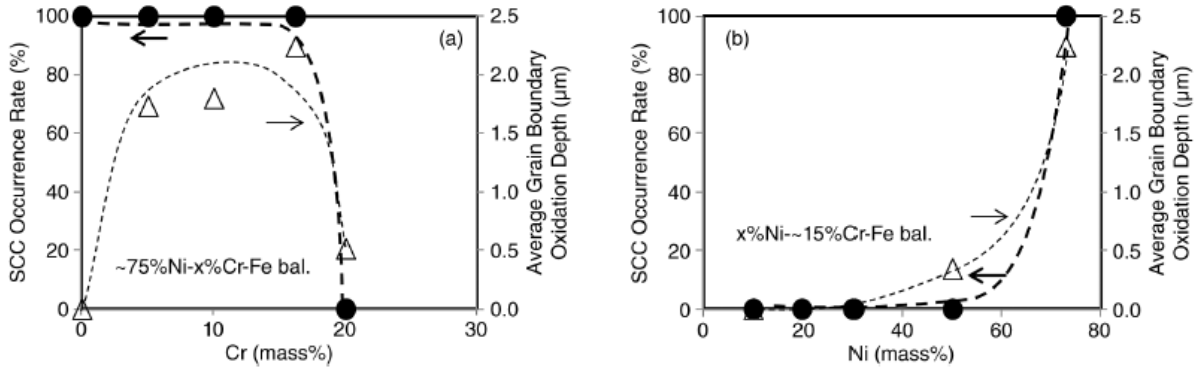

Figure 22. Correlation of susceptibility of Ni-Cr-Fe alloys to PWSCC and their propensity to intergranular oxidation with a) the effect of Cr content in Ni based alloys and b) the effect of Ni in Fe based alloys [73].

With a strong association with PWSCC having been established, the above investigation concluded that the intergranular oxidation behaviour plays an important role in the PWSCC mechanism. Arioka et al. reported similar findings and both have suggested further research is required in order to establish the mechanism to explain the sensitivity of Ni-Cr-Fe alloys to chemistry with respect to their susceptibly to PWSCC and intergranular oxidation [24].

The above investigations found that 316L stainless steel would fall into the category of neither being particularly susceptible to PWSCC nor having a strong tendency to develop marked intergranular oxidation. Nevertheless, in order to develop a credible predictive model of PWSCC initiation in 316L stainless steel, and considering the long term operation of light water reactors, it is necessary to determine the kinetics of intergranular oxidation at different temperatures. None of the above investigations have established such a data set.

Another application of the FIB technique is the automated routine known as ‘slice-n-view’ by which it is possible to reconstruct a 3 dimensional structure of the material. Through a sequence of repeated imaging and incremental milling of the surface the technique captures a collection of images that can be collated into a 3D reconstruction. After the sequence is complete features of interest can be automatically selected using intensity thresholding methods from the set of images. Once the images are reconstructed the features can be analysed in 3 dimensions, which provides an advantage over a 2 dimensional view alone.

Lozano-Perez, et al., used this technique to examine surface and intergranular oxidation of 304 stainless steel after exposure to simulated primary water at 360°C for 1500 h [75]. Their paper was more of a demonstration for the technique rather than a quantitative measure of

oxide growth. It could be criticised for deriving data from sample areas (of the order 20 x 15 μm^2) of each sample which cannot adequately be representative of the sample. Yet the results were able to provide statistical variation of the oxide depth along a single grain boundary and compare the oxidation depth between grains and different boundaries. In particular the study was able to capture the high localised oxide growth at intersecting grain boundaries or deformation bands. The introduction of cold work through unidirectional cold rolling to 20% reduction in thickness showed a possible marginal increase in oxidation depth.

Therefore this automated sequential FIB analysis is useful to extract statistical data from a small sample that includes a single grain boundary or triple point, to study particular microstructural features. However, considering the time required, it is not feasible to apply the same technique across an area that includes a sufficient number of grain boundaries to represent the bulk of an austenitic stainless steel.

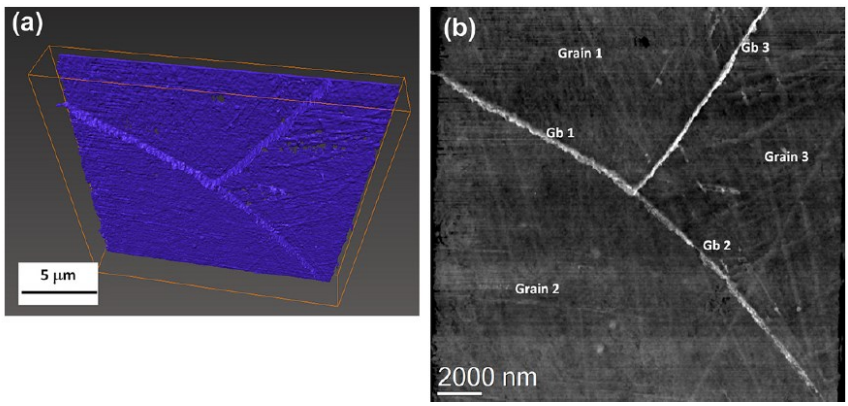

Figure 23. Intersecting grain boundaries on a 304 stainless steel sample exposed to simulated primary water viewed with a) selective 3D reconstruction of the Cr-rich inner oxide showing preferential growth along the grain boundaries, and b) a contour map of the same area with brightness corresponding to the depth of oxide penetration [75].

6.6. Modelling of oxide growth

Over the years a number of different oxide models have emerged to quantify the growth rate of passive films on metals [62,76–79]. Each has been based on observed structure, as well as the growth and stabilisation of passive films, but differed in their interpretation of the processes involved to establish and maintain the film. Nevertheless, all the models attempt to mathematically account for the various electrochemical reactions, the electric field and the migration of ionic species, all of which are necessary to form an oxide layer.

A schematic of the common understanding of passive film growth, in simplistic form, is given below in Figure 24. It is known that when placed in an aqueous solution a potential difference is established between the metal and electrolyte. This potential creates the driving force for surface metal atoms to ionise and bond with oxygen ions to form an adherent oxide film. For the passivation to be effective the film must not be porous, but should form a continuous dense barrier layer. This film will continue to grow until a steady state is reached where the film thickness reaches a maximum due to the dielectric nature of the oxide film that maintains the potential difference. The final steady state thickness will depend on the ease with which ionic species can enter the oxide film and migrate through it under the influence of the electric field.

The mechanisms necessary for the film to grow include the following:

i) Metal dissolution at the metal/oxide interface creating cations (M^+) that occupy either interstitial or substitutional positions in the oxide matrix.

ii) The generation of oxygen anion vacancies within the oxide at the metal/oxide interface.

iii) The migration or diffusion of the oxygen vacancies through the oxide to the oxide/electrolyte interface.

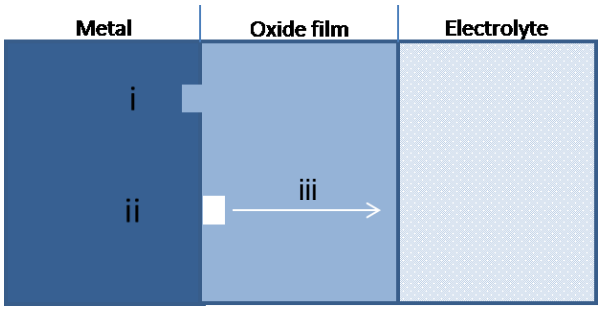

Figure 24. Schematic of the oxide film growth forming a passive barrier between the metal and electrolyte.

While a large amount of work has been published on this subject, there have been a few authors who have produced some critical and comparative reviews of the various models that have proved to be useful reference points [78–80]. Seyeux provides an overview of three distinct but established models describing oxide growth kinetics: the Mott-Cabrera model that is dependent on the migration of interstitial cations through the film for oxide growth: the Fehlner-Mott model that is dependent on interstitial anion migration; and the Point Defect Model which initially was dependent on anion vacancy migration but later evolved to be dependent on interfacial reactions [78]. The first two models were originally developed to describe and predict growth of metallic oxide films when exposed to air, and

consequently they do not consider the potential drop at the oxide/electrolyte interface. In the case of the Mott-Cabrera model, the growth of the oxide at the metal/oxide interface due to the migration of oxygen anions to this interface is not considered. While the Fehlner-Mott model does not consider the contribution from cations that migrate through the oxide from the metal/oxide interface to the oxide/solution interface.

The point defect model (PDM) was initially developed and published by MacDonald et al. in 1981 after the other models mentioned above [76]. This model was principally designed to describe the passive film formation on metals exposed to high temperature water. It was therefore, in contrast, an electrochemically formed oxide film [78].

One of the main distinguishing features of the model to emerge, particularly in later refinements thereof, was how the driving force for film growth differed from other high field models. Films have been observed to rapidly develop when exposed to a conducive environment, either air or electrolyte, but that the rate of growth decreases until a steady state thickness is achieved. The driving force for growth in the high field models of Mott-Cabrera, Fehlner-Mott, Vervey and others, is the electric field strength which diminishes as the film grows [76,78,81]. Whereas the PDM assumes a constant electric field across the film but that the electrostatic potential drops across the metal/film interface, the film/solution interface, and linearly decreases across the film itself; see Figure 25 that includes a schematic of potential across the film [76]. Therefore, the film will grow under the potential difference but a steady state film thickness will be achieved once this potential difference has been accommodated by the potential drop over the film thickness. Another distinguishing feature is that the PDM predicts that film growth occurs at the metal/film interface as opposed to the film/solution interface predicted by the high field models [76].

The PDM was refined and developed over time, and it was later modified to adopt an oxide structure of 2 layers; an inner dense and protective barrier film, and an outer porous layer [76]. The outer layer is formed from the hydrolysis of metallic cations that have migrated through the barrier layer and entered into solution, where they react with water and precipitate on the surface. It is therefore considered a net flux of metal cations that entered the film layer at the metal/film interface, and exited this layer at the film/solution interface to be incorporated in the outer layer. This is consistent with the observations from austenitic stainless steels, where some dissolution of iron in particular at the film/solution interface is necessary to maintain the chromium rich stoichiometry of the inner layer. The dissolved iron cations then redeposit on the surface as magnetite crystals to form the outer layer. The PDM was unique in considering the dissolution reaction at the barrier layer/solution interface [76,82].

Since the PDM has been designed to model the growth of a double layered oxide structure formed electrolytically it has been favoured in the present investigation to model the growth of oxides formed on stainless steels in primary water. Confidence is also derived that the model has been validated in several aqueous studies involving passive film forming materials where there was better correlation between the PDM and experimental data than the alternative models [83–85].

The essential PDM mechanisms that create and annihilate defects to facilitate film growth are illustrated in Figure 25 below, with the corresponding reactions provided as an extract from MacDonald's paper in Figure 26. At the metal/film interface the metal ions enter into the film either to substitutional cation vacancy positions or interstitially within the oxide. It has been reported that Fe and Ni cations migrate interstitially while Cr cations occupy substitutional positions in the oxide [86–88]. Oxygen anions then have the opportunity to replace these vacant positions thus effectively extending the barrier layer interface into the metal, and simultaneously creating anion vacancies. These anion vacancies migrate toward the solution interface where they are annihilated as oxygen anions enter the film.

Note that the mechanism ***i*** in Figure 25 corresponds to reactions 1, for substitutional cations, and 2, for interstitial cations, in Figure 26, mechanism ***ii*** corresponds to reaction 3, and mechanism ***iv*** corresponds to reaction 4.

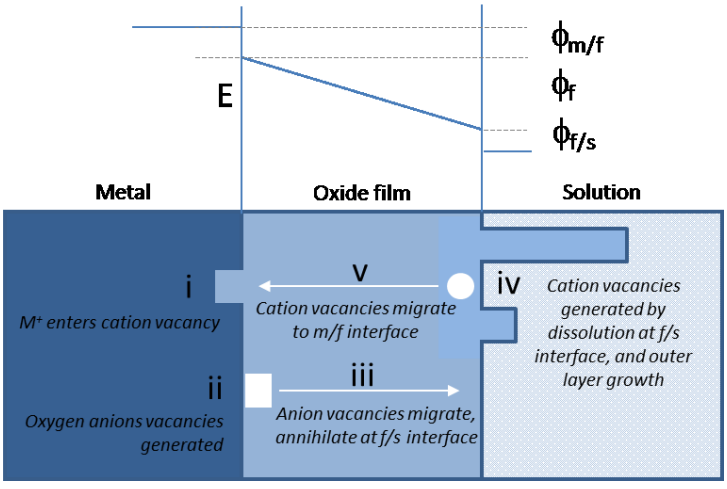

Figure 25. Schematic of the point defect model essential mechanisms of metal passive film oxide growth.

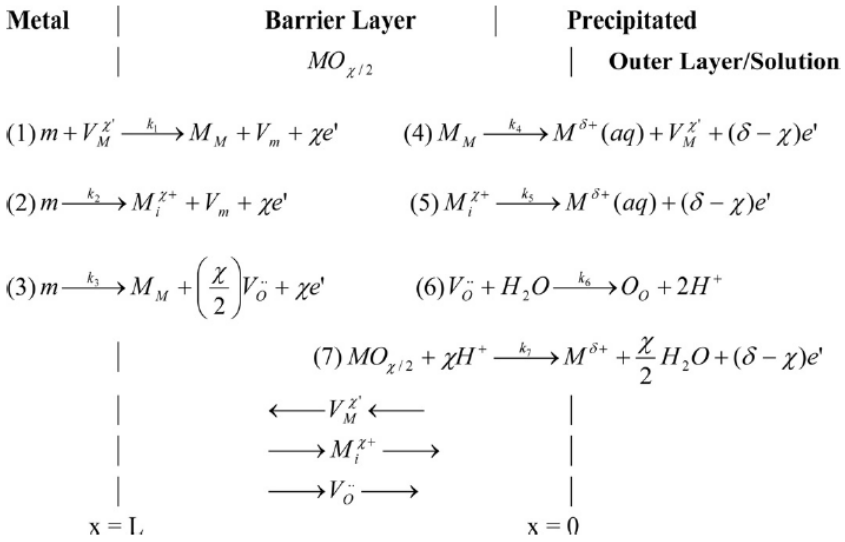

Legend

m	- metal
χ	- cation oxidation state in barrier layer
V_m	- metal vacancy
$V_M^{\chi'}$	- cation vacancy
$M_i^{\chi+}$	- cation interstitial
$V_{\ddot{o}}$	- oxygen anion vacancy
$M^{\delta+}(aq)$	- cation in outer layer/solution interface
M_M	- cation in cation site
O_o	- oxide anion in anion site
$MO_{\chi/2}$	- barrier layer oxide

Figure 26. Summary of the reactions considered by the point defect model in the growth of the inner barrier and precipitated outer layer of a metal in solution [76].

6.6.1. Mixed-Conduction Model

The mixed-conduction model (MCM) was developed by Bojinov as a modification of the Point Defect Model to introduce a more explicit relationship between the point defect structure and the electronic properties [89]. It was originally designed to apply to stainless steels exposed to light water reactor primary water. Essentially the model quantitatively describes the growth of the inner layer of oxide in terms of:

i) A metal dissolution reaction rate constant at the metal/film interface. This process involves metal moving into the oxide as cations, whilst injecting vacancies into the metal, thereby allowing oxygen ingress.

ii) The diffusion-migration rate to the film surface. The transport of the cations generated at metal/film interface is considered to occur either interstitially or via vacancies in the film.

Each of the metal constituents (i.e. Fe, Cr and Ni) are treated separately and given their own rate constants and diffusion. Later developments of the model included the additional consideration of the outer layer, treated as porous layer since it is composed of discreet crystallites, as well as the possible addition of cations from the electrolyte i.e. Zn. The MCM is described schematically in Figure 27 for an Fe-Cr-Ni alloy with each of the alloy constituents treated with separate rate constants at the metal/inner layer interface as well as the inner layer/outer layer (IO/OL) interface.

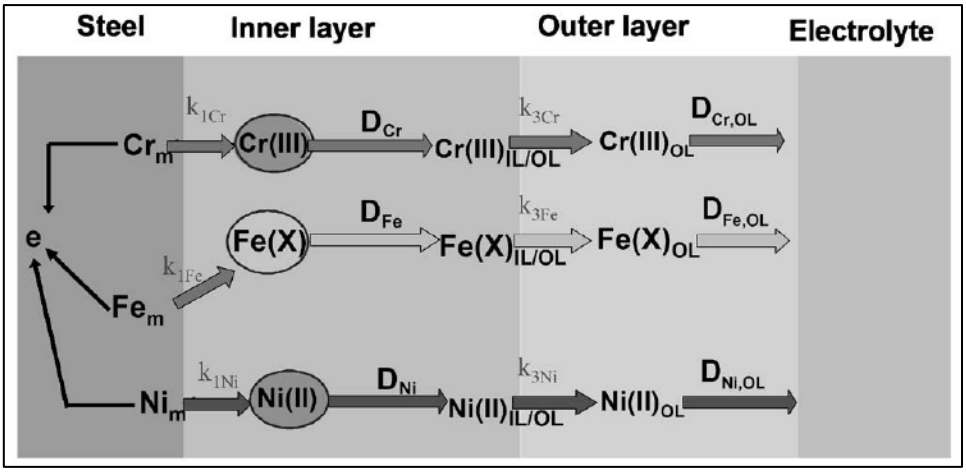

Figure 27. Simplified view of the process considered by the MCM, with k representing the reaction rate at the interfaces, while D represents the diffusion of the various constituents [62].

Predicting the kinetics of film growth amounts to solving a set of simultaneous equations that include an Arrhenius type of temperature dependency, and the electrical field strength within the inner layer. A procedure has been described to determine the respective rate constants and transport parameters through experimentally fitting the sigmoidal curves to oxides grown at various temperatures and solution potentials.

Thereafter the calibrated parameters were used fairly successfully to predict oxide film growth when compared to published data acquired from Ziemniak for 304L material exposed in PWR water, and including Zn additions to the water chemistry [90].

The model includes some declared simplifications including that the field strength remains constant in the inner oxide layer during the growth, and that no oxide layer is considered present when the material is first exposed to the high temperature water. However, consistent with other models such as the point defect model, the MCM does not consider the contributions of the cathodic reactions to the overall mechanism, nor the transport of hydrogen ions.

7. EXPERIMENTAL TECHNIQUES

7.1. Material

The material used in this investigation was sourced from a single length of seamless stainless steel pipe which was procured for industrial use at a PWR Nuclear Power Station, which met the requirements for grade TP316L in the ASME SA312-07 standard, equivalent to UNS S31603 and commonly known as type 316L stainless steel. The material was received with a solution annealing heat treatment at 1050°C, consistent with the manufacturer's certificate given in Appendix A.

The chemical composition of the material was independently verified using an external laboratory which used inductively coupled plasma mass spectrometry to measure the relative proportions of elements present in the material. The values are given in Table 3 which are consistent with values quoted by the heat analysis supplied in Appendix A, and meets the chemical specification of ASME SA312-07 grade TP316L.

Table 3 Measured chemistry of material (in mass %) versus the TP316L grade standard.

	C	Mn	S	P	Si	Cr	Mo	Ni	Cu	Al	V	Fe
TP316L	≤ 0.035	≤ 2.00	≤ 0.030	≤ 0.045	≤ 1.00	16.0-18.0	2.00-3.00	16.0-18.0	-	-	-	Bal
Measured	0.017	0.63	0.07	0.018	0.87	16.3	2.54	13.3	0.34	0.101	0.066	Bal
Material certificate 1009-76	0.021	0.790	0.011	0.036	0.450	16.51	2.098	11.23	-	-	-	Bal

The mechanical properties of the material were measured using a tensile test where specimens from a section of material were prepared according to ASTM A370-12a. Two flat tensile specimens were prepared with a gauge length of 60 mm, width of 12.5 mm, thickness of 6 mm and a fillet radius at the reduced width of 20 mm. They were pulled in tension using a Zwick universal tensometer from which yield strengths (determined using the 0.2 % offset method), ultimate tensile strength (UTS) and elongation could be measured with the tensile charts given in Appendix B. All values met the standard criteria for grade TP316L in the ASME SA312-07 which are given in Table 4.

Table 4. Measured mechanical properties verses the TP316L grade standard.

	Yield Point (MPa)	UTS (MPa)	Elong. %
TP316L	≥ 170	≥ 485	≥ 35
T002	239	542	73.5
T003	245	548	74.8

7.2. Material Conditions

The influence of cold work has proved to be significant with respect to PWSCC. Therefore in order to investigate the influence of cold work on the intergranular oxidation kinetics, the material, which was received in the solution annealed condition, was cold worked either through uniaxial tensile extension or by cold rolling in a single direction.

The cold rolling, conducted in the laboratory, reduced the thickness by 20% of the original. Since samples from the rolled material would need to be inserted into the titanium short duration autoclave loop (see 7.7), the final target thickness was approximately 1.2 mm (to allow up to 0.2 mm loss during polishing). Two different thickness were used nominally 6 mm and 1 mm. Since the 6 mm thickness would need to be reduced to 1 mm by machining there was a concern that the through thickness residual surface stress profile would be disrupted resulting in reduced surface residual stress. While the original samples were rolled from a nominal 6 mm thickness, later samples were rolled to the target thickness so no further machining was required. The latter samples resulted in a nominal increase in residual stress but not sufficient to disqualify the former samples.

The 6 mm samples were prepared from a single length of material that was cold rolled with 3 passes to achieve a reduction in thickness of 21.0%. Two lengths cropped from the original pipe section were rolled. The final thickness was achieved in 3 passes for both lengths of material which ended with reduced thickness values of 20.7 % and 21.1% respectively, see Table 5.

Table 5. Cold rolling reduction in thickness measurements.

	6 mm	1 mm	
Original thickness	6.13	1.21	1.51
Final thickness	4.84	0.96	1.19
Ave. reduction in thickness	21.0 %	20.7 %	21.1 %

During cold rolling the surface of the material is prevented from flowing since it is constrained by contact with the rollers while the majority of the flow is apportioned to the centre of the material. Consequently rolling introduces a distribution of residual stresses

through the thickness of the rolled material with the surfaces having a tensile residual stress which is balanced with an internal compressive stress. Therefore the 20% cold rolled samples represent a material condition that has both a high dislocation density but also a surface residual stress. In an attempt to isolate the role of residual stress and dislocation density, the material was uniaxially pulled in tension to the equivalent cold work but without the residual stress.

The following equations can be used to calculate the true strain in samples from cold rolling and tensile deformation.

Cold rolling:

$$\varepsilon_R = \frac{2}{\sqrt{3}} \ln\left(\frac{h_i}{h_f}\right)$$

Tensile deformation:

$$\varepsilon_T = ln\left(\frac{l_i}{l_f}\right)$$

Where h_i and l_i are the initial thicknesses and h_f and l_f are the final thicknesses respectively. Using these equations the equivalent true strain to 20% reduction in thickness by cold rolling is 30% elongation by tensile deformation.

$$\varepsilon_R = \frac{2}{\sqrt{3}} ln\left(\frac{1}{0.8}\right) = 0.258$$

$$\therefore if\ \varepsilon_T = 0.258 = \ln\frac{l_i}{l_o}, then\ \frac{l_i}{l_o} = 1.29,\ \ equating\ to\ a\ 29\%\ elongation.$$

In addition to a 30% elongated condition a 20% elongated by uniaxial tension condition was introduced to represent an intermediate cold work material condition. Therefore in total 4 material conditions were created for the exposure tests to study the influence of cold work on intergranular oxidation.

The level of cold work was compared between the samples using both hardness measurements and XRD data, as shown in the following sections.

7.3. Hardness

The hardness of each sample in the matrix was measured with between 4 and 7 measurements using a Vickers hardness indenter with a 3kg load. Before each set of samples was measured the operation of the hardness indenter was verified with a standard block (BCS0160-02739). The hardness indenter was considered acceptable for use provided the result was within 10 HV of the quoted value of 210.5 HV30 for the standard block, which was the case on each occasion that the hardness of the samples were measured.

Table 6 below indicates the difference in hardness as well as the spread in results between the various material conditions. Theoretically, the 30% elongated samples should have equivalent cold work as the 20% cold rolled material. However, the latter proved to have marginally increased hardness, which may partly be accounted for by the additional cold work partitioned to the surface. The 20% cold rolled material also had more variation across the samples, as could be appreciated from the more complex strain distribution.

The hardness between the four material conditions can be compared in Figure 28, which gives an indication of the consistency in the hardness between the samples within each material condition.

Table 6. Average and standard deviation of the material conditions.

		Ave. Vickers Hardness (3kgf)	Std. Deviation
Annealed		138.1	6.6
20% Elongated		235.9	6.8
30% Elongated		252.6	12.9
20% Cold rolled	6 mm	286.6	16.1
	1 mm	269.1	17.3

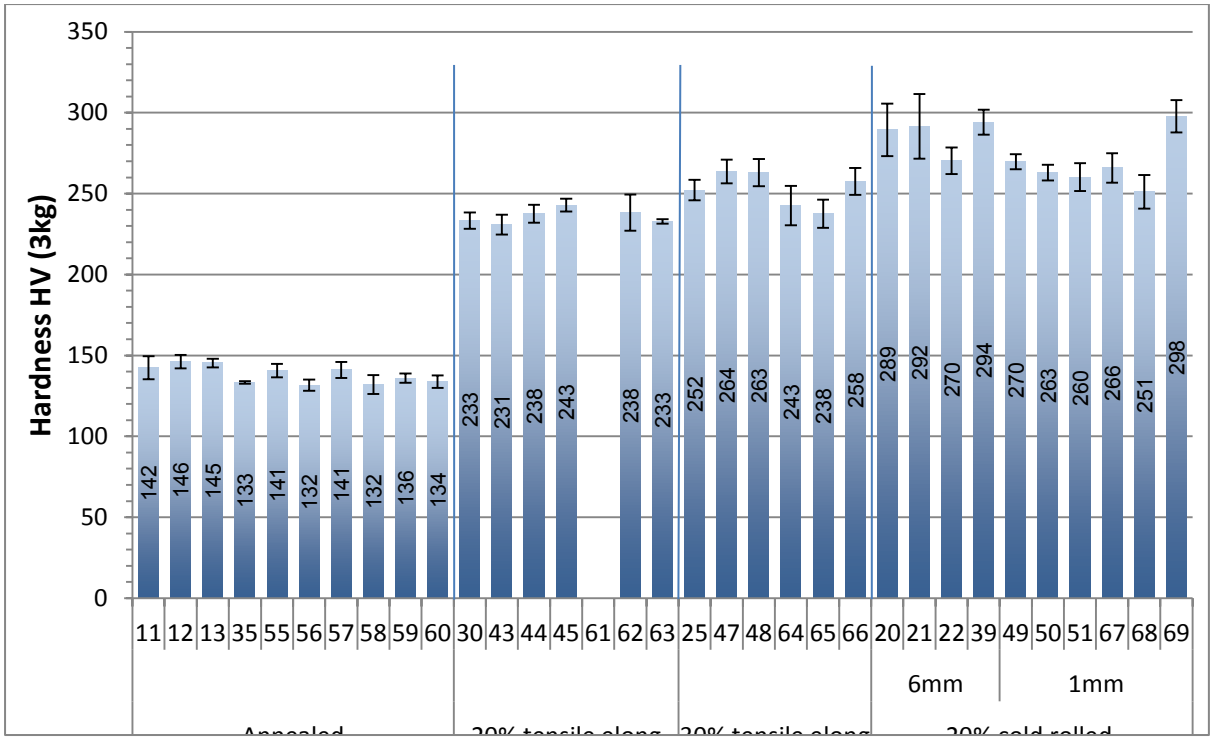

Figure 28. Average Vickers hardness of all samples across the material conditions (3kgf), with error bars indicating the associated standard deviation.

7.4. Sample Preparation

From the four material conditions produced from a single piece of 316L pipe, several samples were prepared and characterised prior to them being exposed to the primary water environment.

The size of the samples was largely defined by the titanium loop used for the short duration tests, which required the dimensions of the samples to be 12 x 11 x 1 mm in order to fit into their sample slots with the least disturbance to the flow of water. The stainless steel autoclaves were more accommodating of sample dimensions, nevertheless the samples for these tests were 1 mm in thickness and slightly longer to enable one end to be secured to the autoclave internals via an insulated bolt, see Figure 29.

The samples were cut to the required dimensions using electric discharge machining (wire cutting) and were mounted in resin for metallographic preparation. To remove any residual strain introduced during sample preparation all samples were polished with successively finer media starting with SiC polishing paper (1500 – 2400 grit), followed by diamond paste (3 µm and 1 µm), and finally polishing for 20 min with a colloidal silica suspension. Subsequent EBSD mapping confirmed that the polishing technique resulted in a negligible

amount of residual deformation on the surface with indexing rates in excess of 99% for the annealed samples.

To ensure traceability each sample was indented on the sample surface with a unique binary code using Vickers hardness indents. Similar indents were used to mark out an area of the samples for EBSD mapping. While each map was 1 x1 mm^2 the indents were spaced 2 x 2 mm^2 around the area to prevent the residual deformation around the indents from encroaching on the mapped area. These reference markers were useful in locating the mapped regions after the exposure tests which in some cases had oxide growth that masked the microstructure.

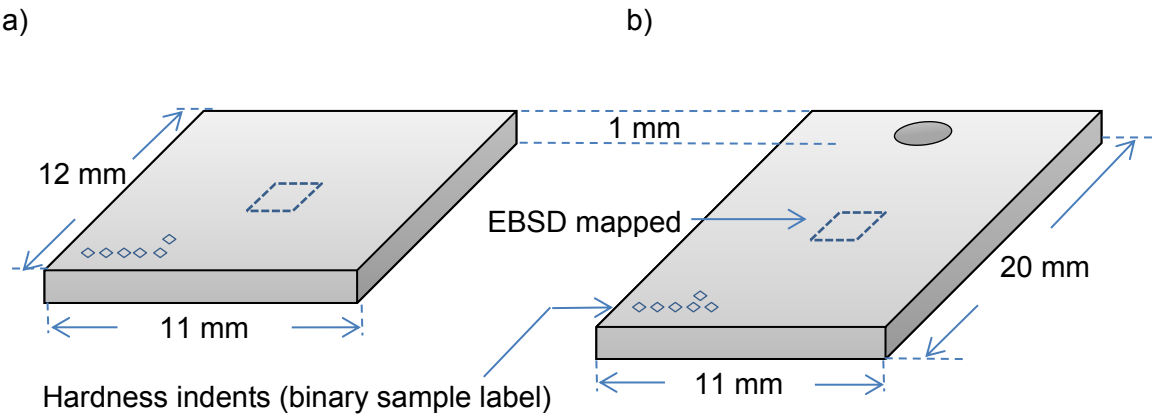

Figure 29. Design of samples for exposure tests for a) short duration tests in the titanium loop and b) longer duration exposures in the stainless steel autoclaves.

7.5. EBSD

Electron back-scattered diffraction (EBSD) data were acquired from the samples prior to them being exposed to primary water. The growth of the oxide during the exposure to primary water, particularly for the longer durations, would have prevented the possibility of obtaining any quality orientation data from the samples' surface after the exposure tests.

This technique involves analysing the diffraction pattern, called a Kikuchi pattern, produced from a source of tilted electron beam with respect to the sample surface which is captured on a phosphor screen. Provided the possible crystal structure in the material is known and the pattern quality is good enough, which largely depends on the degree of deformation within the surface of the material, an orientation can be assigned to the point where the beam was striking the sample's surface i.e. it can be indexed. Therefore by scanning across a sample surface in discrete steps with a processor to automatically index the orientation at

each point a crystal orientation map can be generated. Such a map provides the opportunity to quantitatively analyse many aspects of the microstructure such as preferred orientation (texture), grain size, phase distribution etc. But in this project grain boundaries could be categorised as random or co-incident site lattice boundaries, and the orientation of each oxidised grain relative to the surface could be determined.

For each sample a 1 x 1 mm^2 EBSD map was acquired with a step size of 1 µm. Each of the maps were acquired with Jeol JSM-7001F scanning electron microscope (SEM) fitted with a field emission gun (FEG), set with an accelerating voltage of 15 KeV and the sample tilted to 70.0° with respect to the incident beam.

It would not be possible to obtain any orientation data by EBSD from the samples subsequent to the exposure tests due to the growth of surface oxide.

Examples of the EBSD maps are given in Figure 30 of an annealed and a 20% cold rolled structure. The EBSD maps serve to confirm that the mapped areas as suitable for oxidation observations. Firstly, the maps capture sufficient grains (typically >800 grains in the 316l material) to be considered representative of the sample. Secondly, as seen from the annealed sample, it confirms that the sample preparation has not introduced any traceable deformation into the surface; therefore, the exposed surface is representative of the material condition as a whole. Thirdly, the 1 µm step size of the maps has revealed the grain structure in sufficient detail from which orientation information, coincident site lattice boundaries (CSLB), and regions of higher deformation can all be confidently extracted.

a) b)

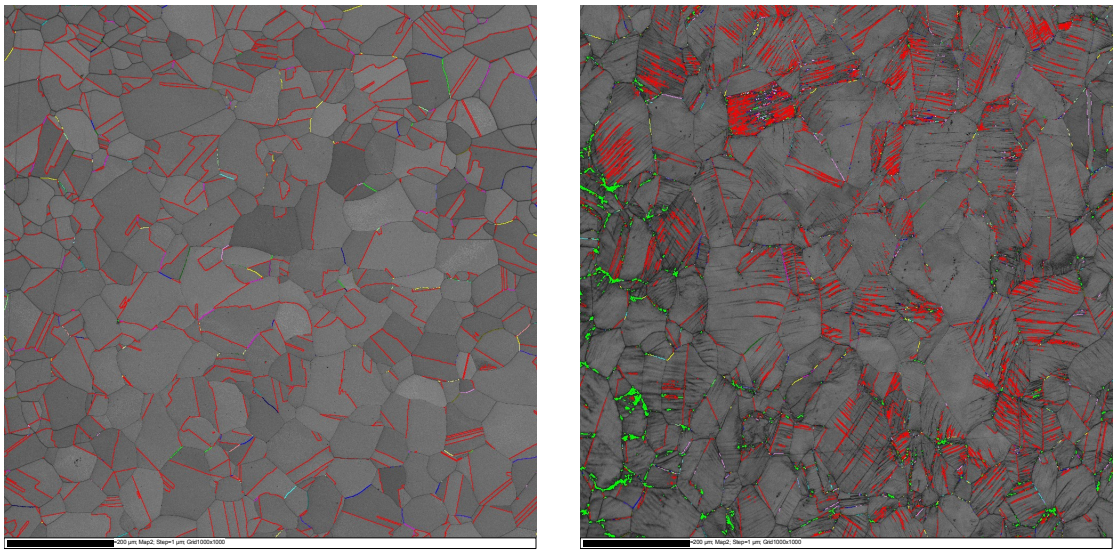

Figure 30. Full size 1x1 mm EBSD maps of a) an annealed and b) 20% cold rolled samples. Band contrast is assigned to a greyscale range and CSL boundaries are shown in red.

7.6. X-ray Diffraction

One of the reasons for introducing cold work into the material through cold rolling was to create residual stress at the surface. The 20% cold rolled samples would have equivalent cold work to the 30% elongated samples, but the effect of residual stress could be independently observed.

The residual stress of the samples was measured using X-ray diffraction (XRD), which measured the superficial stress state without penetrating too deeply into the sample. Using a primary electron beam acceleration voltage of 20 kV and current of 4 mA, an X-ray beam is produced by focussing this beam at a Mn target which then emits X-rays. The maximum depth of penetration in this configuration is approximately 10 μm [91,92]. From these results the principal stress tensor was obtained by quantifying the maximum stress (tensile or compression) and calculating its direction. In addition the level of cold work could also be quantitatively compared between the samples.

The method uses X-rays to measure the lattice spacing of a targeted set of crystallographic planes. When stress is applied to a metal crystal the lattice spacing (d) will change, in turn changing the Bragg diffraction condition (Equation 3). Thus the lattice spacing can be measured by X-ray diffraction, which is sensitive enough to detect the angular shift in 2θ of the diffracted peak when compared to the theoretical unstressed value. It can be shown that the stress within the material can be calculated from the lattice spacing measurements of two different angles of ψ, provided for by the two detectors. However by acquiring lattice spacing measurements for several ψ angles, the stress was calculated from the slope of the plot of lattice spacing (d) vs $\sin^2\psi$, which provides a more accurate result.

Equation 3 $$n\lambda = 2dsin\theta$$

With greater cold work introduced into the material the lattice will be faulted with increased number of dislocations and also include distortions. These effects broaden the targeted diffracted peak width. Therefore an indication of the amount of cold work introduced into the sample can be measured from the full width at half maximum (FWHM) of the peak, after fitting a peak curve to the acquired intensity data over 2θ [91].

The XRD residual stress measurements were performed on a portable difractometer where the source and detectors were attached, in aligned fixed positions, to a goniometeric arm that allows rotations about ψ, as well as ϕ, see Figure 31. The $\sin^2\psi$ technique was used to

determine the residual stress at 11 angles of ψ. In addition the measurements were repeated through 3 angles of phi: 0° (aligned to direction of strain), 45° and 90°.

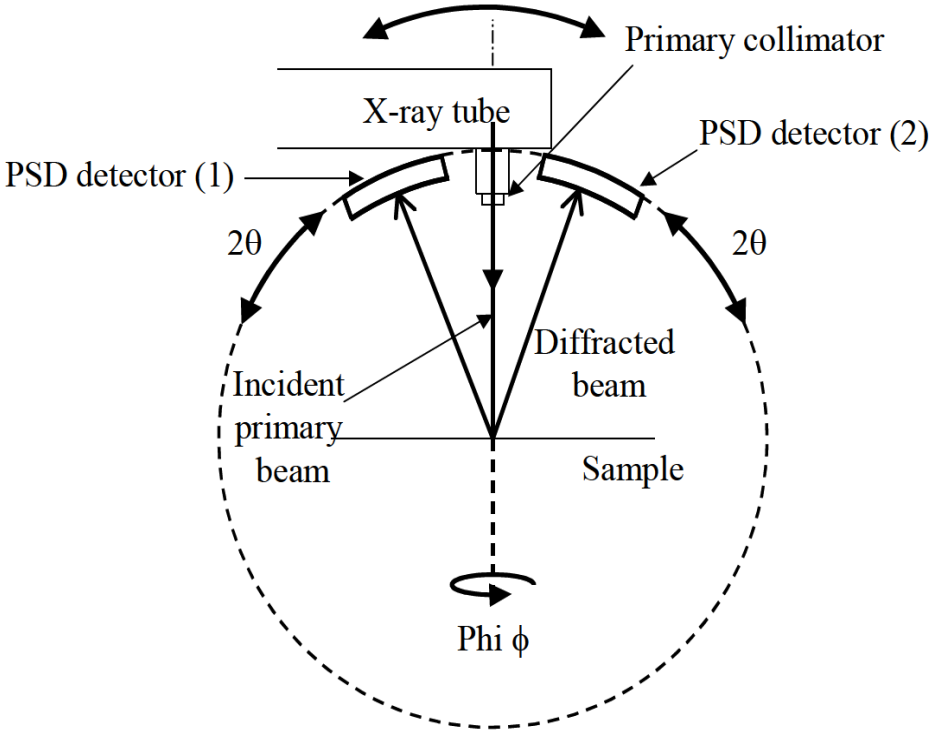

Figure 31. Schematic of the portable XRD, with the two detectors fixed and aligned on either side of the incident X-ray beam. With the sample stationary the instrument rotates and acquires X-ray peaks at various angles of ψ, and swivels about the sample normal to repeat the measurements at 3 angles of ϕ for a tri-axial principal stress calculation[93].

A Mn source was used to generate the X-rays, and the measured peak was the k_α emission line diffracted off the {311} planes. A 1 mm aperture was selected and the incident beam was visually aligned to strike the sample in the same area as the 1 mm^2 EBSD map (which was demarcated by remote hardness indents).

Before each set of measurements a standard high stress sample (ID: SSS112610-19), -675±35 MPa, as well a zero stress sample (ID: LSS1110-1) were measured, as well as the high stress sample after each set, to verify the equipment's reliability for measurements.

Maximum principal stress tensors were determined for each sample tested, see Figure 32 below. For each measurement the direction associated with the maximum tensile stress, or in some cases the least compressive stress, was recorded. It is evident that the cold rolled samples did maintain a level of residual tensile stress at their surface, which is expected to be balanced by internal compressive stress. Those samples which were rolled to a final

1 mm nominal thickness achieved a greater surface tensile stress compared to those finished at nominally 6 mm, and subsequently reduced to a 1 mm thickness. It is suspected that the latter samples lost some surface stress by removing some of the balancing internal stress when machined.

In addition the degree of cold work could be compared for each set of material conditions. A Pearson fit was applied to each XRD peak measured and an average FWHM was calculated for each sample represented in the matrix. This FWHM, with associated standard deviation given in the error bars, is represented in Figure 33.

A general trend is seen with increased peak broadening with greater cold work introduced. Samples 11-13 have significantly broader peaks than the remaining annealed samples, considered to be residual cold work from polishing. The preparation technique was subsequently improved to achieve a deformation free surface, confirmed by the corresponding EBSD maps being clear of surface deformation with an indexing rate >95% for annealed samples. The 20% cold rolled samples have slightly broader peaks than the 30% tensile elongated samples, which in theory should have equivalent cold work. A similar result was observed when comparing the average hardness data between the samples in Figure 28. This suggests that while the average cold work introduced between these conditions may be equivalent, greater cold work may be partitioned to the surface of the cold rolled samples while the cold work is expected to be more uniformly distributed through the tensile elongated samples.

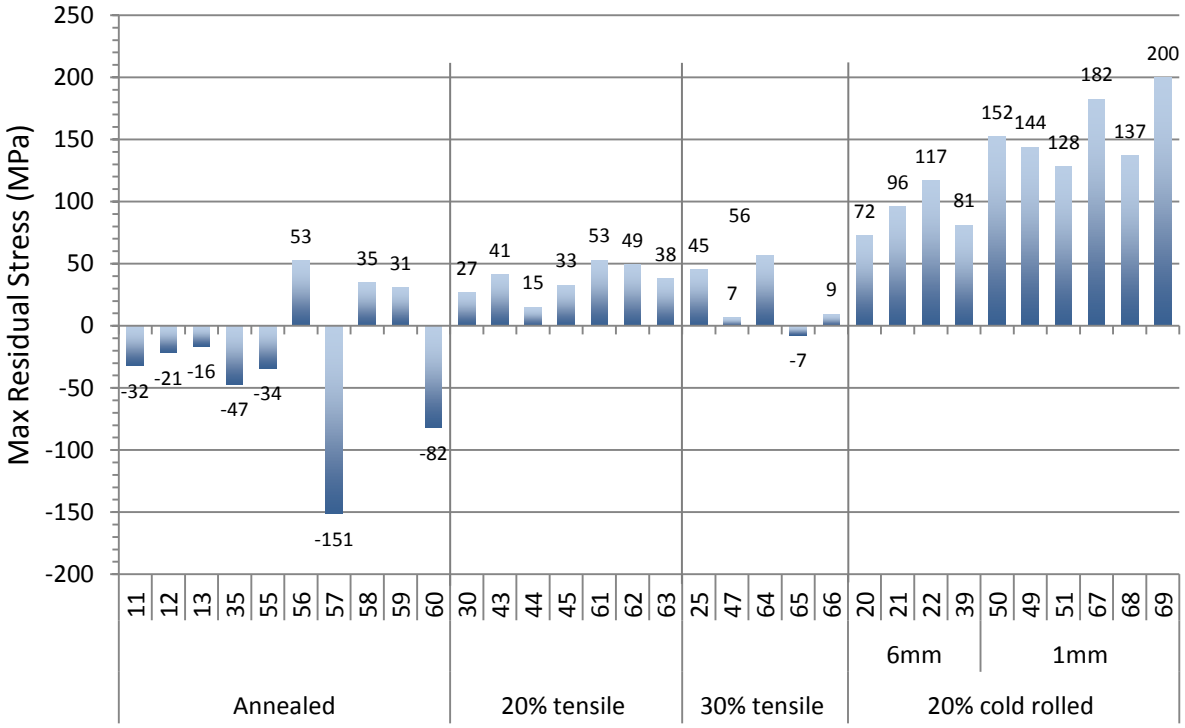

Figure 32. Tensile stress maxima of samples within matrix. Negative values represent compressive stresses. The cold rolled samples, particularly those rolled to 1mm, achieved higher residual tensile stresses than the other conditions.

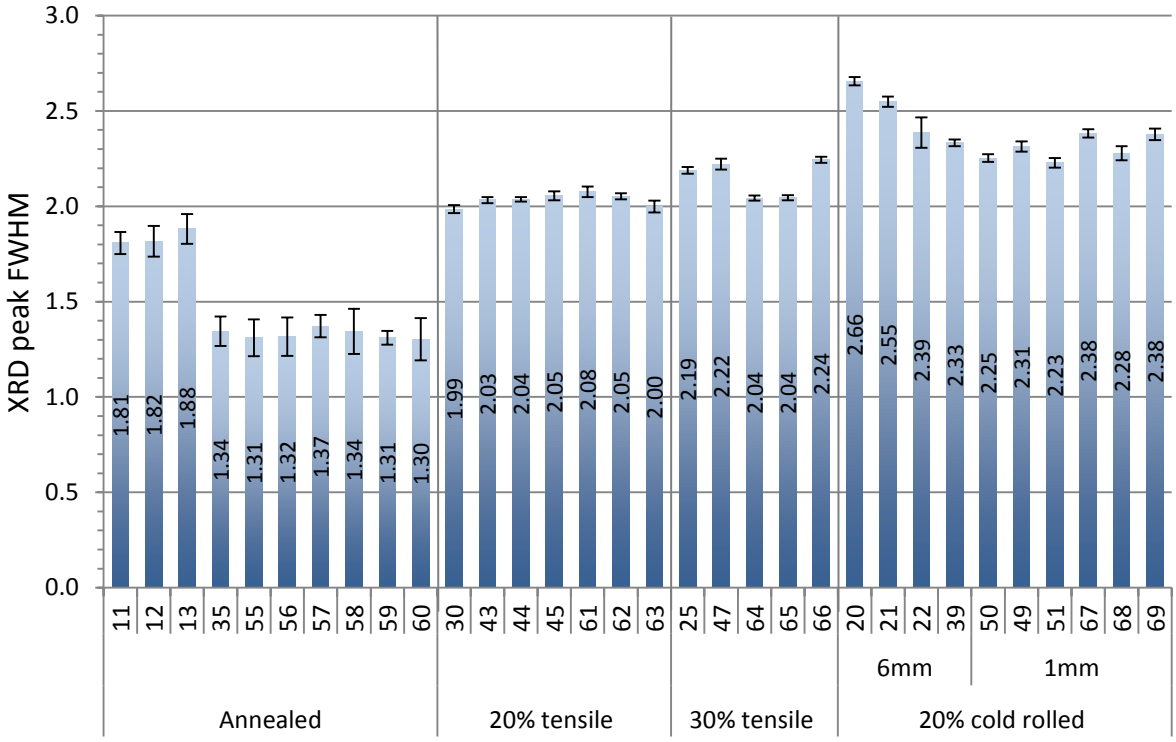

Figure 33. FWHM values for samples within the matrix, which correspond to the level of cold work introduced into the samples. Samples 11-13 are higher than the general annealed conditions, thought to be a result of cold work not removed by polishing. The preparation technique was subsequently improved.

7.7. Exposure to Simulated Primary Water

Once the respective surface conditions had been characterised through EBSD and XRD they were exposed to the prescribed environment in autoclaves. The samples in the autoclaves were exposed to high temperature water which was circulated through pressurised closed loops and whose chemistry is controlled and monitored to simulate the primary water chemistry. All the exposure tests were conducted in Électricité de France (EDF) laboratories at Les Renardières, France. Examples of the laboratory reports from EDF R&D can be viewed in Appendix C.

Two different loops were used for the exposure tests: a titanium loop particularly designed for short duration exposures up to 100 hours; and more conventional stainless steel autoclaves were used for the longer duration tests. The short duration loop is constructed completely from titanium which ensures that any Fe, Cr or Ni oxide that develops on the sample would have originated from the sample. It has the facility to isolate the section containing the samples and purge it of air and replacing it with the inert gas Argon, and then preheat the samples to the test temperature. A total of 4 samples could be exposed together in a single test. Once the samples have been preheated to required temperature, the conditioned water is then released to flow into the sample section. In this way very short duration tests, from 1 min, can be conducted while avoiding any changes to the oxide structure during the ramp up to target temperature and down after the test to room temperature[58,72].

The autoclaves for the longer duration tests were constructed from 316L austenitic stainless steel where many samples can be exposed to the environment simultaneously. The 1000 hr and 6000 hr tests were conducted within the stainless steel autoclaves. The latter tests were occasionally interrupted to allow samples for other investigations to be introduced or removed; however, these interruptions were minimised to have a negligible effect on the longer term exposure tests in these autoclaves.

In both types of autoclaves the samples were electrically isolated from the autoclave materials by using ceramic attachments to avoid any galvanic effects that could affect corrosion and oxidation growth rates.

In all tests the chemistry of the water was controlled to simulate the normal PWR primary water chemistry with 1000 ppm boron (added as boric acid H_3BO_3), 20 - 35 cc/kg hydrogen, 2 ppm lithium (added as LiOH) and buffered to a $pH_T = 7.2$. Since all the autoclaves were

connected to recirculating loops the stability of the water chemistry within each autoclave was ensured by continuous refreshing the medium throughout the duration of the test.

7.8. Grain Boundary Selection

Once the exposed samples were returned from the EDF laboratories the process of measuring the grain boundary oxidation was initiated. The intention with the measurements was to measure the maximum possible intergranular oxidation depth for each set of conditions. However, as will be detailed in the following sections, this process is complex and time consuming and therefore it was not feasible to measure a statistical representative number of grain boundaries. Instead relatively few grain boundaries, in some cases only two, could be measured for each condition. Therefore, it is acknowledged that it was unlikely, given the low numbers measured, to section through the grain boundary with the deepest oxidation, in the deepest spot along the boundary. However, grain boundaries were selected based on three criteria to have the highest probability of having the deepest intergranular oxidation, which was applied to the EBSD mapped 1 x 1 mm^2 area that typically included more than 800 grains. The criteria are described below.

7.8.1. Coincident Site Lattice Boundaries

Firstly, no coincident site lattice boundaries (CSLB) were selected. Early in the process of refining the preparation technique, it was observed that CSLB were not favourable for intergranular oxidation. The vast majority of these boundaries are of the CSL Σ3 type, which are typically annealing twin boundaries in austenitic stainless steel and have a tight packing arrangement at the boundary with a 60° misorientation about <111>. Therefore these boundaries have relatively low disorder, vacancies and as a result low diffusion coefficients. An example is given in Figure 34 where a TEM sample was prepared from an annealed sample after 1 hour exposure containing two sectioned boundaries. In this figure grain boundary 1 represents a CSL type 3 boundary which has no observed oxidation penetrating down the boundary (note that some of the surface oxide was removed in this sample during FIB polishing but there was a residual amount left at the surface to confirm that no oxide had penetrated down the boundary). The second boundary has a random misorientation and some preferential grain boundary oxidation was observed.

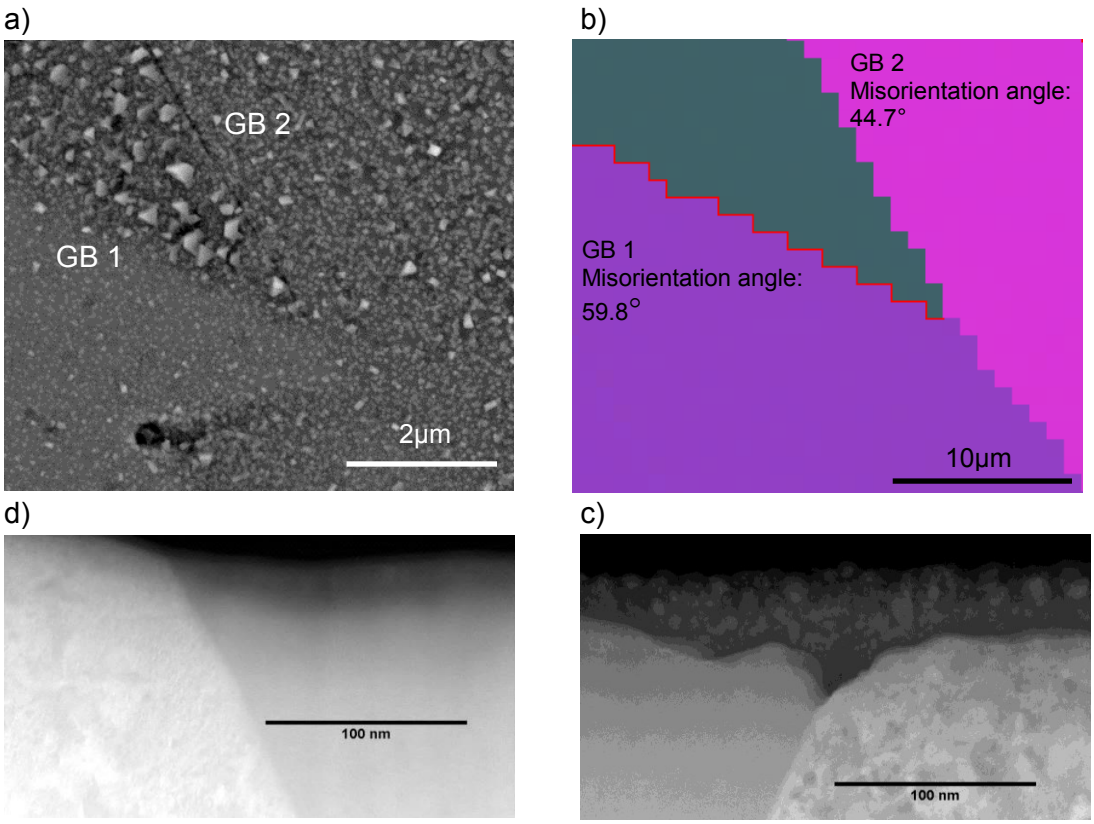

Figure 34. Images of an exposed annealed sample for 1 hr at 320°C with including two grain boundaries showing different contrast from a BS SEM image (a), GB 1 is a CSLB (b) which is not evident in the SEM image and has no intergranular oxide (c), while GB2 is random boundary, has a dark contrast SEM and has some intergranular penetration (d).

The Σ3 CSLBs account for a significant proportion of the total high angle boundaries exposed at the surface: typically about 45% in annealed samples; and in the cold work samples the proportion would be greater with many deformation bands being Σ3 CSLB. Therefore this type of boundary was not included in further selections. Note that similarly, CSLBs have previously been found to be unfavourable for intergranular stress corrosion cracking (IGSCC) and intergranular corrosion for similar reasons[3,94,95].

7.8.2. Back-scatter contrast

Secondly, the variation in the inner layer oxide thickness could be viewed across the surface of the sample when using a back-scattered detector in the SEM coupled with a relatively high accelerating voltage. As the accelerating voltage is increased the electrons have greater energy to penetrate the sample and therefore have a larger interaction volume. The oxide has a lower atomic density than the metal and consequently emits less primary back-scattered electrons than the higher atomic density metal. As a result areas of deeper oxide

thickness can be observed to correspond to areas of darker contrast when observed with a back-scatter detector. An example can be seen from Figure 34 above where the oxidised grain boundary 2 has a darker contrast when viewed with back-scattered electrons (BSE) at 14 keV, while grain boundary 1, with no observable intergranular oxidation, cannot be distinguished under the same conditions. Similarly, Figure 35 below is another example where the back-scattered contrast, provided sufficient accelerating voltage is applied, can be used to determine where the inner oxide layer beneath the surface is thicker. Note in this example how the width of the oxide from the SEM view corresponds to the width of the oxide in the TEM cross section. In this way grain boundaries that are more likely to have deeper intergranular oxidation could be selected.

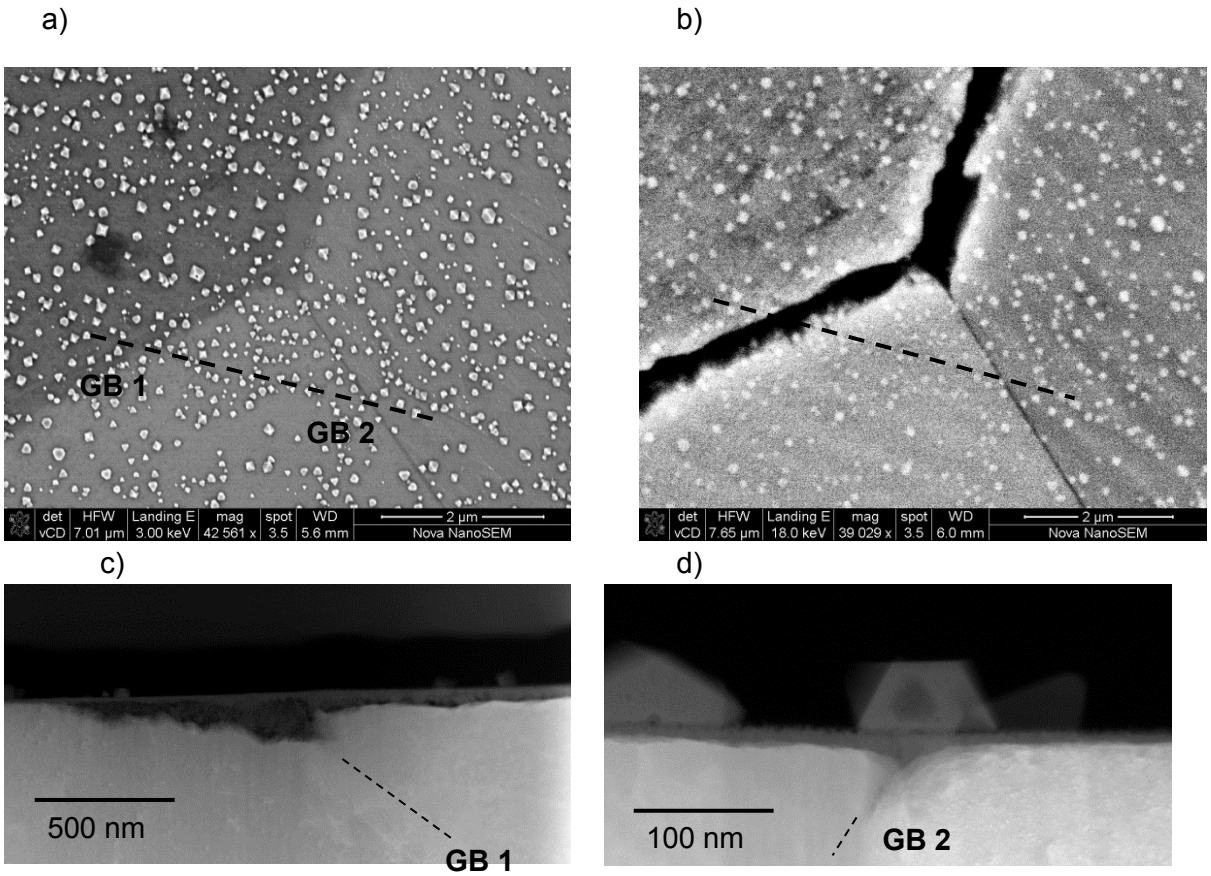

Figure 35. Micrographs highlighting how BSE contrast of an oxidised surface, here an annealed sample exposed for 100 h at 320°C, is used to identify underlying oxide depth, a) a BSE SEM view of the surface at 3 keV, b) the same view at 18 keV revealing the dark inner oxide contrast of grain boundary 1 (GB 1) and less so for GB 2, as well as dark field TEM images of the oxide penetration along GB 1 (C) and less along GB 2 (d).

However, the deepest oxide was not always distinguishable from BSE contrast. In order to distinguish between relatively shallow and deep oxide depths in a sample, the variation should be within the back scattered electron portion of the electron probe interaction volume. For a relatively thin average oxide thickness the probe's interaction volume could be reduced by reducing the accelerating voltage accordingly thereby maximising the back-scattered

contrast, although this also has the effect of reducing the overall BSE signal. Some samples however had an average oxide thickness that was too deep and extended beyond the interaction volume even at the maximum accelerating voltage of 30 keV. In particular the long duration 5000 hr at 290°C (samples 50 & 55) had an oxide layer that was too thick for any underlying microstructure to be distinguished. In these samples the interaction volume which produces back scattered electron signal would largely be contained within the oxide. For these samples it was not possible to select any grain boundaries; rather the sections were cut at random from the surface with a possibility of intersecting a grain boundary.

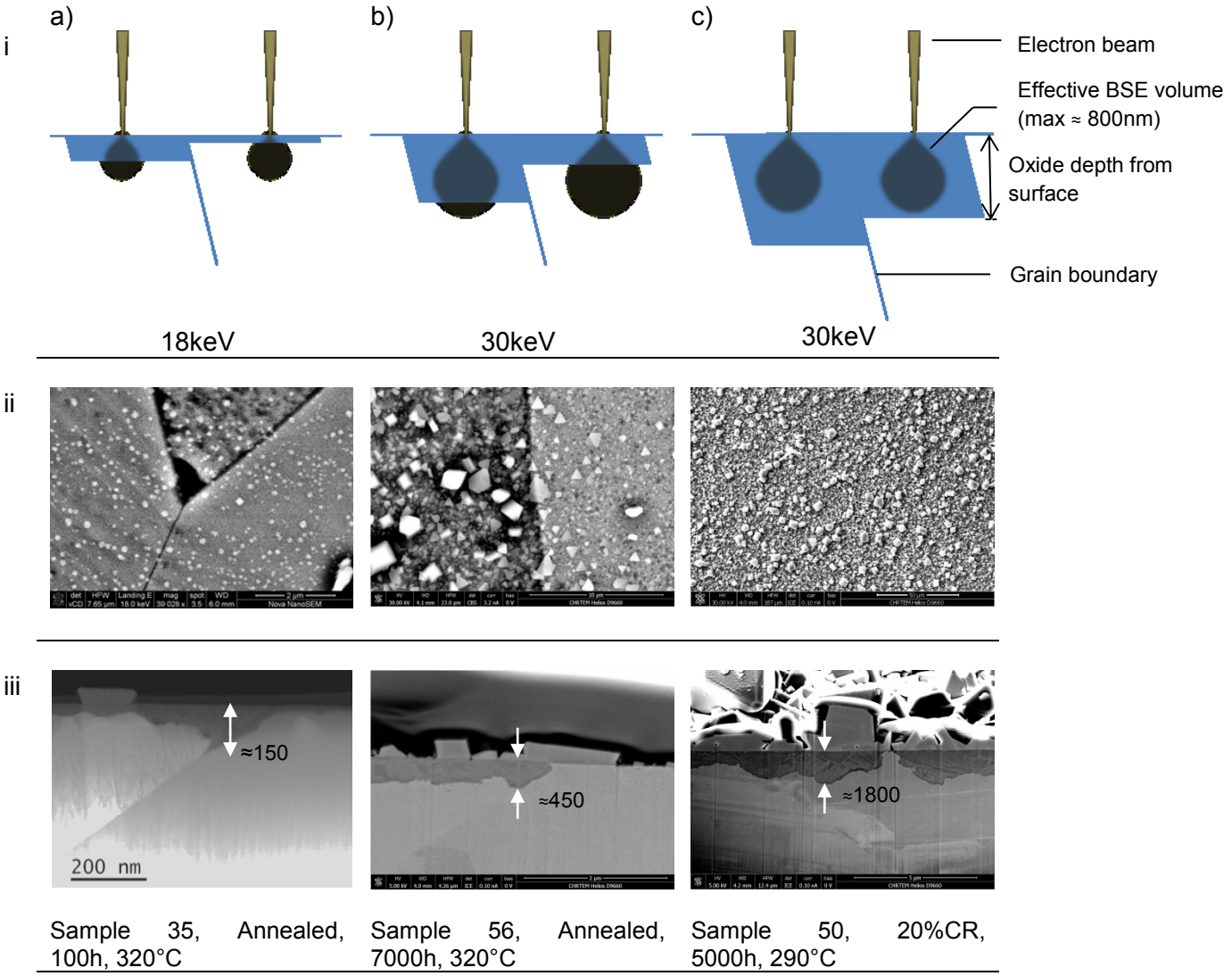

Figure 36. Schematic illustrating the limited benefit of BSE contrast to observe variation in oxide depth using three examples (samples 35, 56 and 50 (a-c)). Sample 35 (a) has relatively thin oxide that can be viewed at lower accelerating voltages with a relatively small interaction volume. Sample 56 (b) has an intermediate oxide depth where the variation in depth in row (iii) is observable with BSE contrast at 30keV. The oxide thickness in sample 50 (c) however, is too thick for any variation to be observed using BSE at 30keV since the BSE interaction volume does not penetrate through the oxide. The maximum interaction depth of the BSE in oxide was observed to be approximately 800 nm, any variation in oxide depth greater than this limit could not readily be observed with BSE contrast.

7.8.3. Surface Crystallites

Lastly, the size of the Fe_3O_4 crystallites that grow on the surface of the exposed samples was observed to correlate well with the thickness of the underlying inner oxide. Identifying regions on the surface with relatively large crystallites compared to surrounding areas would indicate that the underlying inner oxide is thicker in that region compared to surrounding areas. An example is given in Figure 37 where the difference in inner oxide thickness between the two grains is evident from both the difference in BSE contrast as well as the average crystallite size, which is confirmed from a cross-section across the grain boundary. Larger crystallites were often associated with increased inner oxide depth immediately below. Therefore the size of the crystallites on the surface could be used as an indicator of increased inner oxide thickness on a grain to grain scale but also on a more localised scale of the size of the crystallites themselves.

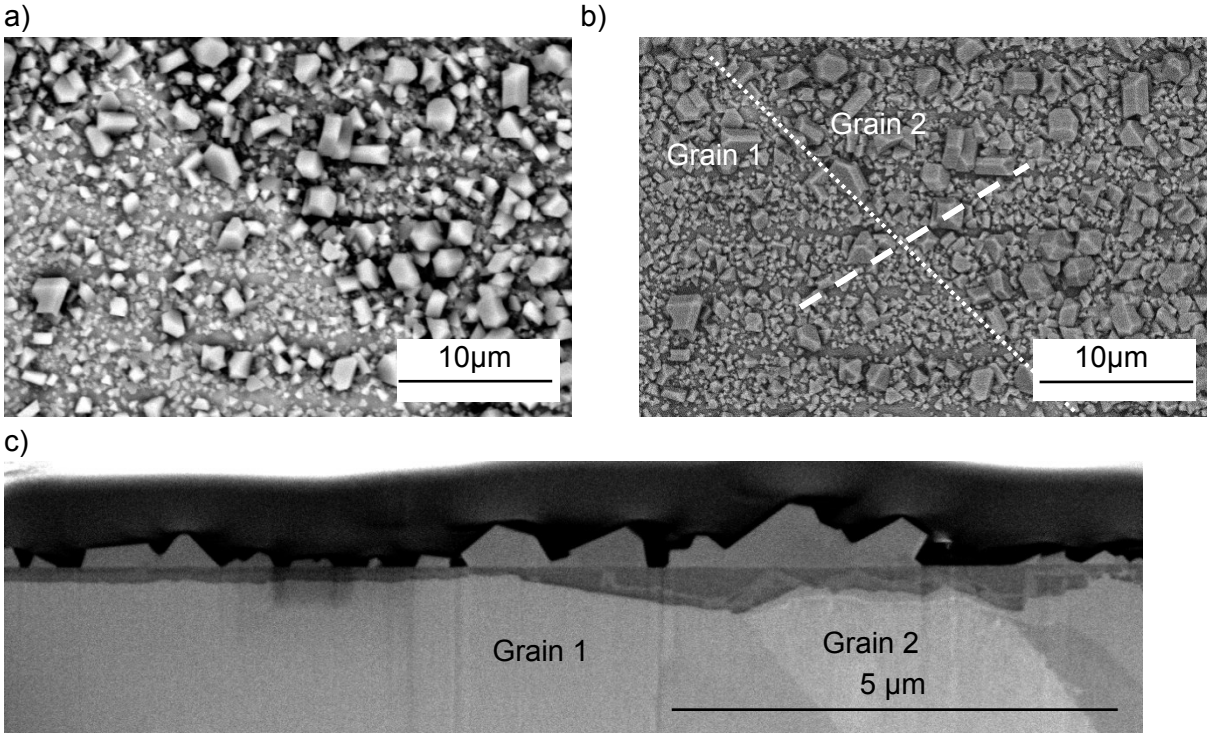

Figure 37. Micrographs of an annealed sample exposed for 1000 h at 290°C with variation in inner oxide thickness across a grain boundary. The BSE image in (a) shows a darker contrast in grain 2 compared to grain 1, the same area viewed with secondary electrons in (b) shows grain 2 has a greater average Fe_3O_4 crystallite size in that grain 1. The cross section across the grain boundary in (c), with the position indicated in (b), confirms the deeper oxide thickness in grain 2.

Therefore these three criteria were used to subjectively select the locations where intergranular oxidation was most likely to be the deepest. However, given that the technique used could only feasibly be applied to a few measurements per sample, the measurements

cannot claim to represent the deepest oxide. Nevertheless given that this is, to the author's knowledge, the first study of this material to measure intergranular oxidation as opposed to previous studies of bulk surface measurements, the data produced is novel with the possibility of future studies to refine the data.

7.9. Thin Foil Preparation

The relatively recent development of incorporating focussed ion beam (FIB) column together with a scanning electron column into a dual beam single microscope has unlocked a vast new ground for the preparation of material specimens previously not possible with conventional techniques. The first of such instruments were commercially available during the 1990's, where they found initial application in the semi-conductor manufacturing industry but soon gained popularity in the wider materials and biological research fields[96,97]. It has made this project possible by being able to select the position of cross-sections through the surface oxides in order to measure oxide depths that correspond to features observed from the surface. Prior to the availability of the FIB-SEM technology, cross-sections would be taken through the sample at random and could not be correlated with surface features.

For both the cross-sections and thin foils an FEI Helios NanoLab™ DualBeam 650 instrument was used, which included an Elstar™ field emission gun (FEG) as an electron beam source, a gallium ion Tomahawk focussed ion beam (FIB) column, a carbon gas injection system and an Omniprobe™ in situ sample lift-out system. Prior to sectioning, the surface oxide at each area of interest was protected by depositing a layer of carbon, first by electron beam (≈ 50 nm thick) and then with the ion beam (≈ 1 µm thick). Those images acquired directly from the SEM were acquired using a secondary electron detector at sample tilt of 52° and were tilt corrected before the extent of oxidation was measured.

The following sequence provides a description of the optimal technique used to prepare surface cross-sections suitable for oxide depth measurements, and corresponds to the steps captured in Figure 38 below.

Once a region of interest was identified using the criteria detailed in the preceding section, the surface was protected with a deposit of carbon. Initially a thin (≈0.1 - 0.3 µm) layer of carbon was deposited on the surface in a strip over the region using the electron beam prior to viewing the sample with the FIB. This was necessary to avoid damaging the surface oxides with the FIB even at low beam currents. It was found that the electron beam deposit was particularly necessary for samples with relatively thin outer layer oxides. Thereafter a thicker layer of carbon could be deposited over the initial carbon strip using the FIB, which is

more efficient at depositing the carbon than the electron beam and reduces the time required.

With the sample tilted at 52° so that the sample surface is normal to the FIB, trenches are milled on either side of the carbon strip using the FIB at high beam currents (0.43 nA at 30 kV), with widths greater than the initial carbon strip. The base of the trenches slope gradually toward the region of interest with a maximum depth of approximately 5 μm. After milling at high currents the edges of the milled area is rough and is then cleaned with a low beam current (9.3 nA at 30 kV).

If the surface oxidation is sufficiently deep, images for intergranular oxidation depth measurements can be captured in the SEM. Note that in these cases it is not necessary for two trenches to be milled but only one to establish an initial section through the oxide.

Alternatively if the sample is to be prepared for TEM examination then it is removed by attaching the Omniprobe™ with carbon and using the ion beam to cut out the region of interest. The cropped sample is then attached to a copper FIB grid finger using a carbon layer as a binder. These grids are specifically designed to accommodate in-situ sample lift-outs by FIB, and are transferable to TEM sample holders. Once attached the ion beam is then used to reduce the thickness of the sample to become electron transparent for TEM use (≈ 50 nm). In order to achieve a suitable TEM sample free of ion beam damage the thickness reduction and polishing is done in several stages. The process is analogous to conventional metallographic polishing with several stages of progressively finer grit and polishing media. Initially the sample is reduced with 30kV, 0.79 nA beam conditions but both the accelerating voltage and beam current are reduced to a final polish with 5 kV, 41 pA with each stage removing surface damage from the preceding FIB step. Note that both sides of the sample are polished during each stage. In an attempt to remove any amorphous damage from the ion beam on the surface a final treatment with 500 V, 0.36 nA is given with the ion beam before the sample is finally suitable for TEM examination.

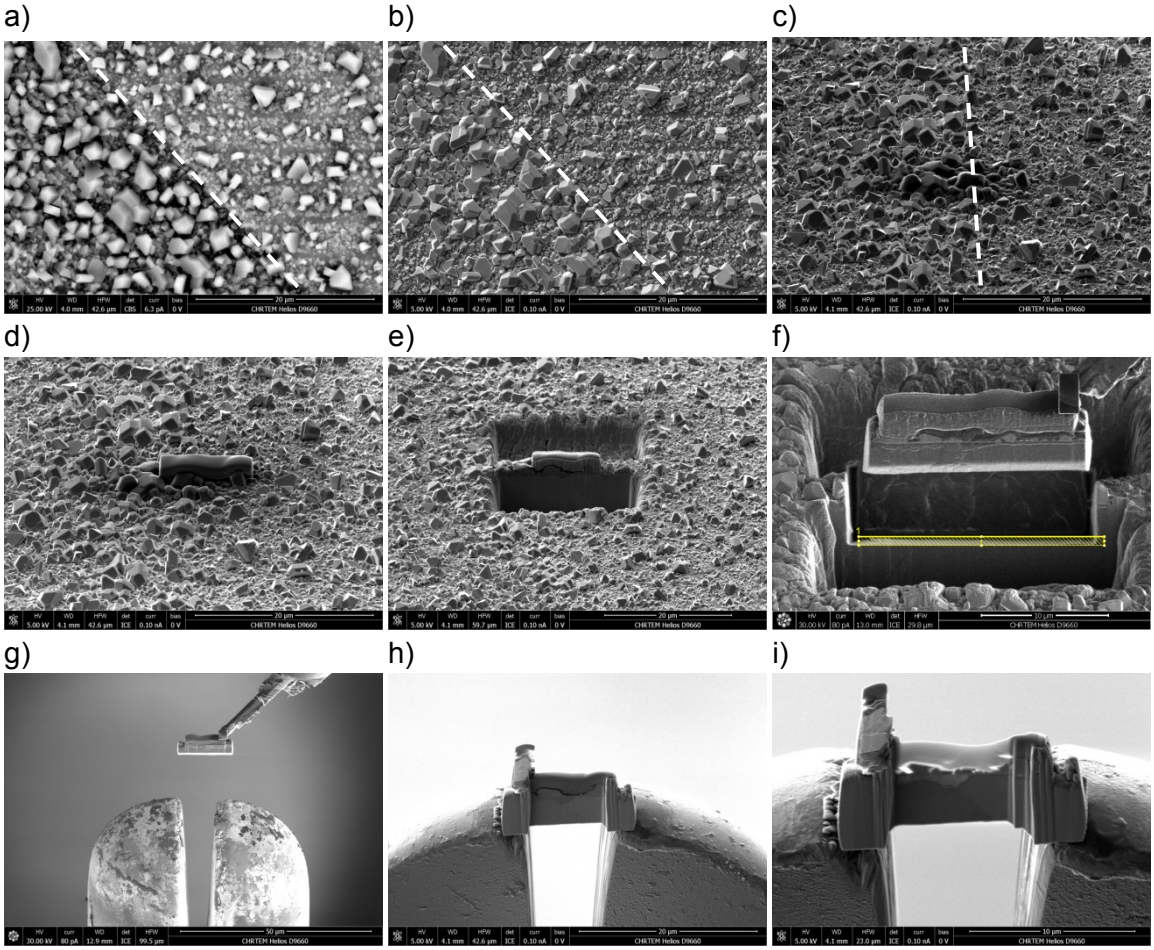

Figure 38. Sequence of SEM images of the TEM sample preparation process: a) A region of interest (ROI) across a grain boundary is identified from BSE contrast, and b) surface crystallite detail; c) the sample is tilted and rotated showing a light carbon layer deposited with the electron beam; d) thereafter a thicker carbon layer is deposited with the ion beam; e) trenches are milled on either side of the ROI; f) the sample can be removed after attaching a probe and milling side and base cuts; g)-i) the sample is attached to a FIB grid finger and progressively ion polished until electron transparent for TEM examination.

7.10. Imaging Conditions of Intergranular Oxidation

7.10.1. SEM Conditions

While the cross-section through the region of interest is prepared and polished by the FIB, the sample is tilted at 52° so that the surface of the sample is aligned normal to the ion beam. Some slight tilt adjustments are made from 52° in order to optimise the milling of the surface; however, when capturing images of the cross-section the tilt was adjusted to 52°. Images to measure the intergranular oxidation were acquired using the electron beam.

The resulting electron image scale from this tilt angle would be correct in the x direction, but does not consider the tilt in the y direction, as illustrated in Figure 39. Therefore before measurements could be taken from the image the tilt had to be accommodated. This was achieved by adjusting the pixel ratio with the image processing software used (ImageJ). The following expression is used to determine the relative pixel ratio for x:y to adjust for the tilt in the y direction:

$$sin\theta = \frac{Y_2}{Y_1} \ , Y_1 = \frac{Y_2}{sin\theta}$$

Where Y_1 represents the real scale in the y direction, while Y_2 represents the captured y scale, and θ represents the angle the sample is tilted to from horizontal. If the sample is tilted to 52° then Y_1=1.269 Y_2.

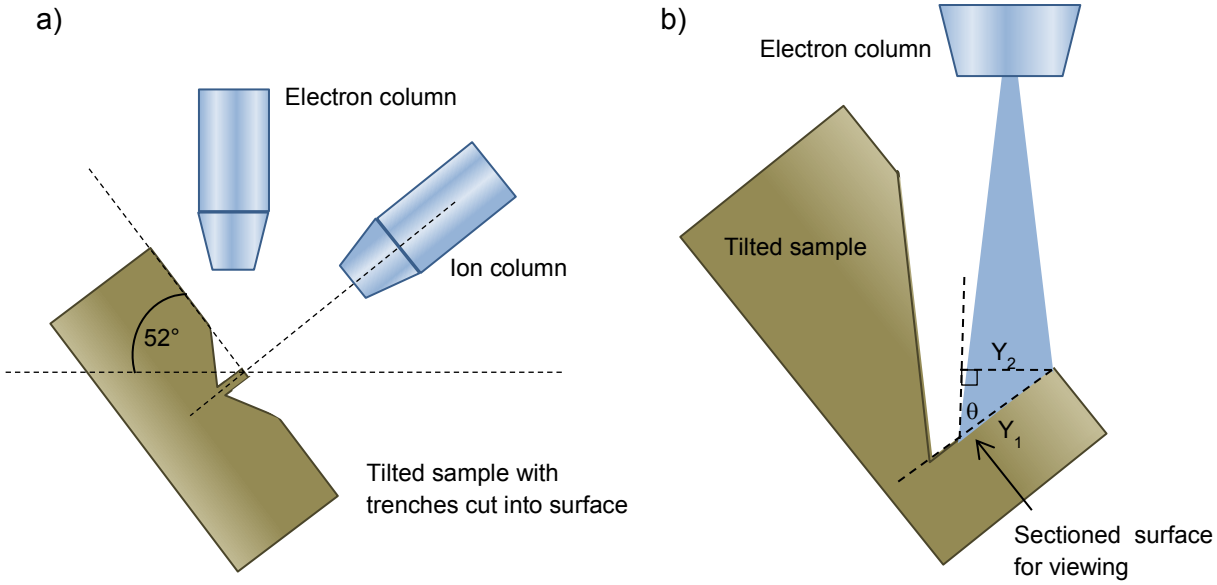

Figure 39. Schematic of the geometry of the sample in the FIB-SEM showing (a) how the sample is tilted to 52° from horizontal to be normal to the ion beam, and (b) how the y component of the electron image captured at this angle is distorted.

The resultant effect on the image after adjusting for the tilt can be seen in Figure 40 where the image is manually stretched in the y direction while keeping the x scale constant. Measuring the extent of the intergranular oxidation will therefore be accurate at any angle that the boundary makes with the surface.

a) b)

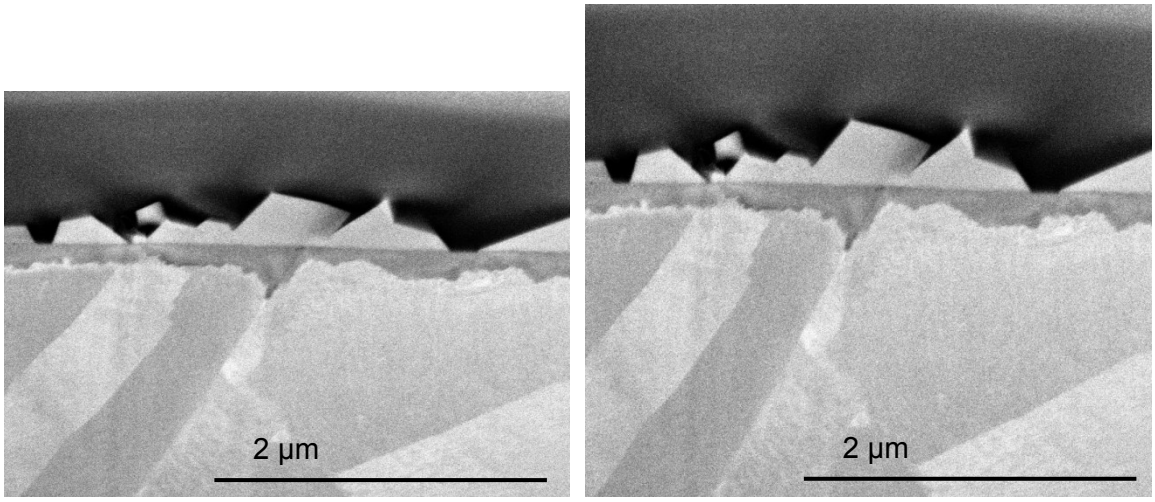

Figure 40. Images of intergranular oxidation captured in the SEM with the sample tilted at 55°, a) shows the image as captured, b) the same image adjusted for the tilt.

With the intergranular oxidation detail being of nanometre scale the FEG SEM setup required optimisation to achieve the images with resolution necessary for accurate measurements. After aligning the microscope's gun, aperture and adjusting for astigmatism the best quality images were acquired with the following conditions:

- Acceleration voltage was set at 5 kV.
- The electron probe current was set to 50 to 100 pA
- The specimen height was adjusted to a working distance of 4 mm.
- The magnetic immersion lens system was selected with a stage bias of +50 V.
- The through the lens (TLD) secondary electron detector was used.

7.10.2. TEM Conditions

The majority of the TEM analysis was conducted with a double Cs corrected JEOL ARM 200F transmission electron microscope (TEM) operated at 200 kV, which included integration correction of spherical aberrations for both the objective and condenser lenses. High angle annular dark field (HAADF) scanning transmission electron microscopy (STEM) imaging sensitive to atomic number variations within the sample, and electron energy loss spectroscopy (EELS) Spectrum Imaging (SI) were performed using the DualEELS^{TM} mode on the Gatan GIF Quantum ERS^{TM} spectrometer.

Scanning transmission electron microscopy (STEM) was used since the raster can be rotated in order to view the sample with the original oxide surface horizontal, this became a standard applied for all TEM images for oxide measurement.

In order to accurately measure the limits of oxidation from the image it was necessary to clearly distinguish the oxide from the base metal. Although there was contrast evident between the metal and oxide in bright field TEM images, the contrast was more distinct in dark field or high angle annular dark field (HAADF) TEM images. Therefore most measurements were taken from the latter type images. The difference between the two imaging techniques can be seen from Figure 41.

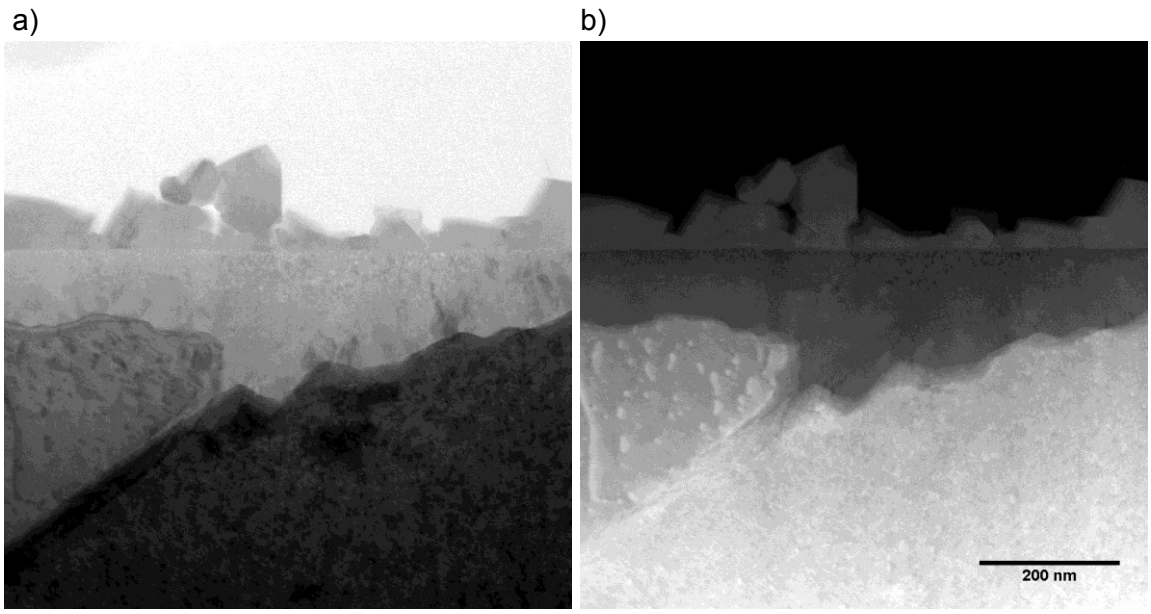

Figure 41. TEM images of the same view of intergranular oxide highlighting the variation in contrast when acquired with a) bright field, and b) with HAADF.

To compliment the acquired TEM images, the extent of the oxide penetration could be determined, with better confidence, by acquiring EELS maps of the area of interest in STEM mode. The dual eels mode of the Gatan spectrometer enabled acquisition of the intense zero loss peak (ZLP) and the elemental edges at virtually the same time. The convergence semi-angle of 21.4 mrad was used for the STEM probe and the collection semi-angle of the spectrometer was 54.3 mrad at a camera length of 1 cm. Low-loss spectra were collected in the energy range 0-512eV at a dispersion of 0.25 eV/channel. The high-loss spectra were collected in the energy range 450 – 962 eV at a dispersion of 0.25 eV/channel. The number of pixels in the map could be defined by the operator but was usually constrained by time, where the possibility of image drift was also considered.

An EELS map size was determined by the minimum map size to achieve the necessary spatial resolution. Once the EELS spectral map was acquired, individual elemental maps could be extracted. The oxygen, chromium, iron and nickel elemental maps were extracted by performing windowed elemental mapping on the 3D data cube. A power law was used to model the background of the spectrum in the range of (450 – 520 eV) for oxygen and chromium, (650-700 eV) for iron and (800-850 eV) for nickel. The elemental signal was extracted using a window of 30 eV over each of the elemental edges (O-K:532 eV; Cr-L:575 eV; Fe-L:708 eV; Ni-L: 855 eV). Therefore the concentration of each of the selected elements within the region of interest could be viewed from the respective EELS maps. The extent of the intergranular oxidation could be confirmed from a plot of the oxygen EELS map at the base of the oxidised portion of the grain boundary, see Figure 42 for an example.

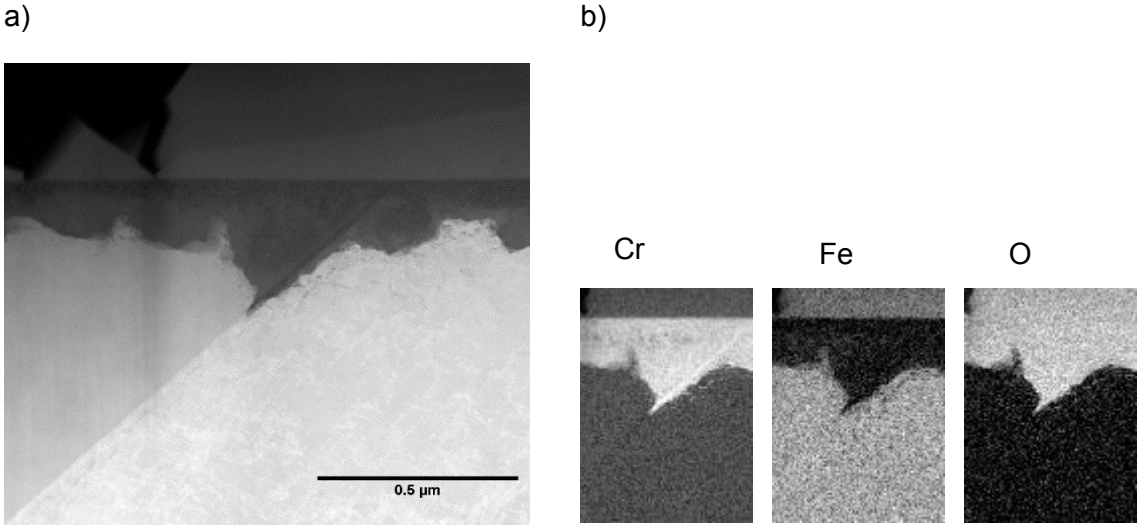

Figure 42. a) HAADF STEM image of a 20% cold rolled sample exposed at 320°C for 1000hrs with b) EELS elemental maps indicating the Fe-rich outer oxide layer formed on the original surface, and confirming the extent of Cr-rich inner oxide penetration beneath the original surface.

7.11. Intergranular Oxidation Measurement

The intergranular oxidation was measured along the length of the grain boundary from where it intersected the original surface to the discernible end of the oxide. This length was measured rather than the depth of the intergranular oxide normal to the surface, since the purpose was to determine the maximum possible rate of intergranular oxide propagation. Therefore if the grain boundary was normal to the surface the intergranular oxide propagation would then represent the depth to which oxide penetration is possible.

It is not possible to know at what angle a grain boundary would make with the surface from a surface view prior to preparing a cross-section. However, the more acute the angle between the grain boundary and the surface, the more the surface oxidation influenced the extent to which the boundary was oxidised. Therefore a minimum acceptable limit of 30° was used, and any grain boundary angles below this limit was disregarded. Figure 43 illustrates this point with examples of oxidised grain boundaries at angles, showing the influence of surface oxidation, and substantiating the 30° acceptance limit.

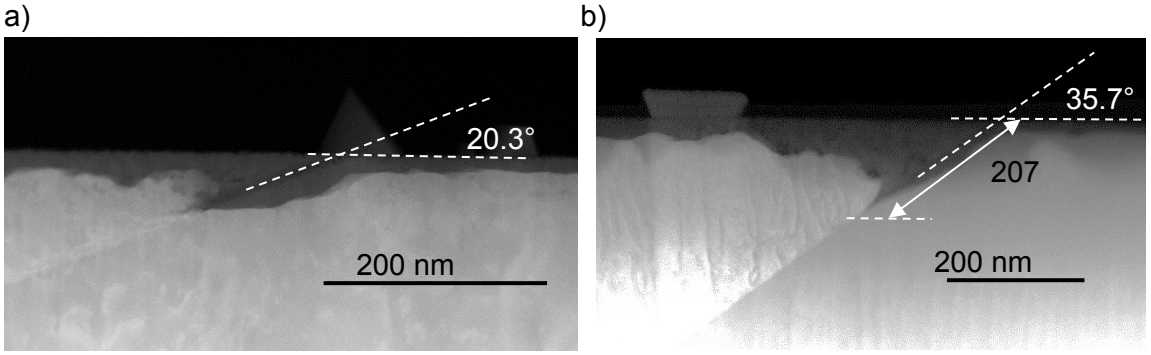

Figure 43. Dark field STEM micrographs of intergranular oxidation with (a) a grain boundary at an angle unacceptable for measurement, and (b) another at an acceptable angle with measurement taken along the oxidised length of the boundary.

7.12. ToF SIMS

The quantitative measurements of surface and grain boundary measurements were selected as far as possible to determine the deepest surface and grain boundary oxidation. However, while the technique of physically measuring oxide depth from FIB prepared cross-sections is accurate, and allows the influence of microtexture to be observed, it is time consuming and resulted in relatively few oxide depth data points per sample. Therefore considering that the statistical significance of these results alone may be criticised, further complementary data were acquired using time-of-flight secondary ion mass spectroscopy (ToF SIMS).

This technique was used to measure the oxide depth across a selected area of 250 µm x 250 µm with the main objective to demonstrate that the physical measurements from cross-sections, as described in 7.11, were statistically representative. However, ToF SIMS cannot measure depth of the oxide directly. The instrument analyses and identifies secondary ions emitted from the surface as heavy bismuth ions bombard the sample surface. It is also able to quantitatively measure the amount of these ions emitted. This analysis is performed across a selected surface area of the sample in an iterative process between which the sample is milled with a separate gun of heavy Cs ions to remove surface material. The thickness of layer removed is, however, unknown and can vary dependent on the composition of the sample, and may vary through a sample that is not homogenous in

composition through its depth. For this reason ToF-SIMS could not be used as the main quantitative technique to measure oxide growth.

ToF-SIMS is usually used as a comparative technique to measure compositional variances across the sample. In this study, however, the technique was applied to 3 annealed samples exposed at 290°C, 320°C and 360°C where the 62500 μm^2 area of interest included areas of oxide that had previously been quantitatively measured through FIB sections. Therefore the depth of the ToF-SIMS could therefore be reasonably calibrated.

The surface chemistry was characterised by analysis of secondary ions emitted from the surface impacted by a primary Bi^+ ion beam with an accelerating voltage of 30 keV, pulsed at 10kHz for 100 µs, with a DC current of 0.4 pA. This beam has an approximate beam diameter of 200 nm. A flood gun of electrons was used to neutralise the sample and avoid charging artefacts interfering with the results. After each analysis a sputter gun of Cs^+ ions was employed to remove material off the surface with an accelerating voltage of 2 keV and a DC current of 150 nA at intervals of 180 s each.

In each of the samples a 250 μm^2 area was analysed with 512 x 512 pixels (0.5 µm resolution) and 4x4 pixel binning. The sputter area was larger at 500 µm x 500 µm and centred around the analysis area.

The analysis and sputter was repeated iteratively for each sample until the oxide ions emitted dropped in intensity and a stable background intensity was reached signalling that only base material was exposed at the surface, at which point the acquisition was stopped. This resulted in a range of total number of scans between 35 (sample 60, exposed at 360°C) and 65 (sample 58, exposed at 290°C), the latter having thicker oxide.

8. RESULTS

In this section the results will be presented in order to first characterise the manner in which the Cr-rich passive film develops on the surface. Therefore, portions of the full set of exposure data are presented first to substantiate these observations. For example, the 1000 h exposures are used to demonstrate the effect of temperature. Once these observations have been discussed the full set of oxide depth measurements over various exposure durations are presented and discussed. These results provide the kinetic data which will be placed in the context of established oxide growth models. The differences between the assumptions in the models and observed behaviour are discussed as well as possible modifications that could be introduced to better fit the experimental data.

8.1. Temperature Sensitivity of Oxide Kinetics

To first demonstrate the effect of temperature across the primary water range of 290°C to 360°C on the growth of the inner Cr-rich layer the results from only the 1000 h exposures are compared. The complete set of 1000 h data from localised physical measurements of sections through the surface oxide were used. In addition a partial set of complementary results from the annealed samples using time of flight secondary ion mass spectroscopy (ToF-SIMS) is presented.

8.1.1. Discreet Physical Measurement Data

The maximum intergranular oxide penetration depth and maximum surface oxide penetration measurements, from individual FIB specimen cross-sections labelled 1-19, are presented in Figure 44 and Figure 45 respectively.

Rather counter-intuitively, the deepest intergranular oxidation penetration after 1000 hours exposure to primary water was measured at the lower 290°C temperature, see Figure 44. Similarly the same trend was observed comparing maximum surface oxidation thickness from the same sample set of cross-sections in Figure 45. This observation was also consistent for both the annealed and cold worked material. While the range of values for the 320°C and 360°C were similar, the maximum value for the 290°C was at least twice the maximum of the other temperatures.

The intergranular oxidation penetration values for the annealed samples were in some cases artificially high due to the contribution of surface oxidation rather than preferential grain boundary oxidation, see cross-section 7 in Figure 44 and Figure 45. The preference for surface oxidation on certain grains was observed particularly in the annealed samples and is addressed in the next section. Apart from the effects of accelerated growth on favourably oriented grains, the inner oxide thickness was marginally greater in the cold worked samples than the annealed samples over all observed temperatures.

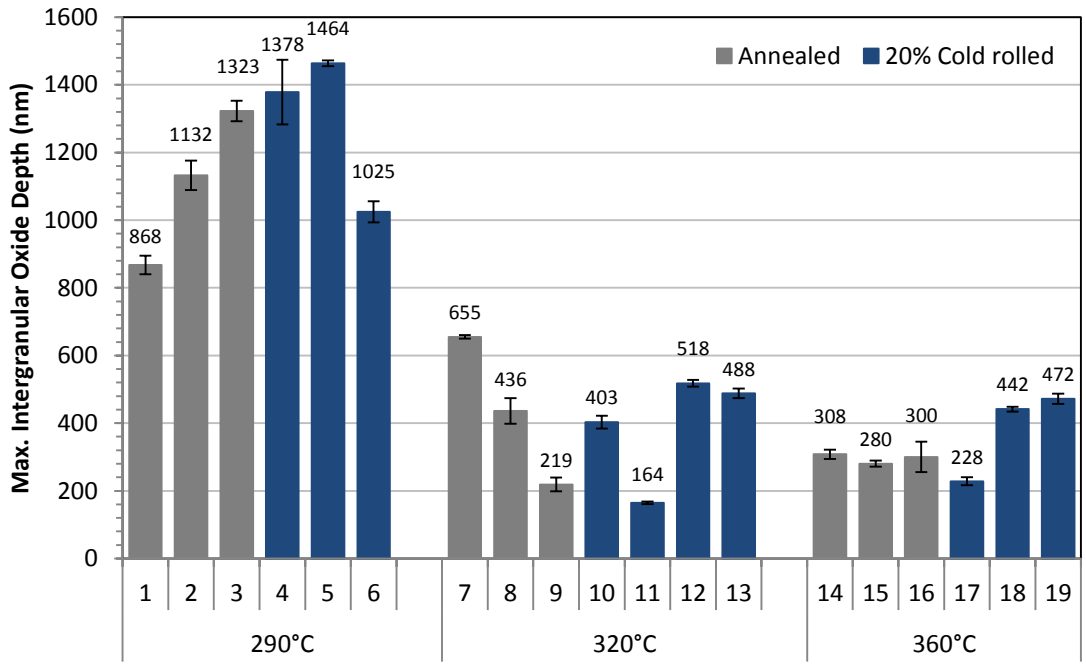

Figure 44. Maximum intergranular oxidation depth measurements of 19 selected regions each containing a least 1 grain boundary. A minimum of 3 regions were measured per sample, where samples representing 2 material conditions (annealed and 20% cold rolled) were exposed to primary water for 1000 hrs at temperatures of 290°C, 320°C and 360°C. Error bars represent 1 standard deviation in measurement uncertainty.

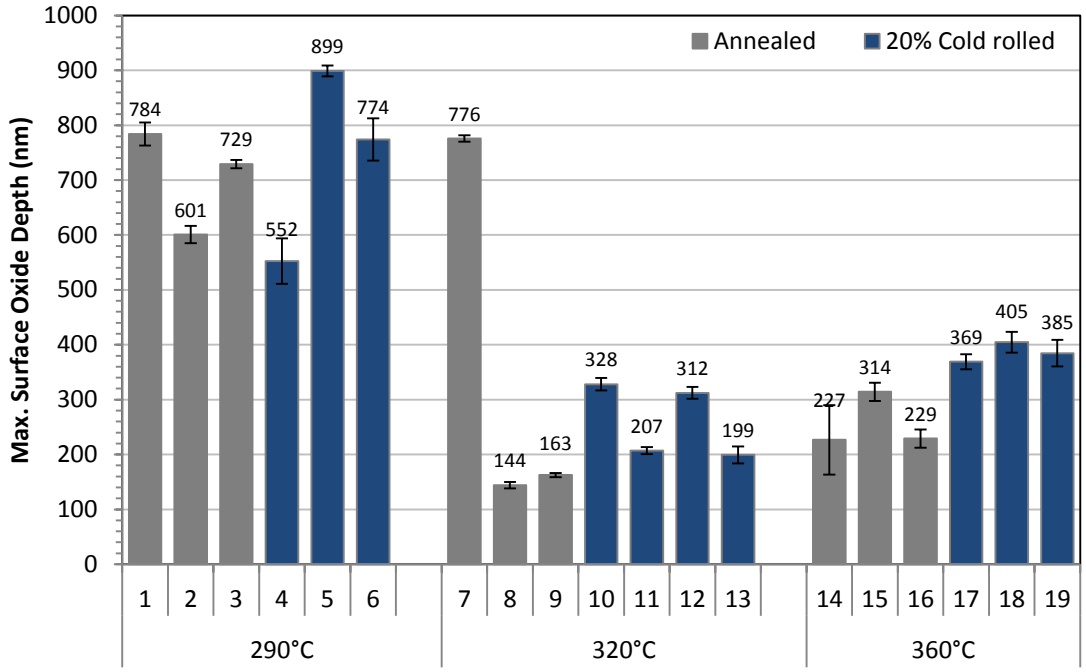

Figure 45. Maximum inner oxide depth captured within each of the 19 prepared cross-sections, corresponding to the same 19 regions of Figure 44. Samples of both annealed and cold worked conditions were exposed to primary water at temperatures of 290°C, 320°C and 360°C. Error bars represent 1 standard deviation in measurement uncertainty.

8.1.2. ToF-SIMS Data

It is acknowledged that the observations regarding the sensitivity to temperature in the preceding section were drawn from relatively few localised measurements of oxide thickness. Therefore to further substantiate the conclusions from this data, a set of bulk measurements of oxide thickness were acquired from a relatively large area of 250 µm x 250 µm in three annealed samples that were all exposed for 1000 hrs, but represented different temperatures of exposure at 290°C, 320°C and 360°C respectively. These measurements were made using the ToF SIMS technique.

The ToF-SIMS technique is able to qualitatively measure the composition of the surface by analysing the secondary ions emitted from a primary beam of heavy Bi^+ ions. By repeating a sequence of analysis followed by removing some of the surface material by ion beam milling, a three dimensional model of the sample can be constructed indicating the compositional distribution. However, since different materials mill at different rates the ToF-SIMS data does not assign a depth but rather uses sputter time as measure of the through thickness dimension. For this reason areas of samples selected for ToF-SIMS analysis included

regions where oxide thickness had been previously measured by the FIB cross-section method.

The areas included with the ToF-SIMS analysis for the 320°C and 360°C are given below in Figure 46; however, due to an error the area analysed in the 290°C sample did not correspond to the planned area of analysis and therefore did not include a FIB sectioned area.

In Figure 47 the relative summed intensities of the O^-, FeO^- and CrO^- secondary ions from the entire area analysed are plotted against sputter time. The intensities of the latter two ion curves were normalised in order to draw comparisons between the curves. Note that the value in the curves was not their absolute value but rather their shape with respect to time. The initial surface before any milling is represented where the sputter time is at 0 s. Note that the intensity data is not quantitative but the relative concentration of each ion can be compared through sputter time to determine the extent of the oxide through the thickness of the sample. It is evident from the plot of the 290°C sample that there is an outer concentration of FeO^- (initial sputter time), which is consistent with the outer Fe_3O_4 oxide layer, and an inner concentration of CrO^- (latter sputter time), consistent with the Cr rich inner oxide layer, while the extent of the O^- ion peak spans both layers.

When the respective ToF-SIM data for the three temperatures provided in Figure 47 are compared, it is clear that the profiles for the ions do not follow similar profiles through sputter time. While the FeO^-, CrO^- and O^- profiles in the 290°C sample both increase to a peak and tail off through time, these profiles are not similarly observed in the other samples. The inner CrO^- profile in the 360°C (Figure 47 c) appears to be complete while both the O^- and FeO^- profiles appear to be truncated at the outer portion of the sample (at 0s). Likewise all three ion profiles appear truncated at 0s in the 320°C sample (Figure 47 b) without any peaks evident. Instead the profiles suggest, with reference to those in 290°C, that only the tailing off portions of the peaks are included.

The most likely explanation consistent with the apparent loss of the first part of the ion profiles in the 320°C and 360°C samples is that the surface in these samples had been damaged by the ion beam during FIB preparation resulting in the loss of outer surface. By this explanation the 320°C sample would have suffered more damage than the 360°C sample, but due to a positioning error the ToF-SIMS area of the 290°C sample did not include a FIB prepared region, and was free of prior ion beam damage and therefore includes the full ion intensity peak profiles.

The initial intention of calibrating the sputter time to real depth to allow the different depths across the samples to be compared could therefore not be achieved. However, it is possible to compare the full width at half maximum (FWHM) results for the inner CrO^- peaks between the 290°C and 360°C samples, which both exhibit full peak profiles. The CrO^- FWHM for the 290°C sample was measured at approximately 3060 s, while the same parameter was measured at approximately 1300 s for the 360°C sample, see Figure 47. This suggests that the average inner Cr rich oxide layer for the sample exposed at 290°C for 1000 hrs was approximately 2.3 times the thickness than the corresponding layer in the 360°C. This result corresponds well with the physical measurements from FIB cross-sections given in the preceding section, where the average maximum surface Cr rich oxide for the annealed samples from 3 data points was measured at 386 nm for the 360°C and 741 nm for the 290°C (1.9 times thicker). Therefore the ToF-SIMS data can, when comparing the 290°C and 360°C data, substantiate the FIB cross-section data that concluded that the Cr-rich layer had significantly greater penetration depth at the lower temperature compared to the higher temperatures.

While the averaged ToF-SIMS data could be compared across the samples to determine the averaged inner layer penetration depth, with limited success, the distribution of oxide depths within each sample area was also analysed. In Figure 48 the variation in oxide depth across the sample is indicated by a map of accumulated O^- intensity, where the sum of all O^- counts corresponding to a spatial co-ordinate pixel is assigned a brightness value on a colour scale. In this way the relative distribution of oxide depth can be appreciated. From this data it is clear that there is a significant variation of oxide depths in the 320°C which corresponds to microstructural features of the underlying metal. This sensitivity to metal orientation is discussed further in the next section 8.2. Less pronounced variation was evident in the 290°C samples with some grain or twin boundaries having brighter contrast, indicative of greater oxide depth. Very little variation in O^- intensity was observed across the 360°C sample area analysed, see Figure 48 (e) and (f).

It is important to note that the apparent variation in the oxide thickness for the 320°C sample measured by FIB cross-sections (see Figure 45) is supported by distinct variation in O^- intensity across the same sample from ToF-SIMS. The greatest surface oxide penetration in this sample was measured from region 3 from a grain that was favourably orientated for oxide growth. However, other grains of similar orientation had similar oxide penetration depths. Therefore, while there is only a single physical measurement obtained representing orientations of greater oxide depth (Figure 45), the ToF-SIMS data provides support with evidence that this point is representative of oxide depths possible in this sample when the metal substrate is oriented favourably.

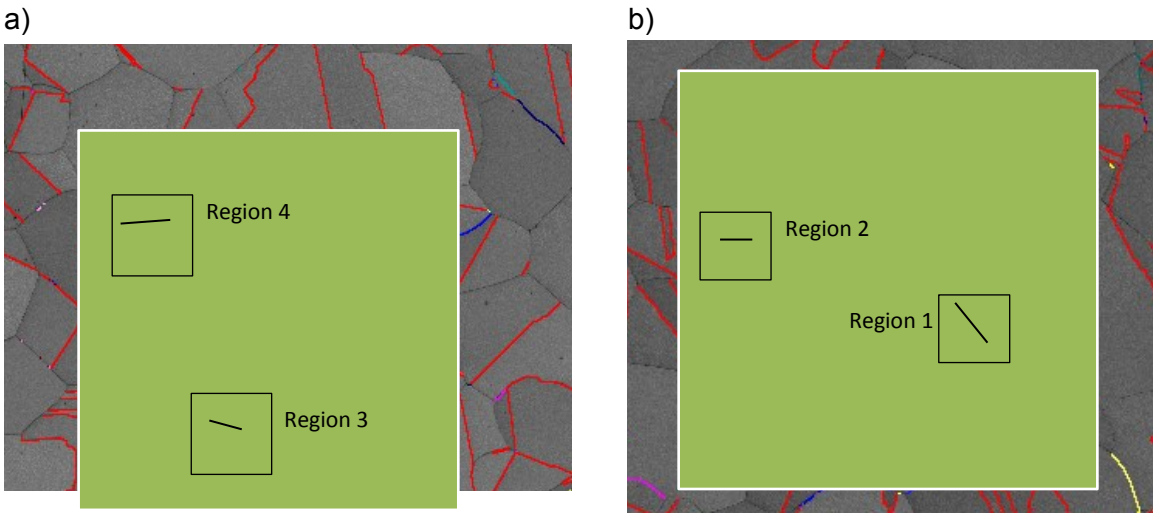

Figure 46. EBSD band contrast images showing the regions sectioned using FIB for physical oxide depth measurements overlaid with the ToF-SIMS analysis area (white edged square area) for a) samples 59 (annealed, exposed for 1000 h at 320°C), and b) sample 60 (annealed, exposed for 1000 h at 360°C).

a)

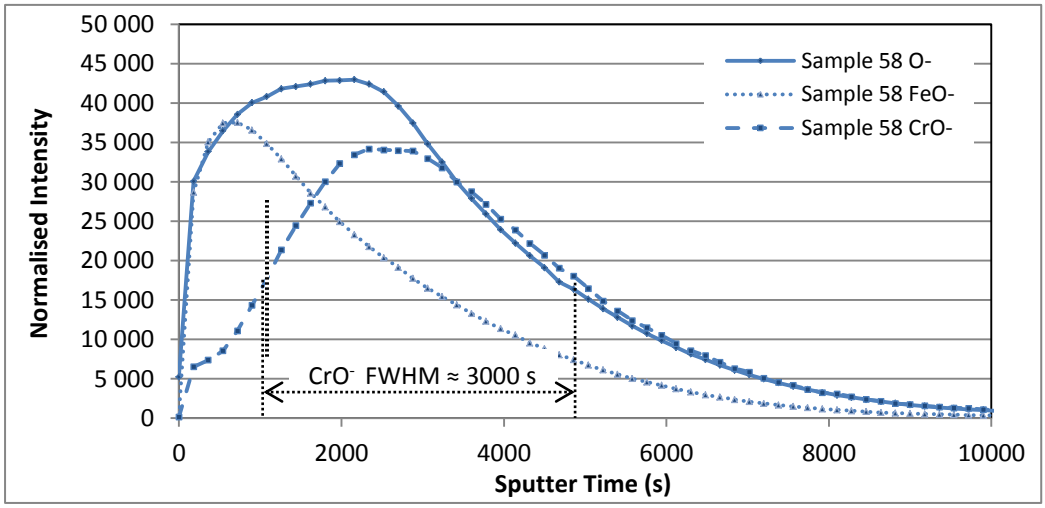

b)

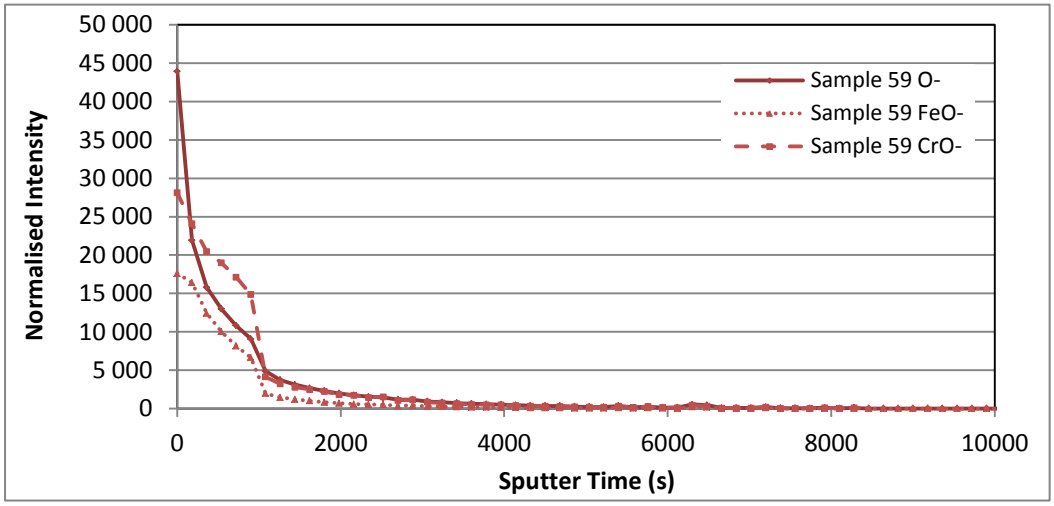

c)

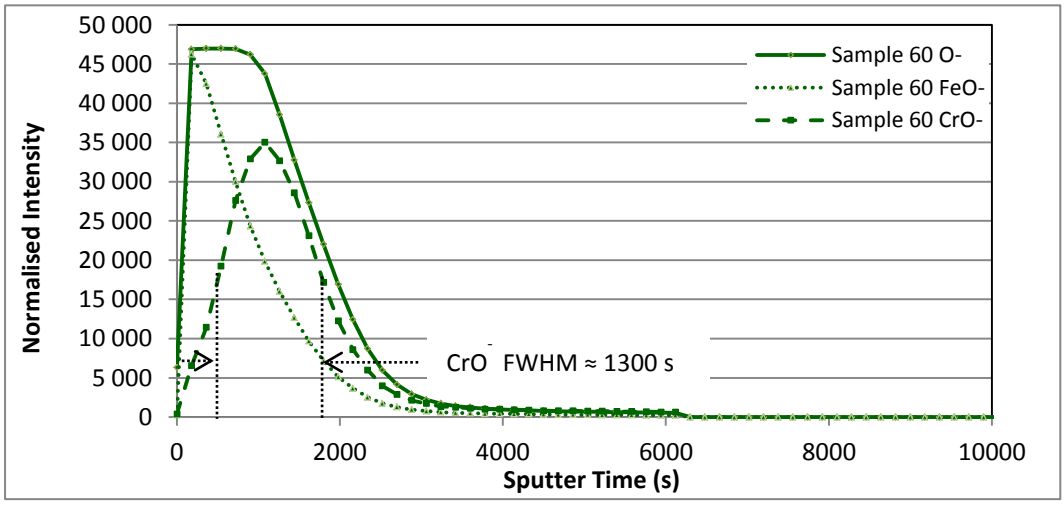

Figure 47. Plots of Tof-SIMS intensity values for three ion species O^-,FeO^-, and CrO^- plotted against sputter time acquired from annealed samples exposed for 1000h at a) 290°C , b) 320°C and c) 360°C respectively.

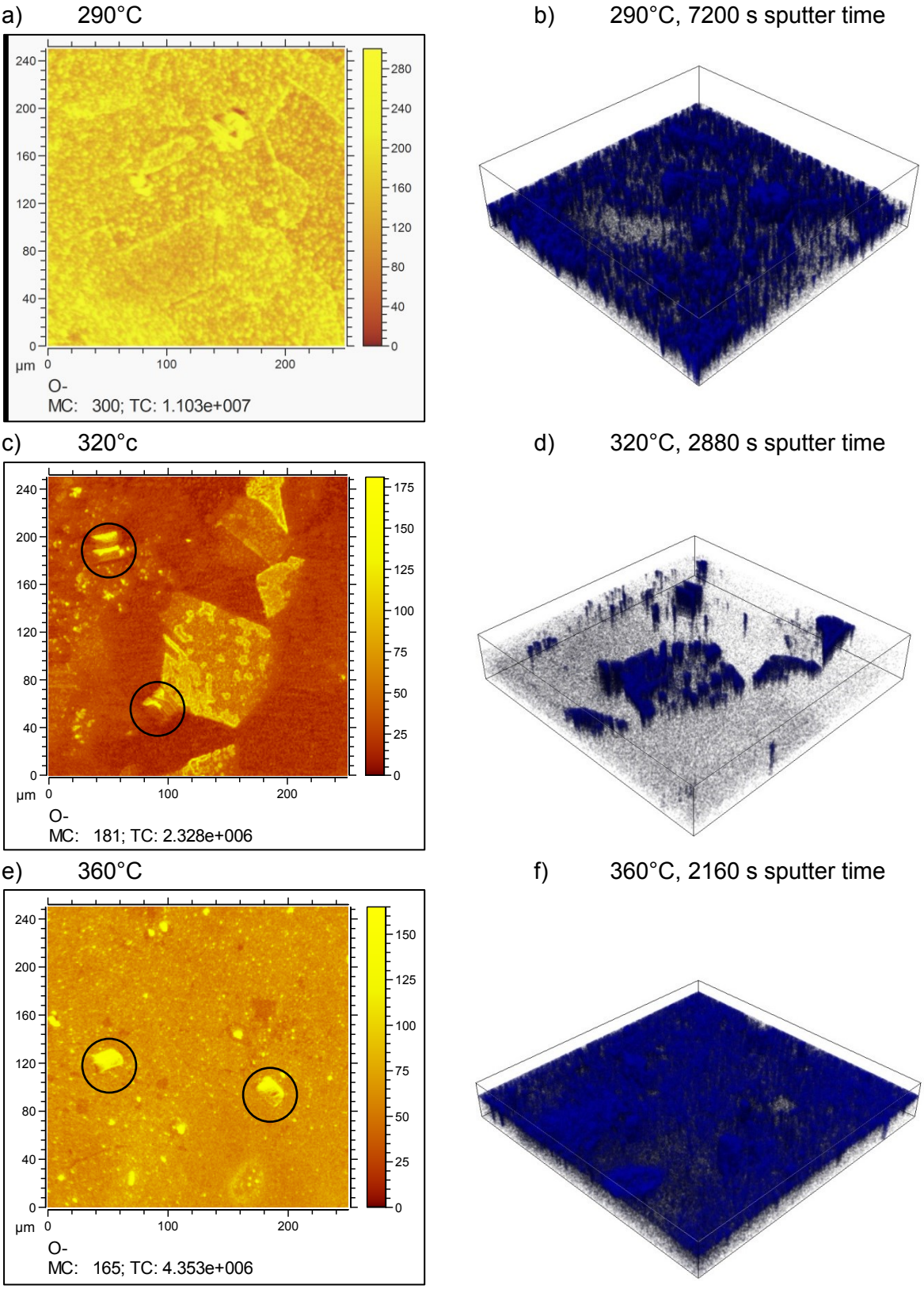

Figure 48. ToF-SIMS data showing (LHS) the accumulated intensity of the O^- ions through the total thickness indicative of the variation in oxide depth across the 62500 µm^2 area analysed (FIB sections circled); and (RHS) O^- ion spatial distributions in blue rendered in 3D after selected sputter time.

8.2. Orientation Dependence of Oxide Kinetics

As mentioned above the thickness of surface oxidation after 1000 hours exposure was observed to vary, in some cases significantly from grain to grain. Figure 49 is an example from an annealed sample exposed at 320°C. From a surface view in a SEM using BSE with a relatively high accelerating voltage, it is possible to distinguish areas of thicker oxide, which correspond to areas of darker contrast. In this example the oxide thickness across the grains differed by greater than an order of magnitude. Without any other difference between adjacent grains with respect to microstructure, chemistry or environmental conditions only metal orientation can account for this significant variation in oxide growth.

Oxide growth was favoured at 320°C when grains were oriented with <001> normal to the exposed surface plane. Compare the inverse pole figures for grain 1 and grain 2 in Figure 49 (c) where the <001> of grain 2 is aligned fairly close to the z direction, which is normal to the sample. The same Figure 49(a) shows a region with distinct BSE contrast across grains (dashed line). A FIB section including the grain boundary of this region confirms that the darker contrast corresponds to the significantly deeper inner Cr-rich oxide thickness at the surface (Figure 49(b)).

The preferred orientation for surface oxide growth was observed more broadly across the surface by selecting a narrow window of orientations from the inverse pole figure centred around <001> parallel to z (i.e. normal to the sample surface). The grains that fell within this orientation selection were highlighted in the EBSD map of Figure 50 accounting for approximately 17% of the total area. When comparing the BSE contrast in the SEM of the same area, see Figure 50, it is clear that grains within the orientation selection have a propensity for deeper oxide penetration at 320°C. This observation is deduced from the darker contrast demonstrated by those grains of thicker oxide.

Similar observations were made from the annealed sample exposed at 320°C for the longer duration of 7000 h. Consistent with the 1000 h sample the orientation with <001> normal to the exposed surface proved to be favourable for growth in the longer exposure sample. In addition this sample indicated that orientations with <111> normal to the surface were unfavourable for oxide growth, see Figure 51 This sample, with greater average oxide thickness than the 1000 h sample, proved to have a spread of oxide depths that were better distributed within the fixed interaction volume of back scattered electrons at 30keV. Therefore the correlation between grain orientation and oxide depth could be observed across the full range of orientations with the back-scattered electron detector. An

explanation of how the differing oxide depths across grains are distinguished with the back-scatter detector and the dependence of accelerating voltage is given in section 7.8.2.

The sensitivity of surface oxidation was most noticeable with BSE in the annealed samples. In the cold worked samples, however, this contrast between grains was not as evident. Rather preferential oxidation at grain boundaries and slip bands appeared to mask the potential BSE contrast between grains of different orientations. See Figure 52 of a 30% elongated sample for a typical example of the view using BSE at high accelerating voltage of the cold worked exposed surfaces. Nevertheless, similar orientation dependence could be observed in cold worked samples with regions of the favourable orientation, <001> normal to the surface, found to have significantly deeper oxidation compared to regions of the unfavourable orientation, with <111> normal to the surface. An example of such can be viewed in Figure 53. Note the cold work in this sample has caused significant orientation rotation within a single grain resulting in only a portion of the grain falling within the selection criteria. This gradual change in orientation across grains of cold worked material also reduced the BSE contrast between grains of differing favourability with respect to orientation, which was distinctive in the annealed samples.

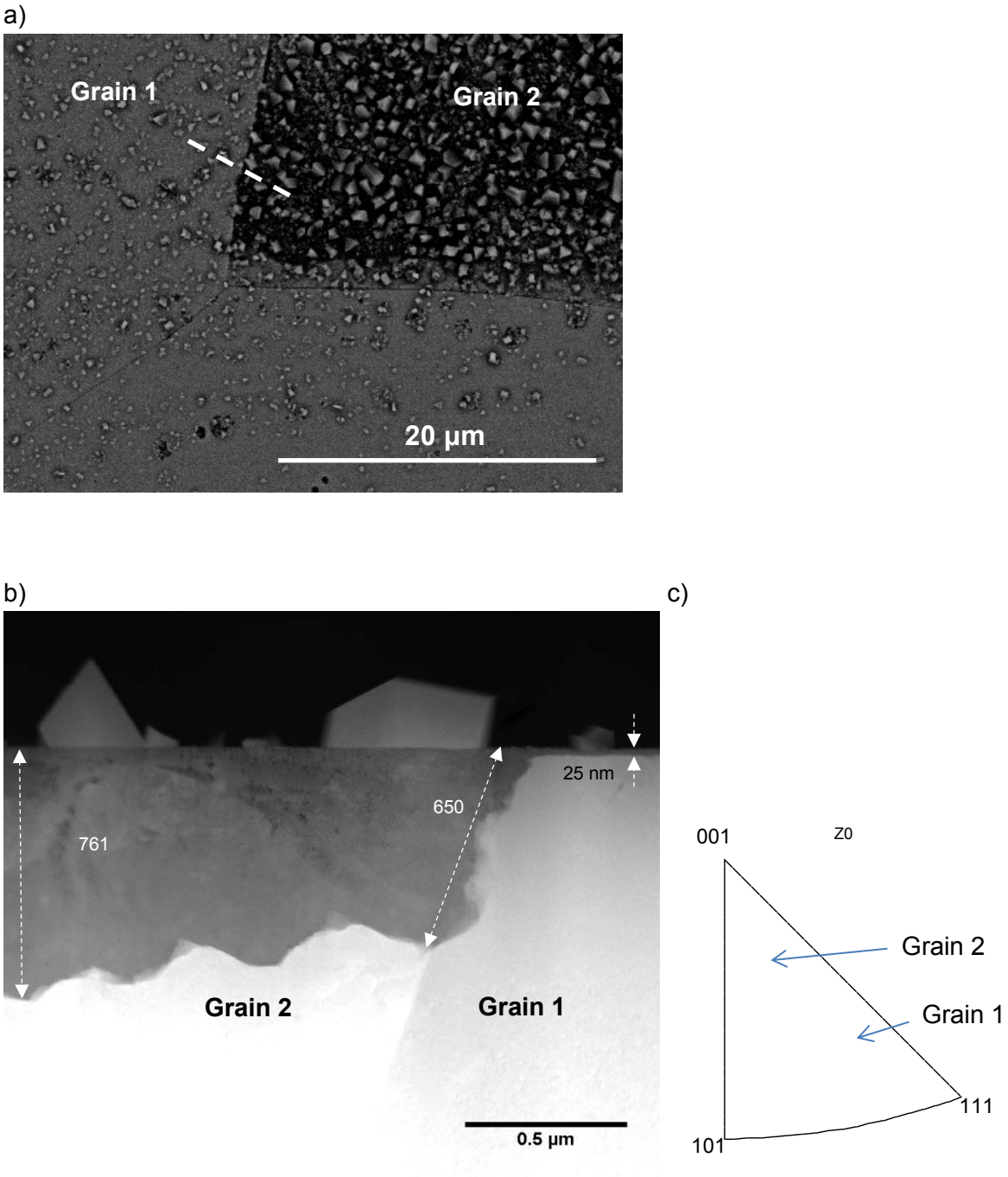

Figure 49. Annealed sample exposed at 320°C for 1000 h with a) back-scatter electron contrast between grains from SEM images with location of FIB section indicated, and b) TEM HAADF image in STEM mode of FIB section indicating the change in Cr-rich inner oxide depth across grain boundary, c) provides the metal orientations with inverse pole figures of grains 1 and 2 indicated.

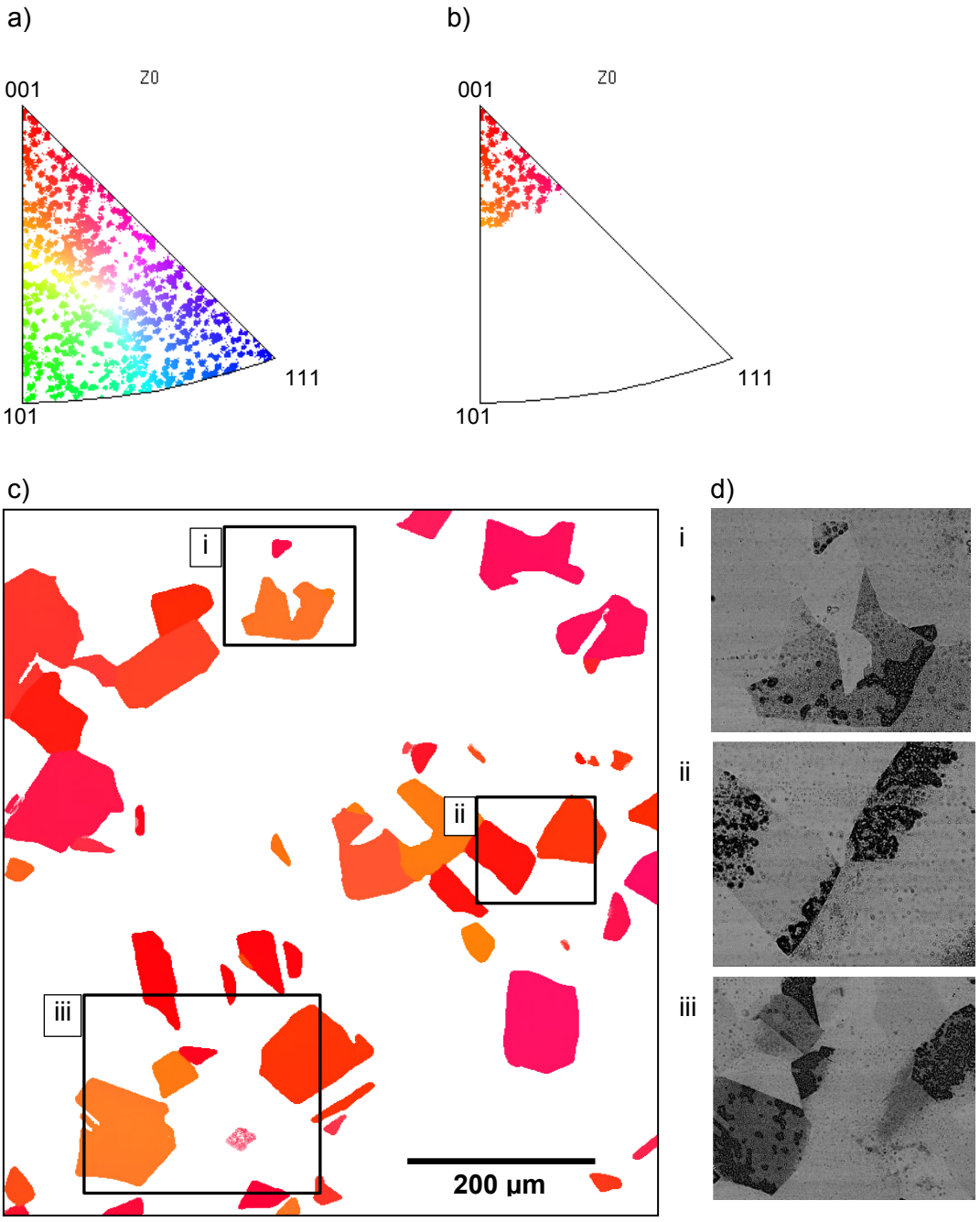

Figure 50. This montage illustrates the correlation of a selected orientation from an annealed sample exposed at 320°C for 1000 h (sample 59) with observed oxide thickness. The inverse pole figures in (a) and (b) indicates normal (z direction) to the exposure surface. From the full set of orientations within IPF in (a), a window of random orientations selected about <001> parallel to the z direction was selected (b), resulting in c) the highlighted portion of the EBSD map (approximately 17%), which corresponds to d) BSE SEM images of three locations from the EBSD map.

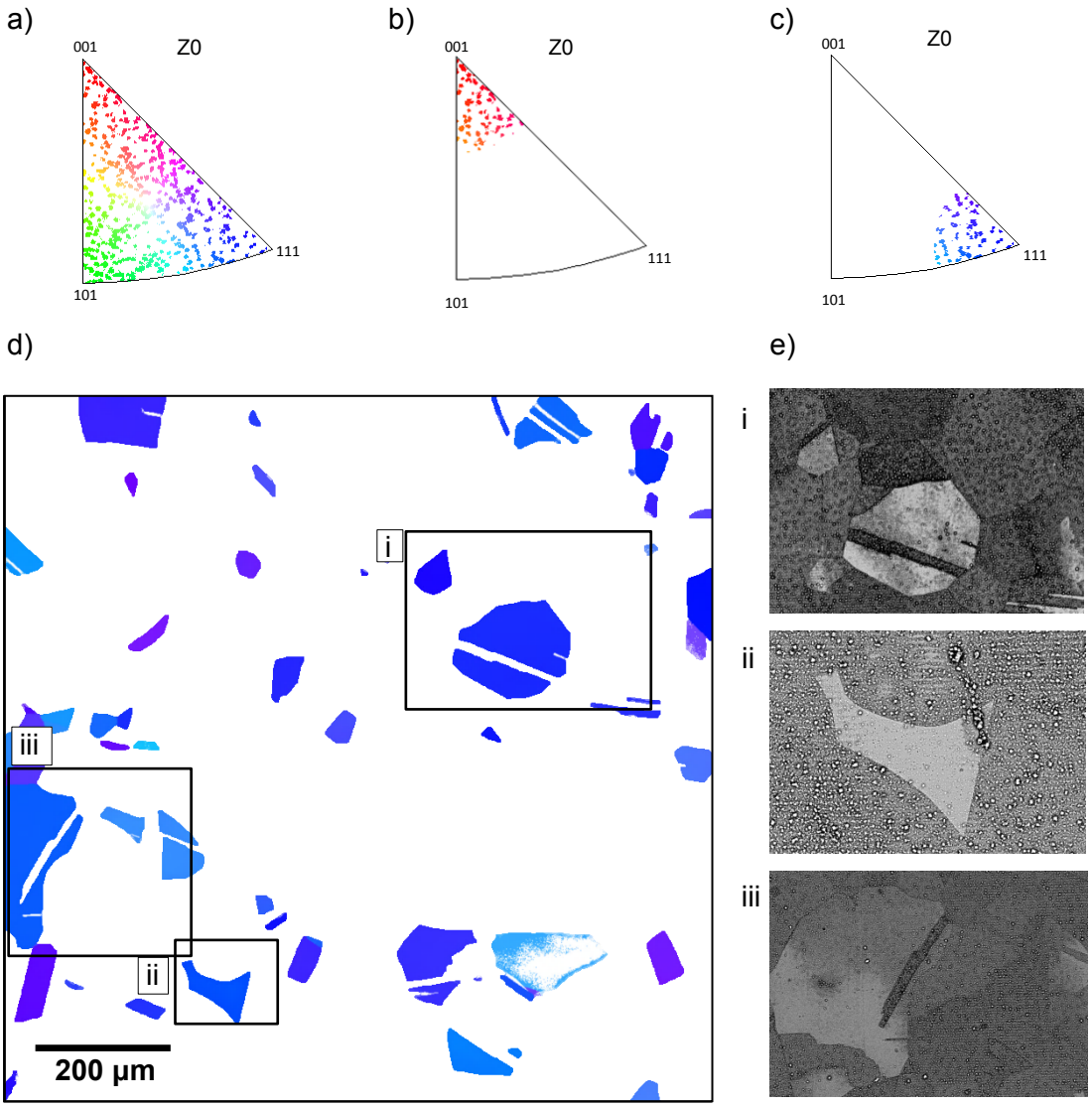

Figure 51. Correlation of two selected orientations from an annealed sample exposed at 320°C for 7000 h (sample 56) with observed oxide thickness: a) full set of orientations in EBSD map, b) a window of random orientations selected about <001> parallel to the z direction (in shades of red) and c) with <111> parallel to the z direction (in shades of blue). These selections resulted in (d) the highlighted portion of the EBSD map with corresponding colours. The three BSE images in (e) indicate that the former (<001>//z) orientation selection is favourable, consistent with Figure 50, while the latter (<111>//z) orientation is unfavourable for oxide growth.

a) b)

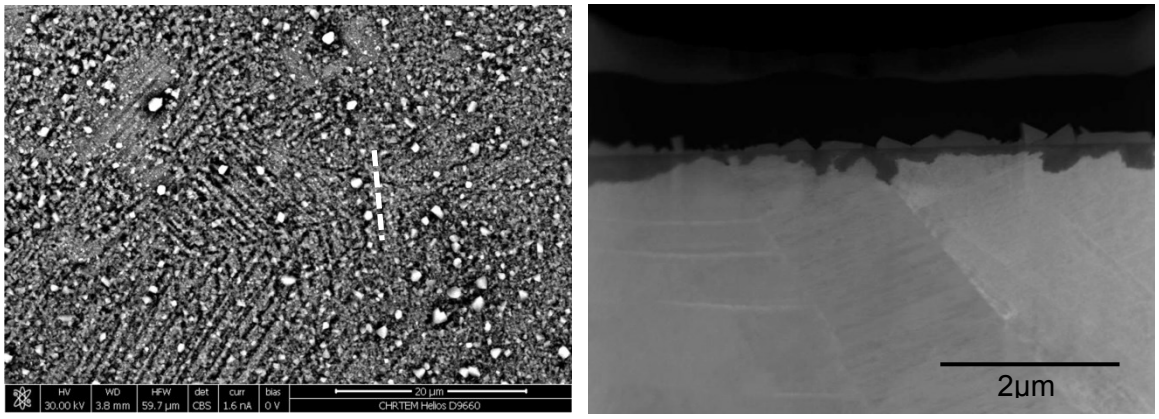

Figure 52. Images of a 20% cold rolled sample exposed at 320°C for 1000 h with: a) BSE image of the oxidised surface at 30keV showing darker contrast at grain boundaries and slip bands, and b) a TEM view of a FIB prepared thin film from the location indicated in (a).

a) b)

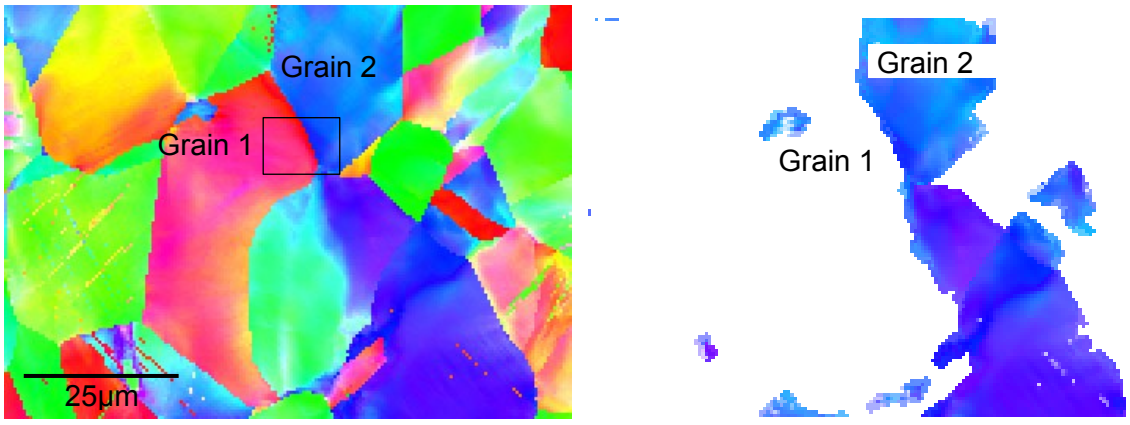

c) d)

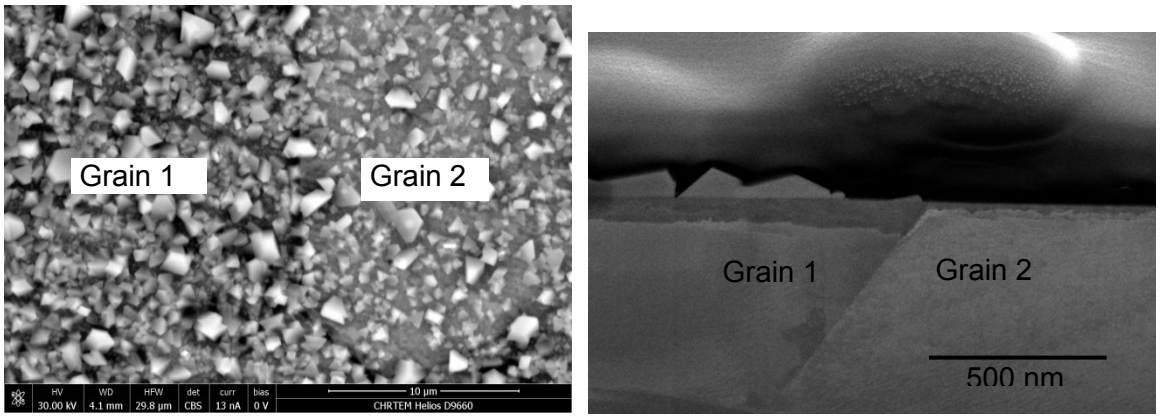

Figure 53. Orientation selection from a 30% elongated sample exposed at 320°C for 1000 h: a) a portion of the EBSD map viewed with IPF; b) the portion of the map corresponding to the same two selection criteria as

Figure 51 highlighting both favourable (grain 1) and unfavourable (grain 2) orientations about a grain boundary; c) a BSE image at 30keV of the area indicated in (a) showing darker

contrast in grain 1; and d) a SE image of the FIB section across the grain boundary showing a clear correlation of inner oxide depth with the favourable (grain 1) and unfavourable (grain 2) orientation for oxide growth.

8.3. Temperature Dependence of Orientation Sensitivity

The orientation relationship with oxide depth of 320°C samples given in the preceding section was, however, not consistent across all the exposure temperatures. At 290°C the same orientation, with <001> normal to the surface, was found to be less favourable for oxide growth than grains of all other orientations. This is substantiated in Figure 54 from an annealed sample exposed for 1000 h at 290°C. Note in this figure the grains that fell within the selected orientation had a brighter BSE contrast compared to the surrounding grains. The selected orientation was confirmed to correspond to lesser inner oxide thickness from a FIB section, see grain 2 in Figure 55, the location of which is highlighted in the map of Figure 54c. It was noted that while it was clear from BSE that those grains with the unfavourable orientation were easily distinguished with light contrast, a favourable orientation could not be distinguished from BSE contrast. This was likely due to the oxide penetration for many orientations having exceeded the optimal depth range within which oxide variation can be distinguished using BSE.

It was also interesting to note that a similar orientation dependence of oxide growth was observed for samples exposed to 290°C and 360°C. An annealed sample exposed at 360°C for 4000 h presents the same unfavourable orientation for oxide growth, seen in Figure 56. Note in this example the BSE images were taken slightly defocussed to avoid having the surface crystallites in clear view which diminishes the grain to grain contrast. There was more contrast variation evident in this sample between orientations. The oxide measurements taken from this sample (360°C for 4000 h), presented in section 8.6.3, indicate that the average oxide thickness was less than the sample exposed at 290°C for 1000 h. It therefore stands to reason that more grains had an oxide thickness that fell within the optimal depth range to be distinguished with BSE; however, a preferred orientation was not clearly observed since the oxides of such orientation was again too deep to be distinguished with BSE.

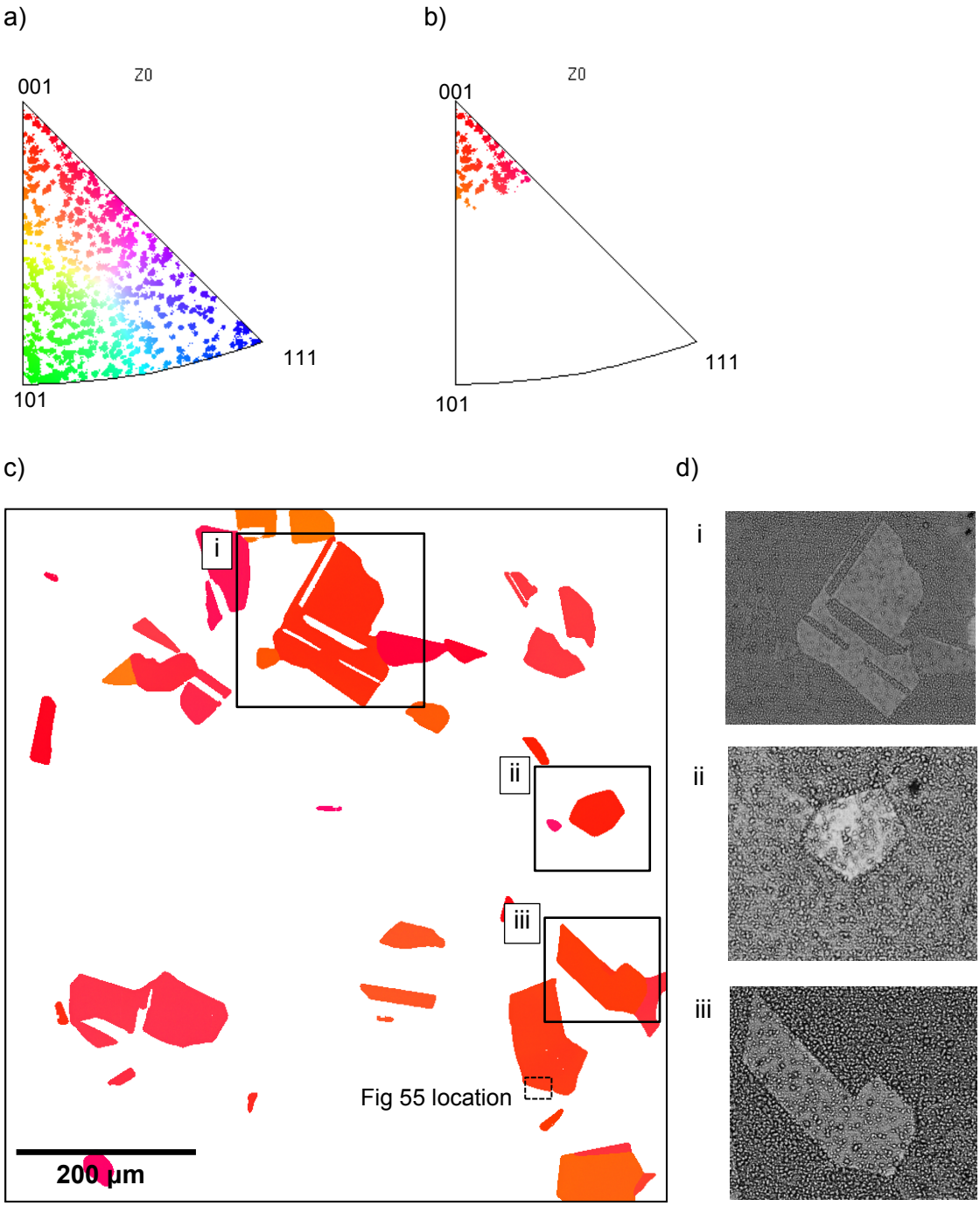

Figure 54. An annealed sample exposed at 290°C for 1000 h with: a) an IPF of the full set of orientations, b) orientations selected about <001> parallel to the z direction corresponding to c) the highlighted grains in the EBSD map (approximately 11%), and d) BSE SEM images of two locations from the selected portions of the EBSD map.

a) b)

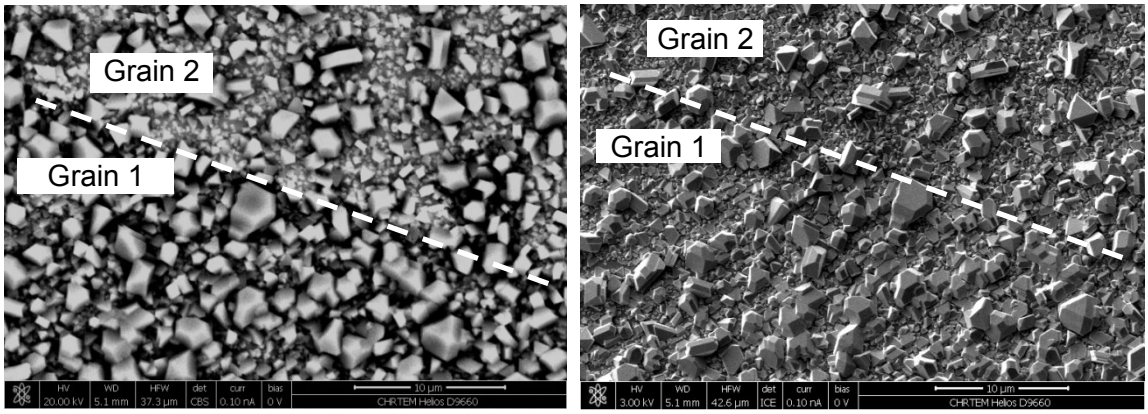

c)

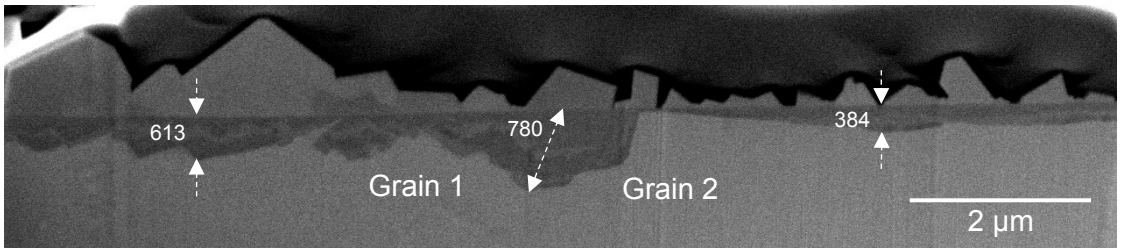

Figure 55. SEM images of the annealed sample exposed at 290°C for 1000 h with a) BSE at 30kV view of the exposed surface showing contrast differences between grains, b) the same location with SE at 3kV showing greater average size of surface oxide crystallites in grain 1, and c) FIB-SEM section across the grain boundary highlighting how the size of crystallites on the surface correspond to the thickness of Cr-rich oxide layer subsurface.

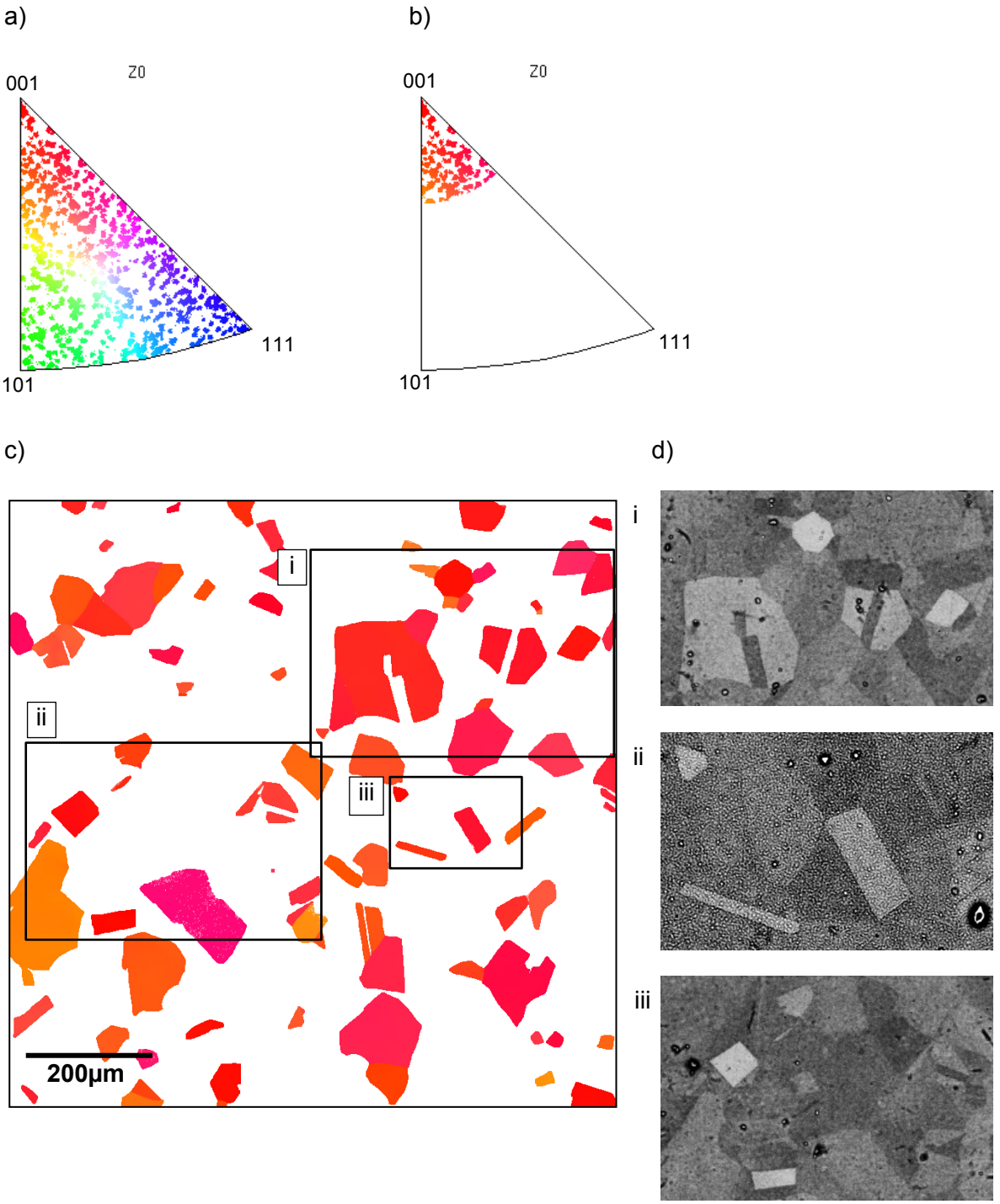

Figure 56. An annealed sample exposed at 360°C for 4000 h: a) the full set of grains plotted in an IPF, b) a selection of grains with <001> normal to the sample surface with the corresponding grains plotted in c), and d) BSE images of three regions indicating the grains of the selected orientation have relatively light contrast (shallow oxide penetration).

8.4. Cold Work Influence on Oxide Kinetics

The effect of cold work on the oxidation growth rate can be evaluated by comparing the intergranular and surface oxidation measurements from all four material conditions exposed at 320°C for 100h, and all but the 20% elongated condition exposed at the same temperature for 1000 h. These measurements are provided in Figure 57 and Figure 58, where the sample numbers and region numbers are given in order to view the corresponding source images within Appendix G and Appendix H. Some intergranular oxide measurements may not be quoted from the list of regions either due to the grain boundary angle disqualifying the measurement, or the grain boundary region being damaged during preparation.

It is evident that the introduction of cold work within the samples presented has not resulted in any consistent observable influence over the oxidation kinetics. The 20% elongated condition was intended to be an intermediate level of cold work but since there was little difference in the oxide growth across any of the conditions, measurements were not obtained of this condition beyond the 100 h exposure. Note that while the data presented below compares the various conditions at 320°C, the oxidation growth can be compared across the different exposure temperatures between the annealed and 20% cold rolled conditions previously presented in Figure 44 and Figure 45 above. A similar conclusion can be drawn since it is clear that at the different temperatures measured the cold work did not provide any oxide growth advantage when compared to the associated annealed samples.

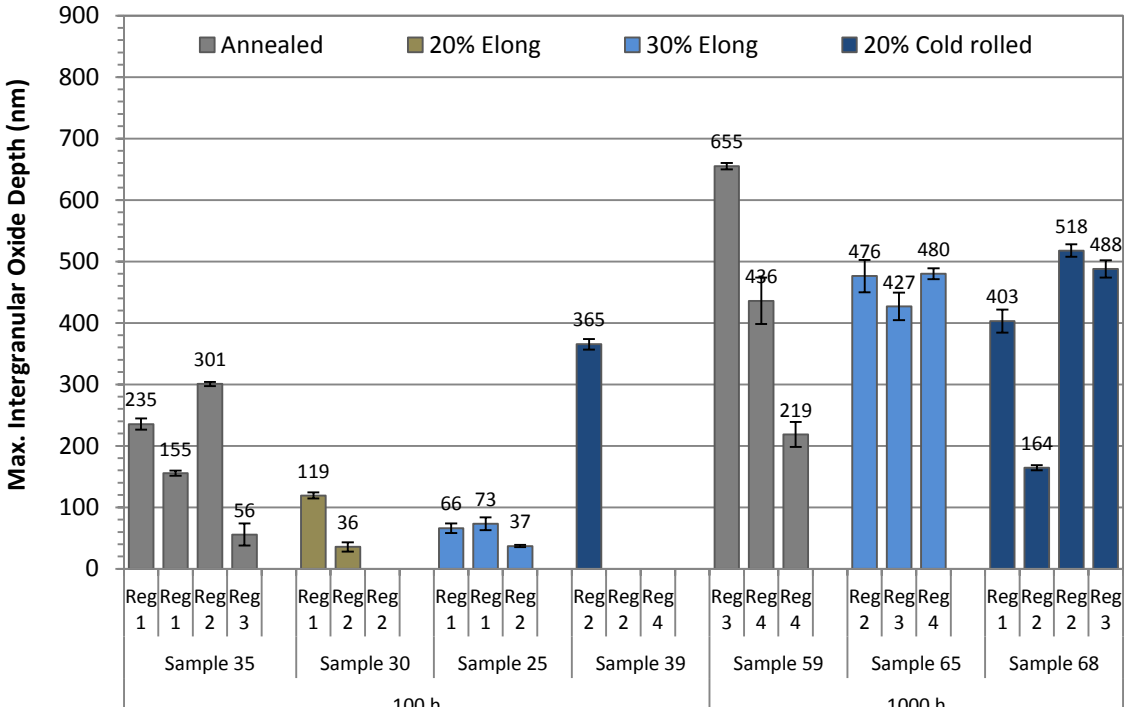

Figure 57. Maximum intergranular oxidation depth measured after 100 h and 1000 h exposures at 320°C. The measurements represent four different cold work conditions: annealed, 20% elongation (100 h only), 30% elongation and 20% cold rolled. The sample numbers and regions associated with each measurement are given for reference. Error bars represent one standard deviation in measurement uncertainty.

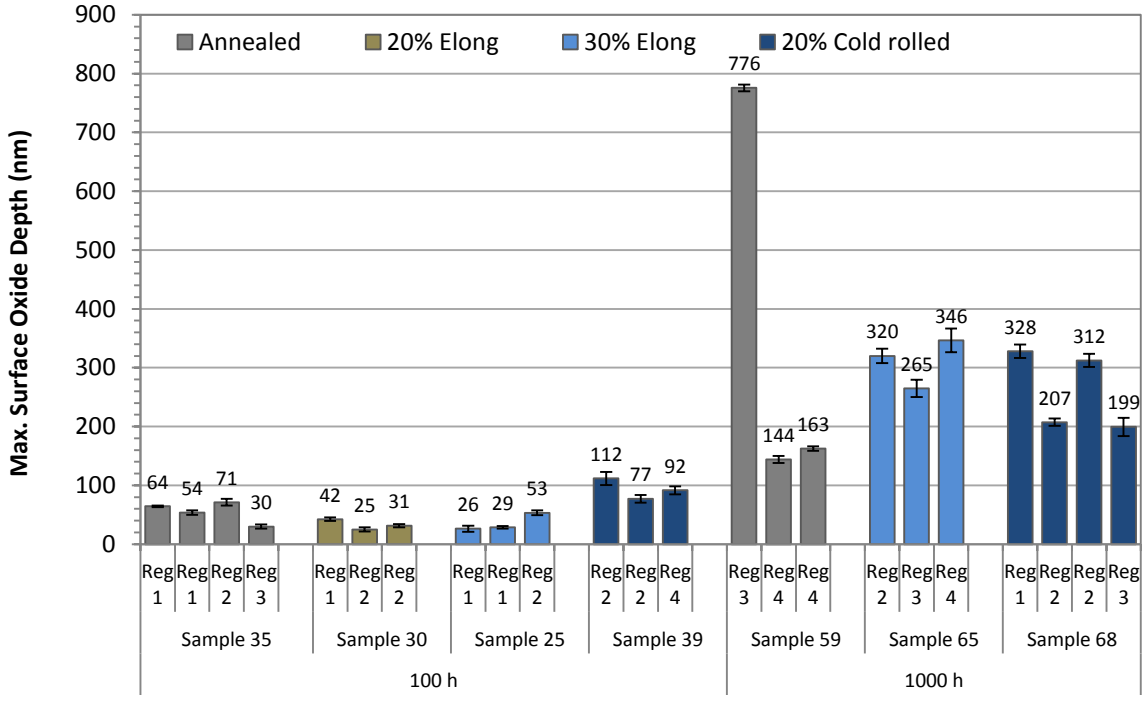

Figure 58. Maximum surface oxide depth measured after 100 h and 1000 h exposures at 320°C. Similar to Figure 57, the measurements represent four different cold work conditions, with surface measurements from the same sample numbers and regions. Error bars represent one standard deviation in measurement uncertainty.

8.5. Origin of Surface Fe_3O_4 Oxides

There was a strong correlation observed between the growth of the outer Fe-rich crystallites and the growth of the Cr-rich inner oxide. In examples where the inner layer was particularly deep, the outer layer had a greater average crystallite size as well as increased coverage of the original surface. The size or coverage of the outer layer was not quantified, however the correlation is clearly evident in Figure 59, with SEM images of typical surface crystallite distribution from various samples exposed for 1000 h. The typical size and coverage of the outer oxide crystallites can be compared at the same magnification between the different material conditions and temperatures. Although there is no significant difference between the material conditions, it is evident that in both conditions the crystallites decrease in size as the exposure temperature is increased. This observation correlates well with the similar trend of inner oxide penetration depths in Figure 45.

The outer oxide crystallite size was also observed to vary across grains of the same sample, and likewise, this variation was met with proportional growth of the inner oxide immediately beneath the surface. Several examples with contrasting inner oxide thickness across a grain boundary can be viewed in Figure 49 (annealed, exposed at 320°C for 1000 h), Figure 53 (30% elongated, exposed at 320°C for 1000 h) and Figure 55 (annealed, exposed at 290°C for 1000 h). Each of these examples have surface and cross-sectional views of the oxidation where the outer oxides were found to be more developed on the surface of grains which had a favourable orientation for inner oxide penetration.

Therefore there is a strong correlation observed between the extent of inner Cr rich oxide penetration depth and the size of the outer Fe_3O_4 crystallites. Since inner oxide is Cr rich, while the metal is mostly composed of Fe atoms, as the oxide grows to consume the metal there must be a net flow of Fe cations diffusing, under the influence of the electric field strength, across the inner oxide film to the solution interface. This correlation suggests then that the Fe ions released into solution at the oxide film/solution interface have little solubility and almost immediately deposit onto the existing spinel oxide crystallites. They will deposit in favourable atomic positions in the spinel lattice to increase the size of the crystals while maintaining their energetically favourable geometric shape.

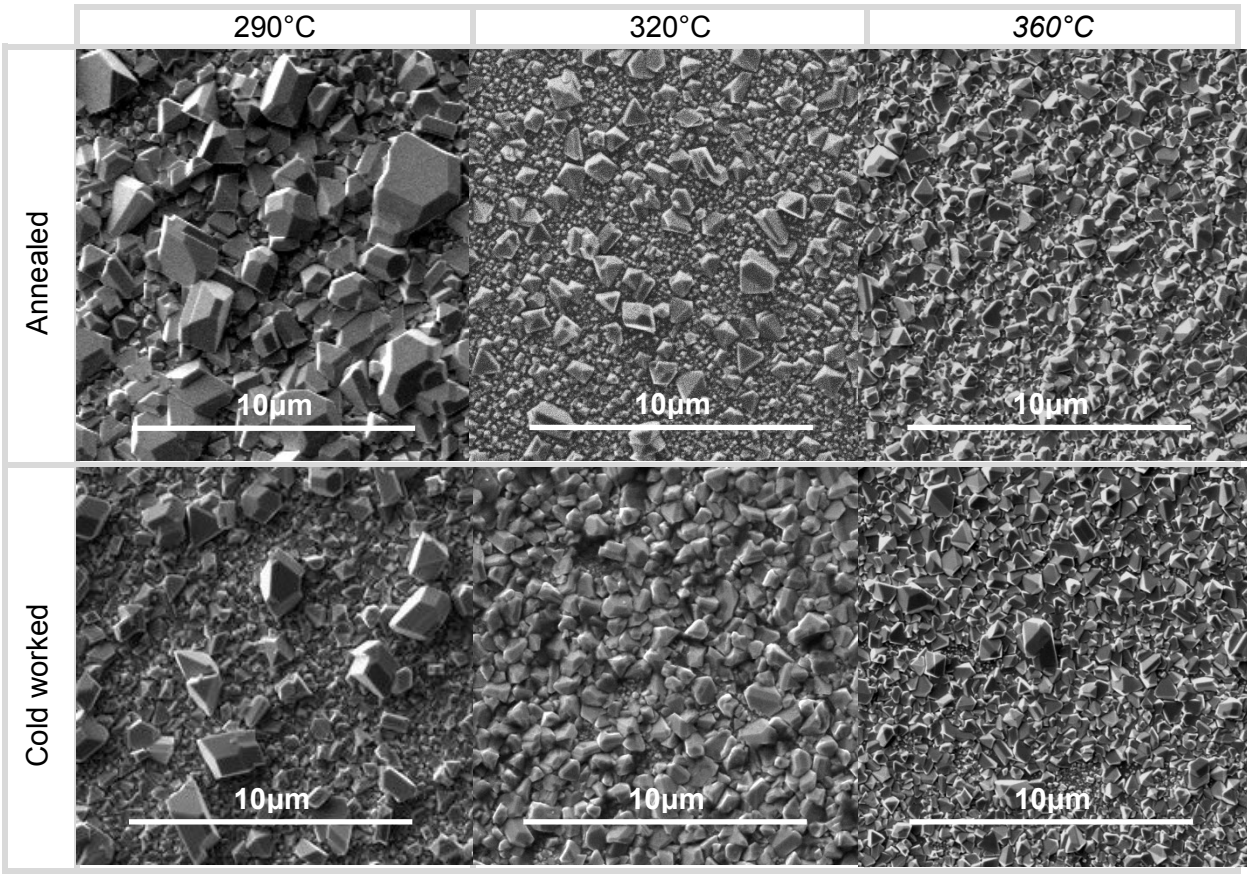

Figure 59. SEM SE images of typical surface oxide crystals on surfaces of annealed and 20% cold rolled samples from the three exposure temperatures at the same magnification.

8.6. Kinetics of Oxide Growth

The growth kinetics of the Cr-rich oxide was measured with two different metrics: depth from the original surface; and intergranular oxide penetration. This was achieved by exposing the samples to the primary water environments for various periods from 1 hour to 7000 hrs at appropriate intervals, and measuring the oxide depth to capture the logarithmic type of growth expected. There was no indication that a steady state oxide thickness, where the theoretical rate of oxide production and dissolution is equal, was reached within the exposure durations tested. Nevertheless sufficient data points were captured to fit a kinetics curve, which could be used to characterise growth and be useful as a tool to predict oxide depth at longer exposure durations by extrapolation.

With the measurement technique being a time consuming operation, an efficient set of data was acquired to achieve the research objectives without redundant or unnecessary data. Only the annealed and the 20% cold rolled material conditions were exposed over the full set of durations. The full set of durations was also exposed only at 320°C. The longer duration

tests from 100 hrs included other material conditions, while the 1000 hours and longer tests also included the variation in temperature.

As discussed in the preceding section, the intention was to arrive at a conservative oxide growth function that could be used as a predictive tool. For this reason regions were selected for their potential to represent the deepest oxide depth in the respective samples.

The full set of kinetics results cannot be distinguished clearly in a single plot of the results. For this reason the variables of the experimental matrix results are presented progressively for discussion.

8.6.1. Characteristic Growth Profile

The measured data of intergranular oxidation of the annealed samples across the full range of exposure durations at 320°C is given in Figure 60. The data is plotted with a time of exposure having a logarithmic time scale. This data can be compared to the surface oxidation depth from the same data set in Figure 61. Note that the surface oxidation measurements are the depth of Cr-rich oxide from the surface while the intergranular oxidation is the length along the grain boundary. The images from which this data, as well as the data to follow, was measured can be viewed in Appendix E to Appendix I.

As previously highlighted from the 1000 hr data, the kinetics of the surface oxidation is strongly dependent on metal orientation. Figure 61 includes an annealed surface oxide depth of 761 nm at 1000 hrs that appears to be far greater than other data points from the same sample. This is indicative of the sensitivity of oxide growth to metal orientation.

The two data sets have been presented with the same vertical axis for comparison. It is clear that over the full range of exposures the intergranular penetration in these samples is not significantly greater in comparison to the surface oxide penetration, and does not show the same propensity for accelerated penetration down grain boundaries as some Ni based alloys previously discussed in section 6.5.3. In some cases, such as the example at 1000 h the surface oxidation can exceed the intergranular penetration under favourable conditions.

The average ratio of intergranular oxidation to surface oxidation penetration for the full set of annealed data at 320°C was measured at 1.7 with a standard deviation of 1.0.

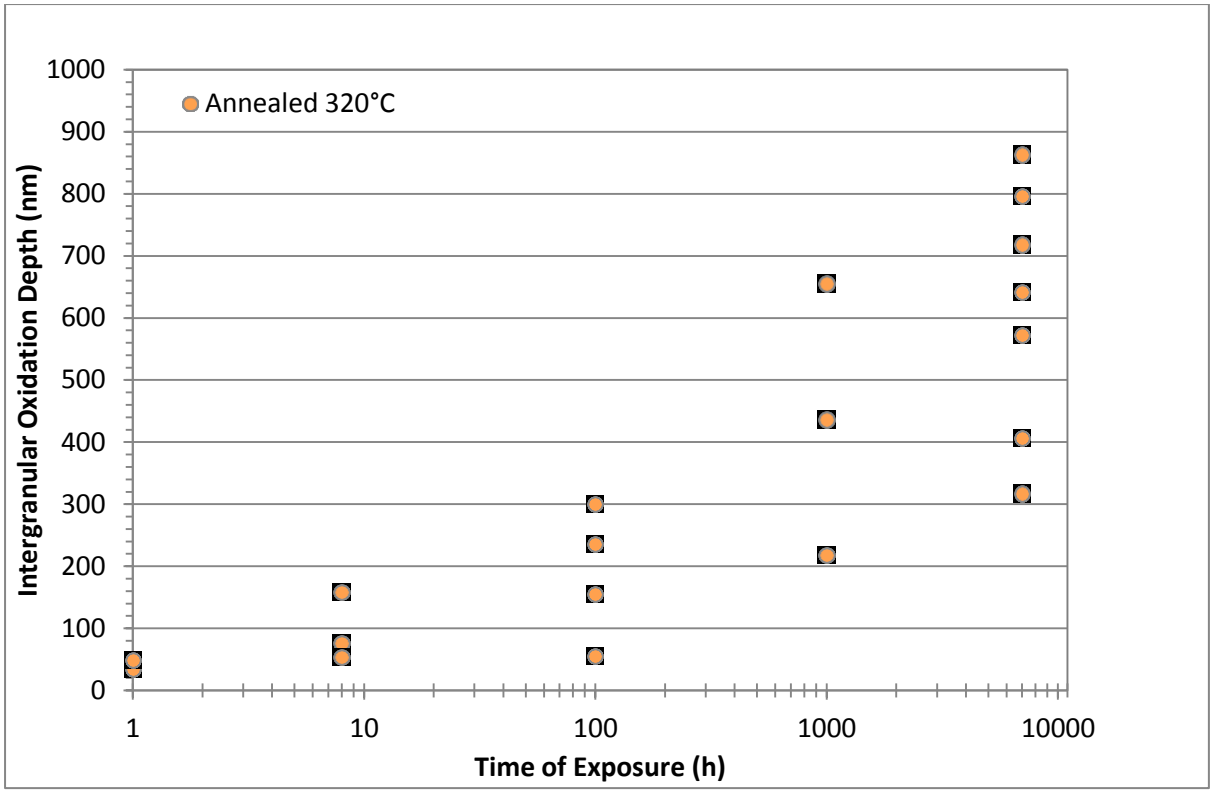

Figure 60. Intergranular oxidation depth for the annealed material after exposures at 320°C over a range of durations from 1 h to 7000 h.

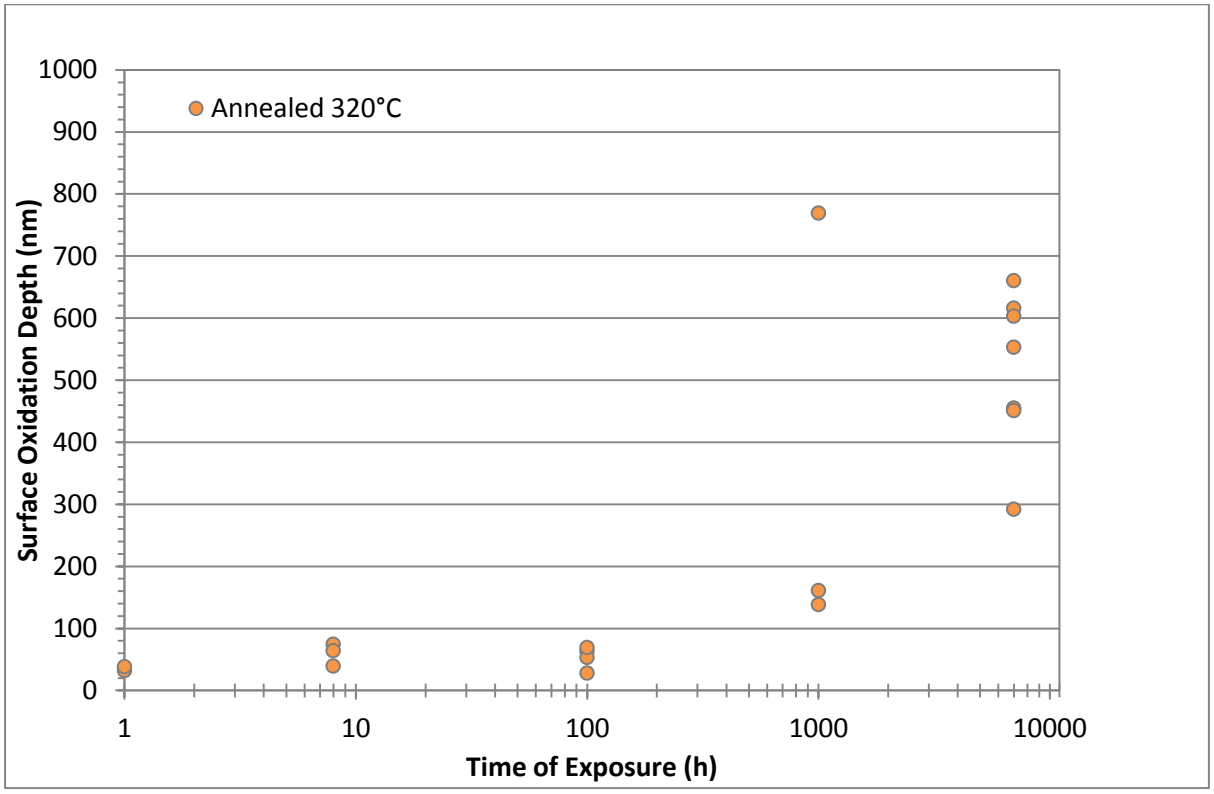

Figure 61. Surface oxidation for the annealed material after exposures at 320°C over a range of durations from 1 h to 7000 h.

8.6.2. Effect of cold work

In Figure 62 and Figure 63 the intergranular and surface oxidation data for all four material conditions (annealed, 20% elongated, 30% elongated, and 20% cold rolled) are presented. The data covers the full range of exposure durations from 1 h to 7000 h at 320°C.

The material conditions representing the extremities of the cold work range, i.e. the annealed and 20% cold rolled conditions, were selected for analysis across the full range of exposure tests. Considering the results presented below from these material conditions across the full range of exposure durations, the two data sets cannot be distinguished. This suggests that the level of cold work introduced in this experiment, including the limited amount of residual tensile stress introduced on the 20% cold rolled surface, did not measurably influence the rate of surface or intergranular oxidation.

The 30% elongated condition, with equivalent cold work as the 20% cold rolled condition, was analysed after a 100 h and 1000 h exposure durations. While the 20% elongated condition, as an intermediate condition, was analysed after a 100 h exposure. The rates of surface and intergranular oxide growth from these conditions were comparable to the other material conditions, therefore it was considered to be of limited benefit to continue analysing these conditions across the other durations.

The ratio of intergranular oxidation to surface oxidation in the cold worked samples was similar to the annealed samples with an average ratio for all the 20% cold rolled material (exposed at 320°C) of 1.8 with a standard deviation of 0.80, and 1.7 with a standard deviation of 0.71 for the 30% elongated samples.

It was considered possible that the introduction of cold work into the material through cold rolling to 20% of the original thickness may introduce sufficient dislocation density to encourage increased diffusion of ion species. This level of cold work was also consistent with that introduced into material in several other studies and therefore was considered to be valuable for comparisons [24,59,98]. However, where the 20% cold rolling material produced a hardness of approximately 287 ± 16 HV (3kgf), this may not have introduced sufficient cold work to create an observable increase in oxidation kinetics.

It is known from stress corrosion susceptibility testing of austenitic stainless steels in primary environments, using constant elongation rate tests (CERT), that the initiation of cracks may occur when the material has sufficient cold work to exceed 250 HV. Nevertheless Couvant et al. has reported that for cracks to propagate hardness needs to exceed 310 HV [99]. It is also evident that the reported cases of SCC in free flowing conditions (under normal primary

water chemistry) all were associated with cold work resulting in hardness >300 HV [30]. Nevertheless, Arioka et al. have demonstrated that with sufficient stress intensity IGSCC can propagate in type 316 stainless steel with the introduction of a minimal amount of cold work to 5% thickness reduction and an associated hardness of 184 HV (1kgf) [98].

In addition to including cold work deformation, the cold rolling resulted in residual tensile stress across the surface. In particular the cold rolled samples used for exposures of 1000 hrs and longer included tensile residual stress values measured from 128 MPa to 200 MPa, but in the 320°C results presented in Figure 60 and Figure 61 the values were with the range of 137 – 144 MPa. However, no difference was observed in the oxide growth kinetics from applying this level of tensile stress.

Therefore, the introduction of cold work and residual stress in this study did not prove to affect the rate of surface or intergranular oxide kinetics; however, increasing the values of either variable may result in observable change in kinetics.

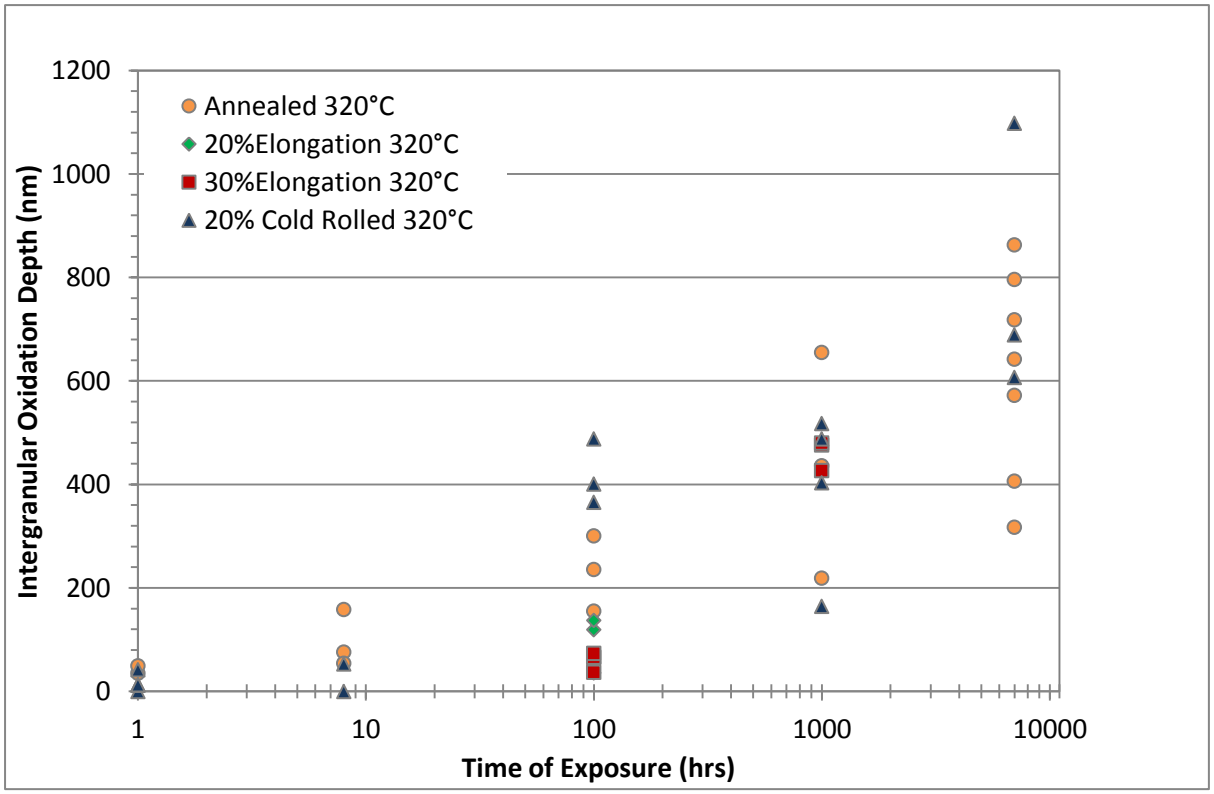

Figure 62. Intergranular oxidation depth (nm) for the four material conditions (annealed, 20% elongated, 30% elongated, and 20% cold rolled) exposed at 320°C for a range of durations from 1 h to 7000 h.

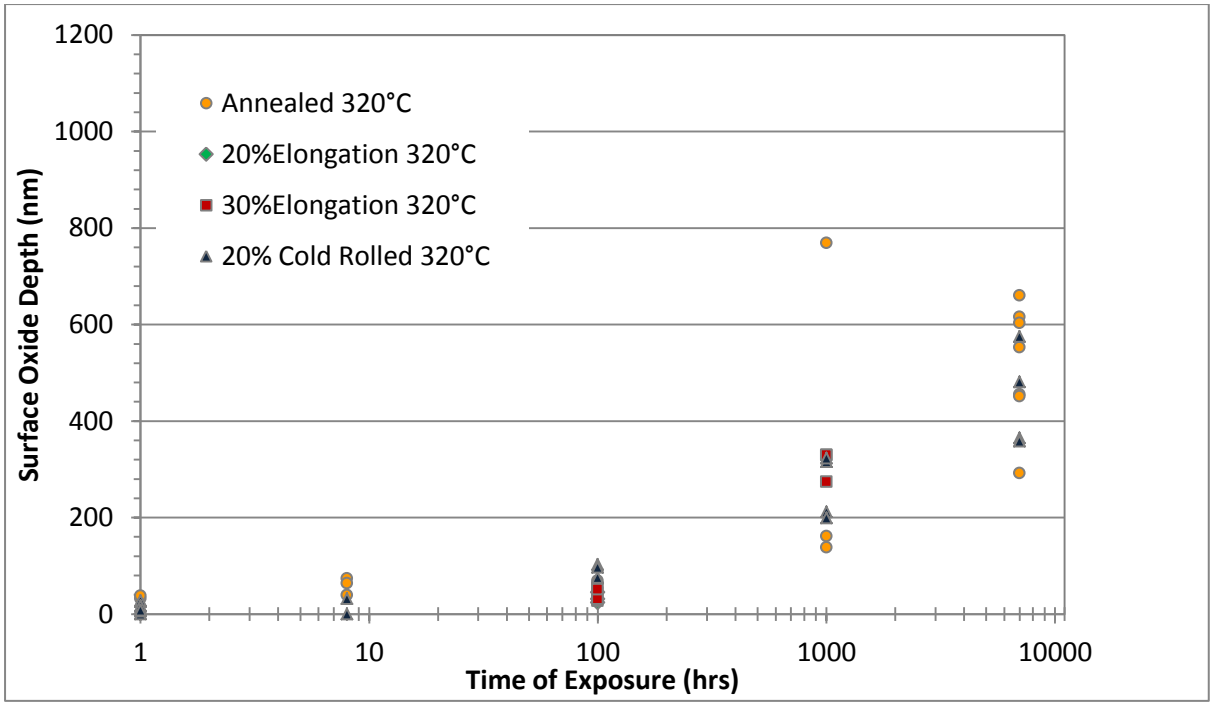

Figure 63. Surface oxidation depth (nm) for the four material exposed at 320°C for a range of durations from 1 h to 7000 h.

8.6.3. Effect of Temperature

Temperature in the 1000 h exposures proved to have an inverse effect on oxide growth within the range of temperatures selected (290°C, 320°C and 360°C). This trend was consistently observed in samples with longer exposure durations.

Figure 64 and Figure 65 plot all data points (intergranular and surface oxidation depth) measured for the two material conditions (annealed and 20% cold rolled) over the full range of exposure durations, and for all three exposure temperatures (290°C, 320°C and 360°C). However, the variation in temperature was observed only at the longer durations of 1000 h and greater. The characteristic kinetic growth curve could be established from the 320°C data which included exposures from 1 h to 7000 h, while the longer duration curves provided data to observe the influence of temperature on the curve. Oxide depth data were acquired at a minimum of 2 exposure durations for each temperature to determine the influence of temperature on the kinetics curve.

In addition to confirming, from the 1000 h data, that the 290°C is significantly more favourable for oxide growth, it was possible, from the longer exposure data, to discriminate between the 320°C and 360°C data sets. It was not clear from the 1000 h exposure data how the growth rate differed between these temperatures, but the longer exposure duration

data confirmed that there is greater oxide growth kinetics associated with exposure to 320°C primary water.

Overall the measurements indicate that oxide growth is profoundly sensitive to temperature, with a counter-intuitive inverse growth law with increasing temperature.

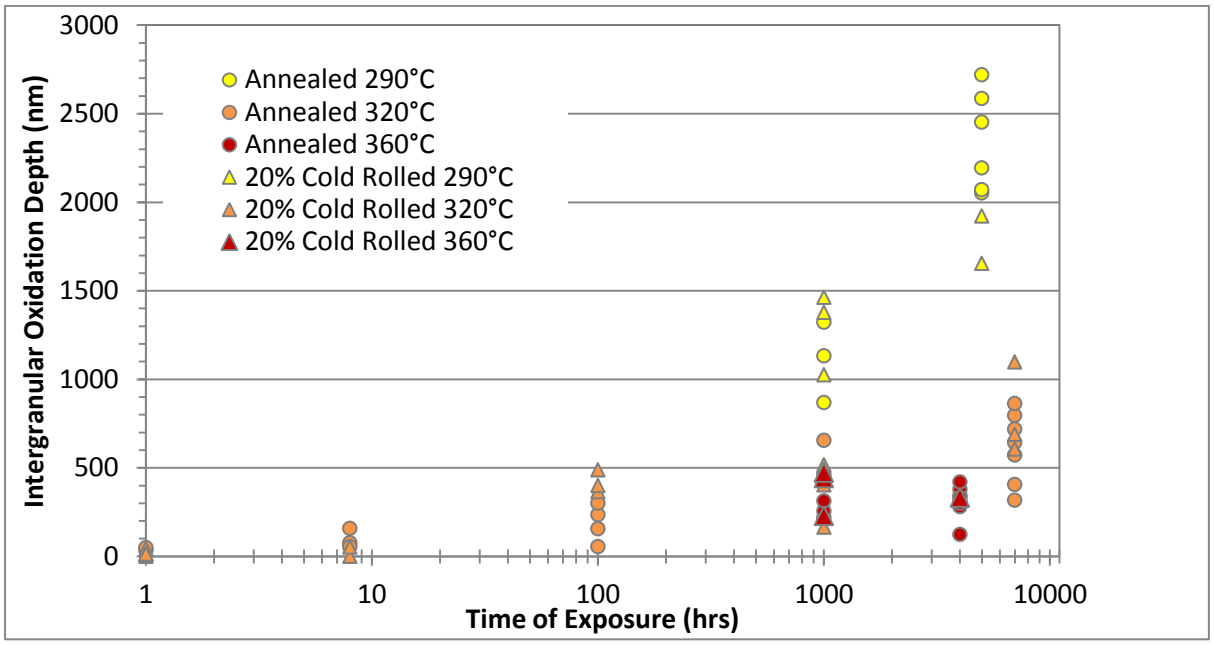

Figure 64. Intergranular oxidation depth of the annealed and 20% cold rolled conditions, over the full range of exposure durations, to primary water at 290°C, 320°C and 360°C.

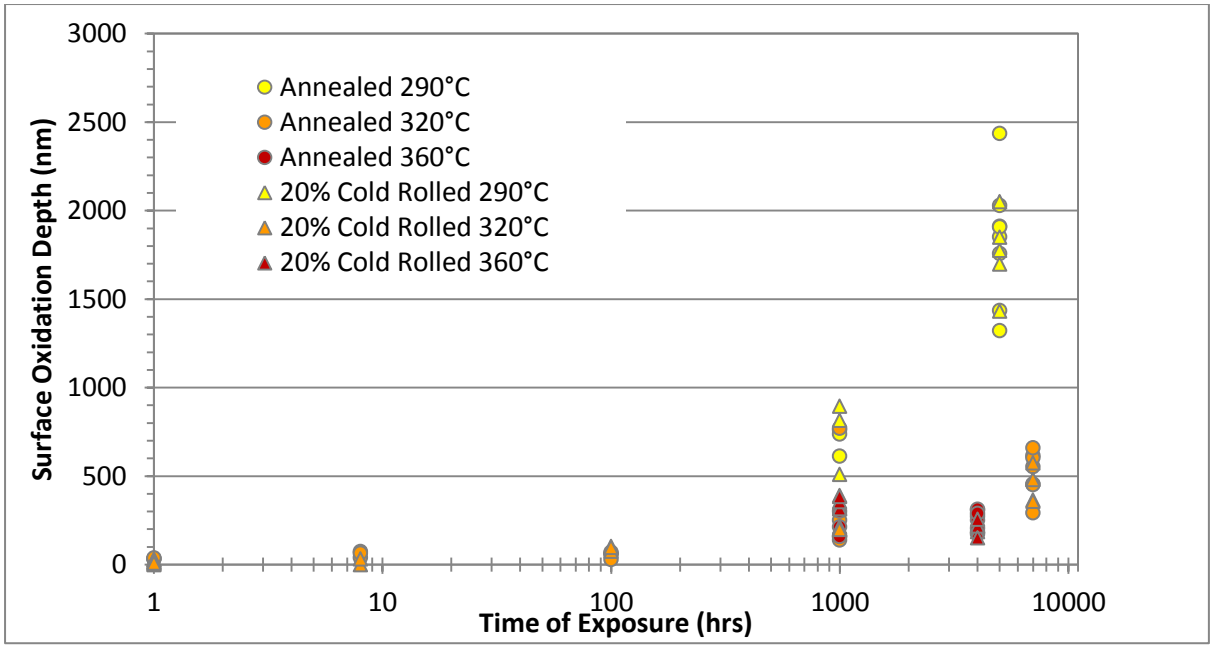

Figure 65. Surface oxidation depth of the annealed and 20% cold rolled conditions, over the full range of exposure durations to primary water at 290°C, 320°C and 360°C.

8.7. Application of the Point Defect Model

As discussed in section 6.6, the point defect model has been well established to predict the behaviour of electrochemically formed passive films. It is a phenomenological model that uses observed oxide behaviour as a foundation to quantitatively describe the change in a metals passive oxide thickness. Therefore it was considered the most appropriate model to use as a basis for modelling the oxide kinetics measured in this investigation.

Figure 66 details, according to the point defect model, the reactions that occur at the respective metal/barrier and barrier/solution interfaces when a passive layer forming metal is exposed to a solution. In steady state conditions these reactions are in a state of dynamic equilibrium resulting in steady state oxide thickness. However, changing one or more dependent variables in the system will result in a change in the reactions and disturb the steady state thickness. This investigation measured the growth in oxide thickness from the time that the sample, with a stable passive film developed in air under ambient conditions, was first exposed to primary water conditions. An expression for oxide thickness as a function of time has been derived by Macdonald et al. who considered only those reactions that result in film formation or destruction i.e. reaction 3 (oxide vacancy generation) and reaction 7 (dissolution of the barrier layer) respectively. The other reactions are considered as lattice conservative and cannot influence the migration of either of the oxide film interfaces [82].

Metal | Barrier Oxide Layer | Solution

(1) $m + V_M^{\chi\prime} = M_M + \nu_m + \chi e'$

(2) $m = M_i^{\chi+} + \nu_m + \chi e^-$

(3) $m = M_M + \frac{\chi}{2} V_{\ddot{O}} + \chi e^-$

(4) $M_M = M^{\delta+} + V_M^{\chi\prime} + (\delta - \chi)e^-$

(5) $M_i^{\chi+} = M^{\delta+} + (\delta - \chi)e^-$

(6) $V_{\ddot{O}} + H_2O = O_O + 2H^+$

(7) $MO_{\chi/2} + \chi H^+ = M^{\delta+} + \frac{\chi}{2} H_2O + (\delta - \chi)e^-$

Figure 66. Reactions present in the maintenance or growth at the respective interfaces (metal/barrier layer and barrier layer/solution) of passive oxide films according to the Point Defect Model [84].

The rate of change in the oxide film thickness can be expressed in terms of reactions 3 and 7 from Figure 66 as [82]:

Equation 4 $$\frac{dL}{dt} = -\frac{2\Omega}{\chi} J_0 - \Omega k_s c_{H^+}^n$$

Where L is the oxide layer thickness, the first term is derived from reaction 3 with Ω is the volume of the oxide layer per mole of cation, χ is the cation oxidation state in the barrier layer, and J_0 (as a negative quantity) is the oxygen vacancy flux at the metal/barrier layer interface. The second term describes reaction 7 with k_s as the rate constant and C_{H+} the concentration of the hydrogen ion at the barrier layer/solution interface and n the kinetic order of the dissolution reaction at this interface.

The oxygen vacancy generation reaction (reaction 3 from Figure 66) in Equation 4 can be described as an electrochemical rate constant k_3 as

Equation 5 $$\frac{2J_0}{\chi} = -k_3 = -k_3^0 e^{a_3 V} e^{-b_3 L}$$

which is further expanded with,

Equation 6 $$a_3 = \alpha_3(1-\alpha)\gamma$$

Equation 7 $$b_3 = \alpha_3 \chi \epsilon \gamma$$

Equation 8 $$\gamma = \frac{F}{RT}$$

Where k_3^0 is the standard rate constant for reaction 3, V is the applied voltage, α_i is the transfer coefficient for the i^{th} reaction, α is the polarizeability of the barrier layer/solution interface, χ is the cation oxidation state in the oxide layer, ϵ is the electric field strength, F is Faraday's constant, R is Avogadro's constant with T as temperature.

Equation 4 can be rewritten in electrochemical terms as

Equation 9 $$\frac{dL}{dt} = \Omega k_3^0 e^{a_3 V} . e^{-b_3 L} - \Omega k_s c_{H^+}^n = a . e^{-b_3 L} - c$$

where a = $\Omega k_3^0 e^{a_3 V}$ and c = $\Omega k_s c_{H^+}^n$.

This expression of oxide growth rate can then be integrated to produce the following expression of barrier layer thickness as a function of time[82,84]:

Equation 10 $$L(t) = L_0 + \left(\frac{1}{b}\right) \ln\left[1 + \left(\frac{a'}{c}\right) e^{-b_3 L_o}\left(e^{b_3 ct} - 1\right)\right] - ct$$

with

Equation 11 $$a' = k_3^0 e^{a_3 (V + \Delta V)} e^{-\alpha_3 \beta \gamma pH}$$

Where V is the applied voltage, and β represents the linear coefficient that relates the potential drop at the film/solution interface to solution pH. Note that if voltage conditions were to change ΔV would represent this change (not applicable in this investigation).

A unique feature of the above function, which distinguishes the Point Defect Model from other oxidation models, is that it considers both the migration of the metal/barrier layer interface into the metal as well as the dissolution of the oxide at the barrier layer/solution interface. In the 316L samples of this investigation, however, no evidence for the inner layer dissolution was observed from the FIB prepared cross-sections. Firstly, in all samples, apart from the few that were damaged by FIB preparation, the outer surface of the inner layer was always observed to be straight line. For example in Figure 49 where a significant difference was observed between the penetration depth of the inner Cr rich oxide layer across grains, the outer surface was a continuous straight line across the grain boundary in this FIB cross-section. If dissolution of the inner layer had occurred it is unlikely that this surface would maintain a uniformly straight line across grains. Secondly, the outer layer is understood to form as a result of the iron cations released into solution at the barrier layer/solution interface and deposited immediately to form a growing outer layer of Fe_3O_4 crystallites. Such crystallites formed early in the exposure tests and were observed in the samples exposed at 1 and 8 hrs, see Figure 34 for example. These crystallites shield the surface of the inner layer from the water environment and if dissolution of the inner layer were active then the Cr rich oxide layer immediately beneath these crystallites would not dissolve. However, the surface of the inner layer was observed in all cases to be continuously flat beneath outer Fe_3O_4 crystallites and areas exposed the environment. These observations provide substantiation to the assumption that the dissolution of the inner Cr rich layer was negligible.

In such a case where the dissolution of the inner layer was negligible, then b_3ct becomes sufficiently small that

$$e^{b_3 ct} \approx 1 + b_3 ct$$

and ct also tends to zero, then Equation 10 will reduce to[84]

Equation 12 $$L(t) = L_0 + \left(\frac{1}{b_3}\right) \ln[1 + a' b_3 e^{-b_3 L_o} t]$$

An explanation for the set of variables used within this expression of oxide thickness is given below.

χ – This represents the valence state of the cation vacancy within the barrier layer oxide. Since our material is an alloy the cation vacancies within the oxide need to

accommodate different cations of various oxidation states. The most common oxidation state of Ni is +2, while Pourbaix diagrams for Cr indicate that it is most likely to oxidise as +3 in neutral solutions. Fe cations could have valence of +2 or +3 and likely a mix of both. Macdonald has used the value of 3 as an estimate value for general passive film forming oxides[100], while Betova et al. reports that the valence state of Fe in the oxide in the passive region is 2.67 [62]. Since the Fe cations will be the most common cation within the barrier film, a value of 2.7 is used consistent with Betova et al.

ϵ - The electric field strength in units of $V.cm^{-1}$ is dependent on the solution environment where both the chemistry of the simulated primary water and the temperature will influence the value. At higher temperature the films are more defective and cannot maintain the same field strength as films formed at lower temperature, resulting in lower field strengths [62]. The point defect model differs from the high field models in that this value remains constant, for any particular environment, as the barrier film grows [83]. At sufficiently high field strengths the migration of the ions through the barrier layer dominates so that the rate determining step for oxide growth remains in the interfacial reactions. The oxide vacancies therefore pile up at the metal/film interface where they are annihilated. Therefore increasing the vacancy gradient through the film, by increasing the electric field strength, will not have a material difference in reaction kinetics [101]. In fact, according to the PDM, the field strength is independent of the applied voltage. This is rationalised by MacDonald who proposed that the electric field is buffered by Esaki band-to-band tunnelling where the distance between the valence and conduction bands at high field strengths decreases and thereby promoting increased tunnelling current [76,81,84,101]. Published values include Penttilä et al. where the theoretical field strengths were calculated by using experimental data with the mixed conduction model to determine transport parameters including field strength for 316L material in supercritical water [85]. The result proves to be a weak function of temperature with ϵ corresponding to approximately 10^5 $V.cm^{-1}$ at 360°C. Betova et al. arrive at a value of $3.5x10^4$ $V.cm^{-1}$ for stainless steel in simulated primary water at 260°C from analysing exposed samples and fitting measured data to the Mixed Conduction Model (based on the PDM) [62]. Therefore $35x10^3$ $V.cm^{-1}$ is used since this value is similar to conditions in this investigation.

α - The polarizability of the barrier layer/solution interface, which is a measure of how the voltage drop ($\varphi_{f/s}$) across this interface responds to the applied potential. This is a dimensionless parameter with $0.2<\alpha<0.8$ for most systems [76], and therefore within this range is a fairly weak influence on growth kinetics. MacDonald assigned a value of 0.50 for a Ti film in an acidic solution (pH 1.5) at 25°C. While these conditions do not

approximate those in the present investigation, the same value was used since it is also midrange for most systems.

k_3^O - The standard rate constant for reaction 3 of Figure 66 represents the rate that oxygen vacancies are generated at the metal/barrier layer interface. This value influences the physical quantity of oxygen vacancies produced, as a result of free oxygen anions that are incorporated as metal oxide, when the interface penetrates the metal in units of $mol.cm^{-2}.s^{-1}$ [76]. The actual value for the oxygen vacancies produced, represented by k_3 in Equation 5, is influenced by the voltage drop across the interface which is a function of applied voltage, barrier layer thickness and electric field strength. The value of this parameter can vary significantly with Macdonald quoting a value of 1.5x10-9 $mol.cm^{-2}.s^{-1}$ for tungsten in a pH 1.5 solution at 25°C [84], while a value of $1.27x10^{-12}$ $mol.cm^{-2}.s^{-1}$ has been used for n-type passive films [76]. This parameter was adjusted to fit the data set in the present investigation.

α_3 - This represents the transfer coefficient for reaction 3 at the metal/barrier layer interface. It is not obvious to associate the transfer coefficient to a physical mechanism; however, they can be determined experimentally by acquiring a potentiodynamic curve for a system by plotting the log of current density vs potential. Using such a curve the Tafel slope can be determined as the slope of the linear portions of the anodic or cathodic curve in the region away from the influence of the opposing reaction (near the rest potential) or influence of solution resistance (at high values of overpotential). The transfer coefficient can then be determined since it is proportional to the inverse of the Tafel slope of the associated reaction [102]. It is a dimensionless parameter and can be defined as

Equation 13
$$\alpha_a = \left(\frac{RT}{F}\right)\left(\frac{dlnj_a}{dE}\right)$$

where j_a is the current density of the anodic reaction. Therefore the transfer coefficient can be determined experimentally by obtaining the Tafel slope $dE/dln|j|$. However, one cannot experimentally isolate the various contributions of the different anodic reactions from Figure 66. This parameter is typically determined by optimising the point defect model from data acquired from electrical impedance spectroscopy (EIS) [76,81].

This value is often not quoted in published literature but Macdonald et al. have calculated a value of 0.05 for Ti film in an acidic solution (pH 1.5) at 25°C [84]. The same author found lower values of ≈ 0.003 from EIS data of nickel in borate buffer solutions [100]. Nevertheless this is another parameter that was optimised to fit the data in this investigation.

The following table summarises the list of constants and known parameters used in the optimisation of the Point Defect Model for the measured oxidation depth data in Table 7.

Table 7. Parameters and constants used in the Point Defect Model optimisation.

PDM Parameter		Value			Units
F –	Faradays Constant	96,485			$C.mol^{-1}$
R –	Universal gas constant	8.3144			$J.mol^{-1}.K^{-1}$
T –	Temperature	563	593	633	K
χ –	Cation oxidation state	2.7			
ϵ -	Electric field strength	35×10^{3}			$v.cm^{-1}$
α –	Polarizability of the interface	0.5			
L_o –	Starting thickness (measured)	4×10^{-7}			cm

Therefore using the parameter values quoted above a simulated oxide growth curve based on the PDM was drawn and optimised on both the transfer coefficient (α_3) and interface rate constant (k_3^0). In addition the effect of temperature is demonstrated on the curve.

8.7.1. Influence of Temperature

Since the PDM, like many other models of oxide growth, includes an Arrhenius type of dependence on temperature, the model predicts a greater rate of oxide growth as the temperature increases. In Figure 67, the influence of temperature on the PDM is demonstrated against a plot of the measured oxide growth data across all exposure times and temperatures for the annealed and 20% cold rolled samples. Keeping all other parameters constant (k_3° = 7E-10, α_3 = 0.052) the PDM is plotted with temperature corresponding to the three exposure temperature conditions. Two observations can be made from the plot below. Firstly, the oxide growth variation from the measured data is far more pronounced than the influence of temperature in isolation on the PDM. Secondly the measured data is inconsistent with the influence of temperature in the PDM i.e. the oxide growth from the measured data decreases with increased temperature, while the PDM predicts the opposite.

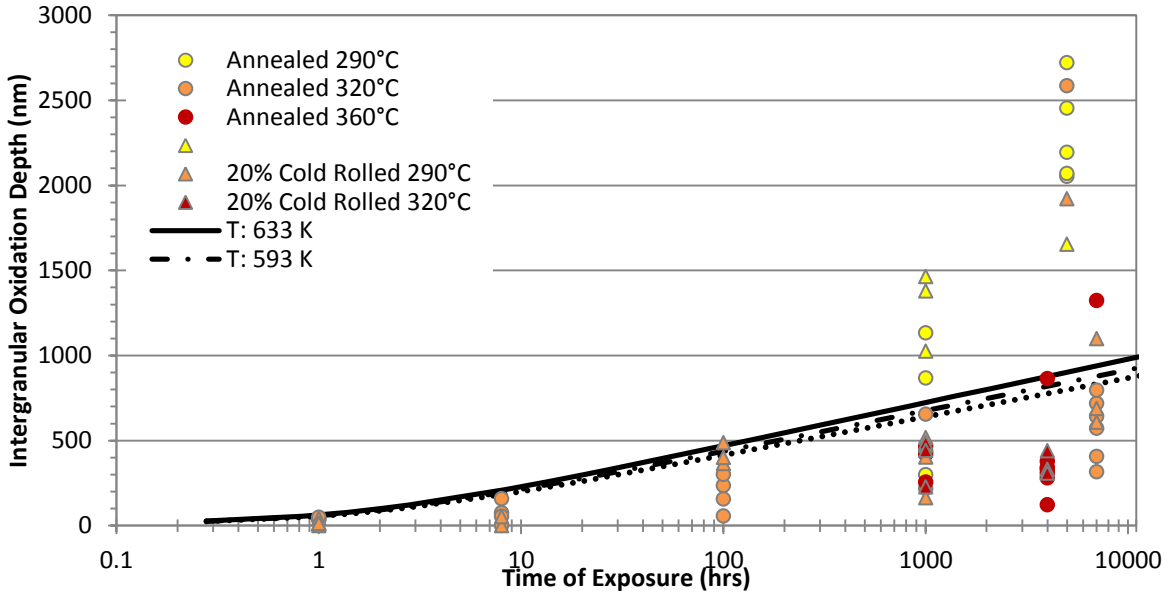

Figure 67. The influence of temperature on the PDM is given by varying the temperature from 290°C to360°C whilst keeping all other parameters constant. The resultant PDM curves are plotted against the annealed and 20% cold rolled measured intergranular oxide depth data in the same temperature range against a log of exposure time.

8.7.2. Influence of Interface Rate Constant

In order to demonstrate the influence of the rate constant of the metal/barrier layer interface reaction ($k_3°$) on the PDM prediction of oxide growth over time, the resulting curves from three $k_3°$ values is given in Figure 68. This plot also includes the full set of intergranular oxidation data for the annealed and 20% cold rolled data. The $k_3°$ values are varied by an order of magnitude between each value, while the remaining variables are kept constant (T= 320° (593K), α_3 = 0.052). It is evident that increasing the rate constant value results in an increased predicted oxide growth rate according to the PDM. However, plotted on a logarithmic scale the resulting curves approach a similar linear slope. Over time these different curves, having the same linear slope, would not converge and therefore the 'steady state' oxide depths would differ dependent on the rate constant.

However, the PDM curve does not provide for a good fit for the complete data set by varying this value alone. For example, it is clear that the plotted curve for $k_3° = 7x10^{-10}$ in Figure 68 may approximate the 320°C data, but the PDM curve cannot reasonably fit the 290°C data considering the relatively steep increase in observed oxide thickness between 1000 h and 5000 h. Therefore in order for the PDM to accurately predict the oxide growth across the full set of temperatures observed, at least two parameters, as well as temperature itself, will need to be treated as variables.

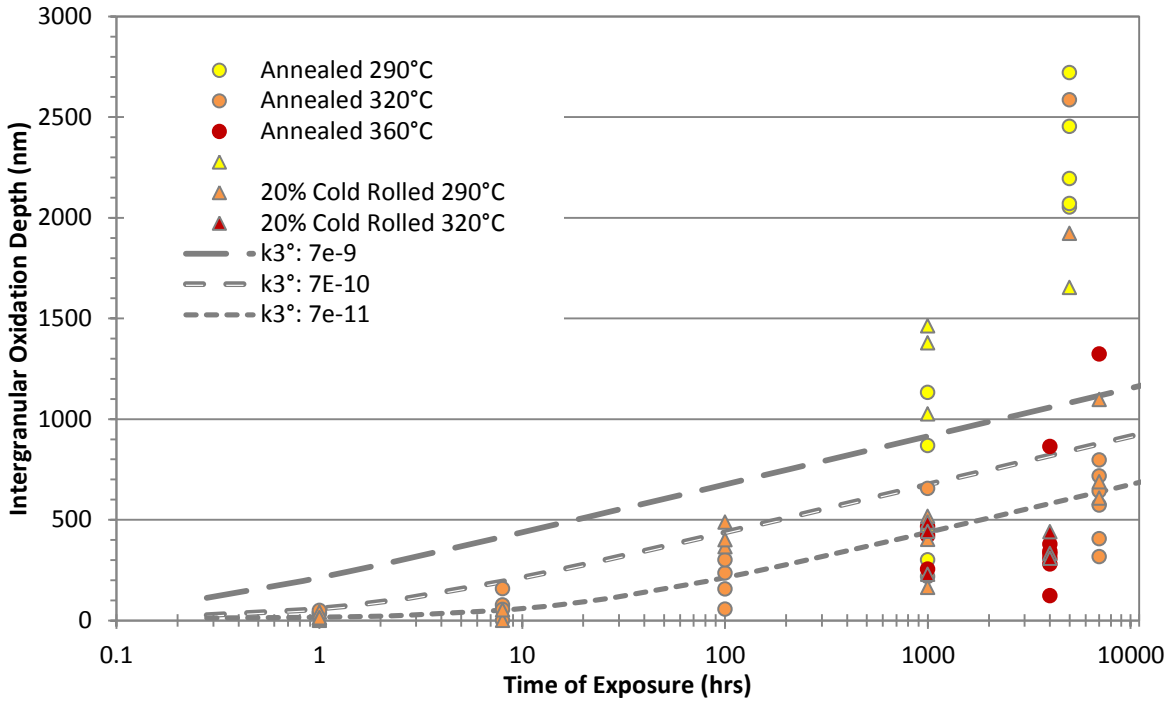

Figure 68. The influence of the rate constant $k_3°$ on the PDM curve of predicted oxide growth is illustrated on a plot of oxide thickness vs time of exposure, by varying this value across 3 orders of magnitude.

8.7.3. Influence of Interface Transfer Coefficient

The influence of the transfer coefficient for the metal/oxide interface reaction is given in Figure 69, which is also plotted with the full set of oxide data from the annealed and 20% cold rolled measured intergranular oxide depth data. It is evident that the PDM is very sensitive to this parameter, which can vary the resultant slope of the oxide growth curve, when plotted with a logarithmic time scale. In the figure the α_3 is varied within one order of magnitude between 0.022 – 0.102, while keeping all other parameters constant ((T= 320° (593K), $k_3°$ = 7E-10), with increased predicted PDM curves as the α_3 value decreases. This parameter is therefore the most influential parameter to predict the oxide depth achieved after longer durations.

It is also clear that it is necessary to vary this parameter in order to approximate the measured data from all the three sets of exposure temperature data since it has been shown that varying the temperature parameter cannot account for the variation in oxide growth alone. Therefore a temperature dependent transfer coefficient is proposed in order for a single expression to approximate all the acquired data sets.

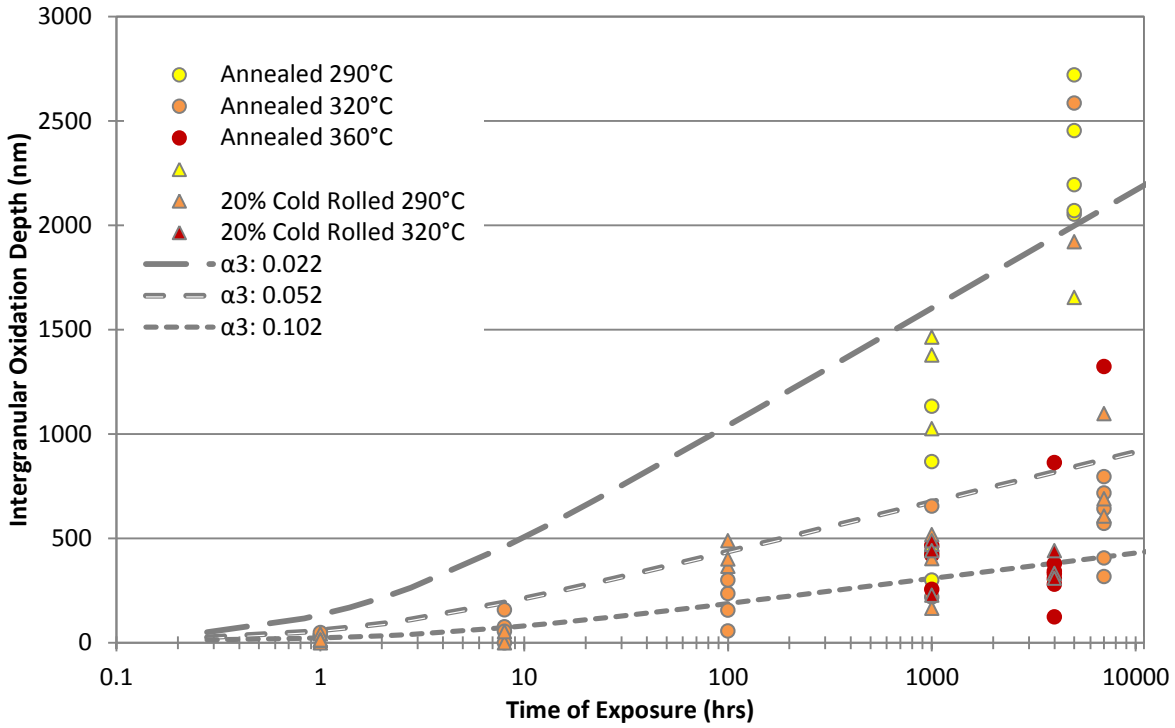

Figure 69. The influence of the transfer coefficient (α_3) on the PDM predicted curve of oxide growth over time using three values of α_3 while keeping other values constant.

8.7.4. Optimisation of PDM Parameters

The intention of the capturing oxide growth rate data was to observe and measure the highest oxide penetration rate for a given set of parameters. This would be an input into other work that aims to develop a conservative stainless steel stress corrosion cracking predictive model for operating PWR plants. To this end the measured data were selected from regions thought to represent the deepest oxidation within grains and at grain boundaries across each sample. Therefore the variables of the PDM were manually optimised to find a curve that describes the upper bound growth rate within each data set. As previously established in section 8.6.2, the 20% cold rolled data could not be distinguished from the annealed data. Therefore, for the purposes of the fitting the PDM, the data from both annealed and the cold rolled material conditions were merged together to form a single data set for each temperature.

Firstly, the optimisation of the PDM for the intergranular oxide growth at the three different exposure temperatures are considered, which are plotted in Figure 70. As mentioned previously both the rate constant as well as the transfer coefficient had to be adjusted together with the temperature parameter when manually optimising the PDM to approximate the oxide depth upper bound for each of the three temperature data sets. Since there was

some uncertainty regarding the best fit of the curve, two curves are plotted for each temperature data set. These curves represent the maximum and minimum plausible values for the transfer coefficient (α_3) to fit the data set with the rate constant ($K_3°$) adjusted in each case to achieve the best fit. The uncertainty was greatest for the 290°C and 360°C for which there were no data points for exposure durations <1000 h. The set of variable parameters selected to fit the PDM to the three temperature data sets is given in Table 8.

The significant oxide growth rate measured for the 290°C data set between the exposure durations of 1000 hr and 5000 hr, in comparison to the higher temperature exposures, is accommodated by a relatively low mean transfer coefficient (α_3) of 0.0055. In order to meet the measured data the curve required a significantly lower rate constant ($K_3°$) value, again relative to the high temperature data, in order to fit the measured data. The curves for the two higher temperature data sets had similar rate constants but they differed largely in the selected transfer coefficient, which was largest for the 360°C data at 0.073 with the same parameter optimised at 0.04 for the 320°C.

The result is that for lower exposure times (< 100 hrs) the rate of oxide growth is predicted to be greater for the higher temperatures but that an inversion occurs in the region of 1000 hrs, where the rate of growth for the 290°C data significantly increases. No measured data could be acquired at the lower exposure times at 290°C to confirm this trend; however, the optimised PDM for two exposure durations suggests that this is the case.

This intergranular oxidation rate inversion with temperature is indicative of a transition in the oxidation mechanism as temperature increases. The PDM fit for the higher temperature data predicts a greater initial oxidation penetration rate than that for the 290°C curve, due to the significantly greater rate constant which may be thermally dependent. However, at the longer exposure durations the 290°C PDM curve predicts a significantly greater oxidation depth than the higher temperature PDM curves. Therefore, at far longer exposure durations, the driving force for growth dissipates at temperatures greater than 290°C. Although the PDM does not predict a steady state oxide thickness, with a lower transfer coefficient (α_3) it predicts that the long term (> 10,000 hrs) intergranular oxidation would stabilise at a significantly greater depth at 290°C than at 320°C or 360°C, even if initially the rate of growth was lower.

Secondly, the PDM curves, optimised to fit the upper bound measured surface oxidation data for the three temperature data sets, are given in Figure 71 with the corresponding variable parameters used in Table 8. The transfer coefficient (α_3) for each of the three temperatures was equivalent to the corresponding intergranular oxidation curve at the same

exposure temperature. Therefore the surface oxidation curves only differed from the corresponding intergranular curves by the rate constants, which were lower in the surface oxidation curves for each exposure temperature.

It is noticeable that the rate constant for the surface oxidation in the 290°C exposure temperature was marginally lower than for the intergranular oxidation curve at the same temperature. In contrast the rate constants for the surface oxidation curves 320° and 360° exposure temperatures were more than an order of magnitude lower than their corresponding intergranular oxidation curves.

Table 8. Variable parameters used when optimising the Point Defect Model to approximate the greatest oxide growth rate for each of the three measured temperature data sets. The uncertainty in the variables is expressed with each parameter having a mean value and a value when maximising and minimising the transfer coefficient for each data set. Note that the subscript 3 indicates that the parameter relates to reaction 3 in Figure 66.

Temp.	Parameter		Intergranular oxidation			Surface oxidation		
			Mean	Min α_3	Max α_3	Mean	Min α_3	Max α_3
290°C	Temperature (k)	T	563			563		
	Rate constant ($mol.cm^{-2}$)	$k_3°$	1.00E-10	7.0E-11	1.3E-10	7.20E-11	3.40E-11	1.10E-10
	Transfer Coefficient	α_3	0.0055	0.004	0.007	0.0055	0.004	0.007
320°C	Temperature (k)	T	593			593		
	Rate constant ($mol.cm^{-2}$)	$k_3°$	1.18E-09	7.50E-10	1.60E-09	7.20E-10	7.90E-10	6.50E-10
	Transfer Coefficient	α_3	0.040	0.035	0.045	0.040	0.035	0.045
360°C	Temperature (k)	T	633			633		
	Rate constant ($mol.cm^{-2}$)	$k_3°$	1.36E-09	2.20E-10	2.50E-09	2.13E-10	6.50E-11	3.60E-10
	Transfer Coefficient	α_3	0.073	0.055	0.09	0.073	0.055	0.09

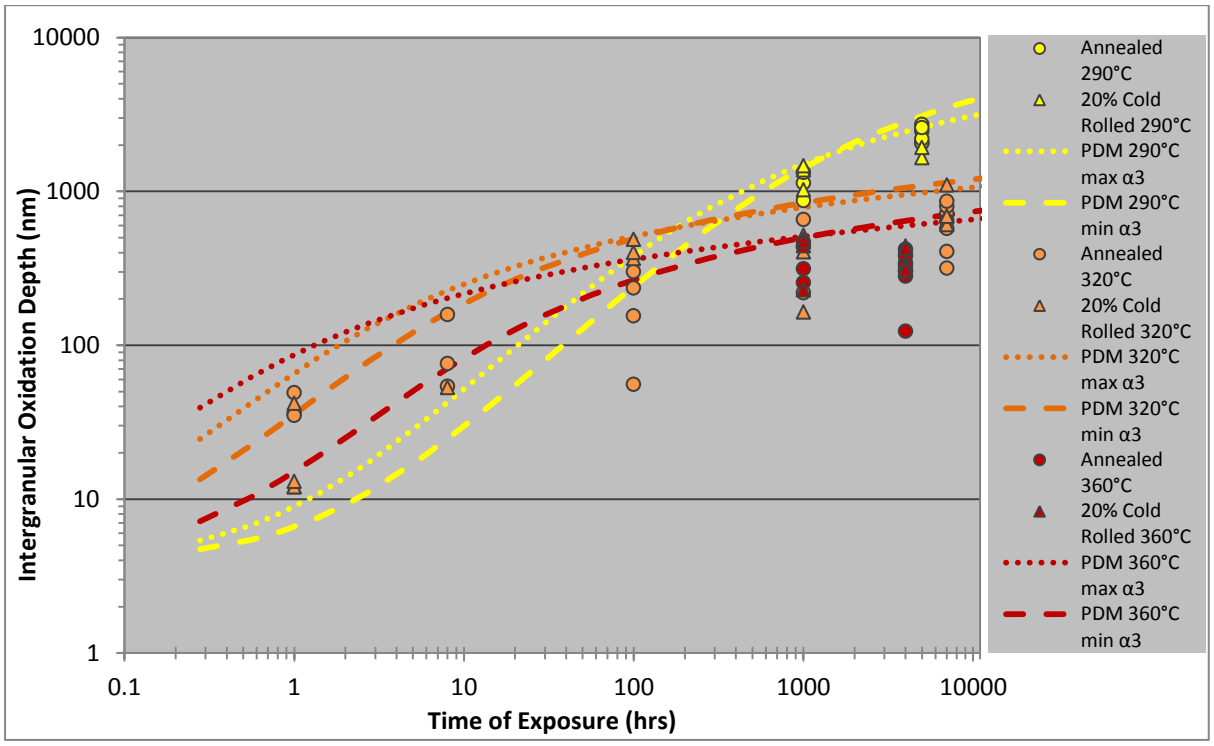

Figure 70. Intergranular oxide depth values verses time of exposure, plotted with both axes on log scales. The PDM was used to approximate the greatest measured depth values for each of the three temperature data sets. The uncertainty of each temperature curve is expressed by fitting two curves when maximising and minimising the transfer coefficient while still approximating the relevant data.

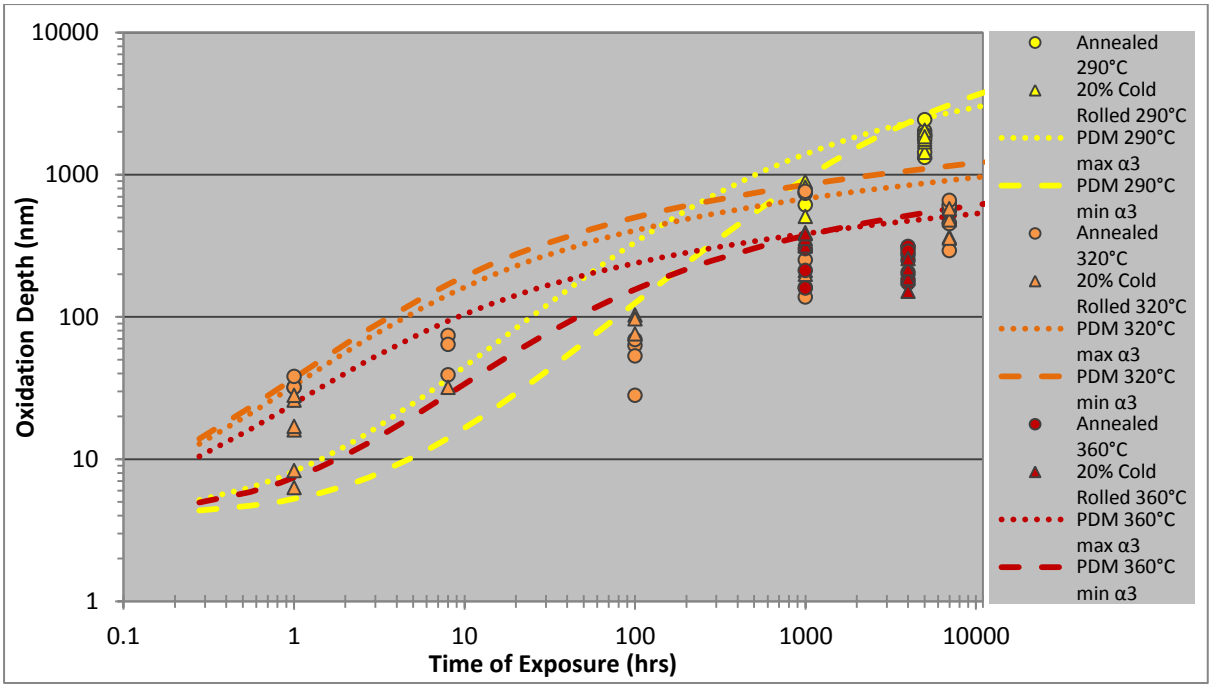

Figure 71. Surface oxidation depth values verses time of exposure, both axes plotted on a log scale. Three PDM curves are plotted to represent the upper bound for the oxidation depth at three different temperatures measured. The uncertainty of each temperature curve is expressed by fitting two curves when maximising and minimising the transfer coefficient while still approximating the relevant data.

8.7.5. Modifying the PDM for Oxidation Growth of 316L Stainless Steel in Primary Water Environment

As demonstrated above the PDM in its published form cannot accurately be used to predict oxide growth behaviour of 316L stainless steel in the primary water environment. Therefore a modification is proposed to improve the capability of the PDM to predict oxidation growth, and time to initiate intergranular stress corrosion cracking. It is possible that the proposed modification to the PDM can be extended to other austenitic stainless steels in the primary water environment.

This investigation has yielded data for samples exposed to typical primary water chemistry for various durations and at temperatures within the range of 290°C - 360°C. However, in this range the rate of oxide growth is shown to decrease with temperature, a trend not consistent with behaviour outside of this temperature range. In order to have confidence other data were required to substantiate the model predictions outside this range. For this reason relevant data were searched in published literature but relatively few papers were available to be comparable to the data from this study. Nevertheless some data were found and detailed below with the limitation for comparison highlighted.

Castle and Clayton (1987) exposed polished 304 type stainless steel samples to high temperature water at three temperatures (120°C, 160°C and 200°C) for short duration exposures (1 and 3 h) to measure and characterise resultant film formation [103]. There was no record of attempting to reduce the oxygen content in the water, and therefore it is assumed to represent oxygenated conditions. The resulting oxides were analysed by incrementally removing material from the surface with an argon ion gun, and acquiring composition profiles using X-ray photoelectron spectroscopy (XPS) after each milling step [104]. The authors were then able to compile a quantitative chemical profile of the samples from exposed surfaces into the material, averaged over the measured surface area. Using a threshold oxygen content of 40% the depth of the oxide layer was defined. It was also noted that a dual layered structure was observed with a Fe rich outer layer and a Cr-rich inner layer. In order to use the most comparative values, the Cr-rich portion of the total oxide thickness was extracted to represent the inner oxide layer. The publication concluded that a significant increase in oxide growth was measured at the higher 200°C temperature compared to the two lower temperatures.

Tapping et al. (1986) studied the composition and morphology of oxide films after exposing 304 type stainless steel to lithiated high temperature water [105]. Polished samples were immersed for several exposure durations (48 – 168 h) at 300°C. While the chemistry of the medium simulated primary water was controlled with respect to reduced oxygen (<4 ppb), it included a lithium concentration resulting in an alkaline solution of pH 10.3. Although this high pH is beyond the upper limits of industry guidelines for chemistry control of PWR primary water, this study formed some early investigations that explored the effects of operating higher pH values. Tapping et al. characterised the resulting oxides after the exposures by measuring the oxide composition as a function of depth. This analysis was achieved by using two complimentary techniques of nuclear microanalysis and auger electron spectroscopy (AES) with ion milling. For comparison the measurements for the Cr rich inner oxide layer were extracted from this publication.

Ziemniak and Hanson (2006) studied the effect of zinc treatment on the oxide development of 304 type stainless steels exposed to the primary water environment [90]. In this investigation samples were exposed to simulated primary water, with the addition of 30 ppb of soluble zinc ions, at 260°C for several durations spanning 1000 – 10000 h. The resulting oxides were characterised using grazing incidence X-ray diffraction and XPS together with incremental argon ion milling to compile the averaged compositional structure and depth of the oxide films. The addition of Zn, however, is expected to reduce the oxide growth rate as demonstrated in a separate paper [62]; nevertheless, the data were used for a reference between 200°C and 290°C. Ziemniak and Hanson quote the total thickness of oxide in their

article. However, using the ratio of inner Cr-rich layer to total oxide thickness from Tapping, where the inner Cr-rich oxide accounted on average 62% of the total thickness, the Cr-rich layer thickness was estimated.

Finally Penttilä et al. (2011) reviewed literature of oxide behaviour of various alloyed steels in supercritical deaerated water in order to calibrate their proposed model based on the mixed conduction model [85]. The data included 316L material exposed to supercritical water at both 500°C and 600°C for a range of durations (10 – 100 h).

The published oxide thickness data is summarised in Table 9. The point defect model was optimised on each set of published data, except for the 120°C and 160°C values where no growth was measured. Similar methods to those described in section 8.7.4 were used to optimise the curves and represent associated uncertainty in the plots. Figure 72 contains both the published data together with the data from this investigation for comparison. In addition the optimised PDM curves for each published data set are plotted. The corresponding optimised parameters for these curves are given in Table 9.

Table 9. Summary of the published literature of measured Cr-rich oxide thickness after exposures to high temperature water, at various temperatures. After optimising the PDM for each data set, with a maximum and minimum possible transfer coefficient, α_3 , respectively, the corresponding rate constant (k_3^o) and transfer coefficient (α_3) values are given.

Publication	Temperature		Exp. Time (h)	Oxide thickness (nm)	Point Defect Model Optimisation					
					k_3^o (mol.cm^{-2})			α_3		
	°C	K			Mean	Min α_3	Max α_3	Mean	Min α_3	Max α_3
Castle et al.[103]	120°C	393	1	1						
			1	1						
			3	2						
			3	3						
	160°C	433	1	2						
			1	3						
			3	2						
			3	2						
	200°C	473	1	4	5.75E-11	8E-11	3.5E-11	0.0900	0.03	0.15
			1	5						
			3	15						
			3	8						
Ziemniak et al.[90]	260°C	533	1000	1330	1.76E-10	8E-11	2.72E-10	0.0075	0.005	0.01
			2000	1533						
			5000	2457						
			5000	971						
			8000	1758						
			10000	2548						
Tapping et al.[105]	300°C	573	48	77	6.91E-11	6.56E-11	7.26E-11	0.0651	0.04	0.0902
			96	83						
			120	65						
			144	98						
			168	106						
Penttilä et al.[85]	500°C	773	97	200	9.50E-11	8.2E-11	1.08E-10	0.0055	0.0025	0.0085
			167	500						
			333	500						
			333	900						
			389	1200						
			667	1100						
			972	1000						
			1167	1800						
	600°C	873	97	97	2.14E-09	1.38E-09	2.90E-09	0.0004	0.0001	0.0006
			333	333						
			333	333						
			639	639						
			972	972						

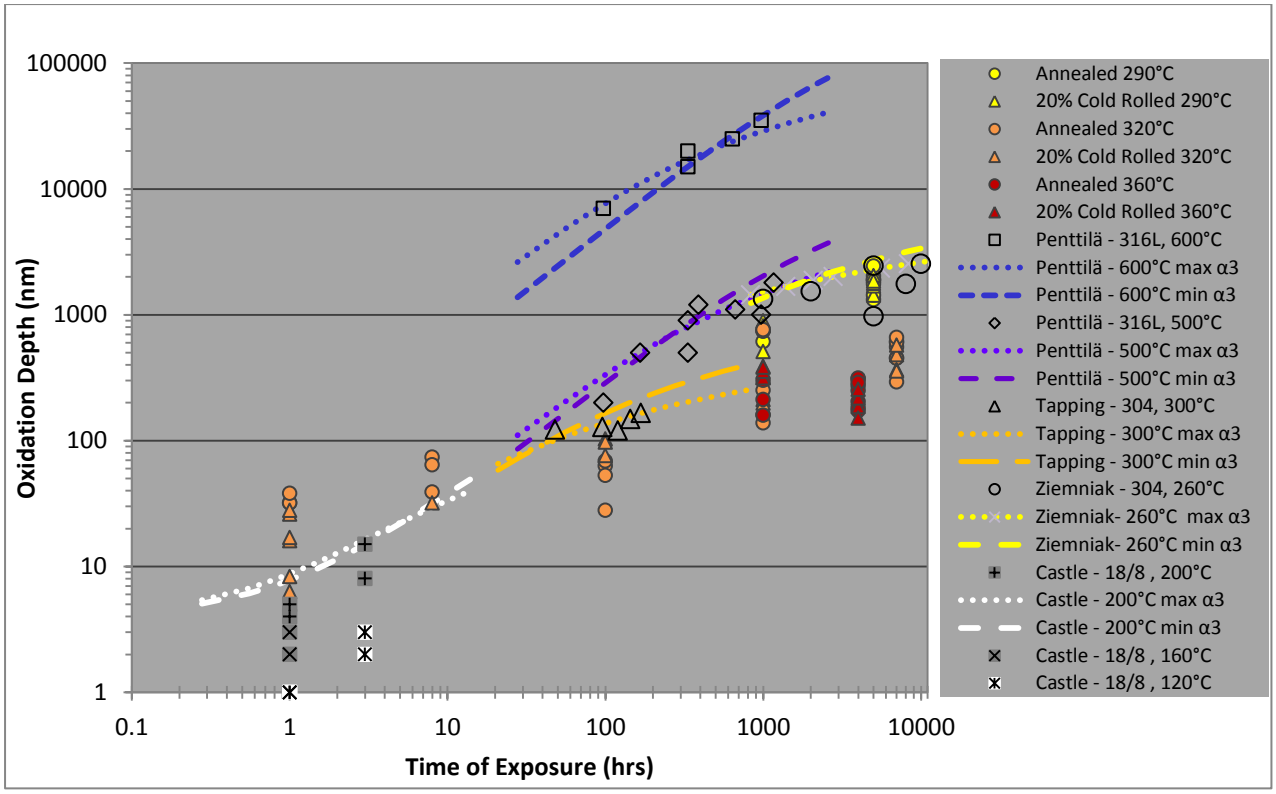

Figure 72. Total data set of measured 316L surface oxide depth vs time together with published data of other austenitic stainless steels in similar environments. Both axes are plotted with log scales. Two PDM curves were fitted to each set of published data, with the curves optimised with a maximum and minimum possible transfer coefficient, α_3 , values respectively.

8.7.6. Transfer Coefficient as a Function of Temperature

In the preceding sections the point defect model has been optimised to fit the oxidation growth data acquired in this investigation as well as those in published literature. It has been shown that the PDM is very sensitive to the transfer coefficient associated with the metal/barrier layer interfacial reactions, which contain the rate limiting step for oxide kinetics. It is clear that treating this parameter as a constant is not sufficient to adequately model the growth of the oxide layer at varying temperatures. In particular the PDM is not equipped in its current form to model the inverse in oxidation kinetics demonstrated by 316L material as temperature increases through the range of 290°C-360°C.

It is therefore necessary to modify the PDM to accommodate the behaviour of 316L, and possibly other austenitic stainless steels by modifying the transfer function, α_3, to be a function of temperature. In Figure 74, the mean values for α_3 are plotted, together with an uncertainty represented by error bars, against temperature after optimising the PDM to the acquired data (from Table 8), as well as the literature data (from Table 9).

The inverse in the decreasing trend of α_3 as temperature increases is evident after 500k. This observation is supported, not only by the data from this investigation, but by other published data in the same temperature range. The original trend is expected to resume after another inverse at approximately 675k, as supported from higher temperature values published.

An empirical function was sought to describe the α_3 behaviour with temperature. Since the PDM could not accept a zero or negative value for α_3 the zero value would need to act as an asymptote. An exponential function with a negative exponent could be used to describe the general decreasing α_3 trend as temperature increases. Then in order to accommodate the inverse in temperature between approximately 500 – 700 K, a polynomial was used in the exponent, see Equation 14, which for the purposes of the explanation has a fifth degree polynomial with respect to temperature.

Equation 14 $$\alpha_3 = e^{mT^5+nT^4+oT^3+pT^2+qT+r}$$

Now in order to determine the fit for the polynomial in the exponent position, the natural log, ln, was taken of both sides of Equation 14:

Equation 15 $$ln\alpha_3 = mT^5 + nT^4 + oT^3 + pT^2 + qT + r$$

In this way, by plotting $\ln(\alpha_3)$, an optimised polynomial could be fitted to the data. For simplicity the least degree polynomial that could model the data would be preferable. Several polynomial degree orders were tested. In Figure 73 $\ln(\alpha_3)$ is plotted with the optimised transfer coefficients from both measured and published data. Included in this plot are polynomials of different degrees with the data for comparison. Note that while an automatic best fit polynomial could be determined in Microsoft Excel, the coefficients were manually optimised to favour the measured data. Since there are some reservations regarding how comparable the literature data is in this plot, as previously detailed, the measured data from this investigation was given preference when optimising the polynomial's fit.

The third degree polynomial could be optimised reasonably to predict the measured data. However, as a result the function deviated significantly from the data on both extremes of the published data range. The optimised fourth degree polynomial was able to better approximate the full set of data, but the curve deviated from the expected behaviour particularly at the higher end of the published temperature range with a minimum occurring between the 773k and 883k data points. For these reasons a fifth degree polynomial was optimised on the data set with better approximation to the data set within the temperature

data range. The coefficients for the various degree of polynomials used are given in Table 10 with the coefficient labels consistent with Equation 14 above. It must be stressed that this is an empirical data curve and its use is limited to within the temperature range of 460 k – 900 k (183°C - 627°C). Nevertheless, this range covers all typical applications involving high temperature water. Note that Castel and Clayton observed a significant increase in oxidation growth of austenitic stainless steels only once the temperature of the solution exceeded 160°C [103].

The coefficients from the 5th degree polynomial were used then to plot the transfer coefficient in Figure 74, which is plotted on a logarithmic scale.

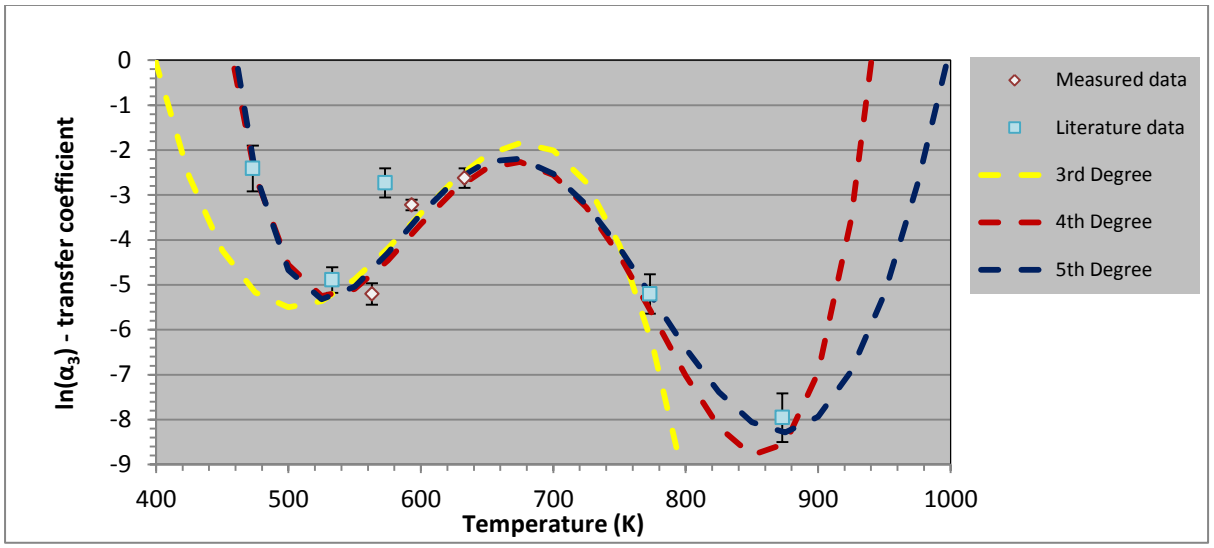

Figure 73. Plot of ln(α_3) data points with respect to temperature, determined by optimising the PDM around the measured oxide data (red) and from literature data (blue). The error bars in the data points represent the range of possible fitted values. Three fitted polynomials of 3rd, 4th and 5th degrees are plotted illustrating how the 5th degree polynomial provides a better approximation across the temperature range of 460 k – 900 k (183°C - 627°C).

Table 10. Coefficient values for the optimised polynomials fitted in Figure 73 above.

Polynomial	m	n	o	p	q	r
3rd degree	0	0	-1.368×10^{-6}	2.428×10^{-3}	-1.405	261
4th degree	0	6.5800×10^{-9}	-1.8062×10^{-5}	1.8242×10^{-2}	-8.0359	1.2994×10^{3}
5th degree	-9.3988×10^{-12}	3.7709×10^{-8}	-5.8835×10^{-5}	4.4640×10^{-2}	-16.483	2.3681×10^{3}

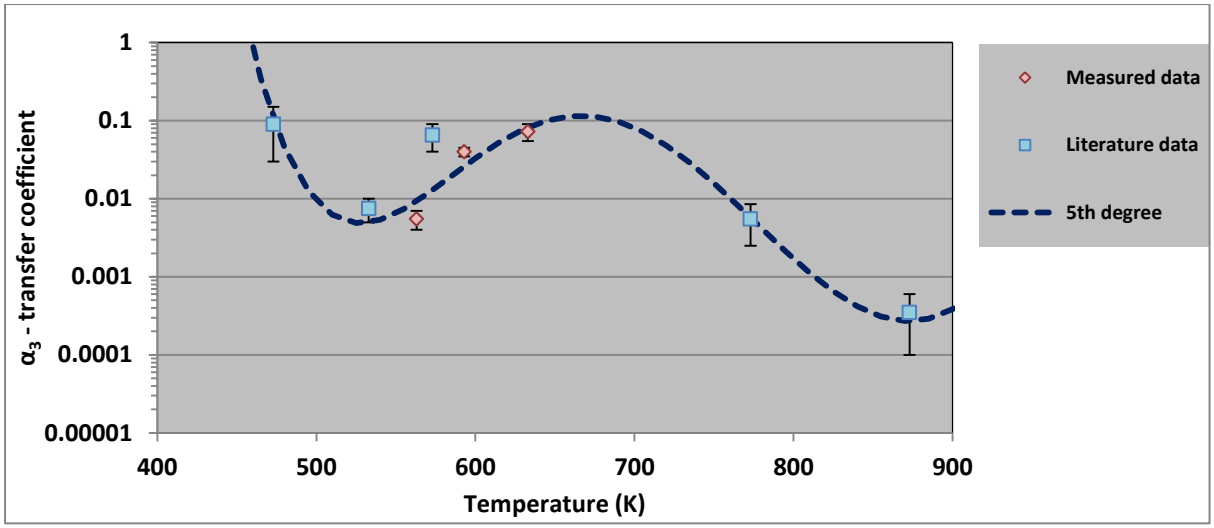

Figure 74. Plot of mean transfer coefficient α_3 values against temperature, with error bars representing the associated maximum and minimum values, on a logarithmic scale. These values were measured after optimising the PDM on acquired (red points) and published (blue points) oxide kinetics, from Table 8 and Table 9. A 5th degree polynomial exponential function has been optimised from Figure 73 to fit the data.

Finally, the transfer coefficient, α_3, of the PDM can be expressed as a function of temperature in kelvin, as plotted in Figure 74, for 316L stainless steels as:

Equation 16

$$\alpha_3 = e^{(-9.3988E^{-12})x^5+(3.7709E^{-8})x^4+(-5.8835E^{-5})x^3+(4.4640E^{-3})x^2+(-16.483)x+2.3681E^3}$$

Note that the transfer coefficient increases rapidly as the temperature decreases below 450k (177°C), indicative of decreased oxide growth kinetics. This is consistent with the work of Castle and Clayton who measured marginal increase in oxide growth as temperature increased to 433k, but as temperature exceeded 473k the growth significantly increased [104].

8.7.7. Rate Constant as a Function of Temperature

The Arrhenius equation has been widely adopted to describe the kinetics of electrochemical reactions that are thermally activated. Once the temperature of the environment is sufficient to overcome the activation energy, the reaction will spontaneously proceed, and at an increasing rate as the thermal energy of the environment increases.

As previously mentioned the PDM as presented by MacDonald does not adequately cater for the increase in passive film thickness in high temperature water [84]. This may be since

MacDonald developed the model from experiments conducted largely at room temperature. Betova et al., as well as Bojinov however, when applying the model in high temperature water found it necessary to accommodate the behaviour of passive films with Arrhenius temperature dependent rate constants [62]. The latter publication sought to develop the mixed conduction model, which takes its basis from the point defect model, and find parameters to predict the growth and composition of passive films formed on austenitic stainless steels when exposed to high temperature water.

The following is the basic form of the Arrhenius equation:

Equation 17 $$k = A.e^{\frac{-E_a}{RT}}$$

This equation describes the rate constant k of the reaction with a dimensionless coefficient A, an activation energy E_a ($J.mol^{-1}$), universal gas constant R (8.314 $J.mol^{-1}.k^{-1}$), and temperature in kelvin. This equation can be rearranged by taking the natural logarithm of both sides to yield:

Equation 18 $$\ln(k) = \ln(A) - \left(\frac{E_a}{R}\right).\left(\frac{1}{T}\right)$$

In this way a linear plot of ln(k) verses T^{-1} can be produced, from which the slope, represented by $-(E_a/R)$, and the coefficient A could be determined.

Therefore in Figure 75 the values of $\ln(k_3°)$, from Table 8 containing the PDM fitted data, and similarly from Table 9 with published data, was plotted to the reciprocal of temperature (k^{-1}). The measured surface oxidation values were included together with the literature data when determining the best linear fit, labelled “surface ox. data” in Figure 75, which is represented by the following equation:

Equation 19 $$\ln(k_3^o) = -17.44 - 3123.\left(\frac{1}{T}\right)$$

Rearranging this equation into the standard Arrhenius format of Equation 17, the rate constant for reaction 3 at the metal/barrier layer interface is given by:

Equation 20 $$k_3^o = (2.667E^{-8}).e^{\frac{25964}{RT}}$$

The values for the measured intergranular oxidation values were also included with $\ln(k_3°)$ values corresponding to surface oxidation at similar temperatures in Figure 75. A separate linear Arrhenius plot was required for the intergranular oxidation; however, with only three values for this linear curve the data points were too few to find the best fit plot. Instead the average difference between the measured surface and intergranular values was added to

the coefficient A, whilst maintaining the same E_a value, to determine the intergranular oxidation plot. These values are given in Table 11. Therefore the intergranular oxidation Arrhenius plot had the same slope as that of the surface oxidation but with a greater constant. The reaction 3 rate constant for intergranular oxidation is therefore given by:

Equation 21 $$k_3^o = (5.5378E^{-8}).e^{\frac{25964}{RT}}$$

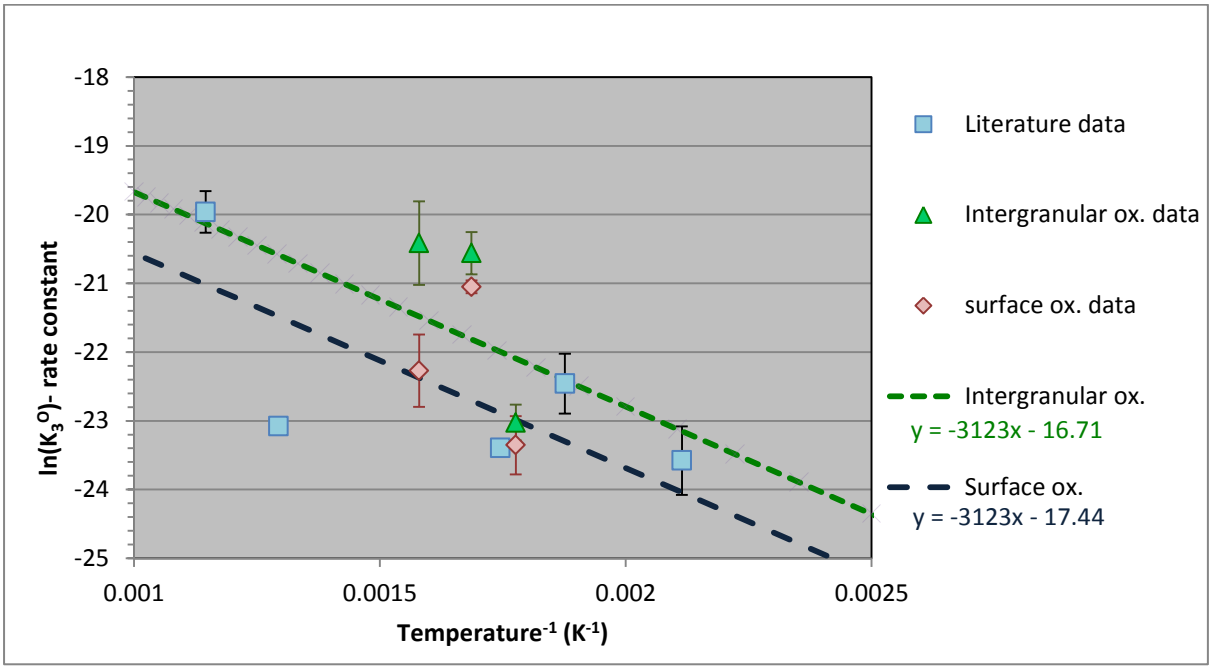

Figure 75. The Arrhenius curves plots are determined for rate constant, $k_3°$, for both surface and intergranular oxidation. Data of the natural logarithm of rate constants, $\ln(k_3°)$, determined by optimising the PDM to oxide growth data, is plotted against the reciprocal of temperature, (k^{-1}). The rate constants, with error bars representing the associated uncertainity, from published data are represented together with those determined from measured data, both of surface oxidation as well as intergranular oxidation.

Table 11. Rate constant values, k_3^0, and the natural logarithms thereof, $\ln(k_3^0)$ for the surface and intergranular oxidation respectively. The average difference between the values is determined, which is used to define the intergranular oxidation Arrhenius plot. Finally the Arrhenius coefficients and activation energies for surface and intergranular oxidation respectively are given.

Temperature		Surface oxidation	Intergranular oxidation	Δ $\ln(k_3°)$	Ave Δ $\ln(k_3°)$
290°C	k_3^0	1.17 E-10	7.90 E-10		
	$\ln(k_3^0)$	-22.87	-23.26	0.39	0.73
320°C	k_3^0	1.07 E-9	6.01 E-10		
	$\ln(k_3^0)$	-20.66	-21.23	0.57	
360°C	k_3^0	7.50 E-10	2.20 E-10		
	$\ln(k_3^0)$	-21.01	-22.24	1.23	
Coefficient A		2.667 E-8	5.538 E-8		
Activation energy, E_a (J.mol^{-1})		25964	25964		

8.7.8. Modified Point Defect Model for Austenitic Stainless Steels

Having established functions of temperature for both the transfer coefficient as well as the rate constant at the metal/barrier layer interface, the modified PDM can be presented for 316L stainless steels. Since the literature data that includes other austenitic stainless steels is consistent with results from this investigation, it is likely that this modified PDM can reasonably be extended to other austenitic stainless steels exposed to similar primary water environments.

In summary, prior to this investigation, MacDonald et al. have established that oxide depth can be expressed as a function of time, with growth kinetics limited by the ion transfer reaction at the metal/film interface (reaction 3 of Figure 66), according to [82,84]:

Equation 12 $$L(t) = L_0 + \left(\frac{1}{b_3}\right)\ln[1 + a' b_3 e^{-b_3 L_o} t]$$

With L_0 as the starting thickness of the oxide, $b_3 = \alpha_3 \chi \epsilon \gamma$, $a' = k_3^0 e^{\alpha_3 (V+\Delta V)} e^{-\alpha_3 \beta \gamma p H}$, $a_3 = \alpha_3(1-\alpha)\gamma$, and $\gamma = \frac{F}{RT}$, with further explanations of symbols given in the preceding sections.

Since this expression cannot adequately accommodate the variation in growth with temperature, functions for both the transfer coefficient and the rate constant with respect to temperature were determined as a modification to the PDM. From data acquired from oxide growth measurements for 316L exposed to simulated primary water, the transfer coefficient at the metal/film interface can be expressed as the following function of temperature in kelvin as:

Equation 14 $$\alpha_3 = e^{mT^5 + nT^4 + oT^3 + pT^2 + qT + r}$$

In addition the Arrhenius curve for the rate constant at the metal/film interface can be given as:

Equation 17 $$k_3^0 = A.e^{\frac{-E_a}{RT}}$$

The complete set of parameter values for these equations is given in Table 12.

Table 12. Parameter symbols and values for the modified point defect model for austenitic stainless steels.

Parameter		Symbol	Unit	Value
Faradays Constant		F	$C.mol^{-1}$	96,485
Universal gas constant		R	$J.mol^{-1}.K^{-1}$	8.3144
Temperature		T	K	563, 593, 633
Cation oxidation state		χ	-	2.7
Electric field strength		ϵ	$v.cm^{-1}$	35,000
Polarizability of the interface		α	-	0.5
Starting oxide thickness (measured)		L_o	cm	4×10^{-7}
Transfer Coefficient, α_3, coefficients		m	K^{-5}	-9.3988×10^{-12}
		n	K^{-4}	3.7709×10^{-8}
		o	K^{-3}	-5.8835×10^{-5}
		p	K^{-2}	4.4640×10^{-2}
		q	K^{-1}	-16.483
		r	-	2.3681×10^{3}
Rate constant, k_3^0	Intergranular ox. coefficient	A_i	-	2.667×10^{-8}
	Surface ox. Coefficient	A_s	-	5.538×10^{-8}
	Activation energy	E_a	$J.mol^{-1}$	25964

The modified PDM is graphically represented in Figure 76, where the predictions for the model can be compared to the measured and published surface oxide growth values. It is evident that for early time durations the oxide growth is dominated by the thermally activated rate constant at the metal/film interface, k_3^0. However, the depth to which the oxide is able to grow is determined by the transfer coefficient, α_3, at the same interface. The latter parameter therefore is dominant for the longer exposure times and accounts for the inverse in growth kinetics between 290°C-360°C.

The model shows reasonable correlation with the various data sets, in particular with the measured data for which greater emphasis was placed. The modified model is shown to deviate somewhat from published data at other temperatures since, as has been established before, the conditions for growth, as well as the methods for acquiring the data differ from the measured data in this investigation. In order to validate the model across a wider temperature range, measured data acquired from comparative conditions would be required. Nevertheless, the methodology has been established in this investigation and if further comparable data were to be acquired from temperatures outside of the 290°C-360°C range, then it is possible that the modified model can be further refined to improve the predictive capability for oxide growth kinetics across a broader range of temperatures.

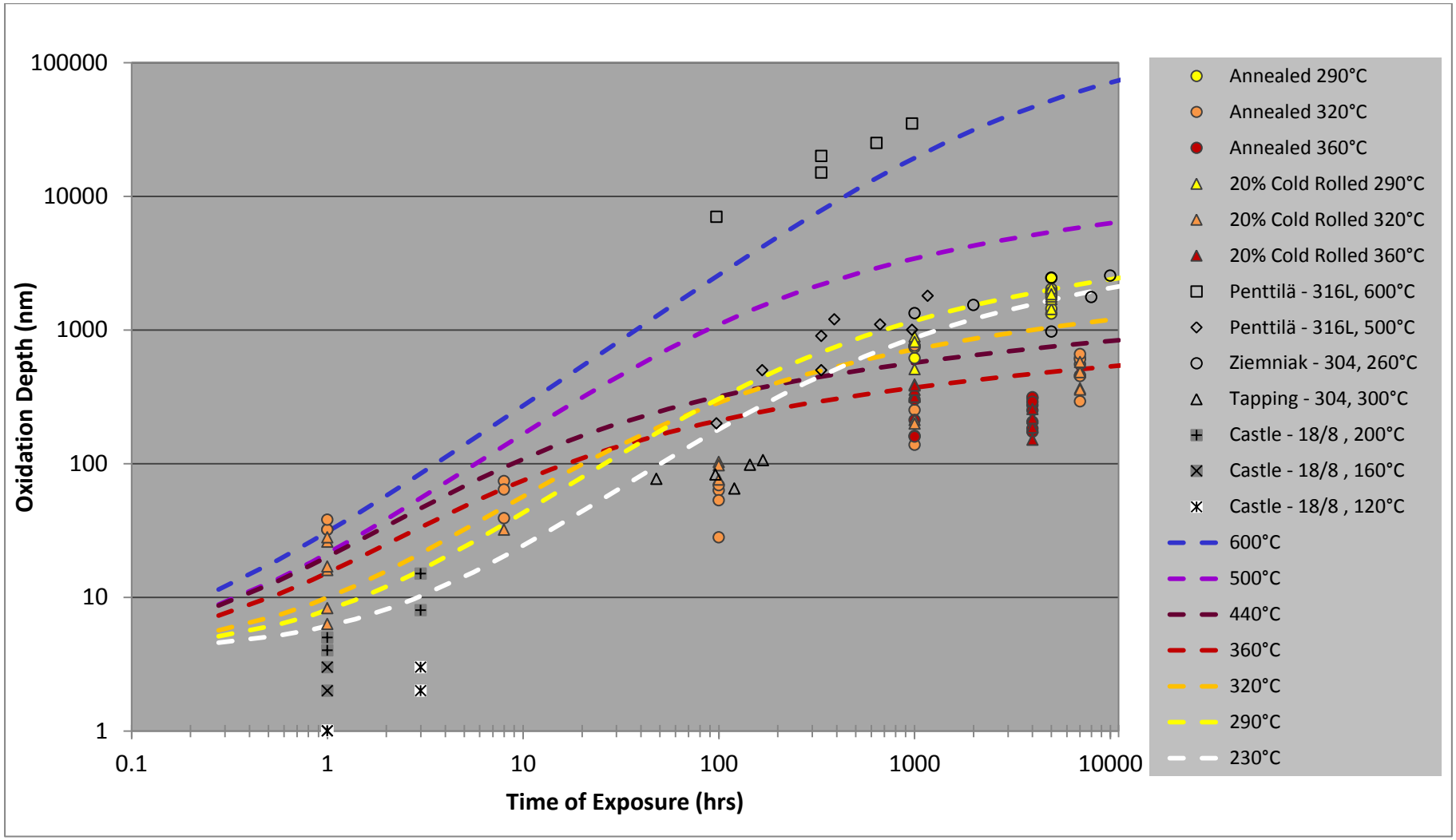

Figure 76. Oxidation thickness plotted against time of exposure with logarithmic axes. The modified point defect model for the surface oxidation of austenitic stainless steels is plotted for various temperatures to illustrate how the modified PDM accommodates the observed inverse in long term oxide thickness between 290°C and 360°C. The measured data as well as published data is plotted for comparison to the model.

8.7.9. Significance of the Transfer Coefficient in the PDM

The point defect model has been modified to predict the oxide growth kinetics of 316L stainless steel by expressing the transfer coefficient, α_3, for the metal/film interface as a function of temperature. It is through this parameter that the inversion of the growth kinetics with temperature is accommodated. In this section the influence of α_3 on the change in potential at the metal/film interface is established and its resulting effect on the steady state oxide thickness is demonstrated.

Firstly, the manner in which the potential change across the metal/film interface, $\phi_{m/f}$, has been presented has differed between PDM related publications. This change in earlier publications has been presented as a potential gain from the metal to the film [100], Figure 77.a, while others have presented this change as a potential drop [76,78,81], Figure 77.b. It is likely that the authors were highlighting the fact that there are potential drops at the interfaces that should be considered when modelling with the PDM, rather than illustrating absolute values. Whether the potential drops across the interfaces are positive or negative may depend on the conditions of the system.

a) b)

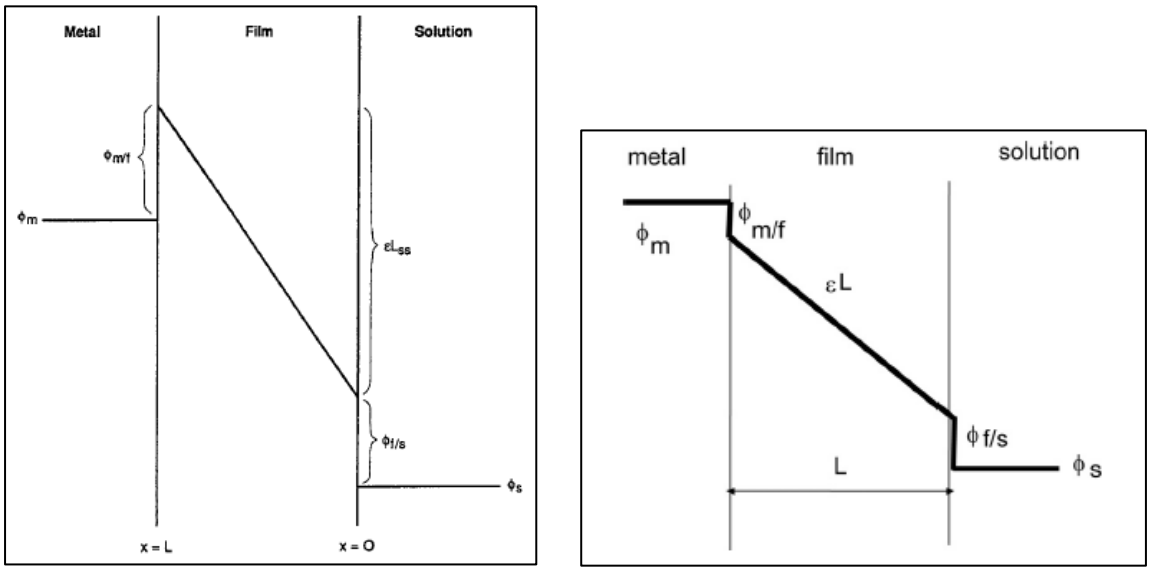

Figure 77. Examples of published schematics depicting the potential distribution across the barrier layer from metal to solution according to the PDM with a) showing a potential gain across the metal to film interface [100] , while the corresponding interface in b) is presented as a potential drop.

To the author's knowledge there was no explicit expression published for this change in potential across the interface, $\phi_{m/f}$, that is written with respect to the transfer coefficient, α_3. Nevertheless, by rearranging other published equations on the PDM such an expression could be determined.

An expression for the steady state barrier film thickness has been derived, provided the oxidation state of the cations from film to solution do not change, which is the case for stainless steels, and is given as:

Equation 22 [76,84] $$L_{ss} = \frac{1}{\varepsilon}[1 - \alpha]V + \frac{1}{\varepsilon}\left\{\frac{2.303n}{\alpha_3\chi\gamma} - \beta\right\}pH + \frac{1}{\alpha_3\chi\varepsilon\gamma}\ln\left(\frac{k_3^0}{k_7^0}\right)$$

In other, fairly recent publications, the change in potential at the metal/film interface can be derived from the expression for the potential drop at the film/solution interface expressed as:

Equation 23 [84,106] $$\phi_{f/s} = \alpha V + \beta pH + \phi_{f/s}^0$$

Where α is the polarizability of the film/solution interface, β is the dependence of the potential drop on the pH, and $\phi_{f/s}^0$ is the potential drop across the interface at 0 V applied potential and 0 pH. Since the potential drop from metal to solution, V, is the sum of the change in potential across the metal/film interface, $\phi_{m/f}$, the linear potential drop across the film, εL, and the drop at the film/solution interface, $\phi_{f/s}$, the following expression is derived:

Equation 24 [84,106] $$\phi_{m/f} = (1-\alpha)V - \beta pH - \phi_{f/s}^0 - \varepsilon L$$

The above equation can be rearranged as an expression for oxide thickness L as:

Equation 25 $$L = \frac{1}{\varepsilon}\left((1-\alpha)V - \phi_{m/f} - \beta pH - \phi_{f/s}^0\right)$$

Therefore, considering steady state conditions, the value for $\phi_{m/f}$ can be expressed by substituting Equation 25 for L_{ss} into Equation 22 and simplifying:

$$\frac{1}{\varepsilon}\left((1-\alpha)V - \phi_{\frac{m}{f}} - \beta pH - \phi_{\frac{f}{s}}^0\right) = \frac{1}{\varepsilon}[1 - \alpha]V + \frac{1}{\varepsilon}\left\{\frac{2.303n}{\alpha_3\chi\gamma} - \beta\right\}pH + \frac{1}{\alpha_3\chi\varepsilon\gamma}\ln\left(\frac{k_3^0}{k_7^0}\right)$$

$$-\phi_{\frac{m}{f}} - \beta pH - \phi_{\frac{f}{s}}^0 = \left\{\frac{2.303n}{\alpha_3\chi\gamma} - \beta\right\}pH + \frac{1}{\alpha_3\chi\gamma}\ln\left(\frac{k_3^0}{k_7^0}\right)$$

$$-\phi_{\frac{m}{f}} = \frac{1}{\alpha_3\chi\gamma}\left[2.303n.pH + \ln\left(\frac{k_3^0}{k_7^0}\right)\right] - \beta pH + \beta pH + \phi_{\frac{f}{s}}^0$$

Equation 26 $$\phi_{m/f} = -\frac{1}{\alpha_3\chi\gamma}\left[2.303n.pH + \ln\left(\frac{k_3^0}{k_7^0}\right)\right] - \phi_{f/s}^0$$

Where α_3 is the transfer coefficient at the metal/film interface, χ is the oxidation state of the cation, $\gamma = \frac{F}{RT}$, and n is the kinetic order of the barrier layer dissolution reaction with respect

to H^+. Therefore, provided the environmental conditions remain constant, it is shown that $\phi_{m/f}$ is i) inversely proportional to α_3, and ii) that it has a negative value if $\phi^0_{f/s}$ is positive.

Equation 27

Note that the modified transfer coefficient for 316L stainless steel established in the previous section is inversely related in value to the associated steady state oxide thickness, L_{ss}. Therefore considering the relation in Equation 26 L_{ss} would increase as $\phi_{m/f}$ increases, which is consistent with presenting the change in potential across the metal/film interface as a gain i.e. such as that depicted in Figure 77.a.

Therefore if the potential drop at the film/solution interface, $\phi_{f/s}$, remains constant, and the potential drop across the film is linear (εL) under a constant electric field, then the oxide film will grow until the steady state thickness is achieved which will be dependent on the potential gain at the metal/film interface, $\phi_{m/f}$. The schematic in Figure 78 illustrates the effect that increasing $\phi_{m/f}$ has on the maximum steady state thickness to which the oxide film can grow, and how by increasing the potential gain the maximum thickness, L_{ss}, increases.

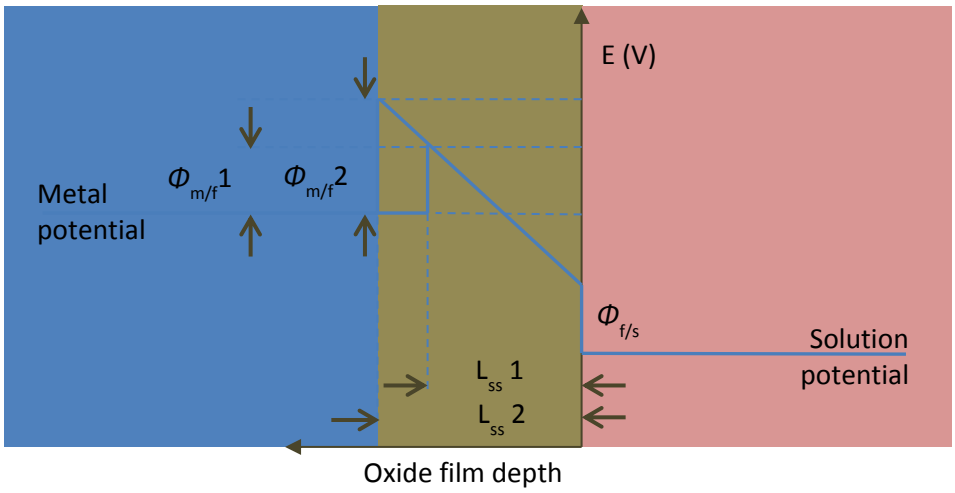

Figure 78. Schematic illustrating how increasing the gain in potential across the metal/film interface from $\phi_{m/f}\,1$ to $\phi_{m/f}\,2$, will increase the maximum steady state oxide film depth from $L_{ss}\,1$ to $L_{ss}\,2$.

9. DISCUSSION

The inverse in the metal/film transfer coefficient, $\phi_{m/f}$, as temperature increases, with the associated peak in oxide growth kinetics in the region of 290°C, is likely due to a degradation of coherency across the same interface. The argument to substantiate this statement is developed below.

9.1. Kinetics Determined within Interfacial Reactions

There have been several review articles published that compare the established models for oxide growth for metals, such as those by Olsson [79], Seyeux [78], and MacDonald [81]. Without repeating the analyses of these authors, the three essential processes necessary for oxide growth common to all metals are:

i) The reactions at the metal/barrier film interface across which oxygen anions and metal cations are exchanged. Via these reactions the interface boundary is able to migrate into the metal, whilst providing a source for anion vacancy generation;

ii) The diffusion/migration of anion and cation vacancies through the barrier film under the influence of an electrostatic field;

iii) The reactions at the barrier film/electrolyte interface resulting in the dissolution of anions and the generation of anion vacancies.

However, one aspect where the models differ is in considering which of the above processes (i-iii) represents the rate limiting step. Macdonald's point defect model (PDM) [81,82] and Cabrera-Mott (with relatively thin films) [77], locate this limiting step at the metal/film interface, whereas the high field models (HFM) of Verwey [107] and Cabrera-Mott (with relatively thick films) [77] predict this step to be in the diffusion across the film. Lastly the Vetter and Gorn model [108] suggest the rate is determined by the reactions at the film/solution interface.

In Section 8.2 the oxide growth sensitivity to the orientation of the metal grain was highlighted. The annealed sample exposed at 320°C in Figure 49 provides an excellent example of how the Cr-rich inner oxide thickness can vary by more than an order of magnitude between neighbouring grains and is therefore strongly dependent on the metal

orientation. A favourable metal grain orientation for oxide growth proved, in this sample, to outweigh the advantage that grain boundaries offer with respect to greater diffusion rates. This provides evidence that the rate determining step for oxide growth in this sample is not the rate of ion migration-diffusion through the oxide but rather the reaction rates at the metal/film interface, which are influenced by grain orientation. The orientation of the underlying metal will not have significant influence over reactions beyond the metal/film interface, and therefore the variation in oxide thickness observed across grains cannot be accounted for by reactions at the film/solution interface, nor by diffusion/migration rates of ion vacancies through the oxide.

Therefore oxide growth kinetics observed in this investigation is determined by the lattice non-conserving reactions at the metal/oxide interface, which result in film formation and is consistent with interface models such as the PDM or Cabrera-Mott. Although the latter model considers the interface reactions to be rate determining for thin films (<10 nm), this would not be consistent with observations in this investigation [77].

Since growth kinetics was observed with metal orientation dependence in samples representing all temperatures in the range, see sections 8.2 and 8.3, the above conclusion would be valid across 290°C-360°C range and likely to extend across the full range modelled.

The only lattice non-conserving reaction at this interface is reaction 3 in Figure 66, the kinetics of which are dependent on the rate constant, k_3^0, and the transfer coefficient, α_3, established in section 8.7. However, it has been demonstrated that the influence of the rate constant on the growth kinetics was limited to the short term rate of growth, while the transfer coefficient had a more significant role in determining the maximum steady state thickness to which the oxide could grow.

9.2. Transfer Coefficient Dependence on Coherency

The transfer coefficient, α_3, is inversely proportional to the potential gain across the metal/film interface, $\phi_{m/f}$. In physical terms it is considered to be a parameter describing the inverse probability for transfer of ions to occur across the metal/film interface. In other words, a low value of $\phi_{m/f}$ represents an interface where ion transfer across the metal/film interface is more likely. In particular an interface where the film forming reaction occurs with relative ease, which requires both i) the oxidation of a metal atom and for it to occupy either

a substitutional vacancy or an interstitial position in the film, and ii) an oxygen ion to occupy the metal vacancy position. While there is an electric field across the film driving this reaction the charged atoms are required to jump into their respective vacancy positions.

From the curve of the transfer coefficient plotted against temperature in Figure 74 it is evident that there is a general trend toward reduced values as temperature increases which would suggest that the transfer of ions across the interface is thermally assisted. As temperature of the system increases, the greater the probability that an atom at the interface (either a metal atom or an oxygen anion) will have sufficient energy to overcome bond energies and jump into a vacancy position across the interface. While this may be intuitively true, the plot in Figure 74 is more complex and cannot be described with a simple Arrhenius based relation.

One explanation considered for this observed inversion with temperature was that it represents the transition of stability between two different oxide structures. This was the explanation offered by Robertson in his review paper that includes the work of Warzee and Maekawa where a peak in corrosion rate of austenitic stainless steels with temperature was observed [109]. Some authors have differed in their characterization of the Cr-rich spinel from the $FeCr_2O_4$ type oxide observed by many. However, these opposing observations were made either after exposures at the lower temperature of 250°C, where Cheng observed Cr_2O_3, $Cr(OH)_3$ and CrO_3 present [67], or at higher potentials such as Lu, who reported Cr-rich oxides present as Cr_2O_3 after exposures at 288°C with a greater dissolved oxygen content of 2 ppm [14]. Notwithstanding this, if the decrease in oxide growth with increased temperature could be accounted for by a transition between stable oxide structures, it is not clear how this can be reconciled with the observations in the present study where there is a strong oxide depth dependence on metal orientation. In addition, this explanation cannot account for how the orientation dependence (preferred metal orientation for oxide growth) changes with temperature.

There was no observed distinction in the nature of the Cr-rich spinel oxide between those developed at the temperatures of 290°C, 320°C or 360°C in this investigation to support the theory. Therefore a transition between different oxide structures was eliminated as a possible cause for the observed temperature inversion.

Instead the transfer coefficient is likely dependent on the coherency across the metal/film interface, since coherency would influence the jump distance required for transfer of ions across the interface. If there is good coherency there would be a regular arrangement of low energy spacing between atoms of the respective lattice across the interface. For a given density of point vacancies within the oxide structure, a coherent interface would present a

relatively high number of transfer opportunities. In contrast an incoherent interface would result in an irregular spacing of atoms across the interface. The atomic spacing distance across the interface can be considered as a statistical distribution, with only a portion being within the probable jump distance of thermally activated atoms at the interface. Figure 79 uses simplistic oxide and metal lattices to illustrate how a coherent interface may present greater ion transfer opportunities, with lower associated transfer coefficient, $\alpha_{3,}$ than an incoherent interface with a greater associated α_3.

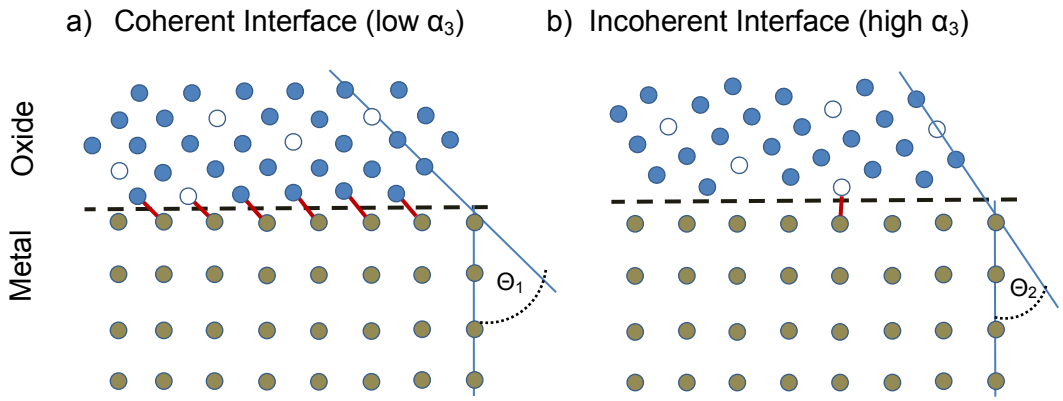

Figure 79. Schematic illustrating, with simplistic lattices of the oxide and metal respectively, the increased probability for ion transfer to occur across a coherent metal/film interface. Coherency increases the number of atomic bonds per unit area across the interface that is within the jump distance for thermally activated ions.

The relation between interface coherency and transfer coefficient is illustrated with the extremes of perfectly coherent and incoherent interfaces, whereas in reality there will always be lattice mismatch between the respective lattices and therefore the degree of coherency may vary while perfect coherency cannot be achieved.

Since the coherency at the metal/film interface would be dependent on the orientation of the metal with respect to this interface, the observed kinetic dependence on grain orientation (section 8.2) would be consistent with the transfer coefficient being dependent on interface coherency. It is also important to note that there were observed examples where oxide depth varied by more than an order of magnitude between neighbouring grains, suggesting that the dominant influence over the transfer coefficient is the interface coherency rather than temperature.

9.3. Degradation of Coherency with Temperature

Considering that the oxide growth is dependent on the degree of coherency across the metal/oxide film interface, it is proposed that the measured inversion of growth kinetics with temperature is caused by a degradation in interface coherency. The observations that substantiate this proposal are discussed below.

As detailed in sections 8.2 and 8.3, the orientation most favourable for inner oxide growth at 320°C proved to be where <100> was oriented normal to sample surface, while orientations with <111> normal to the sample surface were evidently the least favourable for growth kinetics. In contrast, for samples exposed at 290°C the situation is reversed where grains of the former orientation with respect to the sample surface proved to be unfavourable for oxide growth kinetics. The latter orientation was more favourable for growth in the 290°C test than the former but the oxide depths for most orientations in the 1000 hr samples were too deep to establish, using back-scattered electrons, whether there was an optimum orientation for oxide growth kinetics. Indeed, the general oxide depth in the samples exposed for 5000hr at 290°C was also too deep for any growth dependence on grain orientation to be observed with BSE. At 360°C the orientation dependence appears similar to the 290°C samples with grains with <100> oriented normal to sample surface being unfavourable for oxide growth kinetics. Therefore not only is the oxide growth dependent on the underlying grain orientation, but this orientation dependence is sensitive to temperature.

It is important to note that within the range of 290°C - 360°C, where an inverse in kinetics was measured, a change in preferred metal orientation for growth was also observed. Since the kinetics are dependent on temperature and coherency across the metal/film interface, it suggests that as temperature increases through this range the coherency between the spinel oxide structure and the face centred cubic (FCC) metal structure generally degrades.

While coherency may degrade in general terms, specific orientations may differ in their temperature dependence. The orientation with <100> oriented normal to sample surface is more favourable for oxide kinetics at 320°C than at 290°C. This was measured for example when comparing the maximum Cr-rich oxide depth from the surface of grain 2 of Figure 49 exposed at 320°C (761 nm max.), which is greater than that in grain 2 of Figure 55 at 290°C (384 nm max.). Since the coherency is temperature dependent it may be possible to find a characteristic transfer coefficient, α_3, as function of temperature for each metal orientation. Figure 80 is plotted to illustrate how different metal orientations are suspected to shift the average α_3 function along the temperature axis in a positive or negative direction. For

example, since the orientation with <100> normal to the surface proved to be more favourable for growth kinetics at 320°C than other orientations, and less favourable at 290°C, it could result in a shift of the α_3 curve along the temperature axis in the positive direction. While it is known that grains orientated with <111> normal to the surface were the least favourable for oxide kinetics at 320°C. This trend could however not be confirmed without sufficient data for the respective orientations.

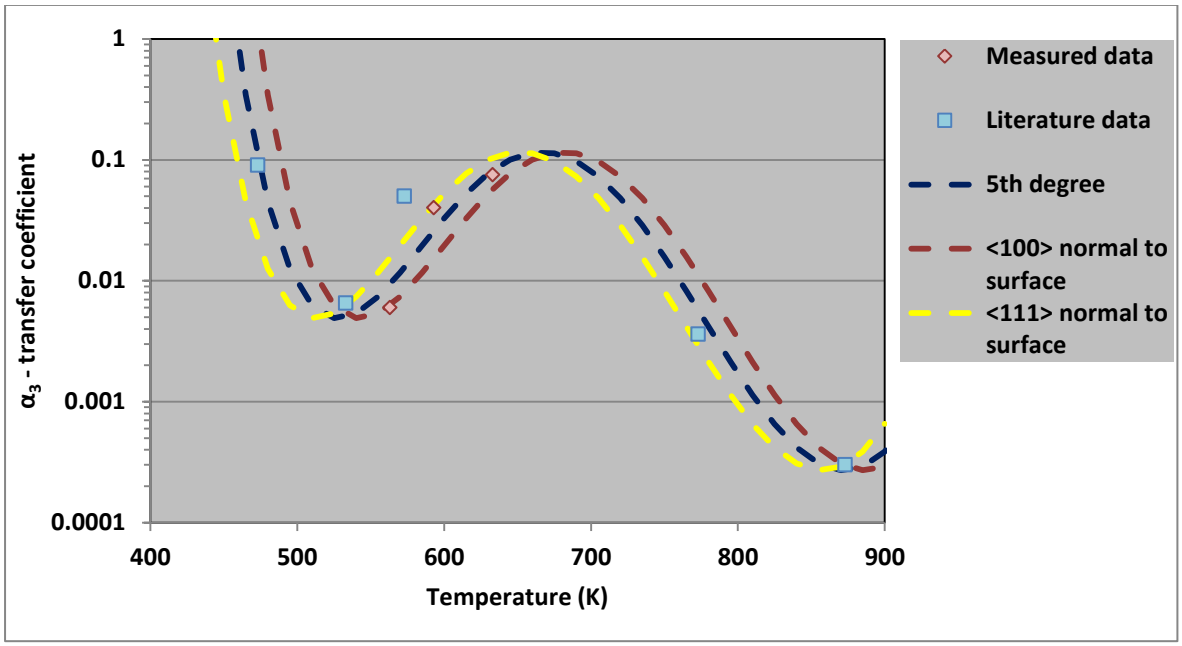

Figure 80. Plot of the transfer coefficient (α_3) function of temperature, (Figure 73) with the suspected influence of different orientations that may shifts the curve along the temperature axis in either a positive or negative direction.

9.4. Degradation of Coherency due to Differential Thermal Expansion

The degradation of metal/oxide interface coherency is likely caused by differential thermal expansion between the respective crystal lattices. There is a relatively large difference in thermal expansion coefficients between the FCC austenitic stainless steel metal, at 16.2 µm/m.°C, and the spinel oxide, at 9.9 µm/m.°C [110], with a differential thermal expansion of 6.3 µm/m.°C. Therefore as the temperature of the system increases any degree of coherency achieved across the metal/film interface, which will be dependent on the relative orientations of the metal and oxide, will become increasingly stressed as one lattice expands relative to the other. This stress may be relieved by introducing dislocations, or in the case of semi-coherent interfaces more dislocations, at regular atomic intervals at either lattice. However, at the higher temperature another set of relative orientations may be

preferable to minimise the interface energy and hence improving the level of coherency. At one point there may be no available orientation combinations that could achieve semi-coherency across the interface without the introduction of a significant amount of dislocations, and this would result in a degradation of coherency.

It is expected that those crystallites within the spinel oxide that nucleate with an orientation favourable for interface coherency, dependent on the metal orientation, will grow at a greater rate than those that are less favourable. Therefore the degree of coherency is maintained as the oxide grows. Due to crystal symmetry within the spinel oxide structure there may be several orientations that could result in equally coherent interfaces, which can result in a nanocrystalline oxide structure growing on a single metal grain.

The likely explanation for the case of the metal orientation with <100> normal to the sample surface, which was unfavourable for growth kinetics at 290°C but favourable at 320°C, is that the additional 30°C allowed for the metal to expand relative to the oxide to the point where better coherency could be achieved across the metal/oxide interface. It was noted that the maximum surface oxide depth measured for a grain with this orientation exposed at 320°C for 1000 h, was comparable to the maximum surface oxide depths measured at 290°C, see Figure 45. Similarly, those metal orientations favourable for oxide kinetics at 290°C had to concede coherency at higher temperatures due to the relative expansion of the opposing structures, resulting in a higher associated transfer coefficient, α_3, lower potential gain, $\phi_{m/f}$, and ultimately reduced potential oxide depths.

9.5. Observation of Coherency

The coherency across the metal/Cr-rich oxide film interface has been observed by Soulas et al. in 316L stainless steel exposed to simulated primary water at 325°C [58]. In this investigation samples were exposed for relatively short durations of up to 24 hrs, and in a similar way thin films of the surface layers were prepared for observations in high resolution with a Cs-corrected TEM. Atomic resolution images of the metal/oxide film interface were acquired from an area where both lattices were close to a zone axis, with the metal on the [100] zone axis, see Figure 81. A Fourier transform of the images was calculated, and by selecting certain calculated reflections a regular pattern of dislocations in the metal lattice was revealed in the observed plane. By tilting the sample to another zone axis, the [110] zone axis, a second set of dislocations could be confirmed. Therefore a semi-coherent

interface was observed in this sample where the misfit of the spinel to FCC lattices could be accommodated in the metal lattice using a set of dislocations in 2 different directions.

This semi-coherency was observed using electron microscopy performed at room temperature, and while the oxide may have been grown at high temperature, the bonding at the interface would need to adjust to the differential contraction of the two lattices as the sample cooled. Therefore the observation is not necessarily representative of the bonding between the structures while the oxide was growing at the exposure temperature. Nevertheless this study has elegantly established that a semi-coherent interface is possible between the inner Cr-rich spinel oxide and the FCC metal structure of 316L stainless steel.

Considering that the interface coherency is suspected to change within the region that Soulas' study was performed, it would be necessary to observe coherency at the interface whilst at high temperature. For this it may be possible to use a specific heating stage for the TEM where the temperature of the sample can be raised in a controlled manner through the range in question to observe any degradation across the interface. However, such observations would require an Cs-corrected atomic resolution TEM together with a specialized heating stage that can be tilted in two directions to find the necessary zone axis. The author did not have access to this equipment in the present investigation but it is recommended for further exploratory work.

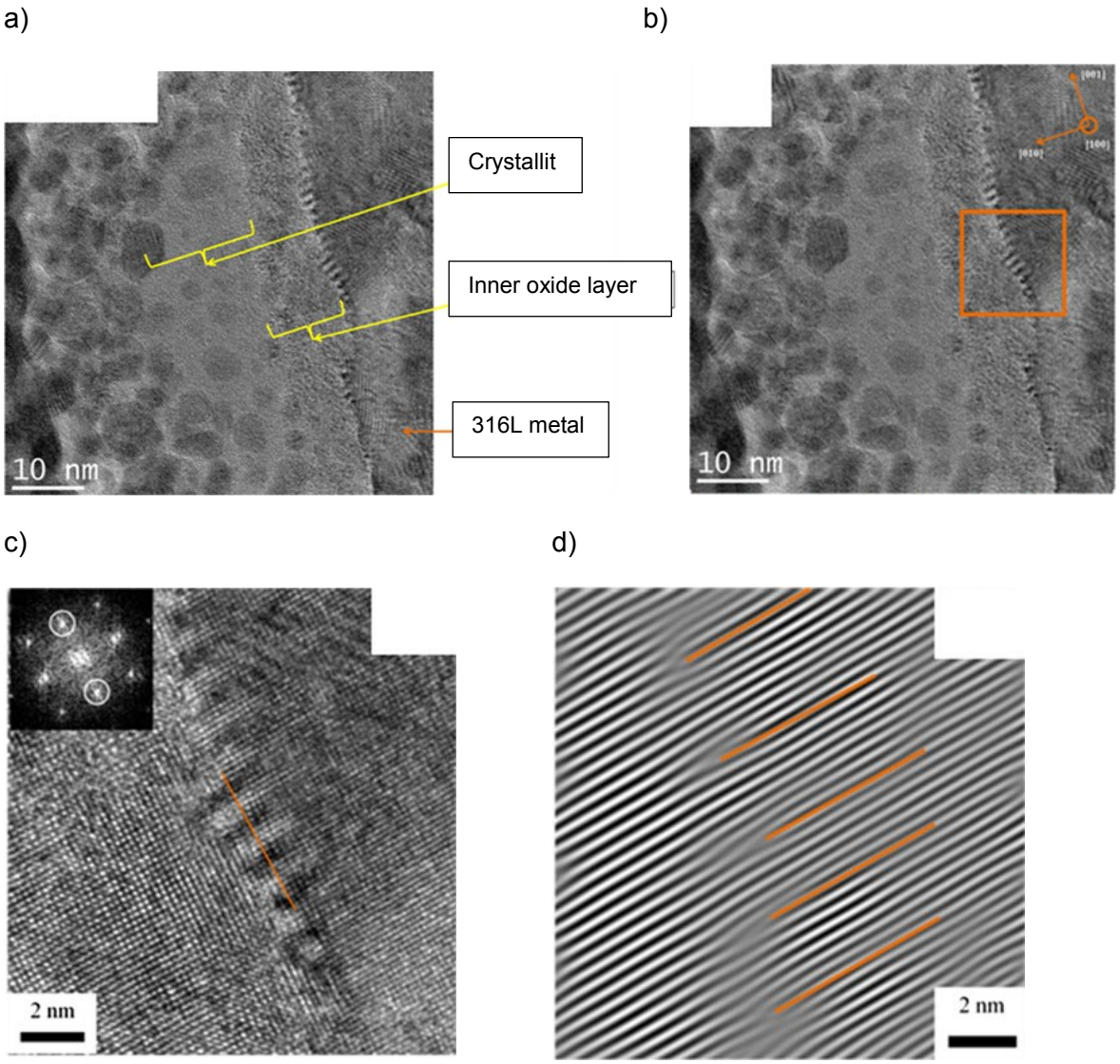

Figure 81. High resolution TEM images of a thin foil 316L sample prepared through the surface oxide after exposure to simulated primary water for 5 h at 325°C. a) Bright field TEM image of the interface area highlighting the location of the external Fe_3O_4 crystallite, the Cr rich inner oxide layer and the metal, b) showing the interface area analysed in c and d, c) an atomic resolution image of the interface on the [0-10] zone axis with the calculated Fourier transform in the insert, d) the inverse Fourier image of those calculated reflects circled in c showing discrete dislocations at regular atomic plane intervals [58].

As an alternative to physical observations of the coherency at temperature within a TEM, it may be possible to develop a credible *ab initio* type model to simulate the type of bonding at such an interface. In this approach the spatial distribution of atoms in the two respective atomic crystal lattice systems can be computationally modelled using the electron energy states that are characteristic of each atom. The model will determine the atomic configuration where the overall energy associated with the bonding is reduced to a minimum. Once the respective models of each lattice have been constructed they can be brought together to form an interface where the electron boundary constraints are relaxed, and by solving a demanding system of interdependent equations, a bonding solution can be found.

This approach can use either density functional theory or molecular dynamics, or a combination of both to determine the most energy efficient bonding configuration across the interface. In turn this approach can be repeated with the introduction of heat into the system to determine how the bonds across the interface are stressed with the relative expansion of the lattices, and at what temperature the coherency of the interface will change to accommodate this expansion.

This alternative approach is complex and requires specialized expertise. There is no publication known to the author that has modelled this interface at temperature. Therefore, this approach is also recommended for further exploratory work; however, it is considered beyond the scope of the current investigation.

9.6. Extension to Intergranular Stress Corrosion Cracking Behaviour

There have been a number of relatively recent publications where the intergranular stress corrosion cracking (IGSCC) growth rate of austenitic stainless steel in high temperature water has exhibited a peak as temperature increases, after which the rate drops off. The results of the present investigation, where a similar trend in the oxidation rate with temperature was observed in the absence of applied stress, may be a significant contribution towards explaining the IGSCC rate phenomenon.

9.6.1. Departure from Arrhenius curve in IGSCC of Type 316 Stainless Steel

Two plots of measured IGSCC growth rate data vs temperature^{-1} from publications by Terachi et al. and Arioka et al. are given in Figure 82 [111,112]. In each of these plots the crack growth rate (CGR) of 316 stainless steel was measured when exposed to simulated primary water at different temperatures using the direct current potential drop method described in ASTM E647-11. Cold work was introduced as a variable through rolling to produce samples representing between 10% – 20% reduction in thickness, which resulted in an appreciable increase in CGR. In all sets of data the plotted crack growth resembled an Arrhenius type increase with temperature from which an activation energy could be assigned according to the level of cold work. However, beyond a certain temperature the CGR departed from the Arrhenius trend and significantly reduced. For the 10% - 15% cold worked samples, this temperature was approximately 320°C, while CGR of the 20% cold worked sample peaked slightly higher at approximately 340°C. No definitive explanation

was offered for this behaviour in each of the publications other than a suggestion that two competing rate limiting reactions are affecting the crack propagation [112].

a) b)

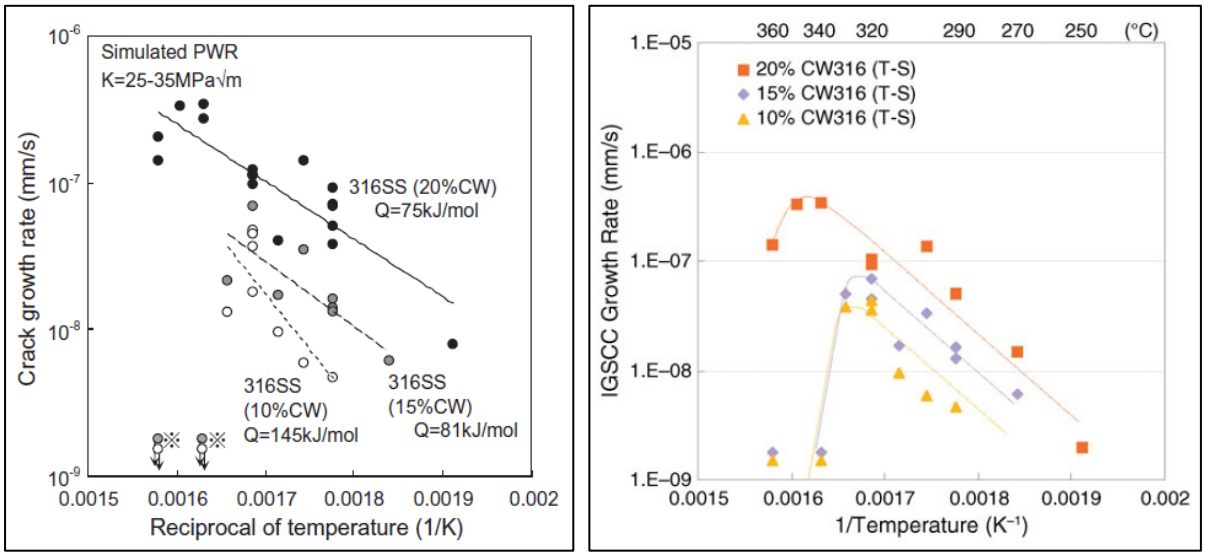

Figure 82. Published IGSCC growth rate data plotted on the reciprocal of temperature axis to demonstrate the Arrhenius type of temperature dependence and the influence of cold work. In both publications of Terachi et al.[111] (a) and Arioka et al.[112] (b) the CGR significantly dropped beyond a certain temperature.

Following the Terachi and Arioka papers, Meisnar et al. recently (2016) published the results of a study that investigated the cause for the IGSCC behaviour in SUS316 stainless steel which appears to be inhibited at temperatures greater than approximately 320°C [113]. The investigation initiated SCC cracks in 316L compact tension (CT) samples that had been cold rolled to 20% reduction in thickness, in simulated primary water environment under a constant load of 30 MPa.m$^{1/2}$. Cracks were grown at temperatures varying between 320°C and 360°C representing the range where it had previously been established that the CGR departs from the characteristic Arrhenius type increase with temperature.

Meisnar's study used microscopy to characterise and compare the crack tips grown at the different temperatures with two main findings. Firstly, Meisnar compared the crack growth rate determined using the traditional method of defining crack depth by an alternative total crack length method. The fracture surface method measures the crack depth by fracturing the CT specimens and measuring the maximum oxidised crack depth accounted for by SCC. However, since SCC was branched, Meisnar et al. measured the total crack length from a cross-section through the specimen. As a result of measuring crack growth rates by the latter method, the peak in CGR shifted to lower temperatures, and the temperature at which the highest CGR was measured was 320°C. Note that the papers by Arioka and Terachi [111,112], discussed above, used the traditional method of determining CGR, whose results

were consistent with Meisnar [113]. However, when considering the branched nature of the propagation the temperature at which CGR peaks was shifted to 320°C and possibly lower. Therefore defining the CGR peak in this way provides for a striking correlation with the temperature at which the steady state surface oxidation peaks in 316L stainless steel in simulated primary water.

Secondly, the transmission Kikuchi diffraction (TKD) was used to measure the misorientation around the crack tips grown at different temperatures. From the misorientation profiles Meisnar determined the extent of a plastic zone around the crack tip. It was found that the plastic zone around the crack tips at lower temperatures was larger than at higher temperatures, and with greater associated dislocation density. From these observations the study concludes that there are competing mechanisms determining CGR with an Arrhenius thermally activated response controlling crack growth rate but that at higher temperatures diffusion of dislocations in the metal becomes dominant. The latter results in a reduced strain gradient and dislocation density at the crack tip, see extracts from the paper in Figure 83b and Figure 84.

In a subsequent paper crack tips from alloy 600, alloy 690 and 316L stainless steel grown in primary water environments were observed and compared using similar techniques [15]. Through this investigation evidence was found in alloy 600 where the deformation intensity ahead of the crack tip was not found to be dependent on temperature in the range of 320°C - 360°C. This suggests that the mechanical deformation-based mechanism was not active in the alloy 600 and may explain why the Ni based alloys do not exhibit the departure from Arrhenius temperature dependence as observed in the austenitic stainless steels.

Contrary to the above view, it is proposed that the peak in oxidation kinetics observed in this investigation may be the cause for the observed peak in IGSCC in type 316 and other austenitic stainless steels. Since the drop in oxide kinetics as temperature increased was observed in both annealed and cold worked material, and in the absence of any applied stress, the mechanism is unrelated to dislocation density. Since IGSCC growth rate is likely dependent, although somewhat disputed, on the growth of this oxide at the crack tip, the results and explanation in the present study cannot be ignored when interpreting the cause of the CGR peak in austenitic stainless steels.

a) b)

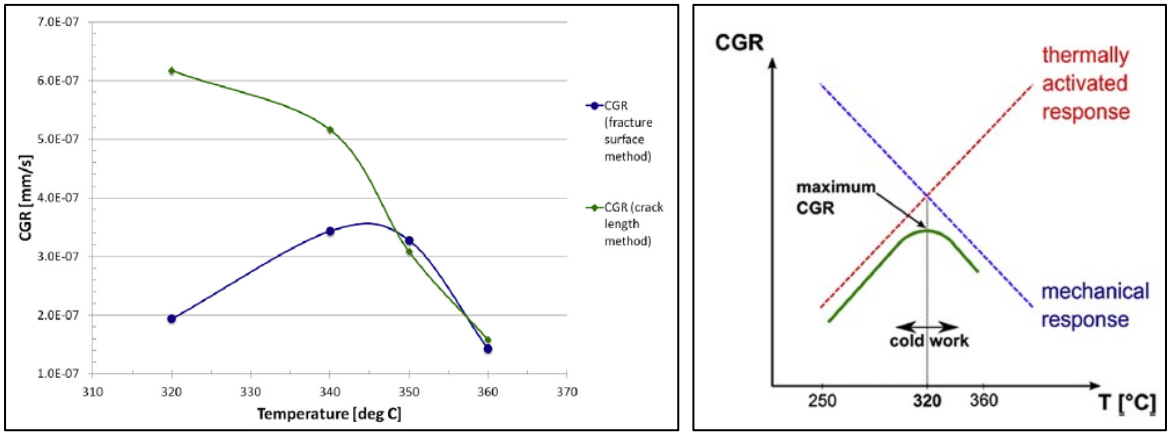

Figure 83. Plots of IGSCC growth rate in type 316 stainless steel verses exposure temperatures with a) crack growth rate measured by two different methods, both showing a decline of growth rate with respect to temperature but peak at different temperatures, and b) the proposed explanation for the CGR peak where the mechanical response becomes dominant at temperatures greater than the CGR peak temperature [113].

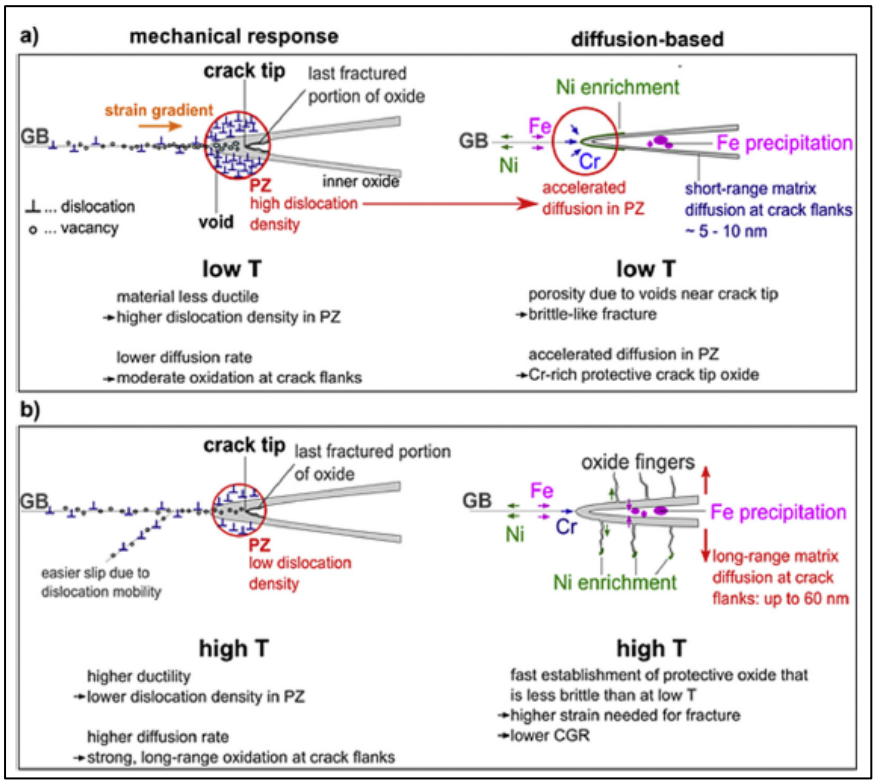

Figure 84. A summary of the mechanism proposed by Meisner et al. for the peak observed in CGR of type 316 stainless steel as temperature increases [113].

9.6.2. Influence of Ni content on IGSCC in Ni-Cr-Fe alloys

In another publication, Arioka et al. investigated the influence of the relative composition within Fe-Ni-Cr alloys on the CGR in the primary water environment [24]. Several heats were produced in the laboratory where the ratios of the Ni, Fe and Cr contents were varied. All samples were cold rolled to 20% reduction in thickness and therefore represent cold worked conditions. In particular the influence of Ni on the CGR curves with respect to temperature was studied by comparing samples where the Cr content was kept constant at 16 wt% in the Ni-Cr-Fe alloys. The CGR data, acquired with samples exposed to PWR primary water conditions, is given for different Ni contents in Figure 85.a. It is evident how increasing the Ni content from 25 wt% shifts the departure from Arrhenius behaviour to higher temperatures and the drop in rates diminishes. It also shows that alloys with Ni content above approximately 70%, such as alloy 600 with a specified minimum Ni content of 72 wt%, do not exhibit a drop in CGR as temperature increases.

In an alternative plot, Figure 85.b, the CGR for various cold rolled alloys is given at a single temperature of 360°C, which represents the highest temperature measured and where the greatest deviation from the Arrhenius rates was measured. It is also evident in this plot how sensitive to the CGR the alloys were to the Ni content, with the rates decreasing as the Ni content decreases from being the majority base metal to an alloying element. Once Ni is reduced below approximately 20 wt% the CGR increases once again. The alloy content with the least Ni content in the investigation was 11 wt% which represented 316 stainless steel.

The results published from Arioka et al. clearly highlight the influence of composition in Ni-Cr-Fe alloys on CGR, with alloy 600 sample with 75 wt% Ni content showing no departure from the Arrhenius curve, while alloys with between 20 – 40 wt % Ni showed the greatest drop in CGR[24]. The paper concludes that there are multiple rate limiting processes that affect the temperature dependence of CGR. However, considering the similarities in observed inverse kinetic behaviour in surface oxidation, in the absence of applied stress, and CGR at temperatures greater than approximately 290°C, it is plausible that similar processes are responsible.

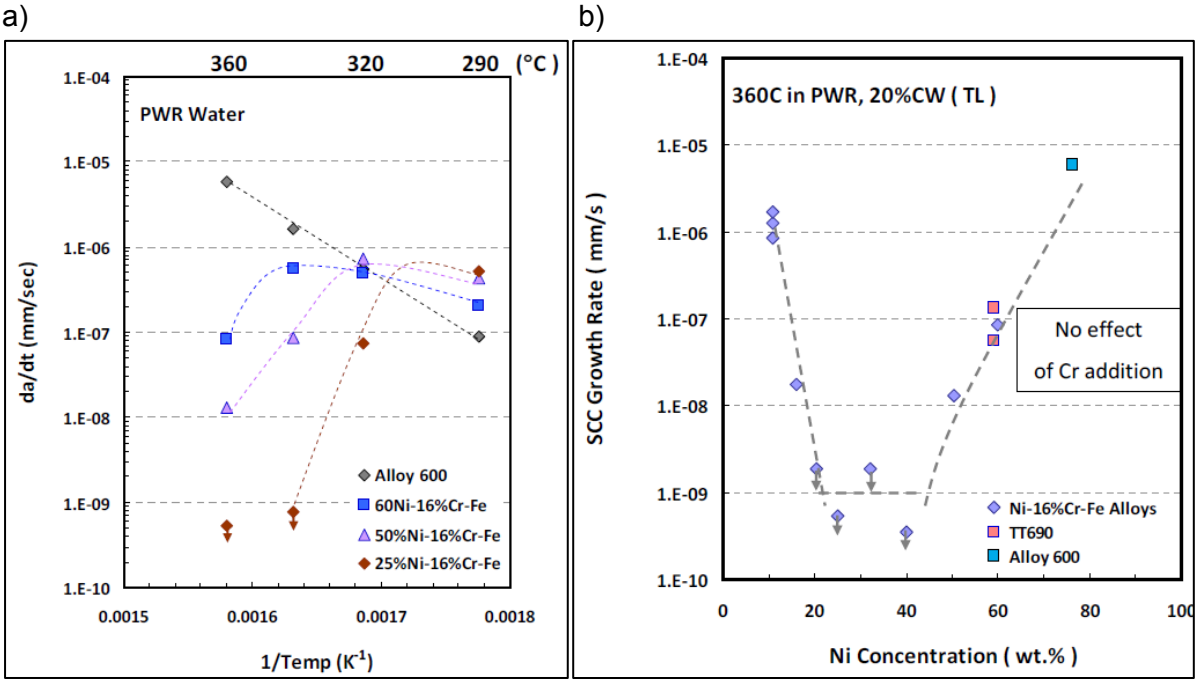

Figure 85. Plots of SCC crack growth rates with temperature of 20% cold worked Fe-Ni-Cr alloys exposed to simulated primary water from Arioka et al.[24], with a) various alloys showing the effect of Ni content on the CGR deviation from Arrhenius behaviour, and b) the CGR at 360°C as a function of Ni content in wt%.

Consider that the proposed explanation from this investigation for the inverse in oxide growth kinetics in 316L stainless steel is the degrading coherency in the metal/oxide interface due to differential thermal expansion between the respective lattices. This explanation is therefore dependent on the respective lattices having different coefficients of thermal expansion. If this explanation is to extend to the SCC observations by Arioka et al., then the thermal expansion coefficients of the respective alloys should be compared to see if there is a correlation between the differential thermal expansion coefficients and the observed departure from Arrhenius CGR kinetics.

Arioka et al. created heats of various compositions specifically for the study and therefore linear coefficient of expansion data for some of these alloys is unknown. However, in Table 13 a number of known Ni-Cr-Fe alloys are given with their nominal compositions as well as published coefficients of thermal expansion. In an attempt to align the compositions with those in Arioka's study, the alloys were selected within a narrow band of nominal Cr contents (15-21 wt%) and minimal other alloying elements. The difference between the published linear coefficient of thermal expansion in the range of 100°C - 204°C for the alloy and the same coefficient for spinel oxide was calculated, and these values were plotted against Ni content in wt% in Figure 86. This plot assumes that the type of spinel oxide characterised for 316L stainless steel is similar to that developed in Ni based Ni-Cr-Fe alloys and that its associated coefficient of expansion is comparable.

Figure 86 can be compared to Figure 85. where the decrease in CGR as Ni content decreases from that of alloy 600 (75 wt% Ni) is accompanied by an increased expansion coefficient differential between the metal and the oxide. Similarly, notice the shift in peak CGR to lower temperatures as the Ni content decreases in Figure 85.a, which is associated with an increased expansion coefficient differential. The explanation proposed for the inverse in oxide kinetics with temperature is consistent with these CGR observations from Arioka et al. Hence alloys with lower expansion coefficient differential between the alloy and its oxide will realise departure from Arrhenius CGR at higher temperatures, or possibly not at all.

The explanation does not account for the increase in CGR at Ni contents below 20 wt% in Figure 85b, however the increase may be related to the increased electrochemical potential due to the drop in Ni content. Note that this is not a rigorous attempt to explain the behaviour of IGSCC with temperature in Ni-Cr-Fe austenitic alloys. However, it serves to highlight that it is possible to extend the proposed explanation for the inverse in surface oxidation kinetics with temperature to the observed IGSCC kinetic behaviour with temperature without apparent inconsistency.

Table 13. Linear coefficients of expansion for various Ni-Cr-Fe alloys in the range of 100°C - 204°C, and the difference between the alloy's expansion coefficient and the spinel oxide at 9.9 x10^{-6}µm/m/°C.

Alloy	Nominal composition (wt%)							Linear coefficient of thermal expansion (10^{-6}/°C) from 100°C - 204°C	Δ expansion coefficient between alloy and spinel oxide from 100°C - 204°C
	Fe	Ni	Cr	Mo	Cu	Ti	Si		
316 SS (1.4401)		8	16	2				16.9	7
Alloy DS	40	26.5	18				2	15.5	5.6
Alloy DS	40	26.5	18				2	15.5	5.6
alloy 800	45	33.6	21			0.4		15.9	6
1.4864	bal	35	16					15.7	5.8
alloy 20	bal	35	20	2	3			15.2	5.3
alloy 825	bal	42	20	3	2			14.9	5
alloy X-750	7	75.5	15					12.6	2.7
	7	75.5	15			2.5		13	3.1
alloy 600	8	75	16					12	2.1
	8	75	16					13.8	3.9

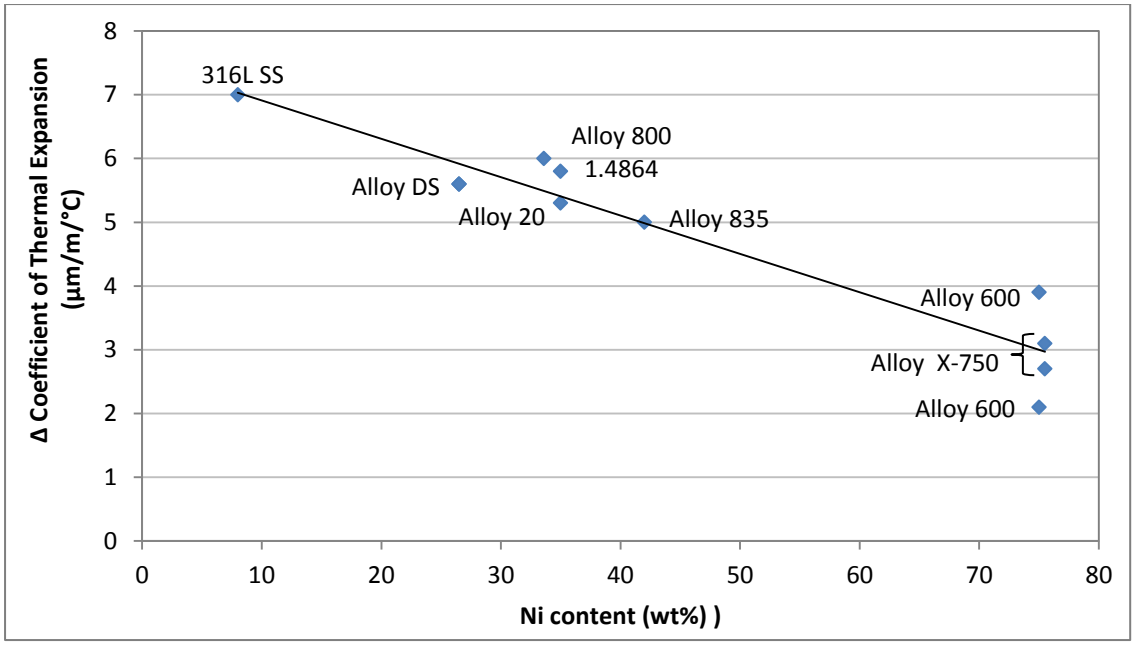

Figure 86. The linear coefficients of expansion of various Ni-Cr-Fe alloys were determined, all of which are specified with approximately 15-21 wt% Cr. This figure plots the difference between these coefficients and the corresponding coefficient of the spinel $FeCr_2O_3$ chromite oxide verses Ni content in wt%. The plot reveals a linear trend which decreases as the Fe content is reduced and Ni wt% is increased.

10. SUMMARY AND CONCLUSION

The oxide kinetics of 316L stainless steel was measured after samples were exposed to primary water conditions for durations from 1 hour to several thousand hours. A unique aspect of this investigation was that rather than measuring bulk averaged oxide depth in the samples, local cross-sections were prepared through the surface at selected positions where the greatest oxide depth was likely. By this methodology the oxide depth could be physically measured and the influence of microtexture on the oxide kinetics could be observed.

The influence of cold work was studied by comparing the oxide kinetics of annealed samples to those with cold work introduced by cold rolling to 20% reduction in thickness, and those deformed in uniaxial tension to 30% elongation. The introduction of this quantity of cold work can accelerate the IGSCC growth rate in austenitic stainless steels (at temperatures below peak CGR). However, it did not result in any discernible difference in oxidation kinetics when compared to the annealed samples exposed to the same conditions.

Intergranular oxidation was measured in particular since preferential oxidation down grain boundaries is considered to be a precursor for intergranular stress corrosion crack initiation. By quantitatively modelling intergranular oxidation, the time to initiate IGSCC could potentially be predicted. The preferential oxidation rate down grain boundaries was measured to be on average 1.7 and 1.8 times the maximum surface oxidation rate for annealed and cold worked samples respectively. This is not particularly high considering some Ni based alloys that have demonstrated that under similar conditions intergranular oxidation depth may exceed the surface oxidation depth by an order of magnitude or more.

Temperature proved to have significant influence on the oxidation kinetics, particularly in the range measured of 290°C, 320°C and 360°C. Measurements for all three temperatures were completed at exposures of 1000 hours and greater. The oxide kinetics were consistently found to decrease as temperature increased through the range, which was a counter-intuitive result.

With relatively few data points acquired from cross-section measurements, which may be considered too few to be representative, ToF-SIMS was used to acquire data from a larger area that could be used to supplement the physical measurements. Three annealed samples exposed for 1000 hours at each temperature were analysed and the results proved to be consistent with the localised cross-section measurements and substantiated the conclusions drawn regarding the influence of temperature as well as preferential orientation.

It was evident that the rate of surface oxidation was dependent on orientation of the underlying metal grain with measured oxide depths varying by more than an order of magnitude between grains in the same sample. This observation provided substantiation for the claim by the Point Defect Model that the rate for oxidation growth is controlled by the reactions at the metal/film interface. It was also observed that the orientation favourable for increased oxidation kinetics varied at different temperatures. For example grains with <001> oriented normal to the sample surface proved to be unfavourable for oxide growth at 290°C, favourable at 320°C, and unfavourable again at 360°C. Therefore the orientation dependence was itself dependent on temperature.

The phenomenological Point Defect Model was used as a basis to develop a quantitative expression for the rate of inner Cr-rich oxide growth in 316L stainless steel over time. The model had to be adapted to accommodate the inverse in oxide kinetics as temperature increased from 290°C to 360°C, while other published oxide growth data from austenitic stainless steels suggested that the kinetics would increase from 120°C until approximately 290°C and would increase again beyond 360°C. The PDM was adapted to model this characteristic kinetic profile through temperature by expressing the transfer coefficient at the metal/film interface, α_3, as a function of temperature. This parameter describes the potential gain across the interface which, under the influence of the electric field, determines the steady state oxide thickness. In addition the rate constant associated with this interface, k_3^o, was expressed with an Arrhenius expression.

It was concluded that the most likely explanation for the inversion in oxidation kinetics measured in the testing range was that the coherency of the metal/film interface degrades as temperature increases. The cause for this degradation is likely due to the difference in thermal expansion coefficients between the metal and the oxide lattices causing relative expansion of the metal with respect to the oxide to the point where coherency breaks down. The following observations are consistent with this proposed theory:

- The oxide kinetics is dependent on metal crystallographic orientation, which is indicative of the rate being determined by reactions at the metal/film interface, rather than dependent on diffusion rates through the film.
- The only parameter in the Point Defect Model that could accommodate the kinetics inversion with temperature is the transfer coefficient at the metal/film interface, which is inversely proportional to the potential gain across this interface.
- The most favourable metal orientation favourable for oxidation kinetics changed as temperature increased through the range of 290°C - 360°C. This suggests that a

metal/film interface that has good coherency favourable for oxidation kinetics at 290°C, could not maintain its coherency at 320°C.

- The chromite spinel oxide and austenitic stainless steel metal have significantly different linear coefficients of thermal expansion.
- The oxidation of Ni-Fe-Cr alloys where the base metal is Ni, with a linear coefficient of expansion closer to that of chromite, does not exhibit the inversion of oxidation kinetics within the same temperature range [72].

This explanation is likely to extend to a similar inversion in the intergranular stress corrosion cracking growth rate in austenitic stainless steels observed in a similar temperature range. The latter phenomenon has been widely reported to occur where the crack growth rate significantly drops as the temperature increases beyond a point which is dependent on cold work but occurs within the 290°C-360°C range. The drop in crack growth rate is not measured for Ni based materials such as alloy 600 with a thermal coefficient of expansion less than austenitic stainless steels. It is proposed therefore that the cause of the drop in crack growth rates is the degradation of coherency of the metal/film interface at the crack tip as temperature increases, reducing the oxide growth rate and ultimately reducing the crack growth rate.

11. REFERENCES

[1] S.J. Zinkle, G.S. Was, Materials challenges in nuclear energy, Acta Mater. 61 (2013) 735–758.

[2] P.M. Scott, 2000 F.N Speller award lecture: stress corrosion cracking in pressurized water reactors - interpretation, modelling, and remedies, Corrosion. 56 (2000) 771–782.

[3] S.M. Bruemmer, G.S. Was, Microstructural and microchemical mechanisms controlling intergranular stress-corrosion cracking in light-water-reactor systems, J. Nucl. Mater. 216 (1994) 348–363.

[4] EPRI, Stress Corrosion Cracking Initiation Model for Stainless Steel and Nickel Alloys, Palo Alto, CA, 2009.

[5] EPRI, Validation of Stress Corrosion Cracking Initiation Model for Stainless Steel and Nickel Alloys: Effects of Cold Work, Palo Alto, CA, 2012.

[6] T. Couvant, M. Wehbi, C. Duhame, J. Crépin, R. Munier, Development of a “Local” Model to Predict IGSCC Preliminary Calibration of Parameters for Nickel Alloy Exposed to Primary Water, in: 17th Int. Conf. Environ. Degrad. Mater. Nucl. Power Syst. – Water React., Ottawa, 2015.

[7] C. Amzallag, S. Le Hong, C. Benhamou, A. Gelpi, Methodology used to Rank the Corrosion Susceptibility of Alloy 600 PWR Components, in: PVP-Vol.4110-2, Assess. Methodol. Prev. Fail. Serv. Exp. Environ. Cosiderations, ASME, 2000.

[8] P.M. Scott, 2000 F.N. Speller award lecture: Stress corrosion cracking in pressurized water reactors—interpretation, modeling, and remedies, Corrosion. 56 (2000) 771–782.

[9] K. Arioka, T. Yamada, T. Miyamoto, M. Aoki, Intergranular Stress Corrosion Cracking Growth Behavior of Ni-Cr-Fe Alloys in Pressurized Water Reactor Primary Water, Corrosion. 70 (2014) 695–707.

[10] D. Féron, ed., Nuclear Corrosion Science and Engineering, Woodhead Publishing, Cambridge, 2012.

[11] H. Dugdale, D.E.J. Armstrong, E. Tarleton, S.G. Roberts, S. Lozano-Perez, How oxidized grain boundaries fail, Acta Mater. 61 (2013) 4707–4713.

[12] M. Meisnar, M. Moody, S. Lozano-Perez, Atom probe tomography of stress corrosion crack tips in SUS316 stainless steels, Corros. Sci. 98 (2015) 661–671.

[13] P. Combrade, P.M. Scott, M. Foucault, E. Andrieu, P. Marcus, Oxidation of Ni base alloys in PWR water: oxide layers and associated damage to the base metal, in: 12th Int. Conf. Environemental Degrad. Mater. Nucl. Power Syst., 2005: pp. 883–890.

[14] Y.H. Lu, Q.J. Peng, T. Sato, T. Shoji, An ATEM study of oxidation behavior of SCC crack tips in 304L stainless steel in high temperature oxygenated water, J. Nucl. Mater. 347 (2005) 52–68.

[15] Z. Shen, M. Meisnar, K. Arioka, S. Lozano-perez, Mechanistic understanding of the temperature dependence of crack growth rate in alloy 600 and 316 stainless steel

through high- resolution characterization, Acta Mater. 165 (2019) 73–86.

[16] IAEA Vienna, IAEA Power Reactor Information System, https://pris.iaea.org/PRIS/WorldStatistics/OperationalReactorsByType.aspx. (2018).

[17] Vatttenfall, http://corporate.vattenfall.com/about-energy/electricity-and-heat-production/nuclear-power/how-it-works/, (2018).

[18] J. Danko, Corrosion in the Nuclear Power Industry, in: ASM Met. Handb., 9th ed., ASM International, 1987: pp. 927–984.

[19] P. Andresen, F. Ford, K. Gott, R. Jones, P. Scott, T. Shoji, R. Staehle, R. Tapping, Expert Panel Report on Proactive Materials Degradation Assessment Brookhaven National Laboratory U . S . Nuclear Regulatory Commission Office of Nuclear Regulatory Research. CR-923, 2007.

[20] B. Pastina, J. Isabey, B. Hickel, The influence of water chemistry on the radiolysis of the primary coolant water in pressurized water reactors, J. Nucl. Mater. 264 (1999) 309–318.

[21] EPRI, Pressurized Water Reactor Primary Water Chemistry Guidelines, EPRI, Palo Alto, CA, 2007.

[22] M.C. Song, K.J. Lee, The evaluation of radioactive corrosion product at PWR as change of primary coolant chemistry for long-term fuel cycle, Ann. Nucl. Energy. 30 (2003) 1231–1246.

[23] EPRI, Materials Reliability Program : Effects of Hydrogen , pH , Lithium and Boron on Primary Water Stress Corrosion Crack Initiation in Alloy 600 for Temperatures in the Range 320-330 ° C, Palo Alto, CA, 2005.

[24] K. Arioka, T. Yamada, T. Miyamoto, M. Aoki, Effect of Ni and Cr on IGSCC growth rate of Ni-Cr-Fe alloys in PWR primary water, in: Fontevraud 8 - Contrib. Mater. Investig. Oper. Exp. to LWRs' Safety, Perform. Reliab., Avignon, France, 2014.

[25] H. Coriou, L. Grall, C. Mahieu, M. Pelas, Sensitvity to Stress Corrosion and Intergranular Attack of High-Nickel Austenitic Alloy, Corrosion. 22 (1966) 280–290.

[26] K. Norring, B. Rosborg, INIS-mf-10506: A Compilation of Experiences of Corrosion in Nordic Nuclear Power Plants, 1982.

[27] EPRI, Steam Generator Management Program: Steam Generator Progress Report: Rev 18, Palo Alto, CA, 2013.

[28] IAEA Nuclear Energy Series Stress Corrosion Cracking in Light Water Reactors : Good Practices and Lessons Learned. No. NP-T-3.13, Vienna, 2011.

[29] EPRI, Materials Handbook for Nuclear Plant Pressure Boundary Applications, Palo Alto, CA, 2013.

[30] Materials Reliability Program: Stress corrosion cracking of stainless steel components in primary water circuit environments of pressurized water reactors (MRP-236), 1015540, EPRI, Palo Alto, CA, 2007.

[31] D. Féron, E. Herms, B. Tanguy, Behavior of stainless steels in pressurized water reactor primary circuits, J. Nucl. Mater. 427 (2012) 364–377.

[32] B.M. Gordon, The Effect of Chloride and Oxygen on the Stress Corrosion Cracking of

Stainless Steels: Review of Literature, Mater. Perform. 19 (1980) 29–38.

[33] T. Tribouilloy, F. Vaillant, J.-M. Olive, M. Puiggali, STRESS CORROSION CRACKING ON COLD-WORKED AUSTENITIC STAINLESS STEELS IN PWR ENVIRONMENT, Adv. Mater. Sci. 7 (2007) 61–69.

[34] T. Shoji, K. Sakaguchi, Z. Lu, S. Hirano, Y. Haseawa, T. Kobayashi, K. Fujimoto, Y. Momura, Effects of cold work and stress on oxidation and SCC behavior of stainless steels in PWR primary water environments, in: Fontevraud 7 Int. Symp., Avignon, France, 2010.

[35] Kansai EPCO, JANTI-OTO-008-002 attachment1 - Flaws Found in Steam Generator A Reactor Coolant Inlet Nozzle Weld, 2007.

[36] P.L. Andresen, F.P. Ford, Response to " On the modeling of stress corrosion cracking of iron and nickel base alloys in high temperature aqueous environments," Corros. Sci. 38 (1996) 1011–1016.

[37] E.M. Gutman, Notes on the discussion concerning the "surface mobility mechanism" of stress corrosion cracking, Corros. Sci. 45 (2003) 2105–2128.

[38] P.L. Andresen, F. Ford, Life Prediction by Mechanistic Modeling and System Monitoring of Environmental Cracking of Iron and Nickel Alloys in Aqueous Systems, Mater. Sci. Eng. A. 103 (1988) 167–184.

[39] F.P. Ford, Quantitative Prediction of Environmentally Assisted Cracking, Corrosion. 52 (1996) 375–395.

[40] D.D. Macdonald, On the Modeling of Stress Corrosion Cracking in Iron and Nickel Base Alloys in High Temperature Aqueous Environment, 38 (1996) 1003–1010.

[41] M.M. Hall, Critique of the Ford-Andresen film rupture model for aqueous stress corrosion cracking, Corros. Sci. 51 (2009) 1103–1106.

[42] A. Turnbull, Modelling of Environment Assisted Cracking, Corros. Sci. 34 (1993) 921–960.

[43] P.M. Scott, Environment-assisted cracking in austentic components, 65 (1996) 255–264.

[44] Q.J. Peng, J. Kwon, T. Shoji, Development of a fundamental crack tip strain rate equation and its application to quantitative prediction of stress corrosion cracking of stainless steels in high temperature oxygenated water, J. Nucl. Mater. 324 (2004) 52–61.

[45] J.R. Galvele, Surface Mobility Mechanism of Stress Corrosion Cracking, Corros. Sci. 35 (1993) 419–434.

[46] J.R. Galvele, Comments on "notes on the surface mobility mechanism of stress-corrosion cracking", by K. Sieradzki and F. J. Friedersdorf, Corros. Sci. 36 (1994) 901–910.

[47] J. Knott, Fundamentals of Fracture Mechanics, Butterworth, London, 1976.

[48] P.M. Scott, M. Le Calvar, Some possible mechanisms of intergranular stress corrosion cracking of alloy 600 in PWR primary water, in: Proc 6 Int Symp Env. Degrad Mat Nucl Power Syst Water React, 1993: pp. 657–667.

[49] P.M. Scott, An Overview of Internal Oxidation as a Possible Explanation of Intergranular Stress Corrosion Cracking of Alloy 600 in PWRs, in: 9th Int. Symp. Environ. Degrad. Mater. Nucl. Power Syst., 1999.

[50] L.E. Thomas, S.M. Bruemmer, High-resolution characterization of intergranular attack and stress corrosion cracking of alloy 600 in high-temperature primary water, Corrosion. 56 (2000) 572–587.

[51] R. Staehle, Z. Fang, Comments on a proposed mechanism of internal oxidation for alloy 600 as applied to low potential SCC, in: Proc. Ninth Int. Symp. Environ. Degrad. Mater. Nucl. Power Syst. - Water React., 1999: pp. 69–78.

[52] S.P. Lynch, Mechanisms and Kinetics of Environmentally Assisted Cracking: Current Status, Issues, and Suggestions for Further Work, Metall. Mater. Trans. A. 44A (2013) 1209–1229.

[53] H.. Birnbaum, P. Sofronis, Hydrogen-enhanced localized plasticity - a mechanism for hydrogen-related fracture, Mater. Sci. Eng. A. 176 (1994) 191–202.

[54] D. Feron, J.-M. Olive, eds., Corrosion Issues in Light Water Reactors, 1st ed., Woodhead Publishing Limited, 2007.

[55] T. Terachi, K. Fujii, K. Arioka, Microstructural characterization of SCC crack tip and oxide film for SUS 316 stainless steel in simulated PWR primary water at 320°C, J. Nucl. Sci. Technol. 42 (2005) 225–232.

[56] Z. Lu, T. Shoji, S. Yamazaki, K. Ogawa, Characterization of microstructure, local deformation and microchemistry in Alloy 600 heat-affected zone and stress corrosion cracking in high temperature water, Corros. Sci. 58 (2012) 211–228.

[57] J. Dohr, E. Tarleton, D.E.J. Armstrong, T. Couvant, S. Lozano-perez, Recent insights in the deformation and fracture Of oxidized grain boundaries in austenitic alloys : a synergistic experimental and finite element study, in: 17th Int. Conf. Environ. Degrad. Mater. Nucl. Power Syst., 2015: pp. 1–18.

[58] R. Soulas, M. Cheynet, E. Rauch, T. Neisius, L. Legras, C. Domain, Y. Brechet, TEM investigations of the oxide layers formed on a 316L alloy in simulated PWR environment, J. Mater. Sci. 48 (2013) 2861–2871.

[59] K. Kruska, S. Lozano-Perez, D.W. Saxey, T. Terachi, T. Yamada, G.D.W. Smith, Nanoscale characterisation of grain boundary oxidation in cold-worked stainless steels, Corros. Sci. 63 (2012) 225–233.

[60] S. Cissé, L. Laffont, M.-C. Lafont, B. Tanguy, E. Andrieu, Influence of localized plasticity on oxidation behaviour of austenitic stainless steels under primary water reactor, J. Nucl. Mater. 433 (2013) 319–328.

[61] T. Terachi, K. Fujii, K. Arioka, Microstructural characterization of SCC crack tip and oxide film for SUS 316 stainless steel in simulated PWR primary water at 320°C, J. Nucl. Sci. Technol. 42 (2005) 225–232.

[62] I. Betova, M. Bojinov, P. Kinnunen, K. Lundgren, T. Saario, Mixed-conduction model for stainless steel in a high-temperature electrolyte: estimation of kinetic parameters of inner layer constituents, J. Electrochem. Soc. 155 (2008) C81–C92.

[63] K. Fukuya, H. Nishioka, K. Fujii, Y. Kitsunai, Characterization of surface oxides formed on irradiated stainless steels in simulated PWR primary water, in: Fontevraud 8, 2015: p. 28.

[64] Y. Han, J. Mei, Q. Peng, E. Han, W. Ke, Effect of electropolishing on corrosion of nuclear grade 316L stainless steel in deaerated high temperature water, Corros. Sci. 112 (2016) 625–634.

[65] S. Cissé, L. Laffont, B. Tanguy, M.-C. Lafont, E. Andrieu, Effect of surface preparation on the corrosion of austenitic stainless steel 304L in high temperature steam and simulated PWR primary water, Corros. Sci. 56 (2012) 209–216.

[66] B. Beverskog, I. Puigdomenech, Pourbaix Diagrams for the Ternary System of Iron-Chromium-Nickel, 55 (1999) 1077–1087.

[67] X. Cheng, Z. Feng, C. Li, C. Dong, X. Li, Investigation of oxide film formation on 316L stainless steel in high-temperature aqueous environments, Electrochim. Acta. 56 (2011) 5860–5865.

[68] M.B. Toloczko, M.J. Olszta, D.K. Schreiber, S.M. Bruemmer, CORROSION AND STRESS CORROSION CRACK INITIATION OF COLD-WORKED ALLOY 690 IN PWR PRIMARY WATER: M2LW-13OR0402035, 2013.

[69] M.L. Sushko, V. Alexandrov, D.K. Schreiber, K.M. Rosso, S.M. Bruemmer, Multiscale model of metal alloy oxidation at grain boundaries., J. Chem. Phys. 142 (2015) 214114.

[70] L.A. Giannuzzi, F.A. Stevie, A review of focused ion beam milling techniques for TEM specimen preparation, Micron. 30 (1999) 197–204.

[71] J. Panter, B. Viguier, J.-M. Cloué, M. Foucault, P. Combrade, E. Andrieu, Influence of oxide films on primary water stress corrosion cracking initiation of alloy 600, J. Nucl. Mater. 348 (2006) 213–221.

[72] M. Wehbi, C. Duhamel, T. Couvant, J. Crépin, GRAIN BOUNDARY OXIDATION OF NICKEL BASE WELDS 182/82 IN SIMULATED PWR PRIMARY WATER, in: 17th Int. Conf. Environ. Degrad. Mater. Nucl. Power Syst. – Water React., 2015: pp. 1–25.

[73] M. Kanzaki, Y. Masaki, T. Kudo, Effect of Cr and Ni on stress corrosion cracking susceptibility in Ni-Cr-Fe alloys under simulated pressurized water reactor primary conditions, Corrosion. 71 (2015) 1027–1035.

[74] S.Y. Persaud, J. Smith, A. Korinek, G.A. Botton, R.C. Newman, High resolution analysis of oxidation in Ni-Fe-Cr alloys after exposure to 315 ◦ C deaerated water with added hydrogen, Corros. Sci. 106 (2016) 236–248.

[75] S. Lozano-Perez, K. Kruska, I. Iyengar, T. Terachi, T. Yamada, The role of cold work and applied stress on surface oxidation of 304 stainless steel, Corros. Sci. 56 (2012) 78–85.

[76] D.D. Macdonald, The history of the Point Defect Model for the passive state: A brief review of film growth aspects, Electrochim. Acta. 56 (2011) 1761–1772.

[77] N. Cabrera, N.F. Mott, Theory of the oxidation of metals, Reports Prog. Phys. 12 (1949) 163–184.

[78] A. Seyeux, V. Maurice, P. Marcus, Oxide film growth kinetics on metals and alloys: I. Physical model, J. Electrochem. Soc. 160 (2013) C189–C196.

[79] C.A. Olsson, D. Landolt, Passive films on stainless steels - chemistry, structure and growth, Electrochim. Acta. 48 (2003) 1093–1104.

[80] J. Robertson, The Mechanism of High Temperature Aqueous Corrosion of Stainless Steels, Corros. Sci. 32 (1991) 443–465.

[81] D.D. Macdonald, Some personal adventures in passivity—A review of the point defect model for film growth, Russ. J. Electrochem. 48 (2012) 235–258.

[82] D.D. Macdonald, Passivity - the key to our metals-based civilization, Pure Appl. Chem. 71 (1999) 951–978.

[83] L. Zhang, On the Kinetics of Growth of Anodic Oxide Films, J. Electrochem. Soc. 145 (1998) 898.

[84] D.D. Macdonald, M. Al Rifaie, G.R. Engelhardt, New rate laws for the growth and reduction of passive films, J. Electrochem. Soc. 148 (2001) B343–B347.

[85] S. Penttilä, I. Betova, M. Bojinov, P. Kinnunen, A. Toivonen, Estimation of kinetic parameters of the corrosion layer constituents on steels in supercritical water coolant conditions, Corros. Sci. 53 (2011) 4193–4203.

[86] F. Mao, C. Dong, D.D. Macdonald, Effect of octadecylamine on the corrosion behavior of Type 316SS in acetate buffer, Corros. Sci. 98 (2015) 192–200.

[87] L. Marchetti, S. Perrin, F. Jambon, M. Pijolat, Corrosion of nickel-base alloys in primary medium of pressurized water reactors: New insights on the oxide growth mechanisms and kinetic modelling, Corros. Sci. 102 (2016) 24–35.

[88] D.D. Macdonald, Passivity: enabler of our metals based civilisation, Corros. Eng. Sci. Technol. 49 (2014) 143–155.

[89] M. Bojinov, P. Kinnunen, K. Lundgren, G. Wikmark, A Mixed-Conduction Model for the Oxidation of Stainless Steel in a High-Temperature Electrolyte, J. Electrochem. Soc. 152 (2005) B250.

[90] S.E. Ziemniak, M. Hanson, Zinc treatment effects on corrosion behavior of 304 stainless steel in high temperature , hydrogenated water, Corros. Sci. 48 (2006) 2525–2546.

[91] A. Boumaiza, V. Ji, N. Rouag, The Nondestructive Estimation of Mechanical Properties of a Carbon Steel by X-ray Diffraction Peak Broadening, J. Test. Eval. 37 (2009) 343–346.

[92] V. Ji, Y.G. Zhang, C.Q. Chen, The non-destructive estimation of the superficial mechanical properties of components in the INCONEL 600 alloy by X-ray diffraction peak width, Surf. Coatings Technol. 130 (2000) 95–99.

[93] M.E. Fitzpatrick, A.T. Fry, P. Holdway, F.A. Kandil, J. Shackleton, L. Suominen, Determination of Residual Stresses by X-ray Diffraction - Issue 2, 2005.

[94] B. Alexandreanu, B. Capell, G.S. Was, Combined effect of special grain boundaries and grain boundary carbides on IGSCC of Ni–16Cr–9Fe–xC alloys, Mater. Sci. Eng. A. 300 (2001) 94–104.

[95] M. Shimada, H. Kokawa, Z.J. Wang, Y.S. Sato, I. Karibe, Optimization of grain boundary character distribution for intergranular corrosion resistant 304 stainless steel by twin- induced grain boundary engineering, Acta Mater. 50 (2002) 2331–2341.

[96] R.J. Young, M. V Moore, Dual Beam (FIB-SEM) Systems, in: L.A. Giannuzzi, F.A. Stevie (Eds.), Introd. to Focus. Ion Beams, Springer US, 2005: pp. 247–268.

[97] P. Russel, Historical Evolution of FIB Instrumentation and Technology, in: I. Utke, S. Moshkalev, P. Russell (Eds.), Nanofabrication Using Focus. Ion Electron Beams Princ. Appl., Oxford University Press, 2012: pp. 36–42.

[98] K. Arioka, T. Yamada, T. Terachi, G. Chiba, Cold work and temperature dependence of stress corrosion crack growth of austenitic stainless steels in hydrogenated and oxygenated high-temperature water, Corrosion. 63 (2007) 1114–1123.

[99] T. Couvant, L. Legras, F. Vaillant, J.M. Boursier, Y. Rouillon, Effect of Strain-Hardening on Stress Corrosion Cracking of AISI 304L Stainless Steel in PWR Primary Environment at 360°C, in: 12th Int. Conf. Environ. Degrad. Mater. Nucl. Power Syst. - Water React., 2005: pp. 1069–1081.

[100] D.D. Macdonald, The point defect model for the passive state, J. Electochemical Soc. 139 (1992) 3434–3449.

[101] L. Zhang, D.D. Macdonald, On the transport of point defects in passive films, Electrochim. Acta. 43 (1998) 670–691.

[102] R. Guidelli, R.G. Compton, J.M. Feliu, E. Gileadi, J. Lipkowski, W. Schmickler, S. Trasatti, Defining the transfer coefficient in electrochemistry : An assessment (IUPAC Technical Report), Pure Appl. Chem. 86 (2014) 245–258.

[103] J.E. Castle, C.R. Clayton, A High Temperature Transition in the Mechanism of Film Formation on Stainless Steel in Water, in: R.P. Frankenthal, J. Kruger (Eds.), Passiv. Met. (Proceedings Fourth Int. Symp. Passiv., Princeton, N.J: Electochemical Society, 1978: pp. 714–729.

[104] J.E. Castle, C. Clayton, The Use of X-ray Photo-Electron Spectroscopy in the Analyses of Passive Layers on Stainless Steel, Corros. Sci. 17 (1977) 7–26.

[105] R. Tapping, R.D. Davidson, E. McAlpine, D.H. Lister, THE COMPOSITION AND MORPHOLOGY OF OXIDE FILMS FORMED ON TYPE 304 STAINLESS STEEL IN LITHIATED HIGH TEMPERATURE WATER, Corros. Sci. 26 (1986) 563–576.

[106] L. Zhang, D.D. Macdonald, E. Sikora, J. Sikorat, On the Kinetics of Growth of Anodic Oxide Films, 145 (1998) 898–905.

[107] E.J.. Verwey, Electrolytic conduction of a solid insulator at high fields The formation of the anodic oxide film on aluminium, Physica. 2 (1935) 1059–1063.

[108] K.J. Vetter, F. Gorn, Kinetics of layer formation and corrosion processes of passive iron in acid solutions, Electrochim. Acta. 18 (1973) 321–326.

[109] J. Roberstson, The Mechanism of High Temperature Aqueous Corrosion of Stainless Steels, Corros. Sci. 32 (1991) 443–465.

[110] F. Yingwei, Thermal Expansion, in: T.J. Ahrens (Ed.), Miner. Phys. Crystallogr. a Handb. Phys. Constants, American Geophysical Union, Washington DC, 1995: pp. 29–44.

[111] T. Terachi, T. Yamada, T. Miyamoto, K. Arioka, SCC growth behaviors of austenitic stainless steels in simulated PWR primary water, J. Nucl. Mater. 426 (2012) 59–70.

[112] K. Arioka, T. Yamada, T. Terachi, T. Miyamoto, Dependence of stress corrosion cracking for cold-worked stainless steel on temperature and potential, and role of diffusion of vacancies at crack tips, Corrosion. 64 (2008) 691–706.

[113] M. Meisnar, A. Vilalta-clemente, M. Moody, K. Arioka, S. Lozano-perez, A mechanistic study of the temperature dependence of the stress corrosion crack growth rate in SUS316 stainless steels exposed to PWR primary water, Acta Mater. 114 (2016) 15–24.

MILL'S INSPECTION CERTIFICATE

CERTIFICATE TYPE 3.1 EN10204

JIAXING ZHONGBAO SPECIAL STEEL PIPE MANUFACTURING CO. LTD
Baibu Industrial Zone, Baibu Town, Haiyan County, Jiaxing City, Zhejiang Province, P.R. China
Tel: 0573 86779889 Fax: 0573 86770773

CERTIFICATE NO: 1009-76

PRODUCT: STAINLESS STEEL SEAMLESS PIPES
SPEC: ASME SA312-07 / ASTM A312-09
CUSTOMER: STEELMOR INDUSTRIES (PTY) LTD

S/C NO. ZD2010101 P/O NO: 2968

NO.	STEEL GRADE	HEAT NO.	BATCH NO.	SIZE (mm)	PCS	WT (kg)	CHEMICAL COMPOSITION (%)							
							C ≤ 0.035	Mn ≤ 2.00	S ≤ 0.03	P ≤ 0.045	Si ≤ 1.00	Cr 16.0~18.0	Ni 11.0~14.0	Mo 2.0~3.0
46	TP316/316L	FK0812-021	3A-060	6" SCH80S X 6000mm	5	1275.60	0.021	0.790	0.011	0.036	0.450	16.51	11.23	2.098

	MECHANICAL PROPERTIES				TECHNOLOGICAL PROPERTIES	HYDROSTATIC TEST P = 14.0mpa 5sec	SURFACE QUALITY		DIMENSION TOLERANCE	
	YIELD POINT Rp0.2≥205Mpa	TENSILE POINT Rm≥515MPa	ELONGATION A≥35%	HARNDESS HRB≤ 90	FLATTENING TEST		IN	OUT	O.D	W.T
46	325	645	56	82/84	Acceptable	Acceptable	Acceptable	Acceptable	Acceptable	Acceptable

REMARKS:
1. We hereby certify that this certificate is issued and signed by the manufacturer.
2. We hereby certify that the properties described herein meet the requirement of the above spec.
3. Material is solution treated, then pickled.
4. Solution Heat Treatment: 1050°C
5. Condition: Cold Finish / Plain End

MANAGING REPRESENTATIVE: _____

STEELMOR QUALITY CONTROL REVIEWED
SIGNATURE: _____
DATE 2010-10-13

DATE: 15 SEPTEMBER 2010

Appendix A

SCROOBY'S LABORATORY SERVICE cc

Spectrographic, Chemical and Mechanical Testing of Materials

CK 1999/047204/23
21 O'Reilly Merry St
Rynfield Benoni 1501
V.A.T Reg. No: 4390188391

TEL: (011) 425-1074 / 0116
FAX: (011) 849-3571 / 086 531 9546
CELL: 082-675-4536
CELL: 082-925-0115

P O Box 13401
Northmead
1511
www.scroobyslab.co.za

Eskom Holdings SOC Ltd
Private Bag 40175
CLEVELAND
2022
ATTENTION: Mr Mhakamuni Makamu

22 October 2013
O/N:

CERTIFICATE of ANALYSIS

REFERENCE No: **15674**

ELEMENT	Nominal Specification* AISI 316 L	Composition in Mass %
Carbon	≤ 0.03	0.017
Manganese	≤ 2.00	0.63
Sulphur	≤ 0.030	0.007
Phosphorus	≤ 0.045	0.018
Silicon	≤ 1.00	0.87
Chromium	16.0 - 18.0	16.3
Molybdenum	2.00 - 3.00	2.54
Nickel	10.00 - 14.00	13.3
Copper		0.34
Aluminium		0.101
Vanadium		0.066
Niobium		≤ 0.005
Titanium		≤ 0.005
Arsenic		≤ 0.0005
Cadmium		≤ 0.0005
Lead		≤ 0.0005
Antimony		≤ 0.0005
Tin		≤ 0.0005
Zinc		≤ 0.0005
Nitrogen		To follow
Iron		Matrix

Description of Sample's
Section as received
FKØ 812-Ø21

Method #: SLS-ICP

The results relate only to the item tested.
Original Certificate Signed A.J. Scrooby

Technical Signatory

Our SANAS accreditation demonstrates technical competency for Spectrographic, Dezincification of Brass and Tensile testing and the operation of a laboratory quality management system. All information in this document is given in good faith, but without warranty or guarantee of any kind whatsoever, whether implied or expressed. The original of this certificate is held at Scrooby's Laboratory Service cc for 5 years. This certificate may not be reproduced other than in full, without the written permission of Scrooby's Laboratory Service

SAMPLES WILL BE RETAINED FOR THREE MONTHS

END OF DOCUMENT

Appendix B **Mechanical Test Data**

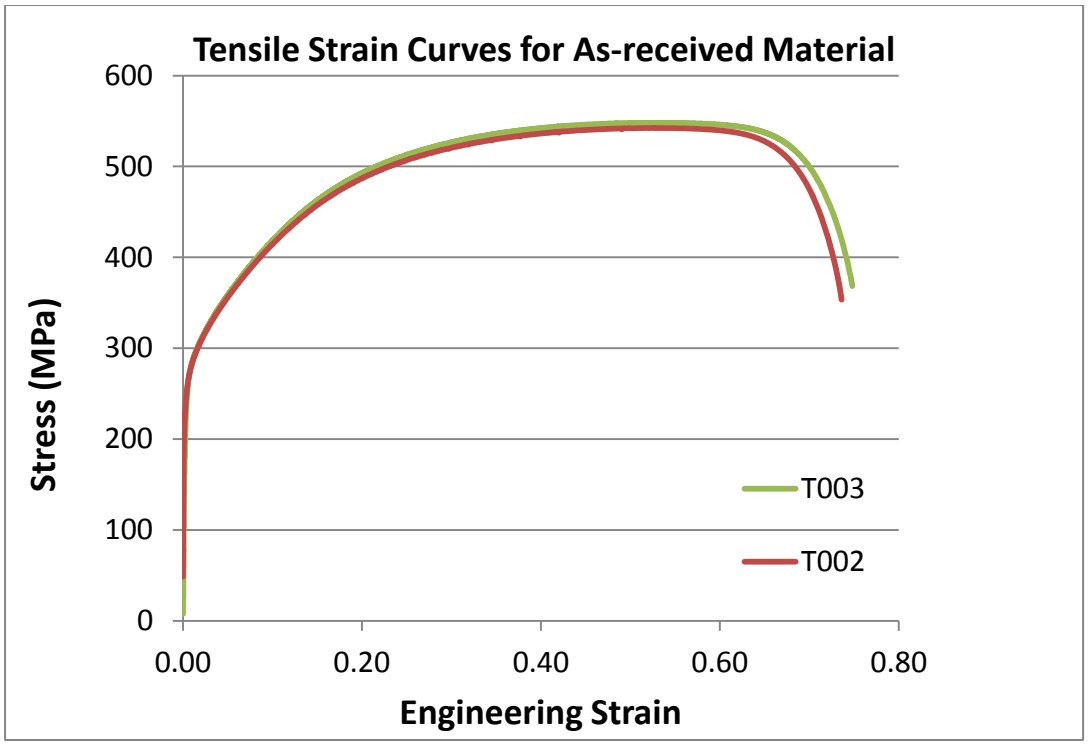

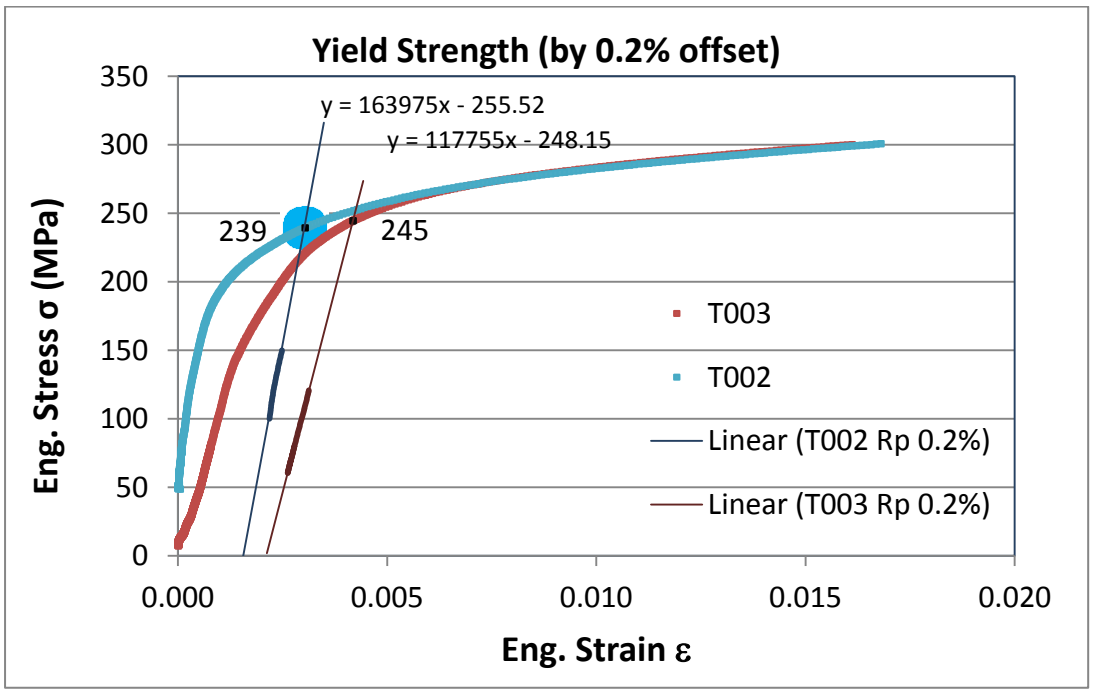

Appendix C **Autoclave Test Laboratory Reports**

This appendix contains a sample of the laboratory reports from the exposure tests conducted by the Corrosion and Electrochemistry section of Électricité de France (EDF) R&D.

Report 1:
Control samples conducted in the titanium loop (TITANE) for samples 11 & 20, exposing the sample to inert argon atmosphere and ramping up the temperature to 320°C and decreasing again to room temperature without any holding time.

Report 2:
Short duration exposures in the TITANE loop for 1 h duration for samples 12 (annealed) and 21 (20% cold rolled) at 320°C.

Report 3:
Short duration exposures in the TITANE loop for 8 h duration for samples 13 (annealed) and 22 (20% cold rolled) at 320°C. This test was originally planned for 100hr, however the test failed after 8 hours and the samples were removed.

Report 4.
Long term exposures in stainless steel autoclaves for samples 56 (annealed) and 49 (20% cold rolled). The tests were interrupted to remove other samples but in total this set of samples received a total exposure duration of 7017 h at 320°C.

Exposure duration:	0 h	1 h	8 h	7000 h
Annealed	Sample 11	Sample 12	Sample 13	Sample 56
20% Cold rolled	Sample 20	Sample 21	Sample 22	Sample 49

Report 1

	Compte rendu d'essai sur la boucle TITANE	Numéro de prestation :14EC03

EDF R&D
Département matériaux et mécaniques des composants
Groupe T29-Laboratoire Etude Corrosion

Prestation n°14EC03
Prestation Ti : 14TI03
Demandée le : 13/02/2014

RESULTATS D'EXAMENS EFFECTUES
A TITRE DE PRESTATION DE SERVICE INTERNE

Laboratoire émetteur : EC Chargé de prestation : T. GIRARD Téléphone : 57-74-18	Destinataire : T.Couvant Numéro de programme : PEX 1739 Imputation : P113L/E6

Nature de la prestation : Essai de corrosion sur la cellule d'oxydation de la boucle TITANE.

Nom du ficher d'enregistrement des paramètres pendant l'essai : Essai Thierry Couvant echantillon 13 et 22 100H

Référence de la procédure : Non référencé	Matériel utilisé : Voir page 2.

RAPPEL DE LA DEMANDE :

Objectif : Réalisation de trois essais d'oxydation brève dans la cellule d'oxydation de la boucle Titane. Les échantillons sont en acier inoxydable 316L (ESKOM).

1. Sur 4 échantillons, en milieu primaire à 320°C pour un $pH_{320°C}$=7.2 ;
2. Sur 2 échantillons uniquement la montée en température dans le gaz inerte : le mélange Crystal (essai de référence).

Echantillons :

Hypertrempés : 11, 12 et 13 ;
Laminés à 20% : 20,21 et 22.

Condition d'essais :

Les conditions chimiques pour l'essai 3 sont : 1000 ppm de Bore (soit 5636 ppm de H_3BO_3) ;
2 ppm de Lithium ;
320°C ;
30 CC/Kg d'hydrogène.

Les conditions chimiques pour l'essai 3 sont : Mélange Crystal 95% Ar, 5% H_2;
320°C

Durées d'essai :

Essai	Echantillons	Milieu	Durée
1	11 et 20	Inerte	2 min
2	12 et 21	Primaire	60 min
3	13 et 22	Primaire	6000 min

CONDITIONS DE MESURES :

Les paramètres enregistrés sont : Les pressions de la bâche et des autoclaves ;
Les températures de la bâche et des autoclaves ;
La teneur en hydrogène.

RESULTATS de l'essai 3 :

Les échantillons ont été remis à Thierry en fin d'essai.

Suite à des travaux sur le circuit d'air comprimé les vannes pneumatiques de la cellule d'oxydation se sont refermées 5h40 après le début d'essai. Ce qui a eu pour conséquence d'arrêter le renouvellement du milieu dans la cellule et de couper la chauffe sur la cellule.

Page 1 sur 6

EDF	**Compte rendu d'essai sur la boucle TITANE**	Numéro de prestation : 14EC03

1. Matériels utilisés.

Boucle TITANE	Autoclave ☐	Cellule d'oxydation ☒
Analyseur :		
Oxygène	Sonde:	/
	Membrane :	29552
	Enregistreur :	Model 3600
Hydrogène	Sonde	/
	Membrane :	2952
	Enregistreur :	Model 3600
Conductimètre	Hors service pour cet essai	
Gaz :		
Hydrare	5% d'Hydrogène	95% d'Argon
Hydrogène	Pureté :	99.99%

EDF	Compte rendu d'essai sur la boucle TITANE	Numéro de prestation : 14EC03

2. Déroulement de l'essai.

Action menées	Date et heure	Remarques		
Remplissage de la basse pression	13/03/2014	Conductivité : HS		
Mise dans le circuit des résines échangeuses d'ions	13/03/2014	Oui ☐ Non ☒	Type de résine :	
Mise dans le circuit du catalyseur	13/03/2014	Oui ☒ Non ☐	Type de catalyseur : Résine Palladium	
Vérification de la concentration en oxygène	13/03/2014	Taux d'oxygène* : –7.78 ppb		
Remplissage de la haute pression	13/03/2014	Pression : 155.6 B	Conductivité : /	
Taux d'hydrogène avant la mise en chauffe de la boucle	13/03/2014	BP : 1.23 B	H_2 : 34.20 CC/Kg	
Démarrage de la chauffe	13/03/2014	Consigne réchauffeur : 285°C	Consigne autoclave : 325°C	
Programmation des conditions d'essai dans la cellule	13/03/2014	Temps d'essai : 60 min	Temps de balayage final : 10 min	
Mise en pression de la cellule par du gaz inerte	13/03/2014	Type de gaz Mélange Crystal H2 :5%, Ar : 95%		
Mise en chauffe de la cellule	13/03/2014	Température de consigne : 320°C		
Atteinte de la température d'essai sur la boucle	13/03/2014	Température d'essai : 320°C		
Démarrage de l'essai	13/03/2014 14H00	Basse Pression : 1.23 B	Haute Pression : 155.6 B	
		Oxygène : -7.78 ppb	Hydrogène : 34.20 CC/Kg	
		Conductivité : /		
Incident en cours d'essai	13/03/2014 14H02	Disfonctionnement à l'ouverture des vannes permettant le passage du milieu sur les échantillons. La pression actionnant les vannes n'était pas suffisante à cause de travaux sur la ligne d'air comprimé. Les vannes se sont ouvertes puis refermer avant de s'ouvrir à nouveau. Il n'y a pas d'incidence sur l'essai		
Fin d'essai	13/03/2014 15H00	Basse Pression : 1.29 B	Conductivité : /	Hydrogène : 34.40 CC/Kg
		Oxygène : -4.32 ppb		
Analyse chimique fin d'essai		Bore : 1022 ppm	Lithium : 2.05	N°presta : 14CH048

* Toute les valeurs négatives indiquées par les mesures d'oxygène le sont par un artefact de mesure du à la présence de H_2. La valeur est égale à 0 ppb.

La couleur indique un incident lors de l'essai ou de ca préparation.

EDF	Compte rendu d'essai sur la boucle TITANE	Numéro de prestation : 14EC03

3. Courbes de suivis d'essai tiré de l'enregistrement Essai Thierry Couvant échantillon 12 et 21 1H

a) Courbe de l'hydrogène en fonction du temps.

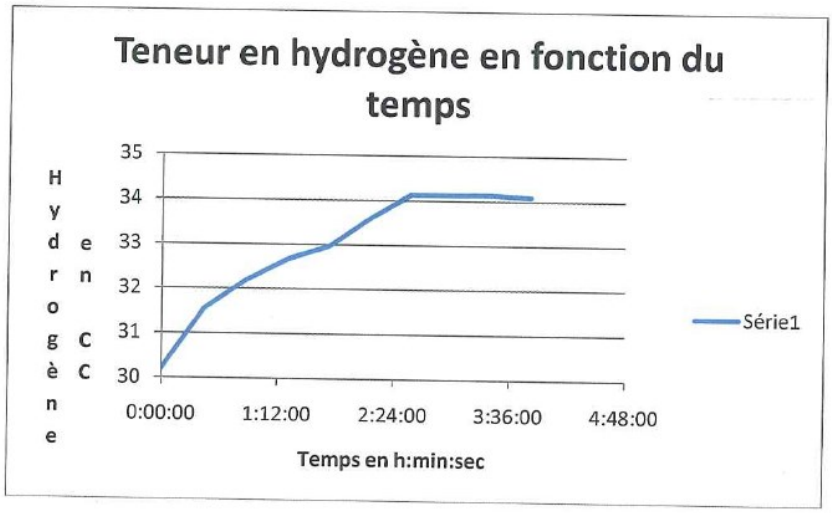

b) Courbe des pressions en fonction du temps.

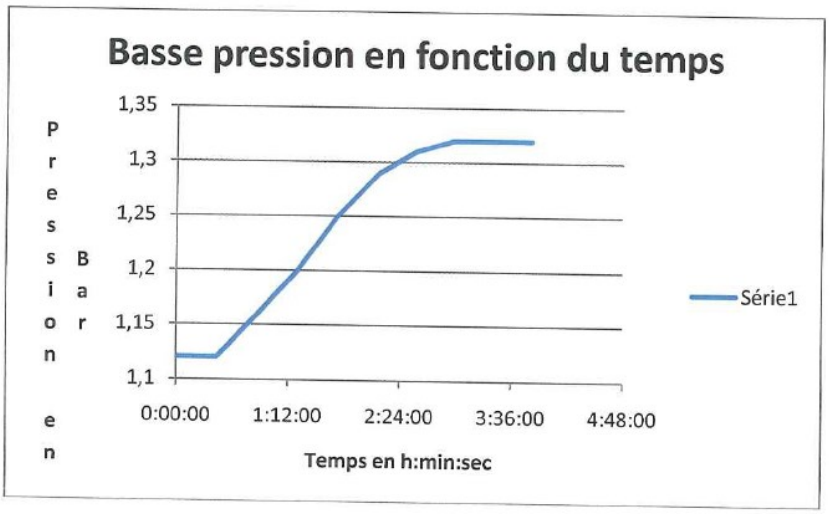

4. Analyses chimiques

a) Début d'essai

N°Presta:	14CH042
Date de prélèvement:	**06/03/2014**
Intérêt du prélèvement:	Vérification milieu fin d'essai de Svetlana en 8 minutes et début Thierry 1H
Passage sur les résines:	NON
Passage sur les palladiums:	OUI
Niveau de prélèvement	Bâche BP

A titre indicatif

Eléments	Concentration (ppm)
B	962
Li	2,02
Cl	<0,02
SO4	<0,02
Fe	<0,01
Ti	<0,01
Cr	<0,01
Ni	<0,01
Pd	<0,01
Si	0,04
Zn	<0,01
Mn	<0,01
F	<0,02
NO3	<0,02
Al,Ca,Co,Cu,Mg,Mo,Na et P	<0,01
K	0,07

	Compte rendu d'essai sur la boucle TITANE	Numéro de prestation : 14EC03

b) Fin d'essai

N°Presta:	14CH048
Date de prélèvement:	**14/03/2014**
Intérêt du prélèvement:	Fin d'essai échantillons 12 et 21 et début d'essai échantillon 13 et 22 PEX 1739
Passage sur les résines:	NON
Passage sur les palladiums:	OUI
Niveau de prélèvement	Bâche BP

A titre indicatif

Eléments	Concentration (ppm)
B	1022
Li	2,05
Cl	<0,02
SO4	<0,02
Fe	<0,01
Ti	<0,01
Cr	<0,01
Ni	<0,01
Pd	<0,01
Si	0,05
Zn	<0,01
Mn	<0,01
F	<0,02
NO3	<0,02
Al, Ca, Co, Cu, Mg, Mo, Na et P	<0,01
K	0,11

5. Observations sur les échantillons.

Echantillons remis au demandeur en fin d'essai. Les examens seront réalisés par le demandeur.

Le 09/12/2014

Signature de l'émetteur	Signature du responsable de laboratoire
T. Girard	A. Lina

Report 2

EDF	**Compte rendu d'essai sur la boucle TITANE**	**Numéro de prestation : 14EC03**

EDF R&D
Département matériaux et mécaniques des composants
Groupe T29-Laboratoire Etude Corrosion

Prestation n°14EC03
Prestation Ti : 14TI02
Demandée le : 14/02/2014

RESULTATS D'EXAMENS EFFECTUES
A TITRE DE PRESTATION DE SERVICE INTERNE

Laboratoire émetteur : EC Chargé de prestation : T. GIRARD Téléphone : 57-74-18	Destinataire : T.Couvant Numéro de programme : PEX 1739 Imputation : P113L/E6

Nature de la prestation : Essai de corrosion sur la cellule d'oxydation de la boucle TITANE.

Nom du ficher d'enregistrement des paramètres pendant l'essai : Essai Thierry Couvant échantillon 12 et 21 1H

Référence de la procédure : Non référencé	Matériel utilisé : Voir page 2.

RAPPEL DE LA DEMANDE :

Objectif : Réalisation de trois essais d'oxydation brève dans la cellule d'oxydation de la boucle Titane. Les échantillons sont en acier inoxydable 316L (ESKOM).

1. Sur 4 échantillons, en milieu primaire à 320°C pour un $pH_{320°C}$=7.2 ;
2. Sur 2 échantillons uniquement la montée en température dans le gaz inerte : le mélange Crystal (essai de référence).

Echantillons :

Hypertrempés : 11, 12 et 13 ;
Laminés à 20% : 20,21 et 22.

Condition d'essais :

Les conditions chimiques pour l'essai 2 sont : 1000 ppm de Bore (soit 5636 ppm de H_3BO_3) ;
2 ppm de Lithium ;
320°C ;
30 CC/Kg d'hydrogène.

Les conditions chimiques pour l'essai 2 sont : Mélange Crystal 95% Ar, 5% H_2 ;
320°C

Durées d'essai :

Essai	Echantillons	Milieu	Durée
1	11 et 20	Inerte	2 min
2	12 et 21	Primaire	60 min
3	13 et 22	Primaire	6000 min

CONDITIONS DE MESURES :

Les paramètres enregistrés sont : Les pressions de la bâche et des autoclaves ;
Les températures de la bâche et des autoclaves ;
La teneur en hydrogène.

RESULTATS de l'essai 2 :

Les échantillons ont été remis à Thierry en fin d'essai. Un disfonctionnement d'ouverture de vannes a eu lieu pendant l'essai, sans conséquence sur l'essai.

EDF	**Compte rendu d'essai sur la boucle TITANE**	**Numéro de prestation : 14EC03**

1. Matériels utilisés.

Boucle TITANE	Autoclave ☐	Cellule d'oxydation ☒
Analyseur :		
Oxygène	Sonde:	/
	Membrane :	29552
	Enregistreur :	Model 3600
Hydrogène	Sonde	/
	Membrane :	2952
	Enregistreur :	Model 3600
Conductimètre	Hors service pour cet essai	
Gaz :		
Hydrare	5% d'Hydrogène	95% d'Argon
Hydrogène	Pureté :	99.99%

EDF	Compte rendu d'essai sur la boucle TITANE	Numéro de prestation : 14EC03

2. Déroulement de l'essai.

Action menées	Date et heure	Remarques		
Remplissage de la basse pression	13/03/2014	Conductivité : HS		
Mise dans le circuit des résines échangeuses d'ions	13/03/2014	Oui ☐ Non ☒	Type de résine :	
Mise dans le circuit du catalyseur	13/03/2014	Oui ☒ Non ☐	Type de catalyseur : Résine Palladium	
Vérification de la concentration en oxygène	13/03/2014	Taux d'oxygène* : --7.78 ppb		
Remplissage de la haute pression	13/03/2014	Pression : 155.6 B	Conductivité : /	
Taux d'hydrogène avant la mise en chauffe de la boucle	13/03/2014	BP : 1.23 B	H_2 : 34.20 CC/Kg	
Démarrage de la chauffe	13/03/2014	Consigne réchauffeur : 285°C	Consigne autoclave : 325°C	
Programmation des conditions d'essai dans la cellule	13/03/2014	Temps d'essai : 60 min	Temps de balayage final : 10 min	
Mise en pression de la cellule par du gaz inerte	13/03/2014	Type de gaz Mélange Crystal H2 :5%, Ar : 95%		
Mise en chauffe de la cellule	13/03/2014	Température de consigne : 320°C		
Atteinte de la température d'essai sur la boucle	13/03/2014	Température d'essai : 320°C		
Démarrage de l'essai	13/03/2014 14H00	Basse Pression : 1.23 B	Haute Pression : 155.6 B	
		Oxygène : -7.78 ppb	Hydrogène : 34.20 CC/Kg	
		Conductivité : /		
Incident en cours d'essai	13/03/2014 14H02	Disfonctionnement à l'ouverture des vannes permettant le passage du milieu sur les échantillons. La pression actionnant les vannes n'était pas suffisante à cause de travaux sur la ligne d'air comprimé. Les vannes se sont ouvertes puis refermer avant de s'ouvrir à nouveau. Il n'y a pas d'incidence sur l'essai		
Fin d'essai	13/03/2014 15H00	Basse Pression : 1.29 B	Conductivité : /	Hydrogène : 34.40 CC/Kg
		Oxygène : -4.32 ppb		
Analyse chimique fin d'essai		Bore : 1022 ppm	Lithium : 2.05	N°presta : 14CH048

* Toute les valeurs négatives indiquées par les mesures d'oxygène le sont par un artefact de mesure du à la présence de H_2. La valeur est égale à 0 ppb.

☐ La couleur indique un incident lors de l'essai ou de ca préparation.

EDF	Compte rendu d'essai sur la boucle TITANE	Numéro de prestation : 14EC03

3. Courbes de suivis d'essai tiré de l'enregistrement Essai Thierry Couvant échantillon 12 et 21 1H

a) Courbe de l'hydrogène en fonction du temps.

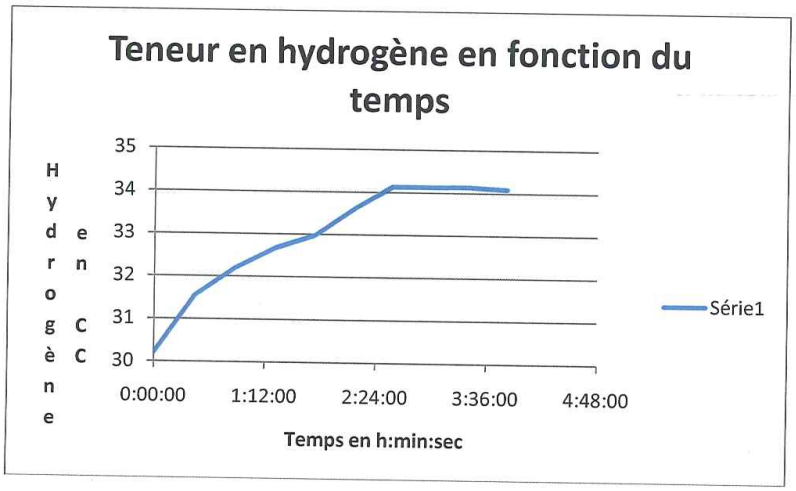

b) Courbe des pressions en fonction du temps.

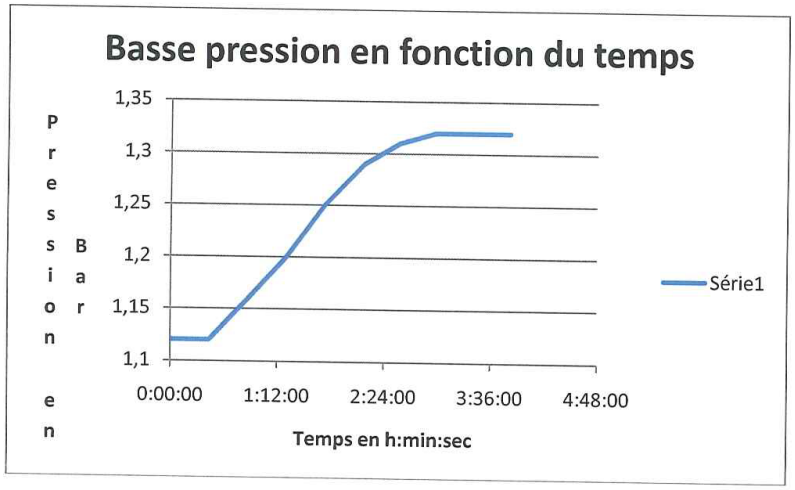

4. Analyses chimiques

a) Début d'essai

N°Presta:	14CH042
Date de prélèvement:	**06/03/2014**
Intérêt du prélèvement:	Vérification milieu fin d'essai de Svetlana en 8 minutes et début Thierry 1H
Passage sur les résines:	NON
Passage sur les palladiums:	OUI
Niveau de prélèvement	Bâche BP

A titre indicatif

Eléments	Concentration (ppm)
B	962
Li	2,02
Cl	<0,02
SO4	<0,02
Fe	<0,01
Ti	<0,01
Cr	<0,01
Ni	<0,01
Pd	<0,01
Si	0,04
Zn	<0,01
Mn	<0,01
F	<0,02
NO3	<0,02
Al,Ca,Co,Cu,Mg,Mo,Na et P	<0,01
K	0,07

EDF	Compte rendu d'essai sur la boucle TITANE	Numéro de prestation : 14EC03

b) Fin d'essai

N°Presta:	14CH048
Date de prélèvement:	**14/03/2014**
Intérêt du prélèvement:	Fin d'essai échantillons 12 et 21 et début d'essai échantillon 13 et 22 PEX 1739
Passage sur les résines:	NON
Passage sur les palladiums:	OUI
Niveau de prélèvement	Bâche BP

Eléments	Concentration (ppm)
B	1022
Li	2,05
Cl	<0,02
SO4	<0,02
Fe	<0,01
Ti	<0,01
Cr	<0,01
Ni	<0,01
Pd	<0,01
Si	0,05
Zn	<0,01
Mn	<0,01
F	<0,02
NO3	<0,02
Al, Ca, Co, Cu, Mg, Mo, Na et P	<0,01
K	0,11

A titre indicatif

EDF	Compte rendu d'essai sur la boucle TITANE	Numéro de prestation : 14EC03

5. Observations sur les échantillons.

Echantillons remis au demandeur en fin d'essai. Les examens seront réalisés par le demandeur.

Le 09/12/2014

Signature de l'émetteur	Signature du responsable de laboratoire
T. Girard	A. Lina

Report 3

EDF	**Compte rendu d'essai sur la boucle TITANE**	**Numéro de prestation :14EC03**

EDF R&D
Département matériaux et mécaniques des composants
Groupe T29-Laboratoire Etude Corrosion

Prestation n°14EC03
Prestation Ti : 14TI03
Demandée le : 13/02/2014

RESULTATS D'EXAMENS EFFECTUES
A TITRE DE PRESTATION DE SERVICE INTERNE

Laboratoire émetteur : EC Chargé de prestation : T. GIRARD Téléphone : 57-74-18	Destinataire : T.Couvant Numéro de programme : PEX 1739 Imputation : P113L/E6

Nature de la prestation : Essai de corrosion sur la cellule d'oxydation de la boucle TITANE.

Nom du ficher d'enregistrement des paramètres pendant l'essai : Essai Thierry Couvant echantillon 13 et 22 100H

Référence de la procédure : Non référencé	Matériel utilisé : Voir page 2.

RAPPEL DE LA DEMANDE :

Objectif : Réalisation de trois essais d'oxydation brève dans la cellule d'oxydation de la boucle Titane. Les échantillons sont en acier inoxydable 316L (ESKOM).

1. Sur 4 échantillons, en milieu primaire à 320°C pour un $pH_{320°C}$=7.2 ;
2. Sur 2 échantillons uniquement la montée en température dans le gaz inerte : le mélange Crystal (essai de référence).

Echantillons :

Hypertrempés : 11, 12 et 13 ;
Laminés à 20% : 20,21 et 22.

Condition d'essais :

Les conditions chimiques pour l'essai 3 sont : 1000 ppm de Bore (soit 5636 ppm de H_3BO_3) ;
2 ppm de Lithium ;
320°C ;
30 CC/Kg d'hydrogène.

Les conditions chimiques pour l'essai 3 sont : Mélange Crystal 95% Ar, 5% H_2;
320°C

Durées d'essai :

Essai	Echantillons	Milieu	Durée
1	11 et 20	Inerte	2 min
2	12 et 21	Primaire	60 min
3	13 et 22	Primaire	6000 min

CONDITIONS DE MESURES :

Les paramètres enregistrés sont : Les pressions de la bâche et des autoclaves ;
Les températures de la bâche et des autoclaves ;
La teneur en hydrogène.

RESULTATS de l'essai 3 :

Les échantillons ont été remis à Thierry en fin d'essai.

Suite à des travaux sur le circuit d'air comprimé les vannes pneumatiques de la cellule d'oxydation se sont refermées 5h40 après le début d'essai. Ce qui a eu pour conséquence d'arrêter le renouvellement du milieu dans la cellule et de couper la chauffe sur la cellule.

Page 1 sur 6

EDF	**Compte rendu d'essai sur la boucle TITANE**	**Numéro de prestation :14EC03**

1. Matériels utilisés.

Boucle TITANE	Autoclave ☐	Cellule d'oxydation ☒
Analyseur :		
Oxygène	Sonde:	/
	Membrane :	29552
	Enregistreur :	Model 3600
Hydrogène	Sonde	/
	Membrane :	2952
	Enregistreur :	Model 3600
Conductimètre	Hors service pour cet essai	
Gaz :		
Hydrare	5% d'Hydrogène	95% d'Argon
Hydrogène	Pureté :	99.99%

EDF	**Compte rendu d'essai sur la boucle TITANE**	**Numéro de prestation :14EC03**

2. Déroulement de l'essai.

Action menées	Date et heure	Remarques		
Préparation du milieu primaire	14/03/2014	Bore 1022 ppm	Lithium : 2.05 ppm	Numéro de presta : 14CH048
		Localisation du prélèvement : Au niveau de la bâche		
Remplissage de la basse pression	20/02/2014	Conductivité : HS		
Mise dans le circuit des résines échangeuses d'ions		Oui ☐ Non ☒	Type de résine :	
Mise dans le circuit du catalyseur		Oui ☒ Non ☐	Type de catalyseur :	
Vérification de la conductivité		Conductivité : H.S		
Désoxygénation de la basse pression à l'argon	06/03/2014	Temps de bullage:/		
Remplissage de la haute pression	20/02/2014	Pression : /	Conductivité : /	
Désoxygénation de l'ensemble de la boucle à l'argon	06/03/2014	Temps de bullage : /		
Introduction de l'hydrogène	06/03/2014	Temps de bullage : /		
Taux d'hydrogène avant la mise en chauffe de la boucle	14/03/2014	BP : 1.09b	H_2 : 31.91 CC	O_2 : -7.99 ppb
Mise sous pression de la boucle	14/03/2014	HP : 155 b		
Démarrage de la chauffe	14/03/2014	Consigne réchauffeur : 180°C	Consigne autoclave : 320°C	
Programmation des conditions d'essai dans la cellule	14/03/2014	Durée essai : 100H	Durée balayage Argon fin d'essai 5min	
Balayage de la cellule d'oxydation par de l'argon	14/03/2014	Temps de balayage : /		
Mise en pression de la cellule par du gaz inerte	14/03/2014	Type de gaz Hydrare Melange Crystal H2 :5%, Ar : 95%		
		Pression de la cellule : /		
Mise en chauffe de la cellule	14/03/2014	Température de consigne : 320°C		
Atteinte de la température d'essai sur la boucle	14/03/2014	Température d'essai : 320°C		
Démarrage de l'acquisition	14/03/2014	Nom : Essai Thierry Couvant échantillon 13 et 22 100H		
Démarrage de l'essai	14/03/2014 12h05	Basse Pression : 1.21 B	Haute Pression : /	
		Oxygène : -9.71 ppb	Hydrogène : 32.02 CC	
		Conductivité : H.S		
Incident en cours d'essai	14/03/2014 12h05	Disfonctionnement à l'ouverture des vannes permettant le passage du milieu sur les échantillons. La pression actionnant les vannes n'était pas suffisante à cause de travaux sur la ligne d'air comprimé. Les vannes se sont ouvertes puis refermer avant de s'ouvrir à nouveau dans un laps de temps très court.		
Incident en cours d'essai	14/03/2014 17h45	Les vannes de la cellule d'oxydation se ferment par manque d'air comprimé arrêtant la circulation du fluide. La chauffe dans la cellule est arrêtée par l'automate qui à détecter une anomalie.		

* Toute les valeurs négatives indiquées par les mesures d'oxygène le sont par un artefact de mesure (à cause de l'hydrogène). La valeur est égale à 0 ppb.

La couleur indique un incident lors de l'essai ou de ca préparation.

3. Courbes de suivis d'essai tiré de l'enregistrement

a) Courbe de l'hydrogène en fonction du temps.

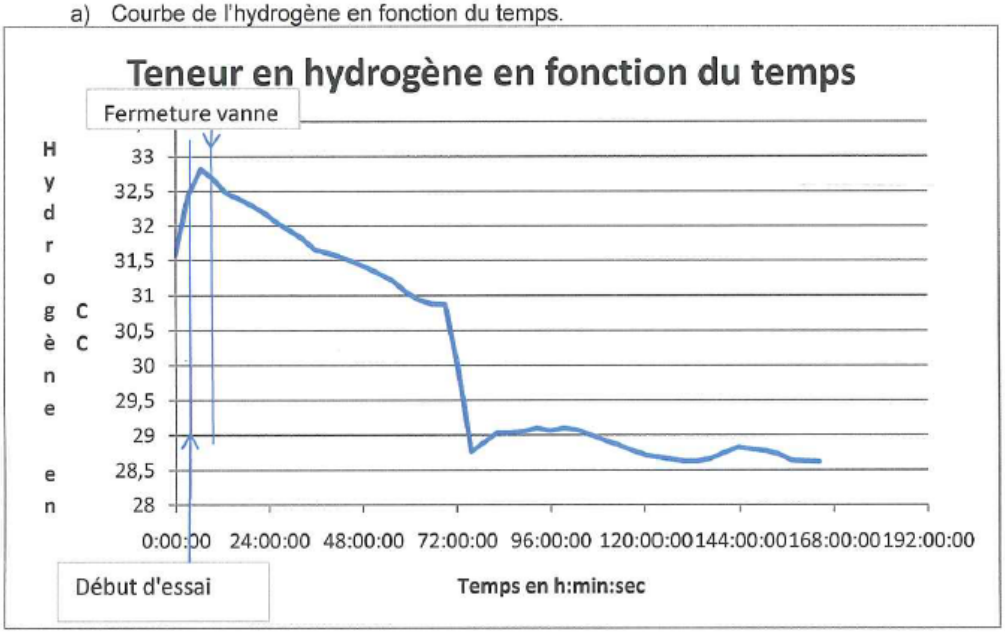

EDF	Compte rendu d'essai sur la boucle TITANE	Numéro de prestation :14EC03

4. Analyses chimiques

N°Presta:	14CH048
Date de prélèvement:	**14/03/2014**
Intérêt du prélèvement:	Fin d'essai échantillons 12 et 21 et début d'essai échantillon 13 et 22 PEX 1739
Passage sur les résines:	NON
Passage sur les palladium:	OUI
Niveau de prélèvement	Bache BP

A titre indicatif

Eléments	Concentration (ppm)
B	1022
Li	2,05
Cl	<0,02
SO4	<0,02
Fe	<0,01
Ti	<0,01
Cr	<0,01
Ni	<0,01
Pd	<0,01
Si	0,05
Zn	<0,01
Mn	<0,01
F	<0,02
NO3	<0,02
Al,Ca,Co,Cu,Mg,Mo,Na et P	<0,01
K	0,11

EDF	**Compte rendu d'essai sur la boucle TITANE**	**Numéro de prestation :14EC03**

5. Observations sur les échantillons.

Echantillons remis au demandeur en fin d'essai. Les examens seront réalisés par le demandeur.

Le 09/12/2014

Signature de l'émetteur	Signature du responsable de laboratoire
T. Girard	A. Lina

Report 4

DEPARTEMENT ETUDES DES MATERIAUX **RESULTATS D'ESSAIS OU D'EXAMENS** EFFECTUES A TITRE DE PRESTATION DE SERVICE	**N° de la prestation :** **LMC-16-090** **Demandée le 08/07/2016**
Labo expéditeur : **T29 /S.VIOLIER**	Destinataire : T.COUVANT
Numéro programme d'étude : Pex : 1883	Imputation : E961/P113L/E0
Nuance : acier inox Repère :fourni par ESKOM Produit : -	Etat : après 5007h essai CSC Sens de prélèvement : -

RESULTAT D'ESSAI DE CORROSION EN MILIEU PRIMAIRE EN BOUCLE DE CIRCULATION DE FLUIDE

BOUCLE D'ESSAI "ACACIA" : ESSAI REALISE SUIVANT LA PROCEDURE REFERENCEE HT/44/00/046/A

Autoclave A3

Conditions expérimentales

Milieu : **Primaire (B : 1000ppm, LI : 2ppm)**

Température : **320 °C**

Hydrogène : **20 cc/hg H2**

Eprouvette

Type : plaquette

Repère :

- **Inox hypertrempé : 1739-056**
- **Traction uniaxiale 20%: 1739-044**
- **Traction uniaxiale 30% : 1739-047**
- **Laminé à froid : 1739-049**

Résultat de l'essai :

Date de début d'essai : **11/07/2016**

Date de fin d'essai : **06/10/2016**

Durée effective de l'essai : **2010 heures** (7017/8000 heures total)

Autoclave utilisé : Autoclave 3 (TOP603)

Observations

Eprouvettes remises au demandeur après essai : **non**

Prélèvement de 100 cc de solution après essai : oui

Fiche d'anomalie associée : non

Date : **11/10/2016**

Visa du Chef de Laboratoire :

Visa du Technicien de Laboratoire :

c:\users\c38070\documents\etudes\cr des travaux prestations\2016\lmc-16-090.doc

Appendix D **Summary Table of Oxide Measurements**

Condition	Sample No.	Exposure (hrs)	Temp.	Sample Region	FIB grid finger	Grain Boundary	Max Surface Oxidation (nm)					Grain Boundary oxidation (nm)					GB Angle to surface
							1	2	3	Ave	Std Dev	1	2	3	Ave	Std Dev	
Annealed	11	0		COR78_40_1 region 1	C												
				COR78_40_2 region 2	E												
	12	1	320°C	COR78_29_1 Area B region 3	A	general											
						GB1	32			32.0		36			36.0		53.0
						GB2	32			32.0		35			35.0		69.5
				COR78_29_2 Area B region 1	B	GB1	38			38.0		49			49.0		63.4
						GB2						-					
	13	8	320°C	COR78_39_1 Area A region 1	B	GB1						0			0.0		
						GB2	39			39.0		76			76.0		65.1
				COR78_39_2 Area A region 2	D	GB1	74			74.0		54			54.0		43.6
						GB2	64			64.0		158			158.0		50.4
	35	100	320°C	COR78_61_1 region 1	E	GB 1	63	66	64	64.3	1.5	239	242	225	235.3	9.1	35.7
						GB 2	53	58	50	53.7	4.0	160	152	154	155.3	4.2	34.2
				COR78_61_2 region 2	D	GB 1	69	78	67	71.3	5.9	297	304	301	300.7	3.5	35.8
						GB 2	28	34	28	30.0	3.5	64	68	35	55.7	18.0	76.8
	59	1000	320°C	COR78_64_1 Region 3	A	GB 1	769	779	779	775.7	5.8	650	660	655	655.0	5.0	70.5
				COR78_64_2 Region 4	B	GB 1	138	150	144	144.0	6.0	402	429	477	436.0	38.0	36.2
						GB 2	161	167	160	162.7	3.8	242	204	210	218.7	20.4	59.4
							251										
	58	1000	290°C	COR78_68 Region 1			760	800	792	784.0	21.2	853	851	899	867.7	27.2	57.7
				COR78_68 Region 2			613	583	606	600.7	15.7	1178	1128	1091	1132.3	43.7	68.2
				COR78_68 Region 3			738	725	725	729.3	7.5	1288	1346	1334	1322.7	30.6	82.8
	60	1000	360°C	COR78_69 Region 1			159	284	237	226.7	63.1	318	292	314	308.0	14.0	60.6
				COR78_69 Region 2			301	333	309	314.3	16.7	270	284	287	280.3	9.1	88.7
				COR78_69 Region 3			212	245	230	229.0	16.5	339	251	310	300.0	44.8	53.2
	55	5000	290°C	COR78_73 Region 1		GB1	2029			2029.0		2053			2053.0		88.6
				COR78_73 Region 2		GB1	1851			1851.0		2720			2720.0		68.7

Condition	Sample No.	Exposure (hrs)	Temp.	Sample Region	FIB grid finger	Grain Boundary	Max Surface Oxidation (nm)					Grain Boundary oxidation (nm)					GB Angle to surface
							1	2	3	Ave	Std Dev	1	2	3	Ave	Std Dev	
						GB2	1322			1322.0		2070			2070.0		75.4
				COR78_73 Region 3			2435			2435.0		no GB					
				COR78_73 Region 4			1911			1911.0		no GB					
				COR78_73 Region 5			1907			1907.0		2453			2453.0		38.2
						GB1	1757			1757.0		2194			2194.0		67.9
				COR78_73 Region 6		GB2	1435			1435.0		2586			2586.0		38.3
				COR78_45 Region1			455			455.0		718			718.0		41.2
				COR78_45 Region1b			451			451.0		642			642.0		63.5
				COR78_45 Region2			616			616.0		796			796.0		42.1
	56	7000	320°C	COR78_45 Region3			553			553.0		406			406.0		59.7
				COR78_45 Region4			292			292.0		317			317.0		71.7
				COR78_45 Region5			603			603.0		572			572.0		60.8
				COR78_45 Region6			660			660.0		863			863.0		61.7
				COR78_74 Region 1		GB1	308			308.0		343			343.0		70.2
						GB2	273			273.0		379			379.0		50.8
				COR78_74 Region 2		GB1	250			250.0		123			123.0		57.5
						GB2	173			173.0		331			331.0		56.2
	57	4000	360°C	COR78_74 Region 3		GB1	313			313.0		420			420.0		42.5
						GB2	183			183.0		255			255.0		46.7
				COR78_74 Region 4		GB1	205			205.0		466			466.0		27.2
						GB2	289			289.0		313			313.0		58
20% Elong	30	100	320°C			GB 1	45	43	39	42.3	3.1	116	125	117	119.3	4.9	42.2
				COR78_62_1 region 1	A	GB 2											
						GB 1	24	29	22	25.0	3.6	40	27	40	35.7	7.5	67.7
				COR78_62_2 region 3	C	GB 2	31	29	34	31.3	2.5	137			137.0		20.3
30% Elong	25	100	320°C	COR78_60_1 region 1	B	GB1	27	31	21	26.3	5.0	69	57	72	66.0	7.9	77.4
						GB2	31	28	27	28.7	2.1	82	76	62	73.3	10.3	83.8

Condition	Sample No.	Exposure (hrs)	Temp.	Sample Region	FIB grid finger	Grain Boundary	Max Surface Oxidation (nm)					Grain Boundary oxidation (nm)					GB Angle to surface
							1	2	3	Ave	Std Dev	1	2	3	Ave	Std Dev	
				COR78_60_2 region 2	C	GB1	51	58	51	53.3	4.0	38	38	35	37.0	1.7	82.9
						GB2											
	65	1000	320°C	COR78_70 region 2			329	325	306	320.0	12.3	481	500	448	476.3	26.3	58.6
30% Elong				COR78_70 region 3			274	248	273	265.0	14.7	431	447	403	427.0	22.3	58.2
				COR78_70 region 4			330	369	340	346.3	20.3	473	490	477	480.0	8.9	63.8
				COR78_41_1 region 1	D												
	20	0		COR78_41_2 region 2	B												
				COR78_41_2 region 3	A		6	4	5	5.0							
				COR78_41_2 region 4	B		3	3	4	3.3							
	21	1	320°C	COR78_38_1 region 3	A	General											
						GB1	26			26.0		?					
						GB2	28			28.0		?					
				COR78_38_2 region 4	E	General											
						GB1						0			0.0		
						GB2						-					
				COR78_38_3 region 5	E	GB1	16			16.0		42			42.0		22.0
						GB2	17			17.0		12			12.0		61.0
20% CR				COR78_38_4 region 6	D	GB1	6.3			6.3		12			12.0		72.0
						GB2	8.3			8.3		13			13.0		64.0
	22	8	320°C	COR78_30_1 Region 3	E	Twins						0			0.0		
						GB	32			32.0		53			53.0		86.9
				COR78_30_2 Region 4	D							-					
	54	0		COR78_47_1 Region 1	A	general											
						GB						-					
				COR78_47_2 Region 2	E	general											
						GB											
		0		COR78_47_3 Region 3	A	general											
						GB											
				COR78_47_4 Region 4	B	general											
						GB											

Condition	Sample No.	Exposure (hrs)	Temp.	Sample Region	FIB grid finger	Grain Boundary	Max Surface Oxidation (nm)					Grain Boundary oxidation (nm)					GB Angle to surface
							1	2	3	Ave	Std Dev	1	2	3	Ave	Std Dev	
20% CR	39	100	320°C	COR78_63_1 region 2	B	GB 1	103	124	108	111.7	11.0	356	367	373	365.3	8.6	39.0
						GB 2	76	84	71	77.0	6.6	488			488.0		17.0
				COR78_63_2 region 4	D	GB 1	97	84	94	91.7	6.8	401			401.0		27.0
						GB 2											
	68	1000	320°C	COR78_65 region 4	SnV	GB1											
				COR78_65 region 1	B	GB 1	316	339	329	328.0	11.5	383	420	406	403.0	18.7	67.9
				COR78_65 region 2	C	GB 1	212	200	210	207.3	6.4	162	162	169	164.3	4.0	61.0
						GB 2	323	313	301	312.3	11.0	506	524	523	517.7	10.1	54.9
				COR78_65 region 3	D	GB 1	199	184	215	199.3	15.5	494	472	498	488.0	14.0	43.1
	69	1000	360°C	COR78_66 region 3	D	GB 1	316	319	288	307.7	17.1	648			648.0		23.5
				COR78_66 region 4			355	382	370	369.0	13.5	235	215	235	228.3	11.5	58.0
				COR78_66 region 5			390	426	398	404.7	18.9	434	448	443	441.7	7.1	48.9
				COR78_66 region 6			384	361	409	384.7	24.0	459	488	469	472.0	14.7	39.9
	67	1000	290°C	COR78_67 Region 1			509	592	556	552.3	41.6	1304	1486	1345	1378.3	95.5	55.7
				COR78_67 Region 2			894	892	910	898.7	9.9	1472	1455	1464	1463.7	8.5	69.6
				COR78_67 Region 3			815	768	739	774.0	38.4	992	1054	1029	1025.0	31.2	55.3
	50	5000	290°C	COR78_71 Region 1			1431			1431.0		3115			3115.0		27.7
				COR78_71 Region 2			2051			2051.0		no GB					
				COR78_71 Region 3			1697			1697.0		1654			1654.0		45.8
				COR78_71 Region 4			1776			1776.0		3544			3544.0		25.7
				COR78_71 Region 5			1849			1849.0		1922			1922.0		44.1
	49	7000	320°C	COR78_75 Region 1			365			365.0		607			607.0		35.2
				COR78_75 Region 2			481			481.0		689			689.0		32.2
				COR78_75 Region 3			358			358.0		1098			1098.0		39.3
				COR78_75 Region 4			575			575.0		-					
	51	4000	360°C	COR78_72 Region 1			186			186.0		332			332.0		71.7
				COR78_72 Region 2			218			218.0		441			441.0		79.3
				COR78_72 Region 3			151			151.0		309			309.0		72.2
				COR78_72 Region 4			256			256.0		427			427.0		62.5

Appendix E **Oxidation Measurements after 1 h Exposures**

Sample 12 – Annealed material exposed at 320°C for 1 hour.

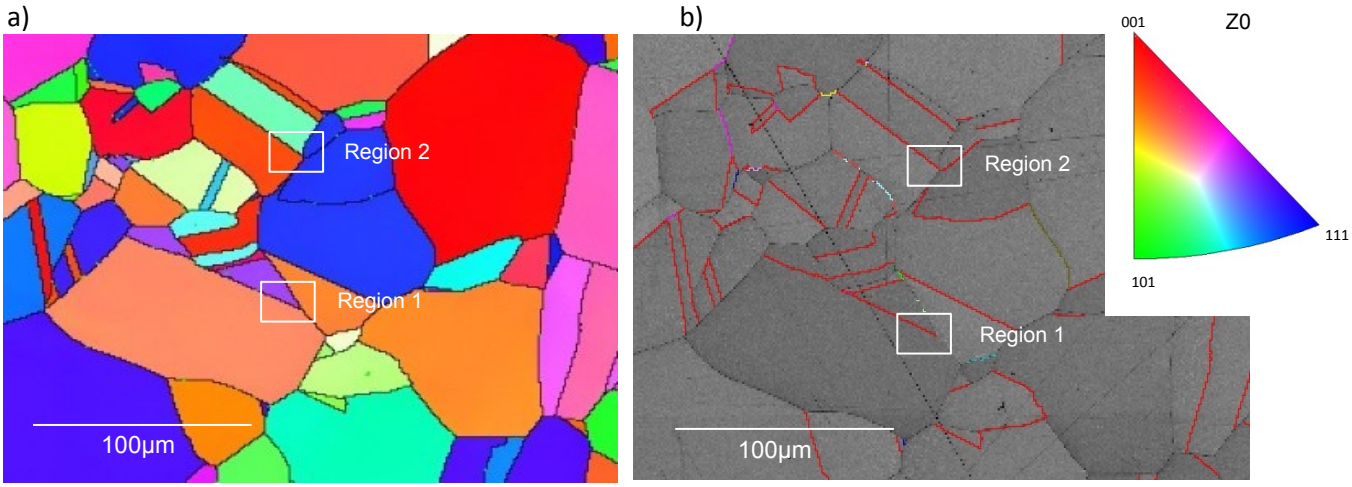

Figure 87. a) EBSD band contrast plot with coloured CSL boundaries, in particular red lines represent Σ3 boundaries, and b) a BSE image of area containing the 2 regions of interest.

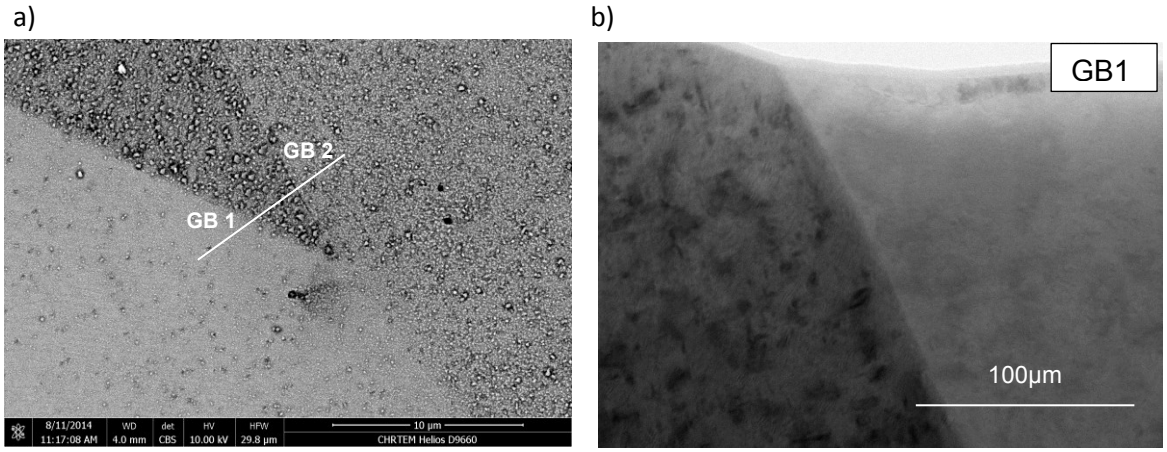

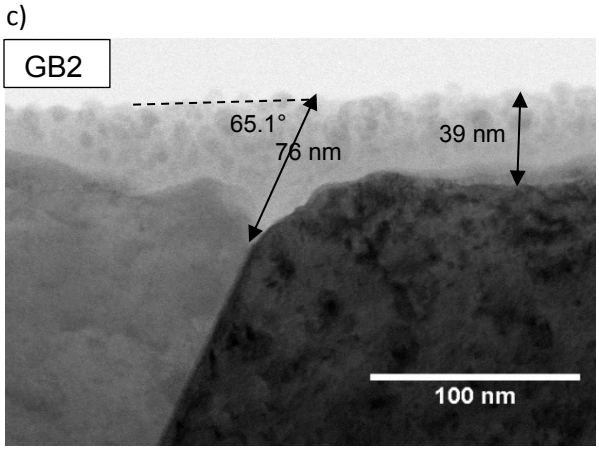

Notes:

i) The surface oxide was damaged by the FIB during preparation, however some oxide layer remained over both grain boundaries.

ii) GB1 is a Σ3 CSL boundary (see Figure 87) with no observable preferential grain boundary attack. It did not present a dark contrast in the BSE image, while GB2 had both darker BSE contrast and intergranular oxidation.

iii) The surface oxide layer of GB1 was too damaged to take a measurement.

Figure 88. Sample 12 region 1: a) BSE at 10kV of the region with the approximate location of TEM section indicated, and bright field STEM images of b) GB1 with no measurable oxide depth and c) GB2 annotated with oxide measurements.

b)

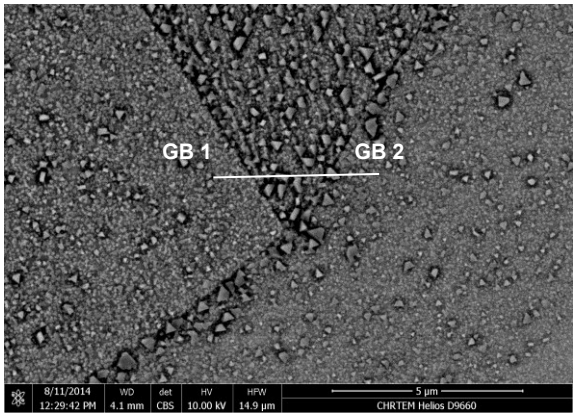

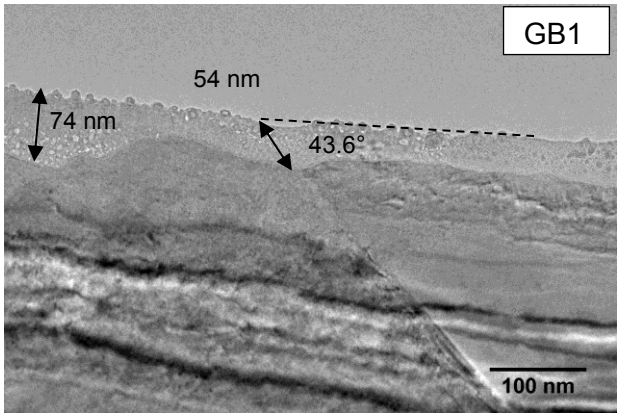

c)

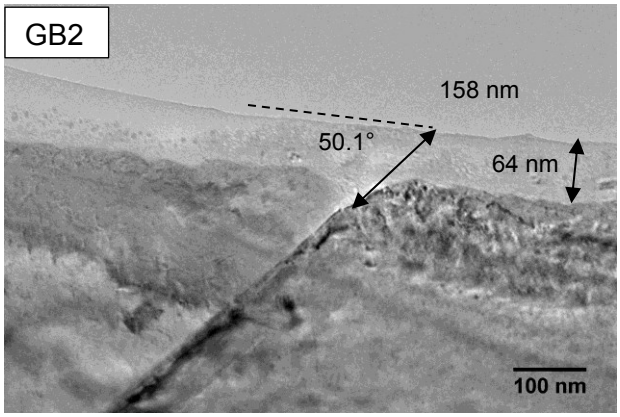

Notes:

i) The oxide of this section was damaged by the FIB that has marginally reduced the oxide thickness measurements.
ii) Both GB1 and GB2 present a dark contrast in the BSE image.
iii) GB1 is a Σ3 CSL boundary (see Figure 87), with no significant preferred intergranular oxidation, while GB2 is a random grain boundary and shows intergranular attack.

Figure 89. Sample 12 region 2: a) BSE image at 10kV of the surface grain boundaries indicating the approximate location of the TEM section that included 2 grain boundaries, and bright field TEM images of b) GB1 and c) GB2 with annotations of surface and intergranular measurements.

Sample 21 - 20% Cold rolled material exposed at 320°C for 1 hour.

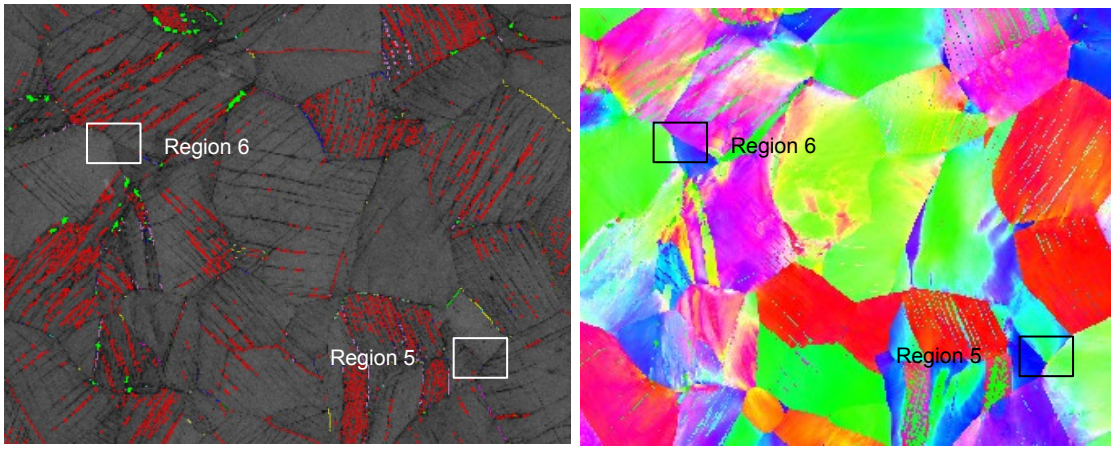

Figure 90. EBSD plots of Sample 21 with a) band contrast plotted with CSL boundaries, note that the twin deformation bands are recognised as Σ3 boundaries in red, and b) IPF colouring plotted. Locations of regions 5 & 6 are indicated.

a)

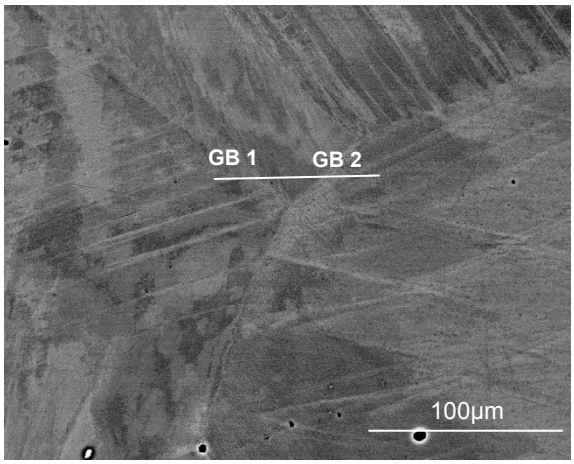

b)

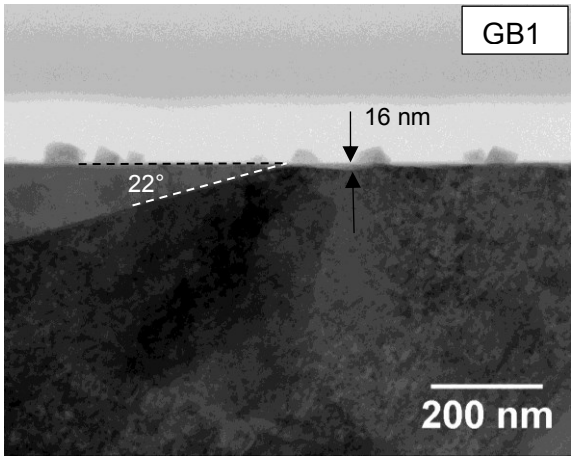

c)

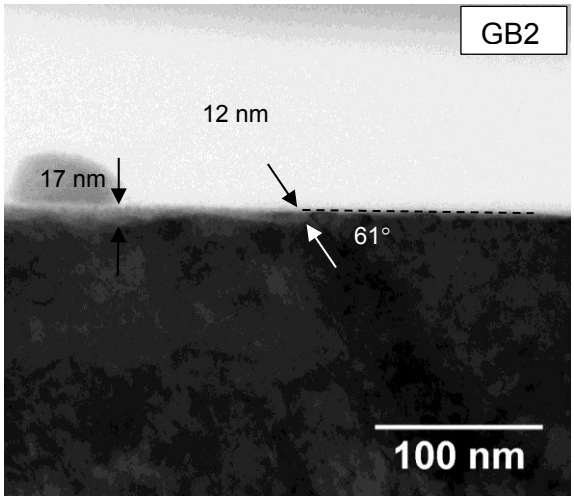

Notes:

i) GB1 was angled too acute to the surface and therefore the ntergranular oxidation of GB1 was considered.

Figure 91. Images of Sample 21 region 5 with a) BSE SEM image at 18 kV of the surface with the approximate location of the TEM section, and bright field TEM images of b) GB1 and c) GB2. The measured oxide measurements are indicated.

a)

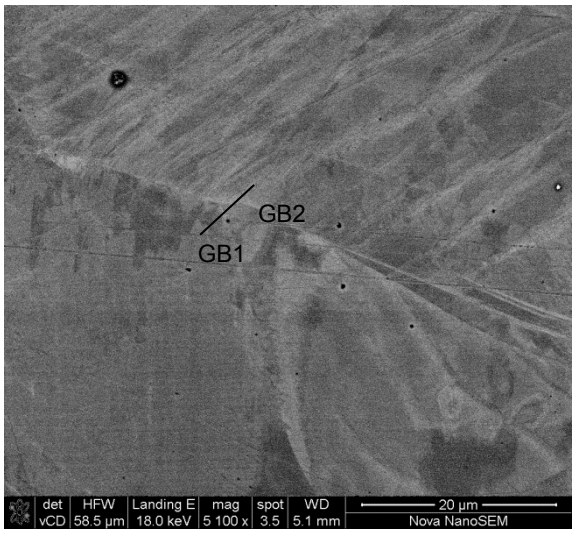

b)

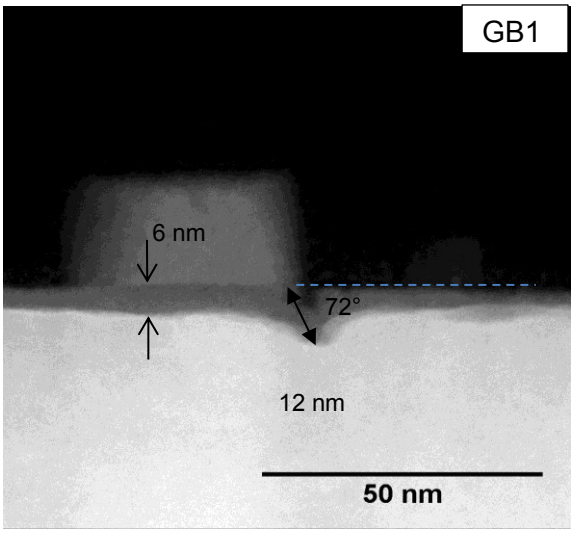

c)

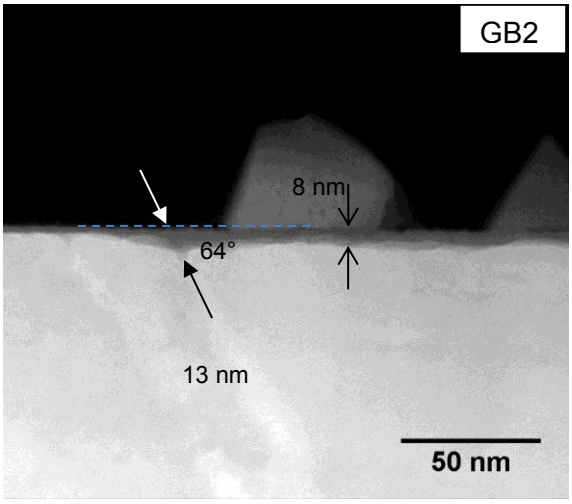

Figure 92. Sample 21 region 6 images with a) BSE image of TEM section location across 2 grain boundaries, and STEM HAADF images of b) GB1 and c) GB2, annotated with relevant measurements.

Appendix F **Oxidation Measurements from 8 h Exposures**

Sample 13 – Annealed material exposed at 320°C for 8 hour.

a) b)

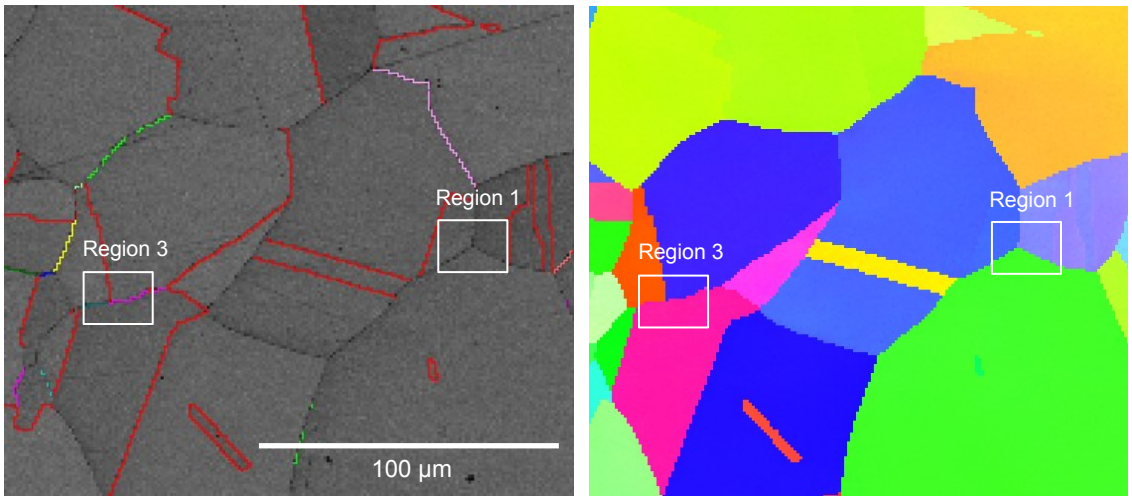

Figure 93. EBSD maps of Sample 13 with the two areas of interest highlighted, a) band contrast and CSL boundaries are mapped (Σ3 boundaries in red, Σ9 boundaries in pink), and b) a plot of the IPF colouring.

a) b)

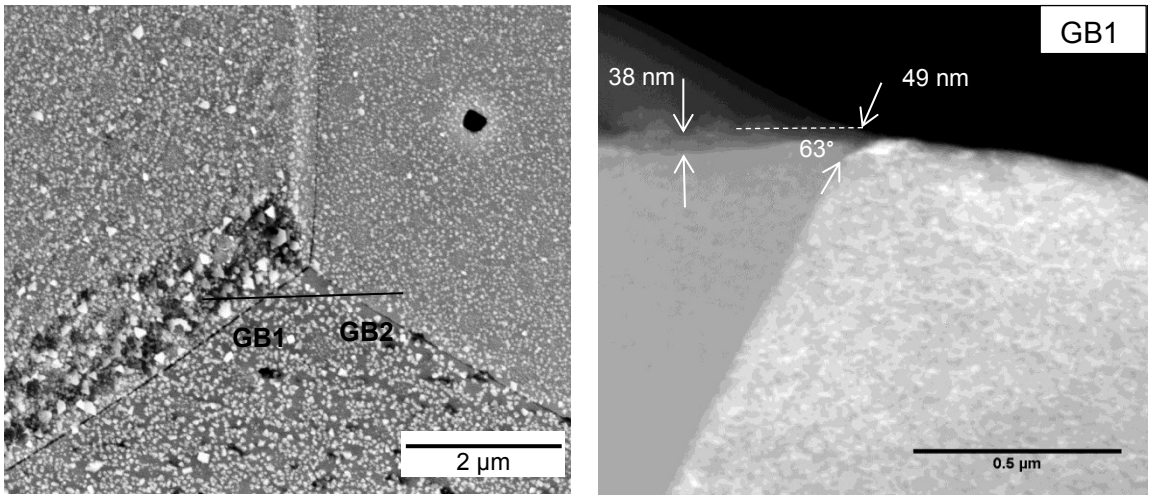

Figure 94. Sample 13 region 1 with a) a BSE image at 15 kV highlighting the location of the TEM sample that contained 2 grain boundaries, and b) DF STEM image of GB1. Note that GB2 was damaged by the FIB during sample preparation.

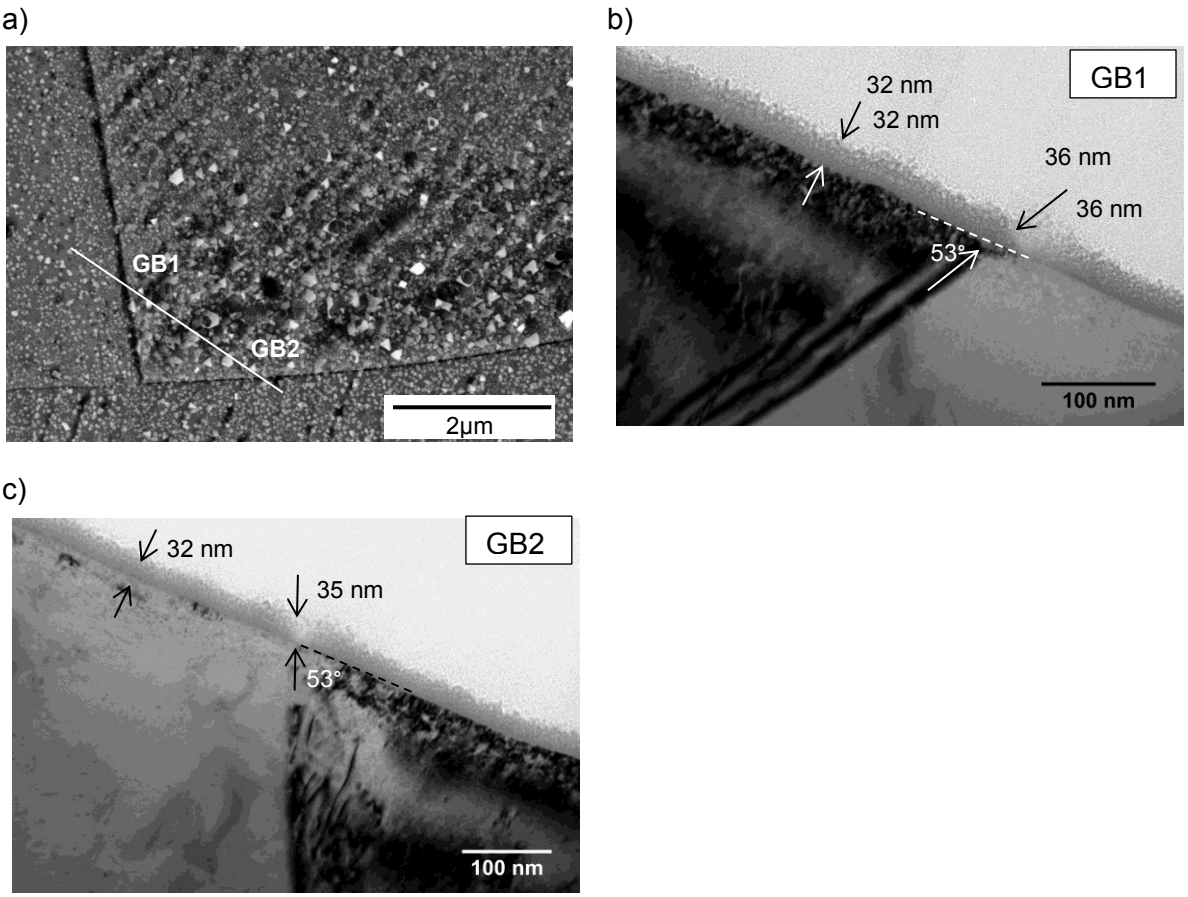

Figure 95. Sample 13 region 3 with a) BSE image at 15kV of the region showing dark grain boundary contrast, the location where the TEM cross-section was cropped from is indicated; and bright field TEM images of b) GB1 and c) GB2.

Sample 22 – 20% Cold rolled material exposed at 320°C for 8 hours.

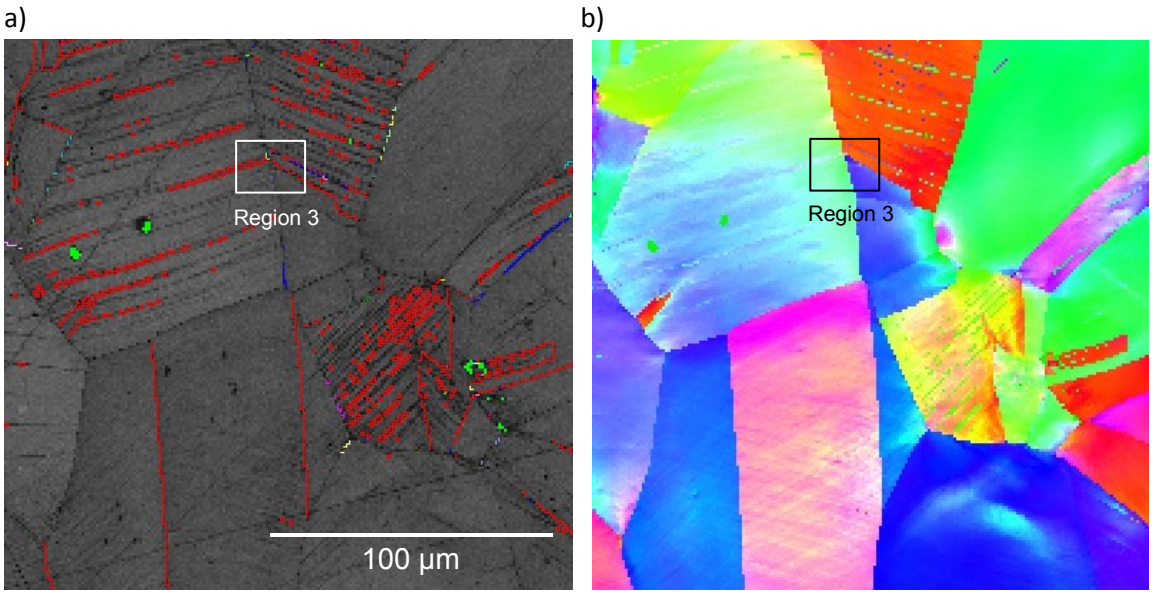

Figure 96. EBSD maps from Sample 22 with the location of region 3 indicated, a) band contrast and CSL boundaries (Σ3 boundaries in red) mapped, and b) IPF colouring mapped.

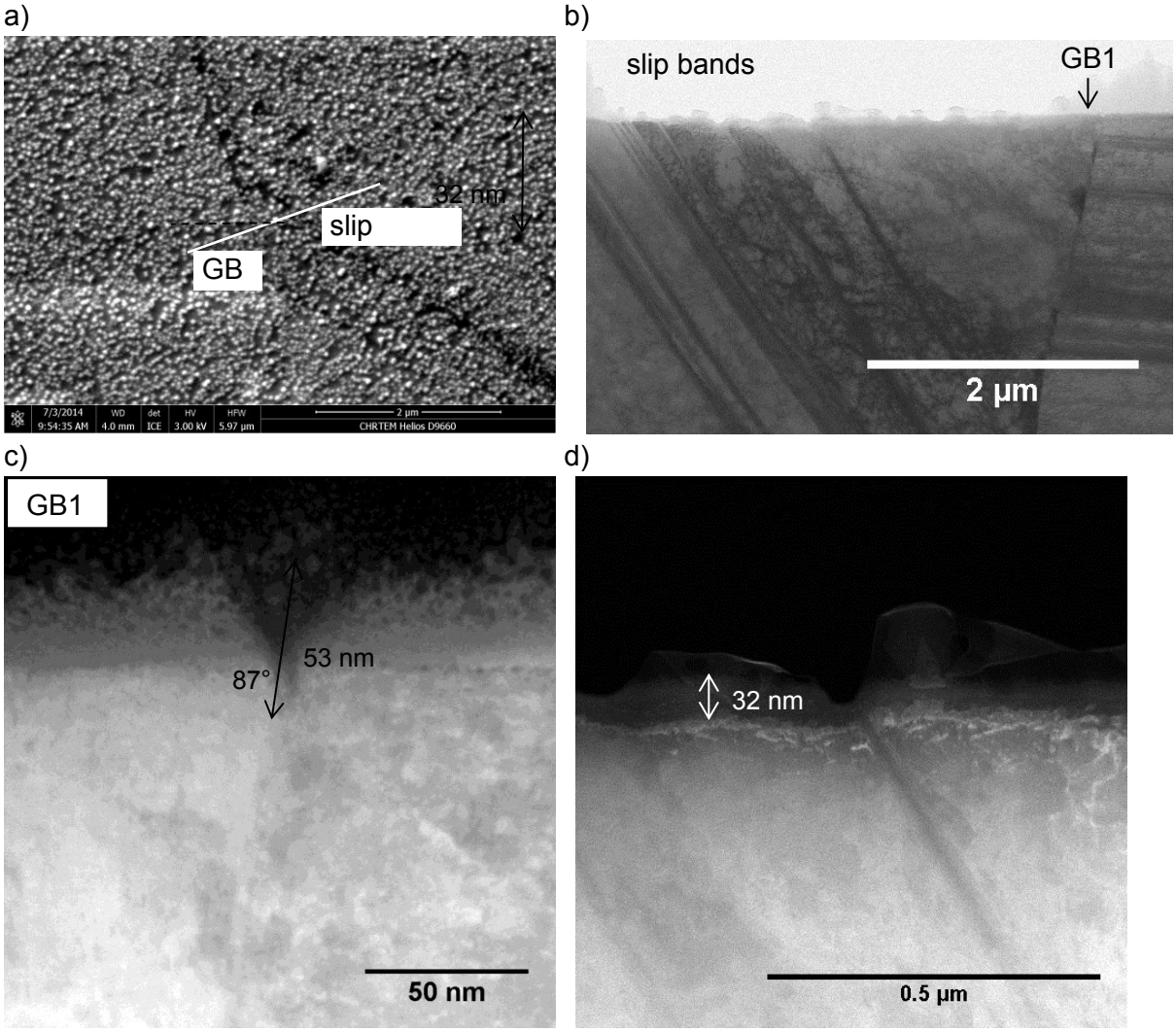

Figure 97. Images of Sample 22 region 3, a) BSE SEM image with dark contrast at GB1 and the slip bands, b) low magnification BF STEM image, c) DF TEM image of GB1 with intergranular oxidation, and d) no preferential oxidation observed to grow down slip bands. Note that some surface oxide damage was incurred during FIB preparation.

Appendix G **Oxidation Measurements after 100 h Exposures**

Sample 35 – Annealed material exposed at 320°C for 100 hours

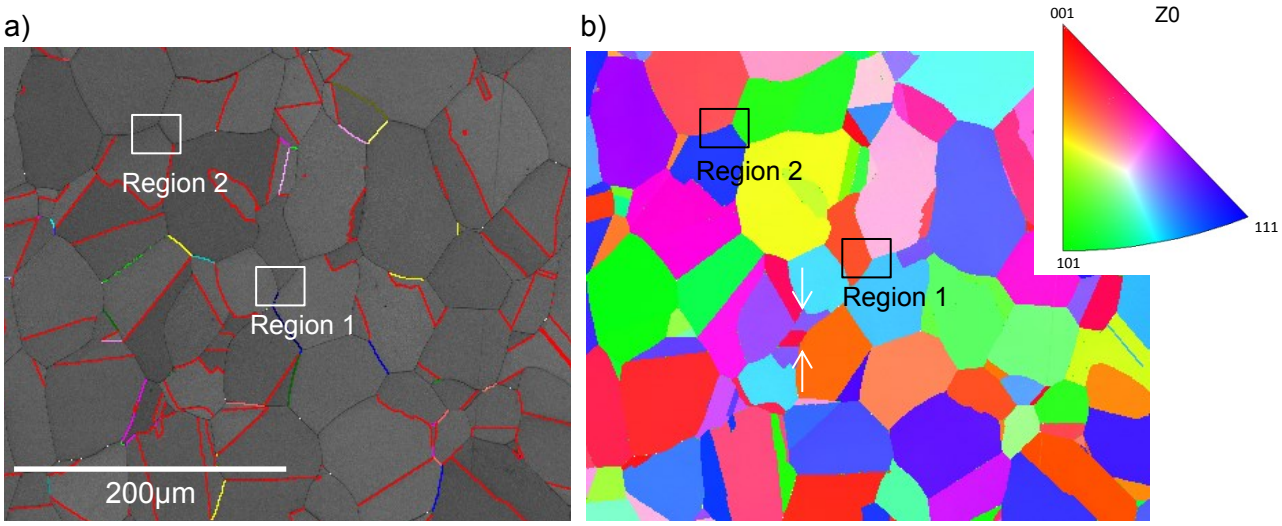

Figure 98. EBSD maps of Sample 35 indicating the locations of region 1 and 2 on the band contrast map (Σ3 boundaries in red, Σ9 boundaries in pink) (a) and the IPF map (b).

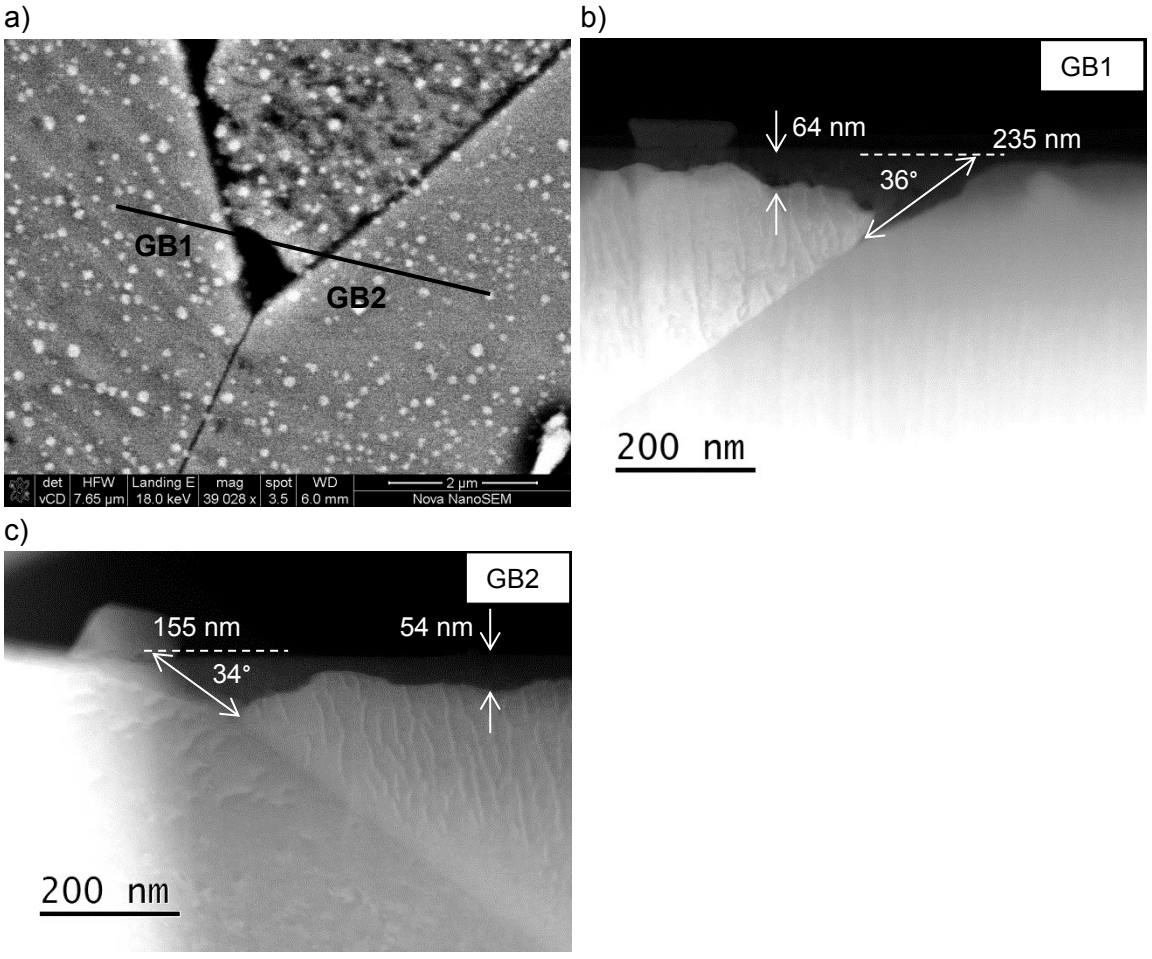

Figure 99. Sample 35 region 1 with a) BSE SEM image at 18 kV with approximate location of the FIB section with grain boundaries labelled, and HAADF dark field TEM images of the b) GB 1 and c) GB 2.

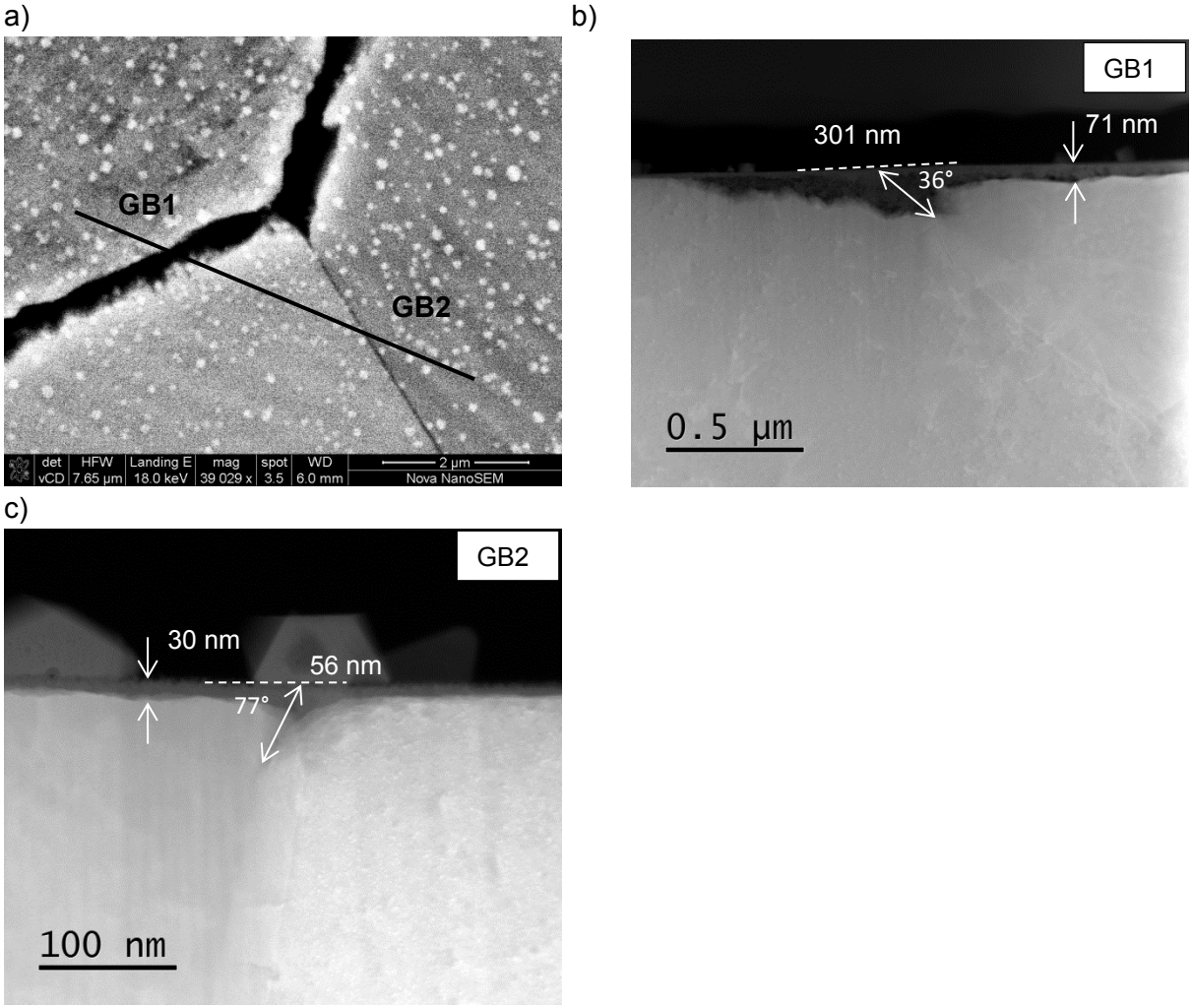

Figure 100. Sample 35 region 2 with a) BSE SEM image at 18 kV showing the dark contrast of grain boundaries and the approximate location of the FIB section, with dark field TEM images of the intergranular and surface oxidation at b) GB 1 and c) GB 2.

Sample 25 – 30% elongated material exposed at 320°C for 100 hours

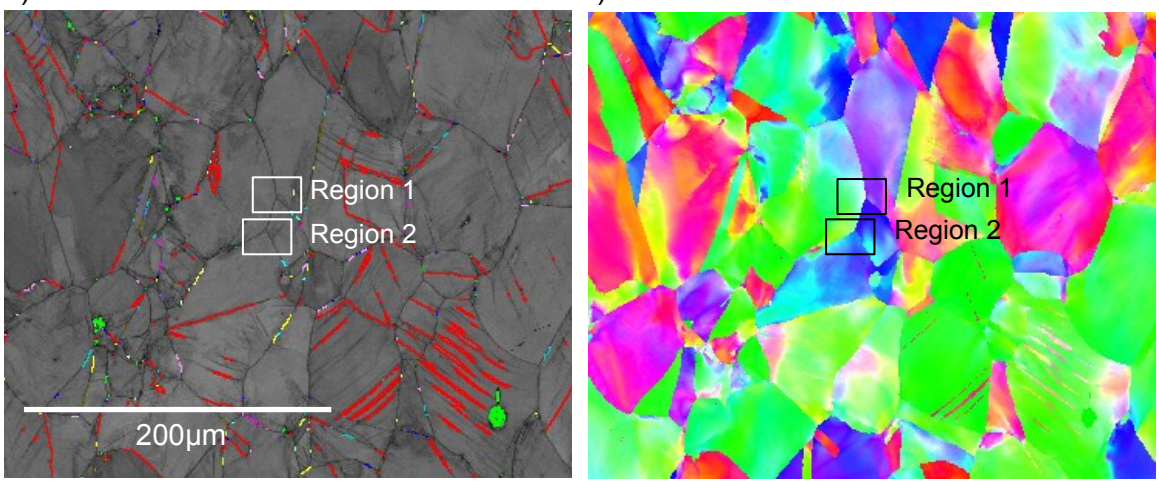

Figure 101. EBSD maps of Sample 25 indicating the locations of region 1 and 2 on the band contrast map (Σ3 boundaries in red) (a) and the IPF map (b).

a)

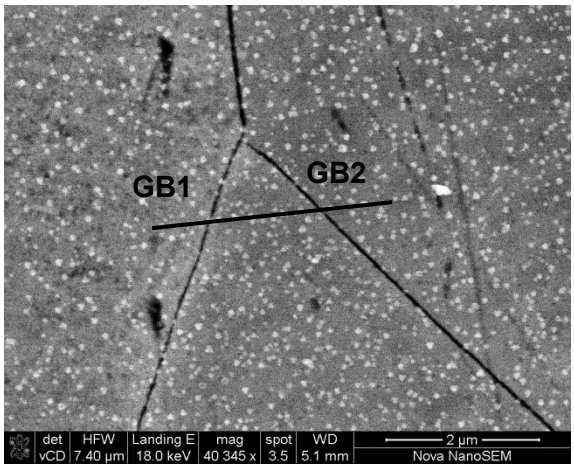

b)

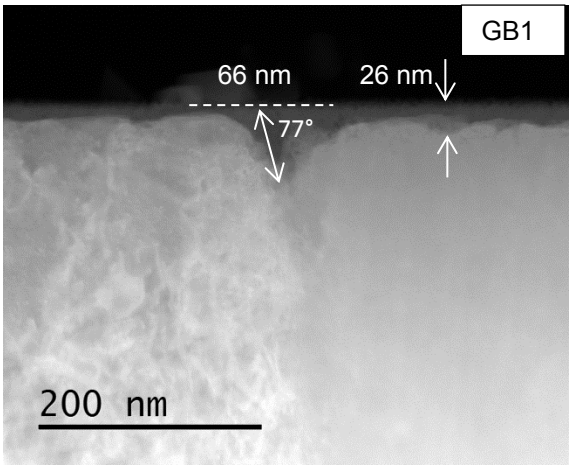

c)

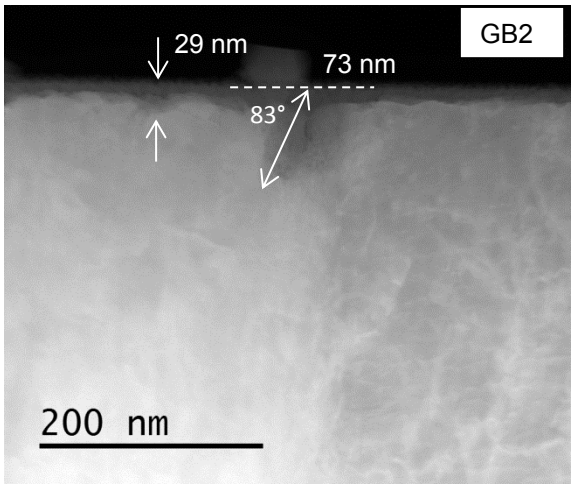

Figure 102. Sample 25 region 1 with a) BSE image at 18 kV with grain boundaries and dark field TEM images of the surface and intergranular oxidation at b) GB 1 and c) GB 2.

a) .

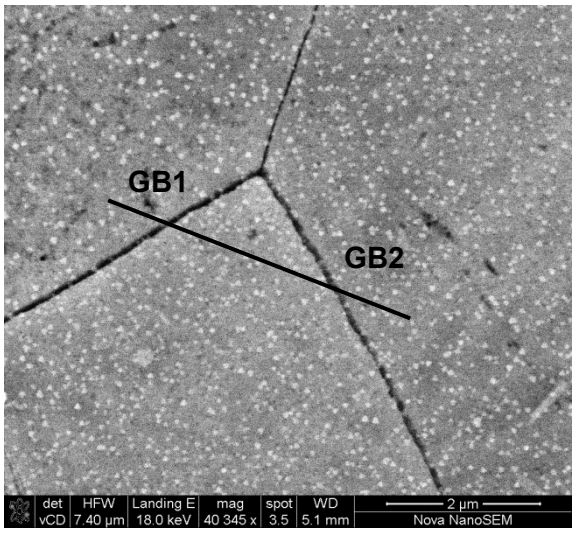

b)

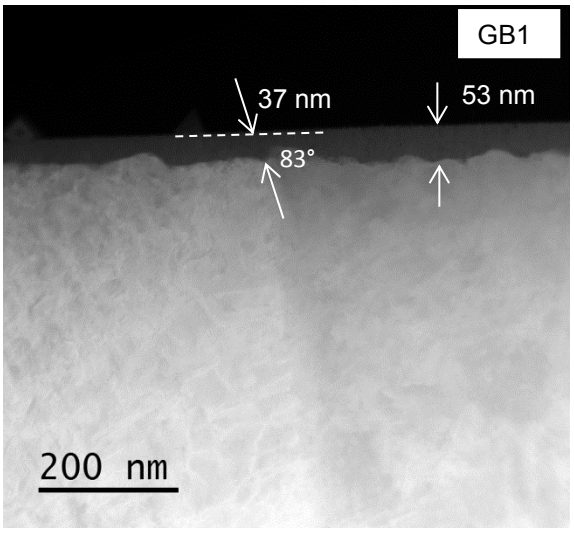

Figure 103. Sample 25 region 2 with a) BSE SEM image at 18 kV with approximate location of the FIB section and b) dark field TEM image of the oxidation at GB 1. GB 2 was lost in the TEM preparation.

Sample 39 – 20% Cold rolled material exposed at 320°C for 100 hours.

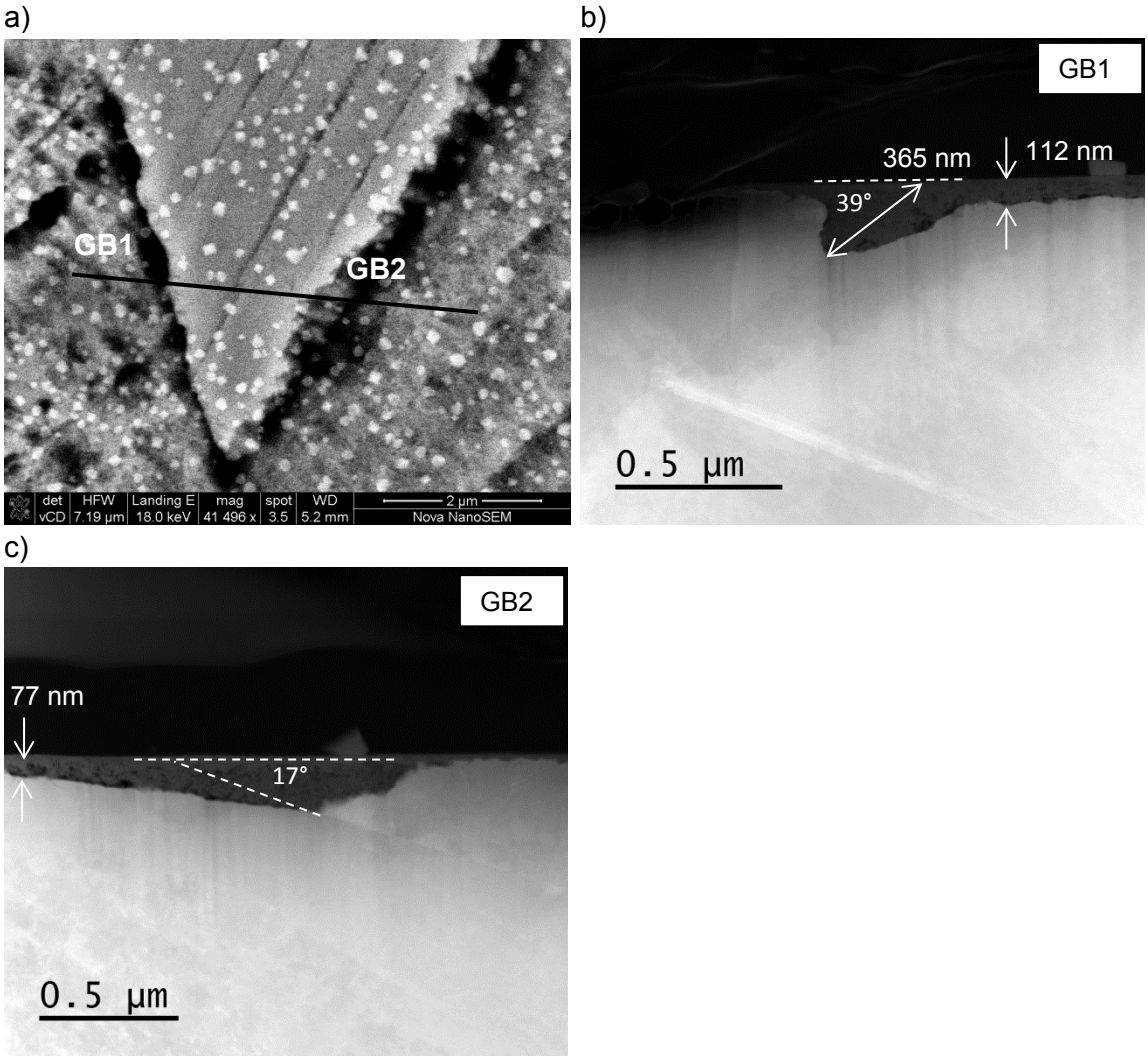

Figure 104. Sample 39 region 2 with a) BSE image at 18 kV indicating the approximate location of the FIB section and dark field TEM images of the surface and intergranular oxidation at b) GB 1 and c) GB 2. The grain boundary angle to surface was too acute to measurement intergranular oxidation.

a) b)

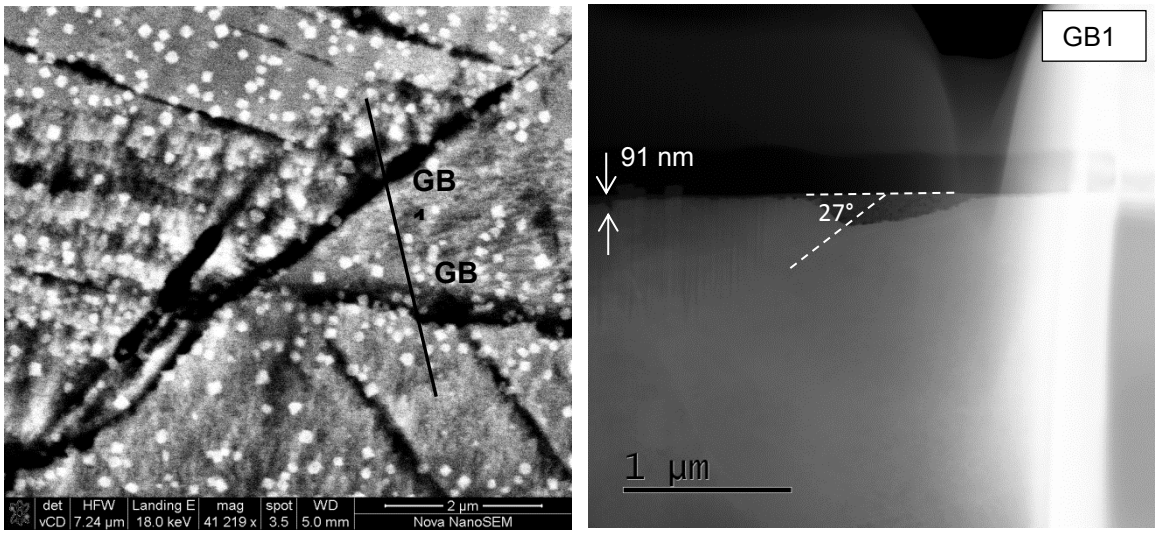

Figure 105. Sample 39 region 4 with a) BSE SEM image at 18 kV indicating the approximate location of the FIB section and b) a dark field image of GB 1, although it was too acute with the surface to have a valid result. GB 2 was lost during sample preparation.

Appendix H **Oxidation Measurements after 1000 h Exposures**

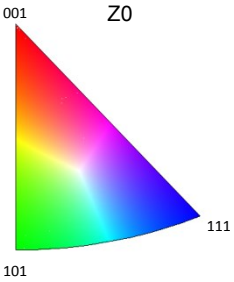

Sample 58 – Annealed material exposed at 290°C for 1000 hours

a) b)

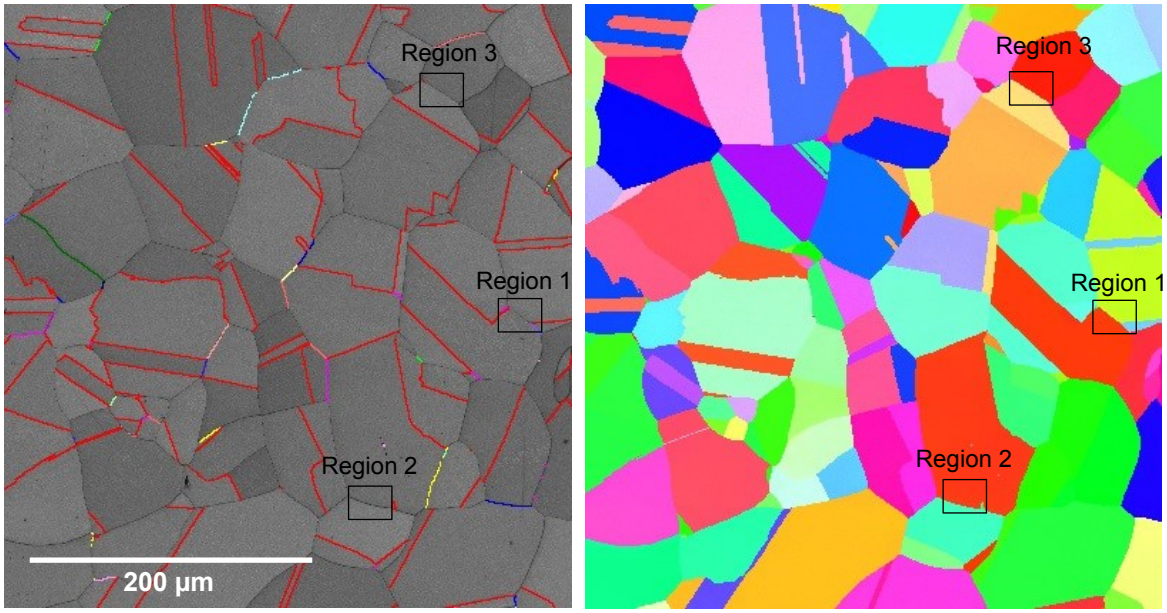

Figure 106. EBSD maps of Sample 58 indicating the locations of regions 1, 2 and 3 on the band contrast map (Σ3 boundaries in red, Σ9 boundaries in pink) (a) together with an IPF map of the same area (b).

a) b)

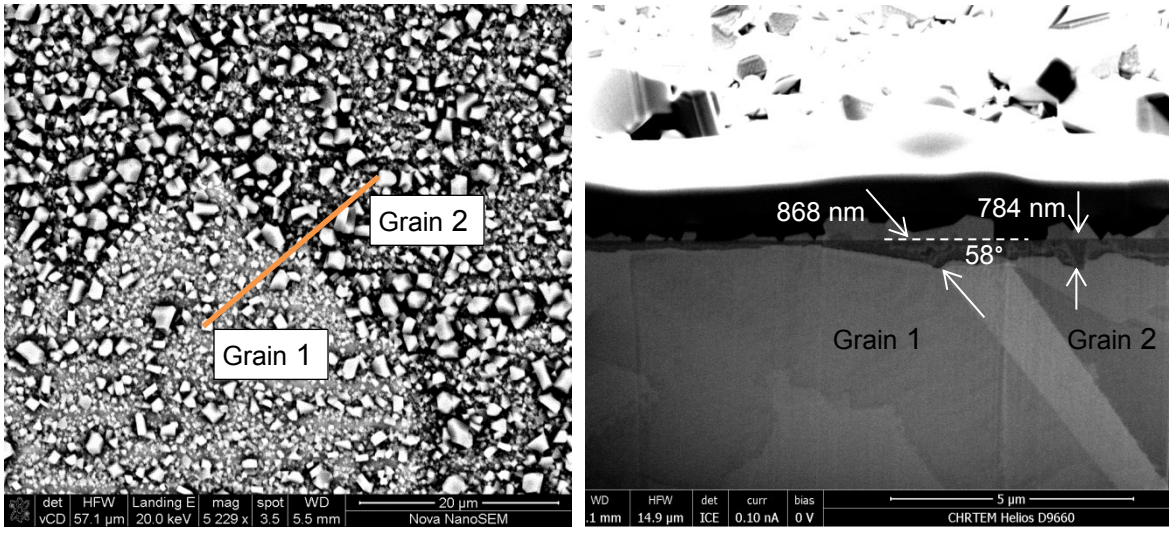

Figure 107. Sample 58 region 1 with a) BSE SEM image at 20 kV with approximate location of the FIB section, and a SEM image of the FIB cross section through the grain boundary.

a) b)

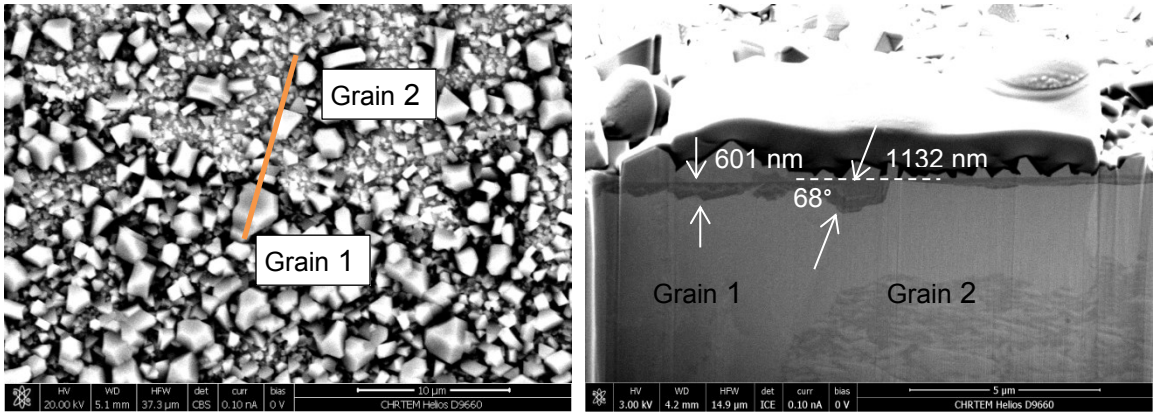

Figure 108. Sample 58 region 2 with a) BSE SEM image at 20 kV with approximate location of the FIB section, and b) a SEM image of the FIB cross section through the grain boundary.

a) b)

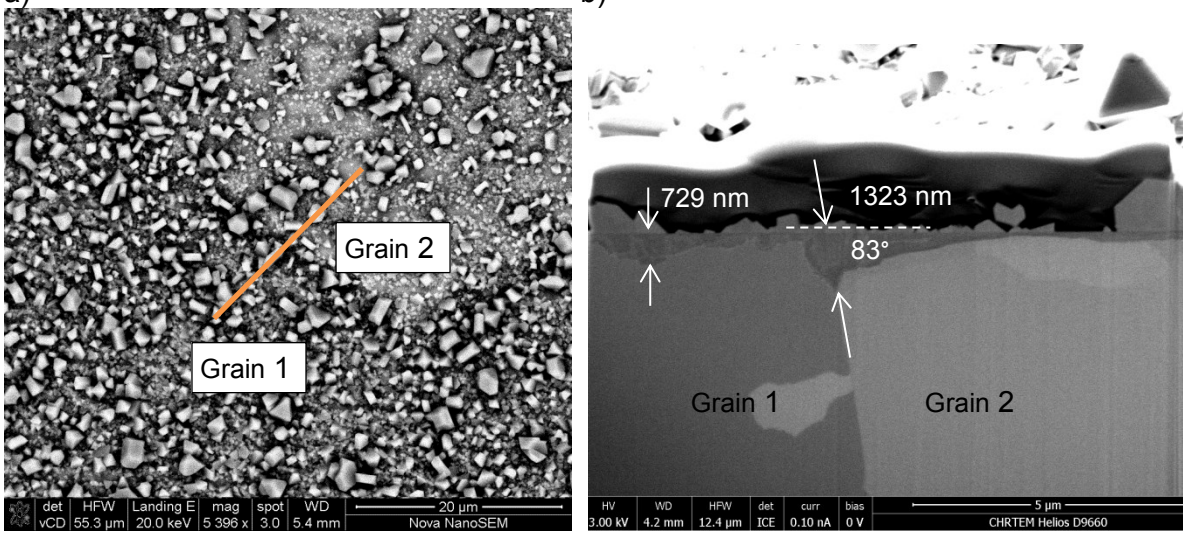

Figure 109. Sample 58 region 3 with a) BSE SEM image at 20 kV with approximate location of the FIB section, and b) a SEM image of the FIB cross section through the grain boundary.

Sample 59 – Annealed material exposed at 320°C for 1000 hours

a) b)

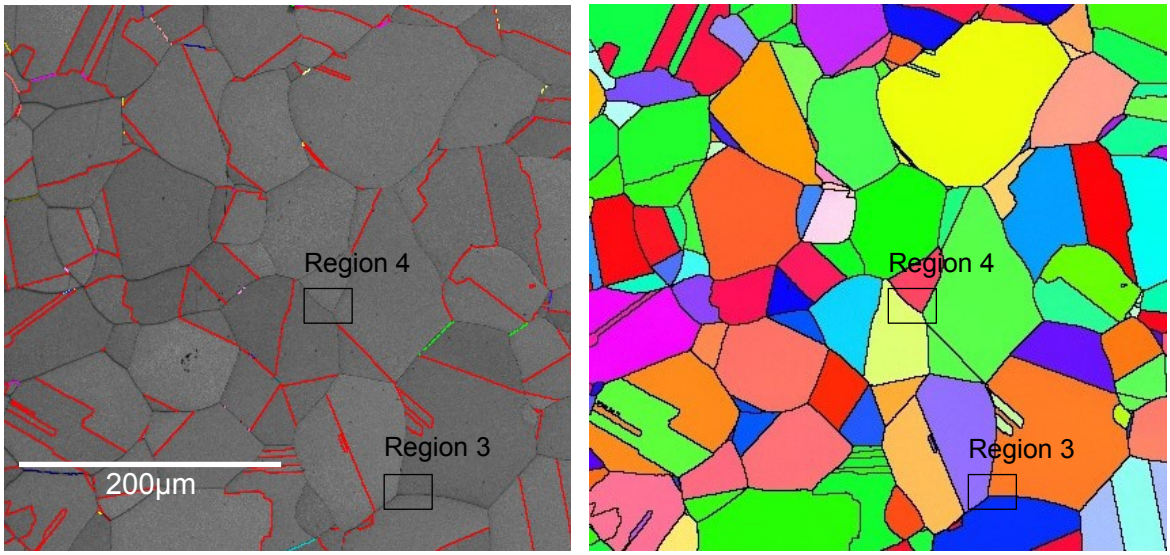

Figure 110. EBSD maps of Sample 59 indicating the locations of regions 3 and 4 on a) a band contrast map (Σ3 boundaries in red, Σ9 boundaries in pink) together with b) an IPF map of the same area.

a) b)

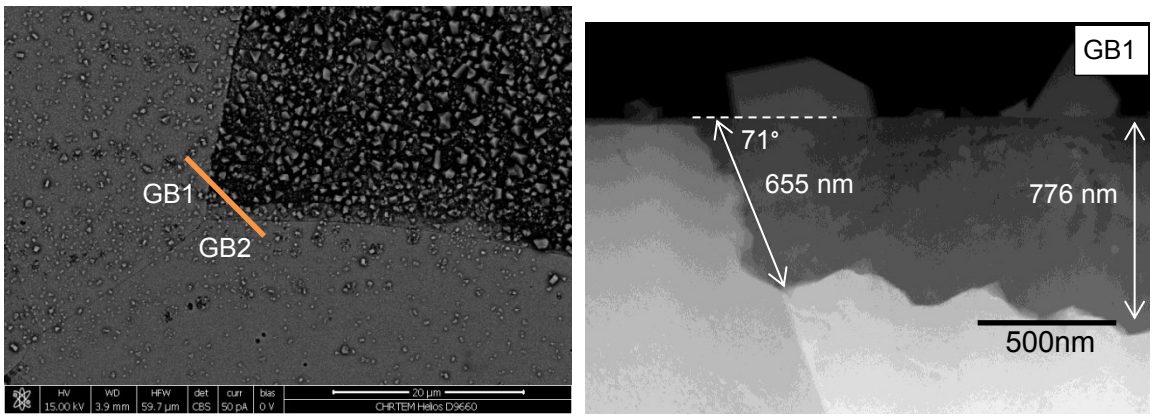

Figure 111 Sample 59 region 3 with a) BSE SEM image at 15 kV with approximate location of the FIB section with grain boundaries labelled, and b) HAADF dark field TEM image of the GB 1. Note that GB 2 was not included in thin foil area.

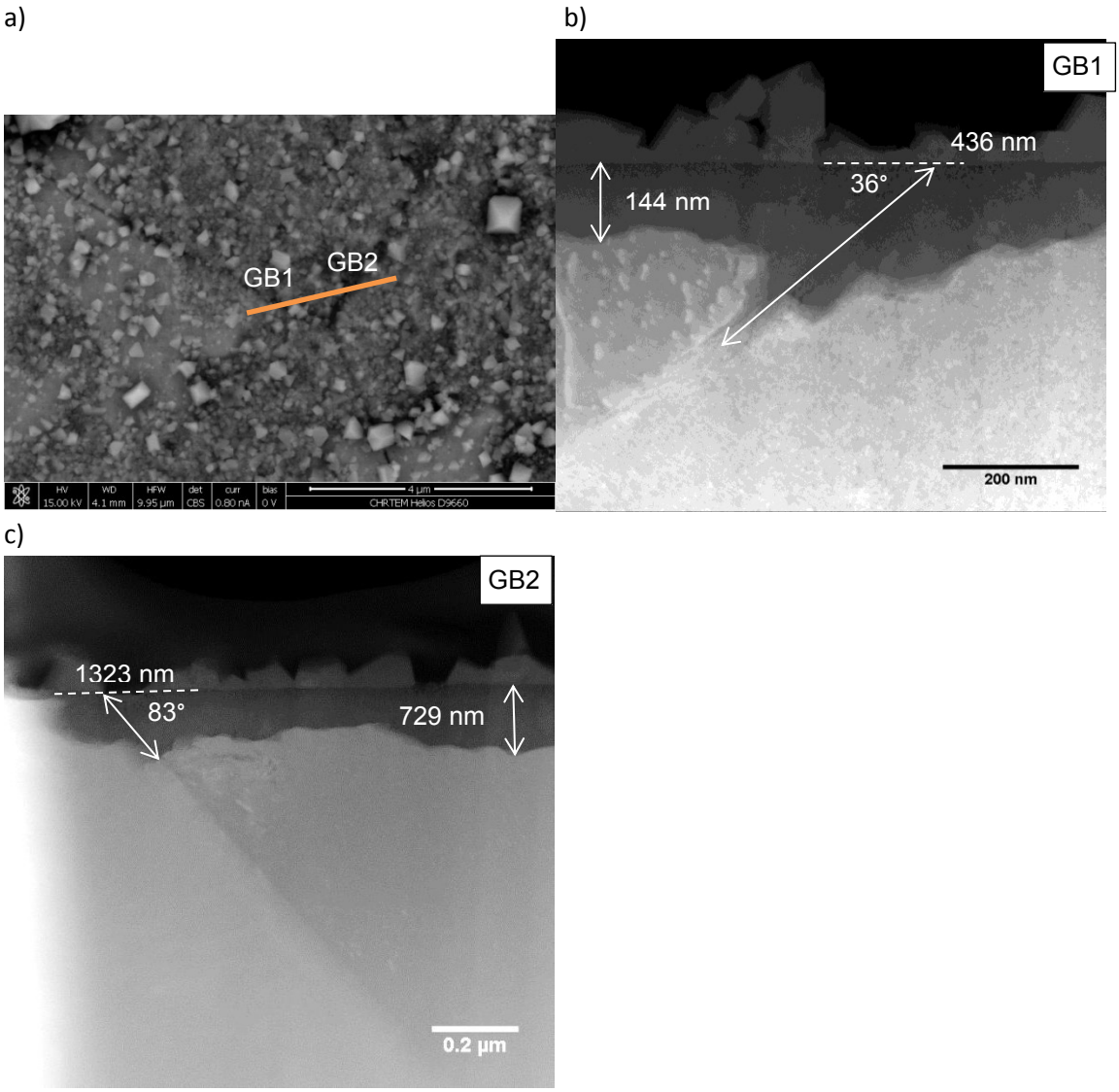

Figure 112. Sample 59 region 4 with a) BSE SEM image at 15 kV with approximate location of the FIB section with grain boundaries labelled, and HAADF dark field TEM image of b) GB 1 and c) GB 2 with measurements of surface and intergranular oxidation.

Sample 60 – Annealed material exposed at 360°C for 1000 hours

a) b)

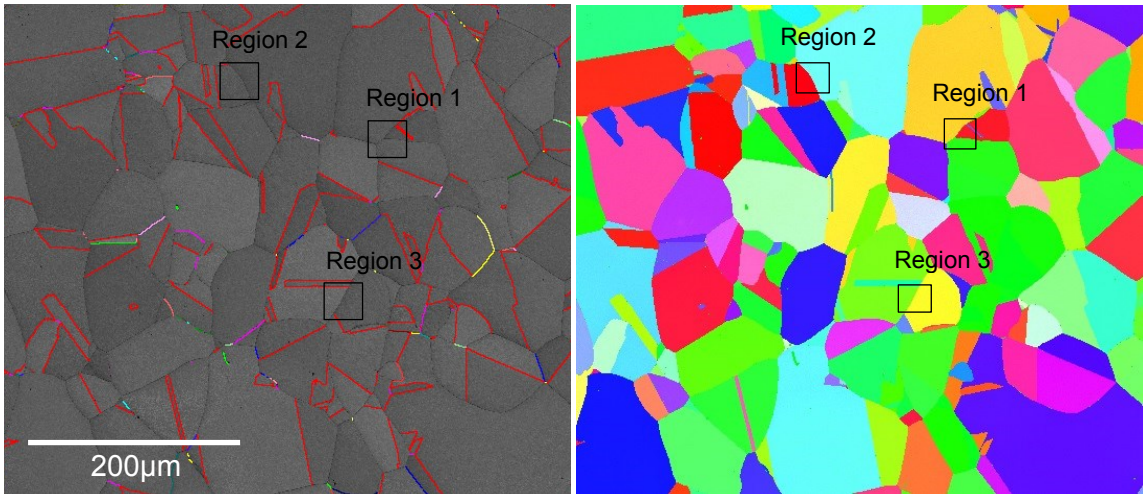

Figure 113. EBSD maps of Sample 60 indicating the locations of regions 1, 2 and 3 on a) a band contrast map (Σ3 boundaries in red, Σ9 boundaries in pink) together with b) an IPF map of the same area.

a) b)

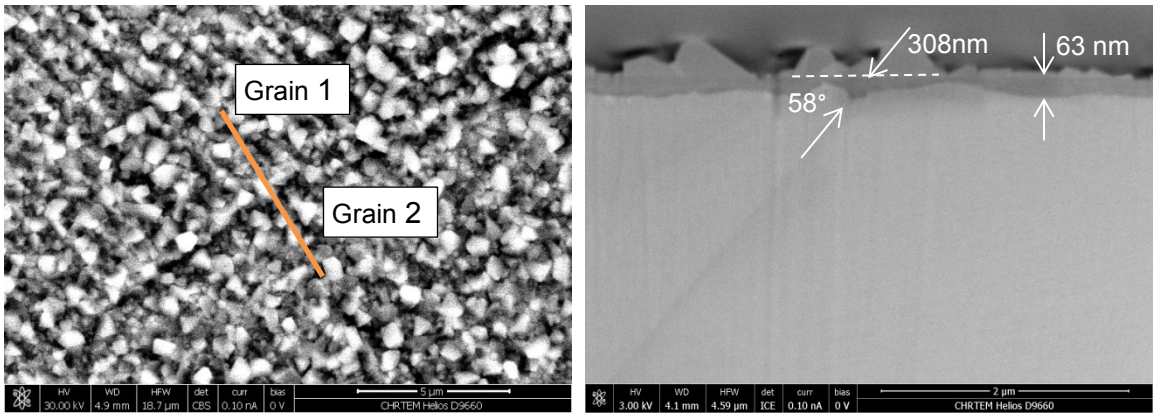

Figure 114. Sample 60 region 1 with a) BSE SEM image at 30 kV with approximate location of the FIB section, and b) a SEM image of the FIB cross section through the grain boundary.

a) b)

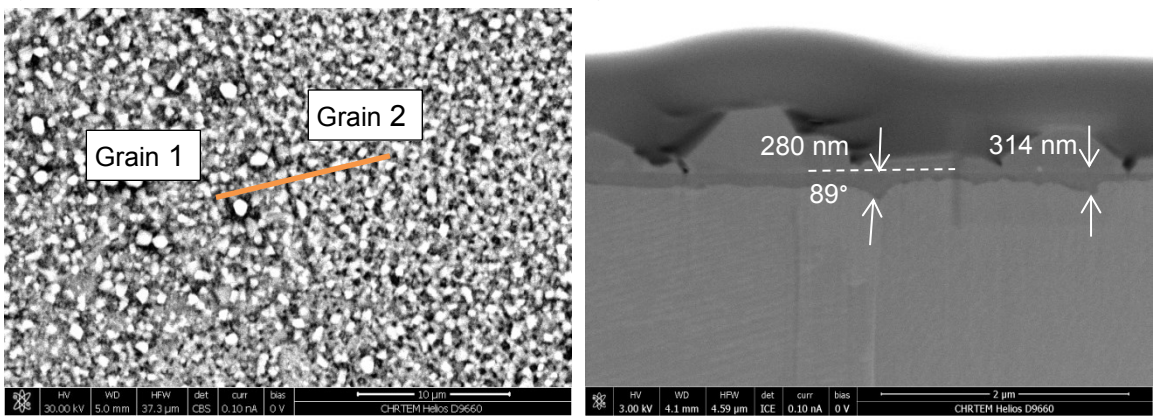

Figure 115. Sample 60 region 2 with a) BSE SEM image at 30 kV with approximate location of the FIB section, and b) a SEM image of the FIB cross section through the grain boundary.

a) b)

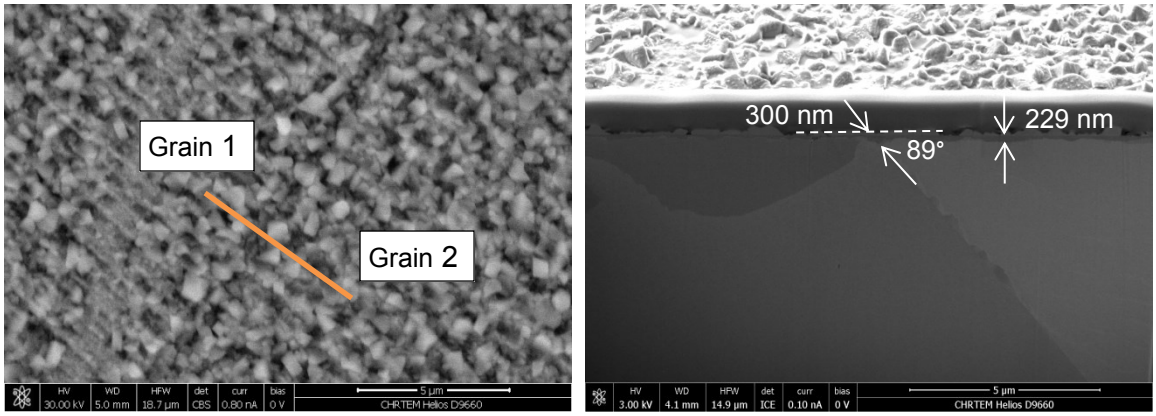

Figure 116. Sample 60 region 3 with a) BSE SEM image at 30 kV with approximate location of the FIB section, and b) a SEM image of the FIB cross section through the grain boundary.

Sample 65 – 30% Elongated material exposed at 320°C for 1000 hours

a) b)

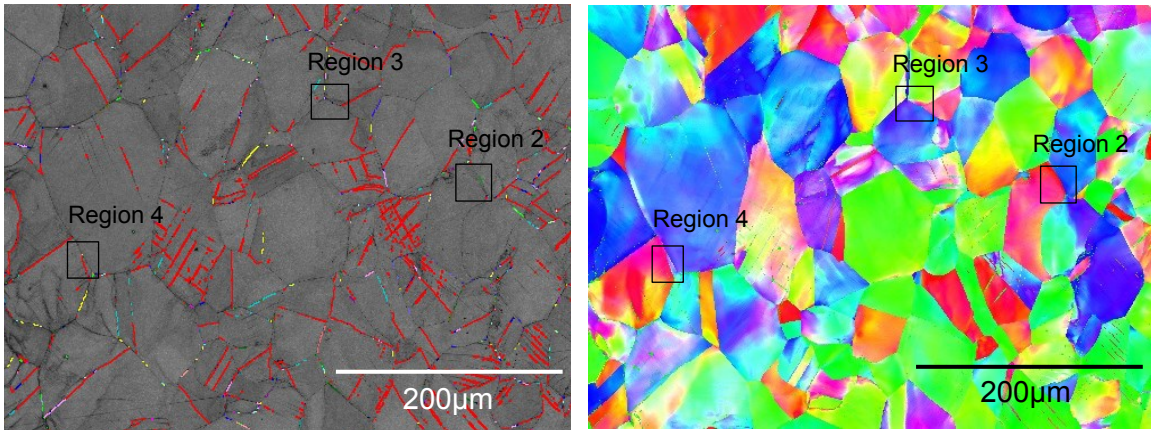

Figure 117. EBSD maps of Sample 65 indicating the locations of regions 2, 3 and 4 on a) a band contrast map (Σ3 boundaries in red, Σ9 boundaries in pink) together with b) an IPF map of the same area.

a)

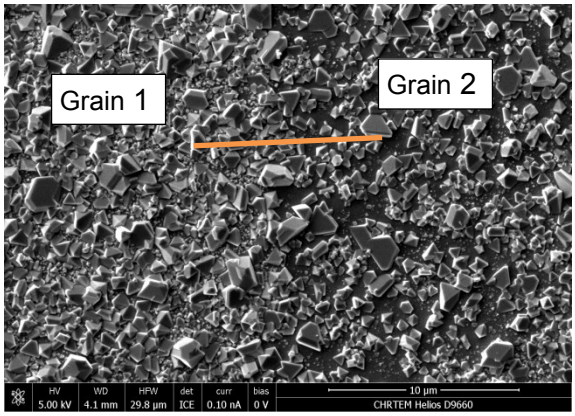

b)

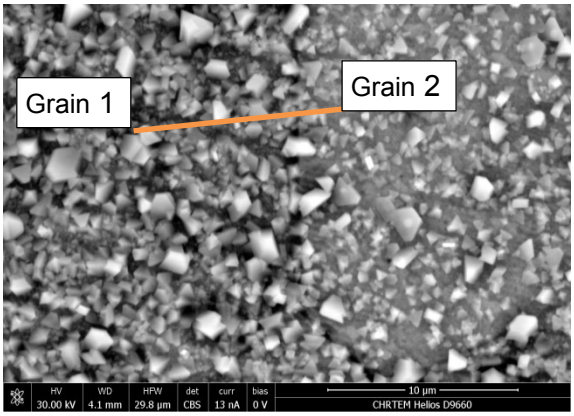

c)

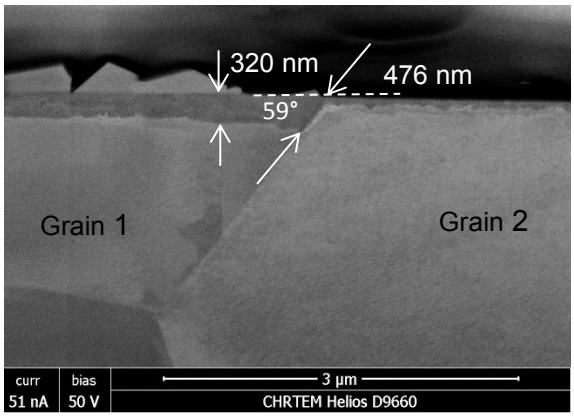

Figure 118. Sample 65 region 2 with a) SEM image at low accelerating voltage of 5 kV with different surface crystallite densities across the grain boundary, together with b) a BSE image at 30 kV with approximate location of the FIB section, and c) a SEM image of the FIB cross section through the grain boundary.

a)

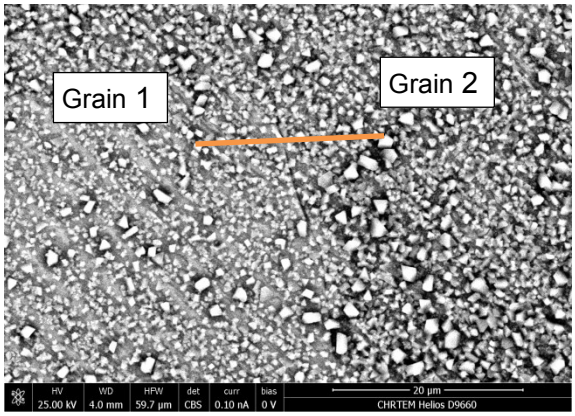

b)

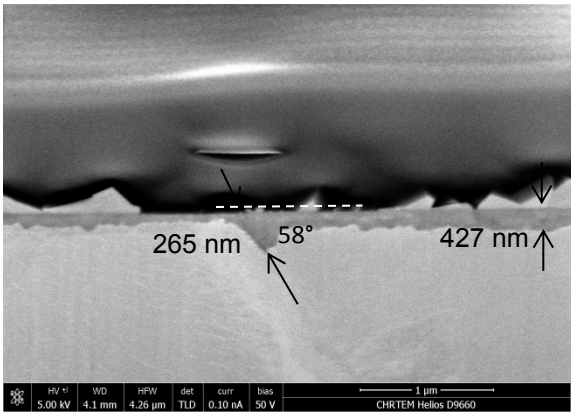

Figure 119. Sample 65 region 3 with a) a BSE image at 25 kV with approximate location of the FIB section, and b) a SEM image of the FIB cross section through the grain boundary.

a)

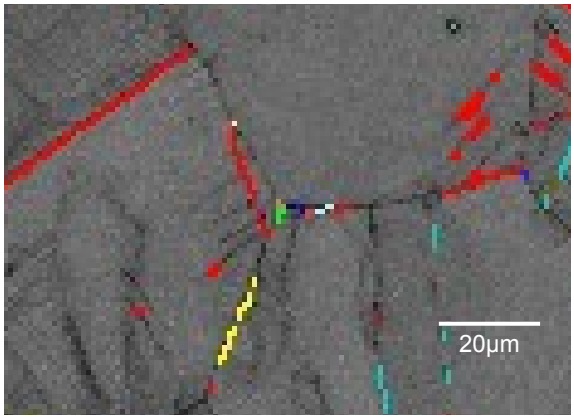

b)

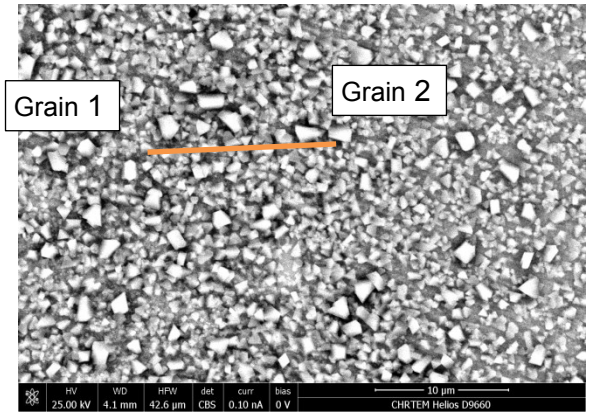

c)

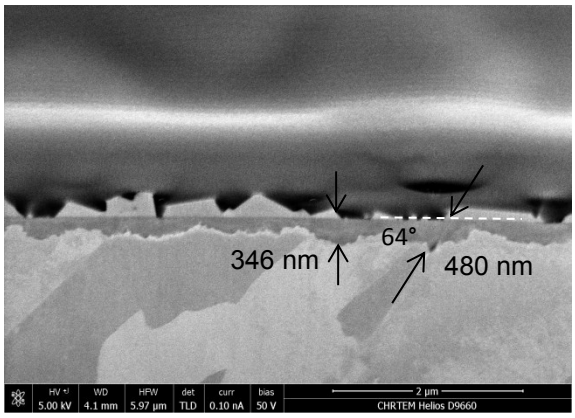

Figure 120. Sample 65 region 4 with a) magnified view of the band contrast EBSD map highlighting the proximity of a Σ3 boundary and a random boundary, b) a BSE image at 25 kV with approximate location of the FIB section, and c) a SEM image of the FIB cross section through the Σ3 boundary and grain boundary.

Sample 67 – 20% Cold rolled material exposed at 290°C for 1000 hours

a)

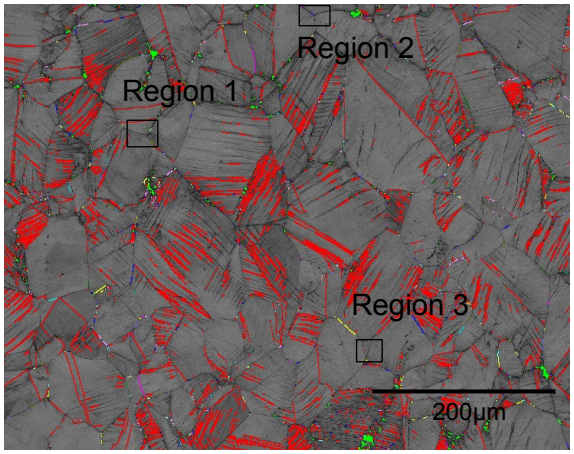

b)

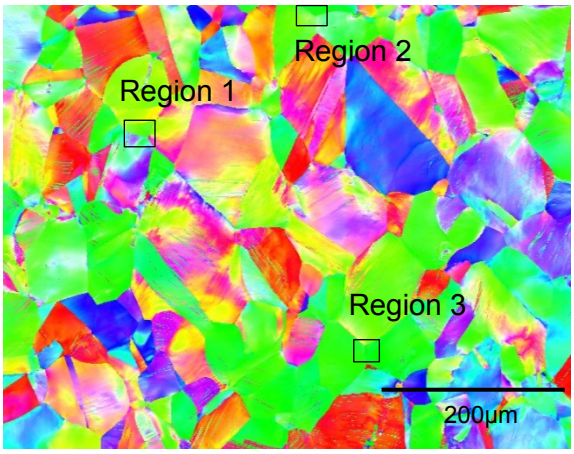

Figure 121. EBSD maps of Sample 67 indicating the locations of regions 1, 2, and 3 on a) a band contrast map (Σ3 boundaries in red, Σ9 boundaries in pink) together with b) an IPF map of the same area.

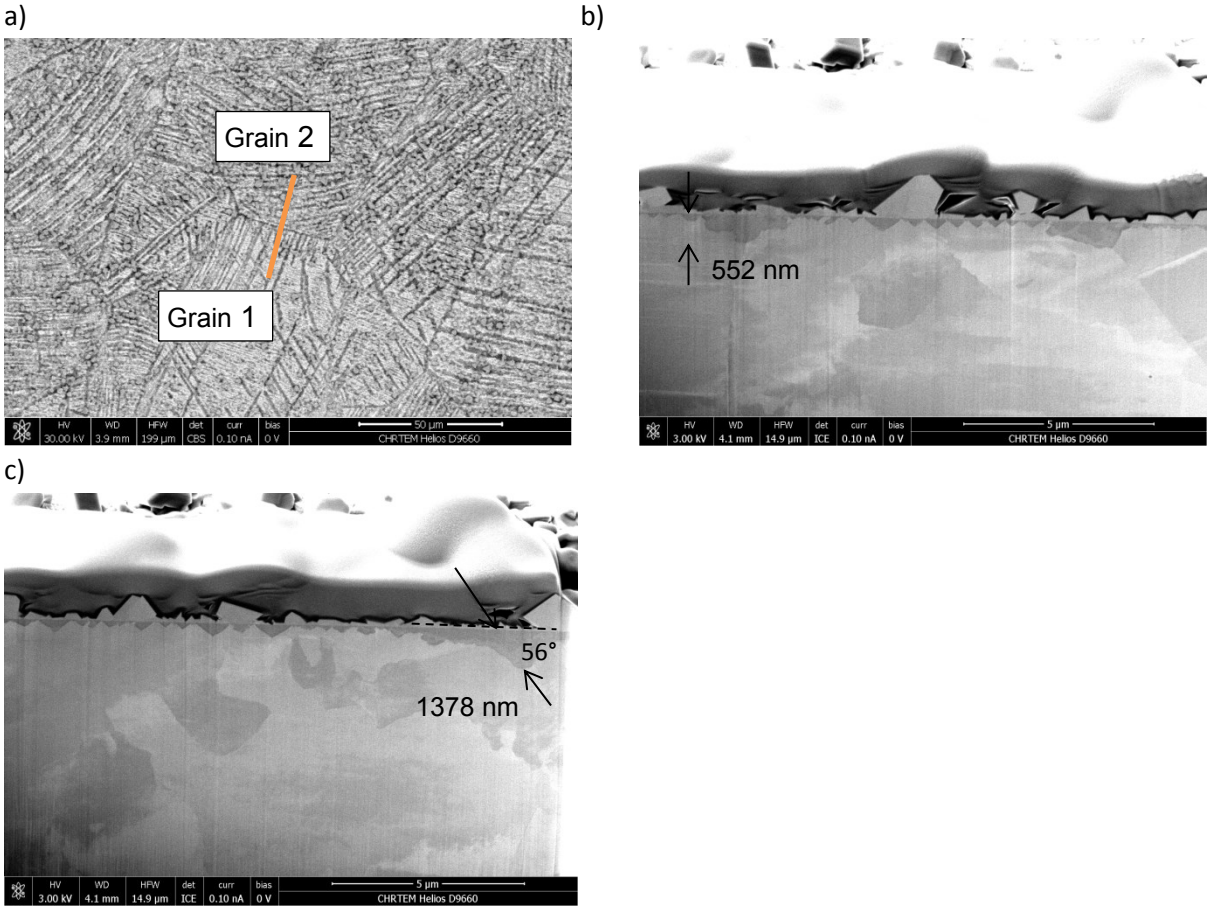

Figure 122. Sample 67 region 1 with a) a BSE image at 30 kV with approximate location of the FIB section; b) a SEM image of the FIB cross section through the grain boundary with the greatest surface oxidation; and c) another SEM image of a different FIB slice with the greatest intergranular oxidation depth.

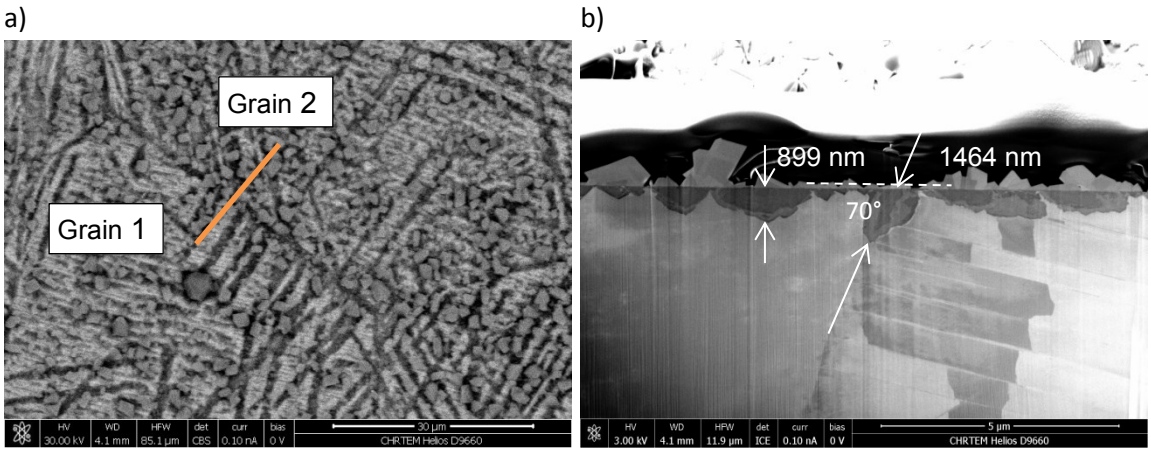

Figure 123. Sample 67 region 2 with a) a BSE image at 30 kV with approximate location of the FIB section; and b) a SEM image of the FIB cross section through the grain boundary highlighting the oxide measurements.

a) b)

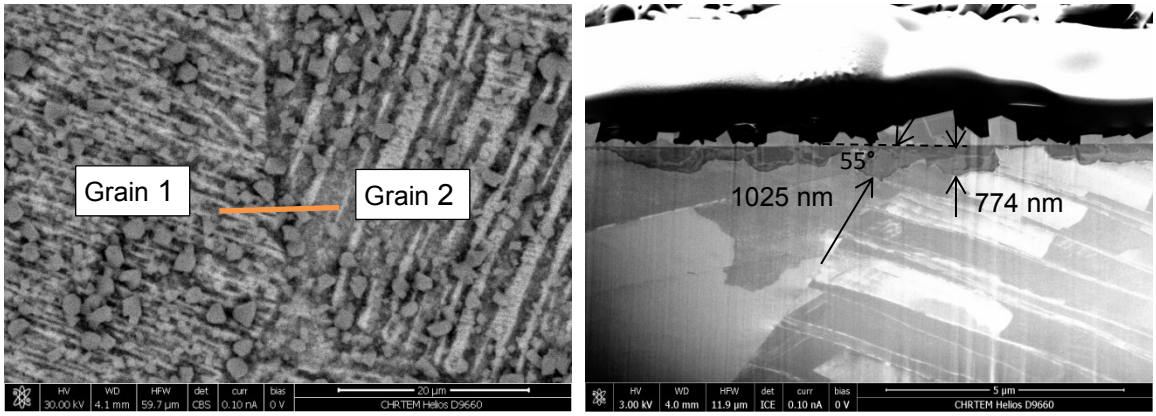

Figure 124. Sample 67 region 3 with a) a BSE image at 30 kV with approximate location of the FIB section; and b) a SEM image of the FIB cross section through the grain boundary highlighting the oxide measurements.

Sample 68 – 20% Cold rolled material exposed at 320°C for 1000 hours

a) b)

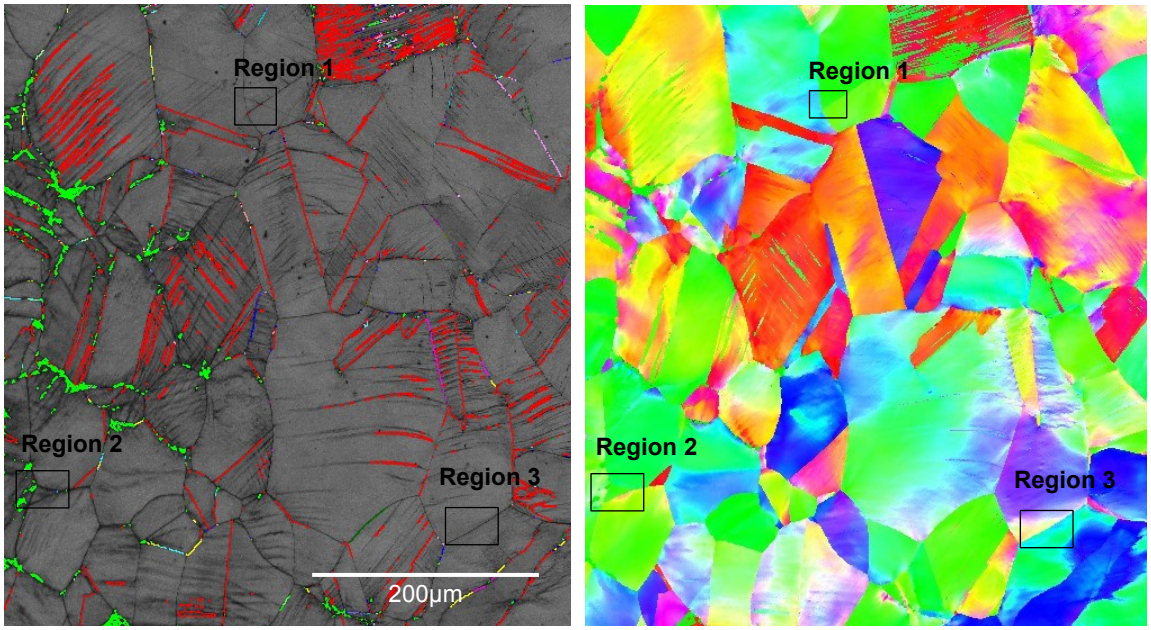

Figure 125. EBSD maps of Sample 68 indicating the locations of regions 1, 2, and 3 on a) a band contrast map (Σ3 boundaries in red, Σ9 boundaries in pink) together with b) an IPF map of the same area.

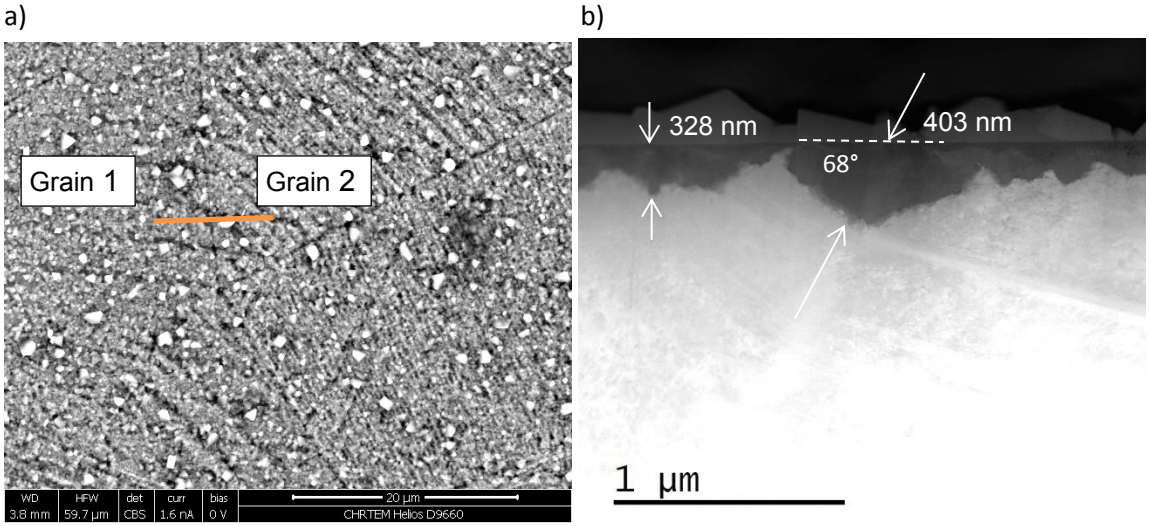

Figure 126. Sample 68 region 1 with a) a BSE image at 30 kV with approximate location of the FIB section; and b) a HAADF dark field TEM image with measurements of surface and intergranular oxidation.

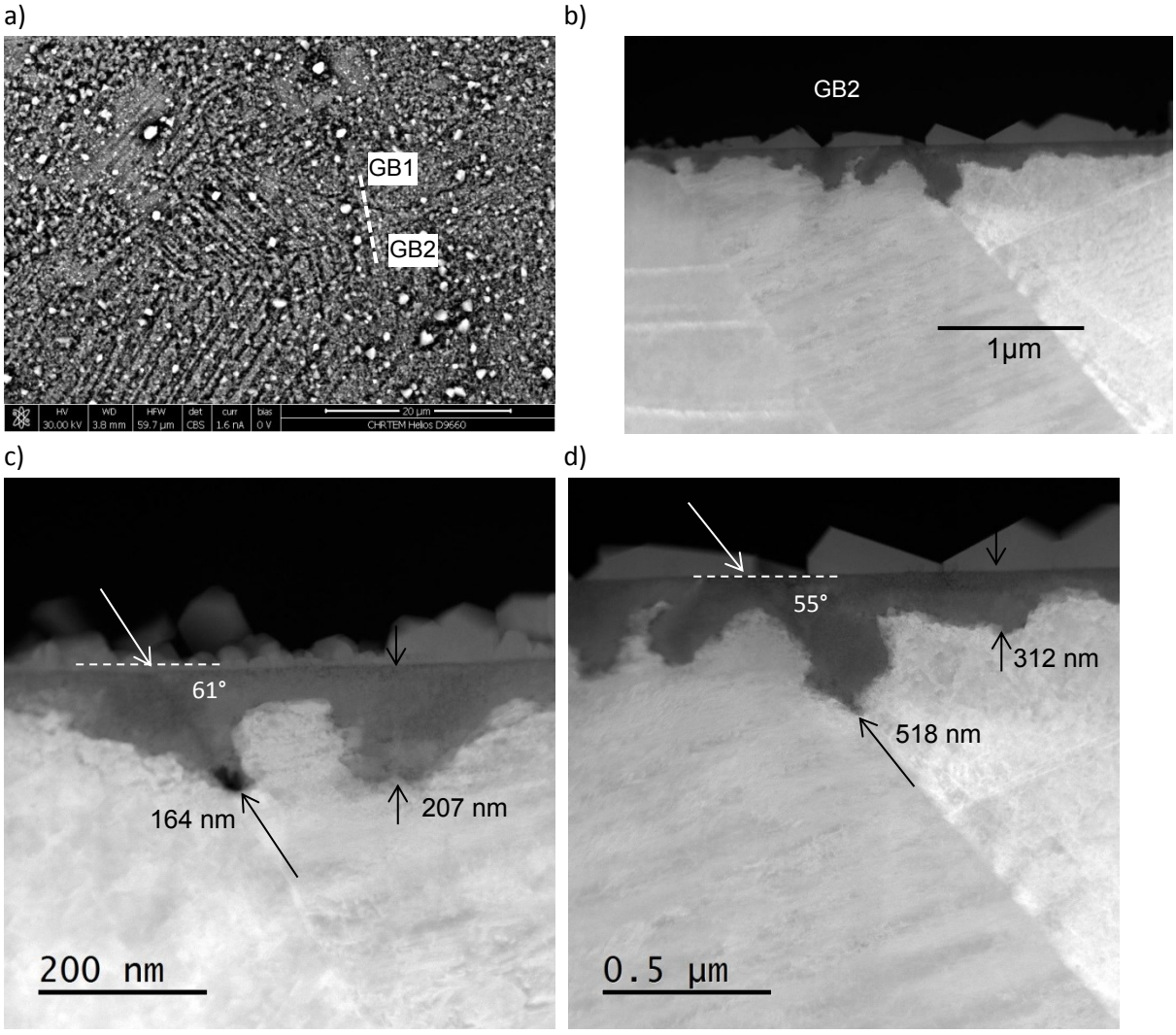

Figure 127. Sample 68 region 2 with a) a BSE image at 30 kV with approximate location of the FIB section; and HAADF dark field TEM images of b) both grain boundaries and images of c) GB1 and d) GB2 with measurements of surface and intergranular oxidation.

a) b)

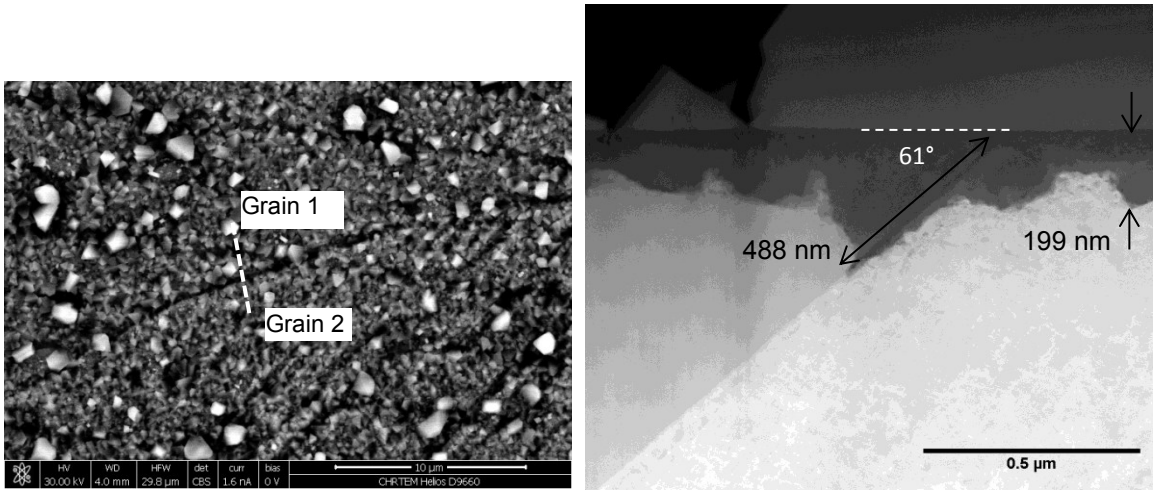

Figure 128. Sample 68 region3 with a) a BSE image at 30 kV with approximate location of the FIB section; and b) a HAADF dark field TEM image of the grain boundary with measurements of surface and intergranular oxidation.

Sample 69 – 20% Cold rolled material exposed at 360°C for 1000 hours

a) b)

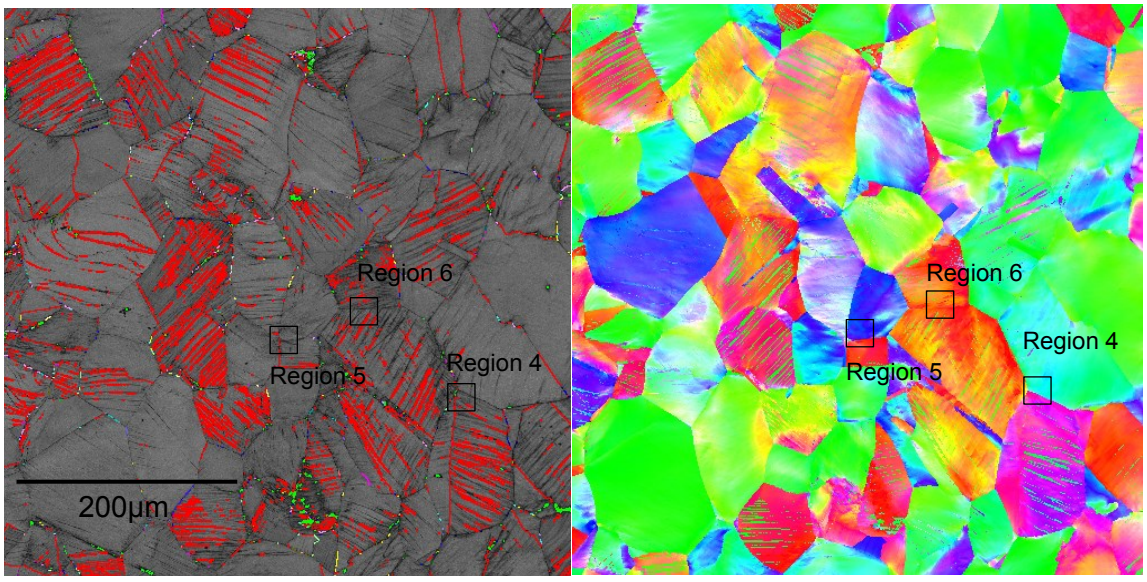

Figure 129. EBSD maps of Sample 69 indicating the locations of regions 4, 5, and 6 on a) a band contrast map (Σ3 boundaries in red, Σ9 boundaries in pink) together with b) an IPF map of the same area.

a) b)

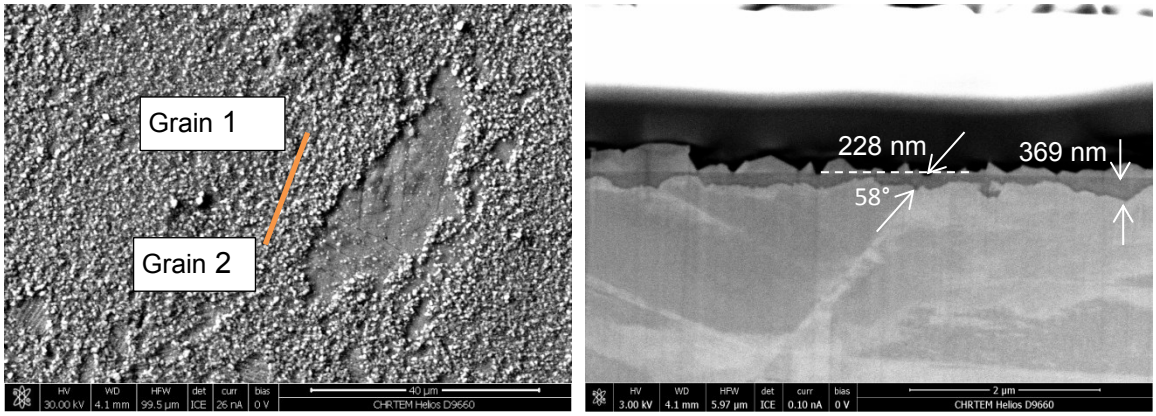

Figure 130. Sample 69 region 4 with a) a BSE image at 30 kV with approximate location of the FIB section; and b) a SEM image of the FIB cross section through the grain boundary with measurements of surface and intergranular oxidation.

a) b)

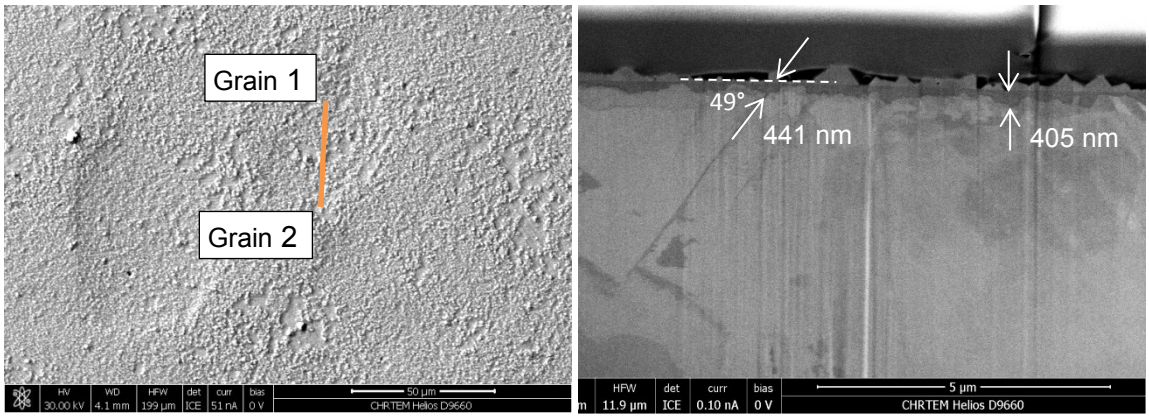

Figure 131. Sample 69 region 5 with a) a BSE image at 30 kV with approximate location of the FIB section; and b) a SEM image of the FIB cross section through the grain boundary with measurements of surface and intergranular oxidation.

a) b)

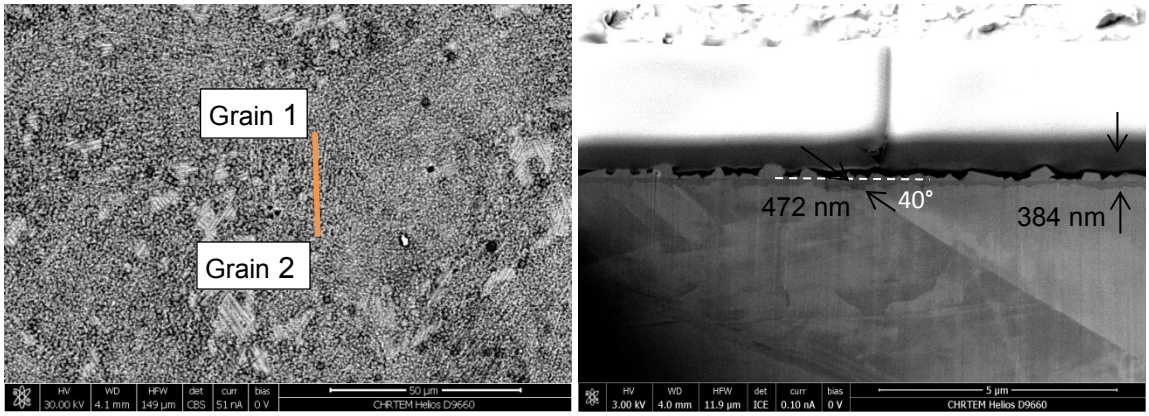

Figure 132. Sample 69 region 6 with a) a BSE image at 30 kV with approximate location of the FIB section; and b) a SEM image of the FIB cross section through the grain boundary with measurements of surface and intergranular oxidation.

Appendix I **Oxidation Measurements after >1000 h Exposures**

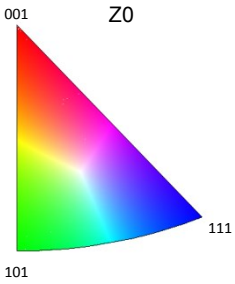

Sample 55 – Annealed material exposed at 290°C for 5000 hours

a) b)

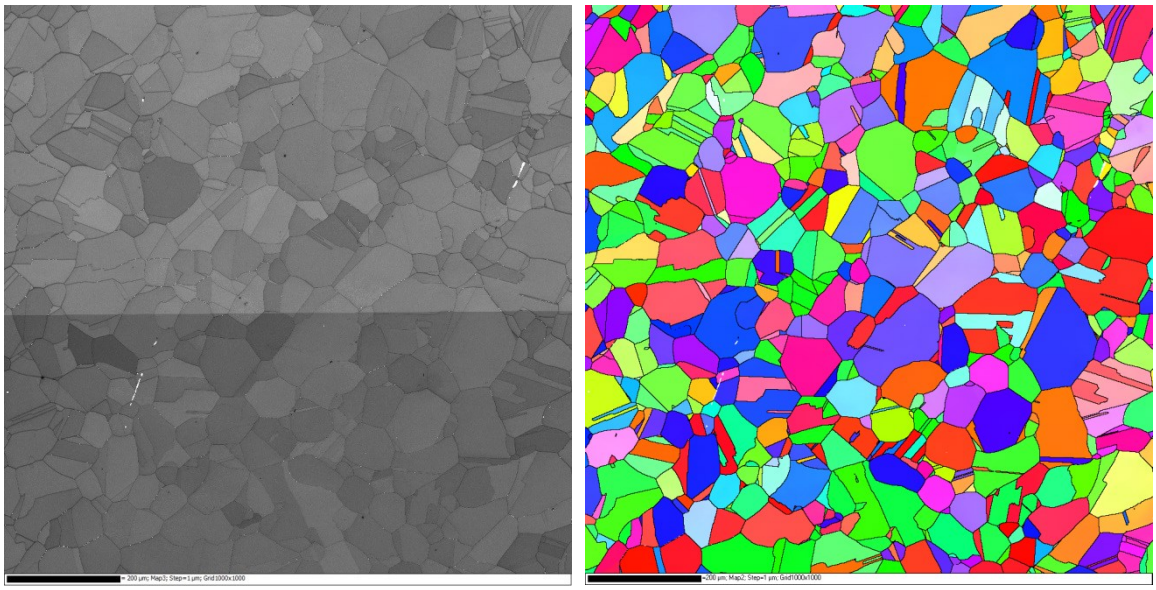

Figure 133. EBSD maps of Sample 55 with a) band contrast image and b) the IPF map of the same area. It was not possible to locate regions where measurements were taken on these maps since the surface oxide was too thick to view the microstructure with BSE.

a) b)

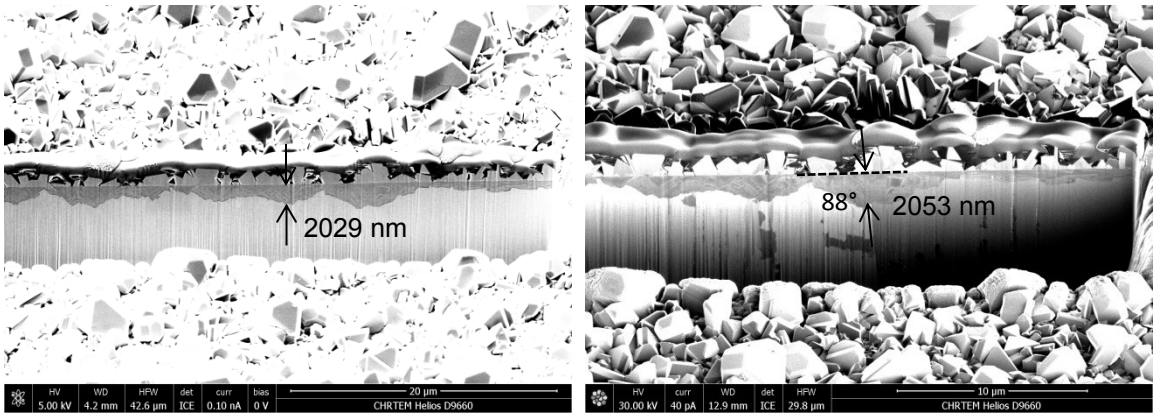

Figure 134. Sample 55 Region 1 with a) SEM image of a cross-section, and b) a FIB image to highlight GB contrast with channelling contrast.

a) b)

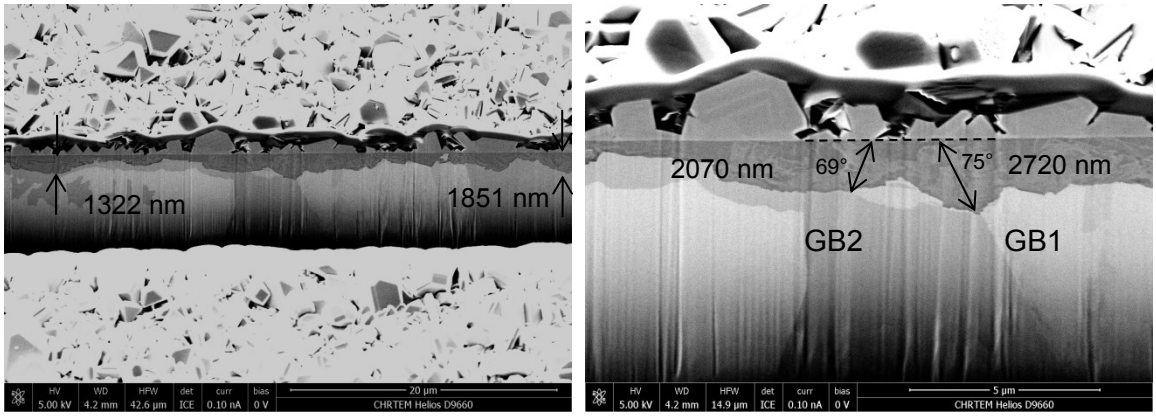

Figure 135. Sample 55 Region 2 with a) a SEM image of a FIB prepared cross section including two grain boundaries and b) magnified SEM image of the grain boundaries.

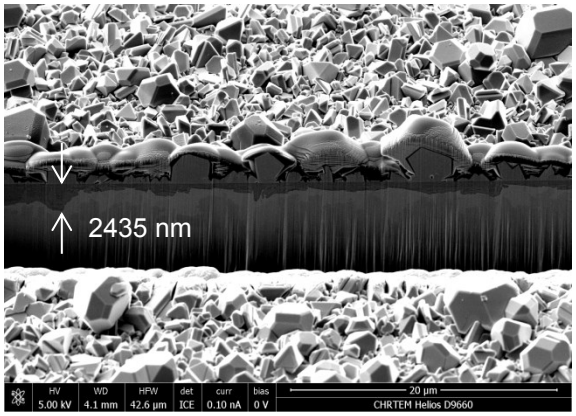

Figure 136. Sample 55 region 3 with a SEM image of a FIB prepared cross-section without any grain boundaries.

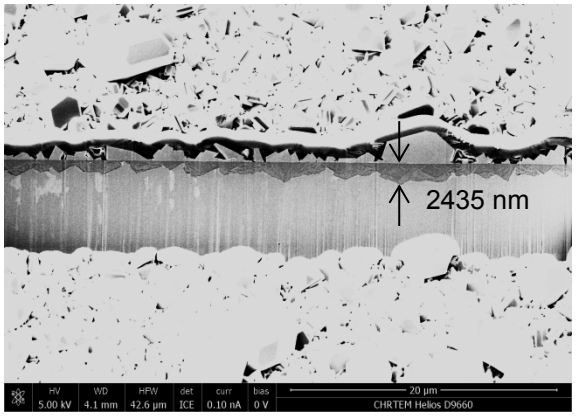

Figure 137. Sample 55 region 4 with a SEM image of a FIB prepared cross-section without any grain boundaries.

a) b)

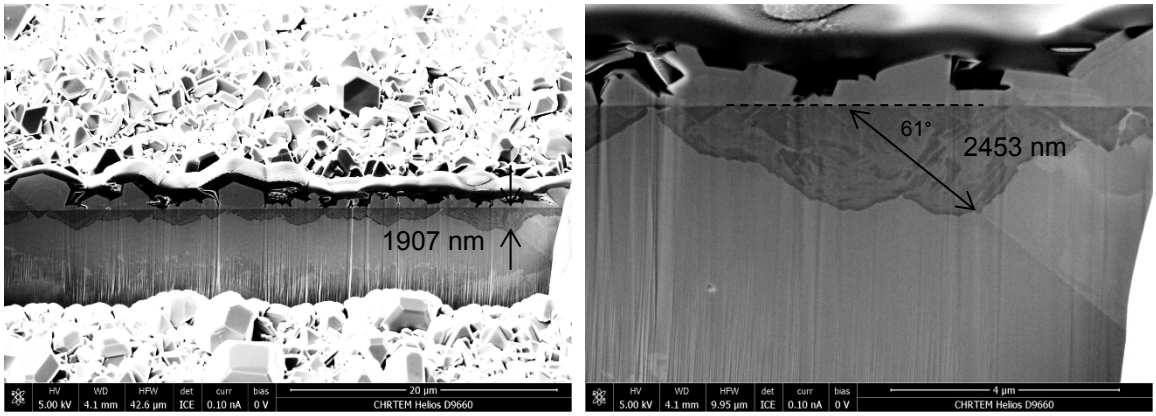

Figure 138. Sample 55 region 5 with a) a SEM image of the full width of a FIB prepared cross-section, and b) a magnified view of the intergranular oxidation at a grain boundary.

a) b)

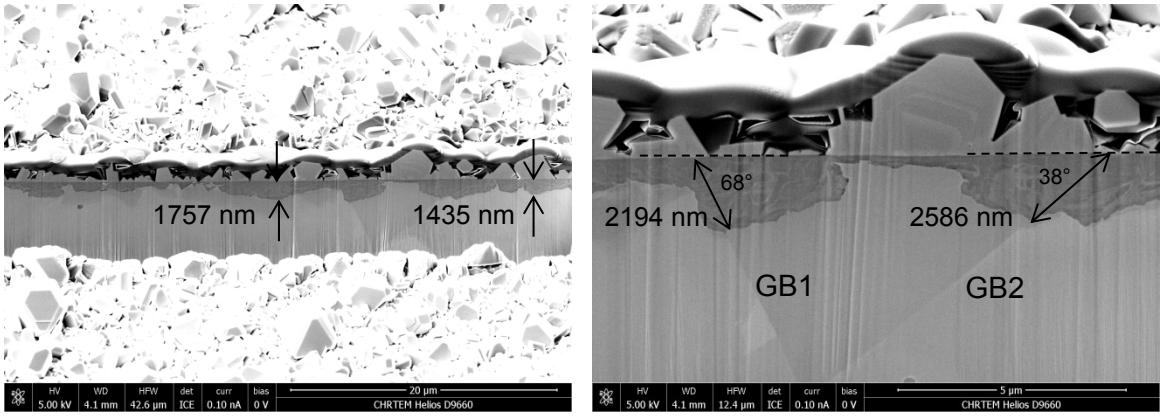

Figure 139. Sample 55 Region 6 with a) a SEM image of a FIB prepared cross section including two grain boundaries and b) magnified SEM image of the grain boundaries.

Sample 56 - Annealed material exposed at 320°C for 7000 hours

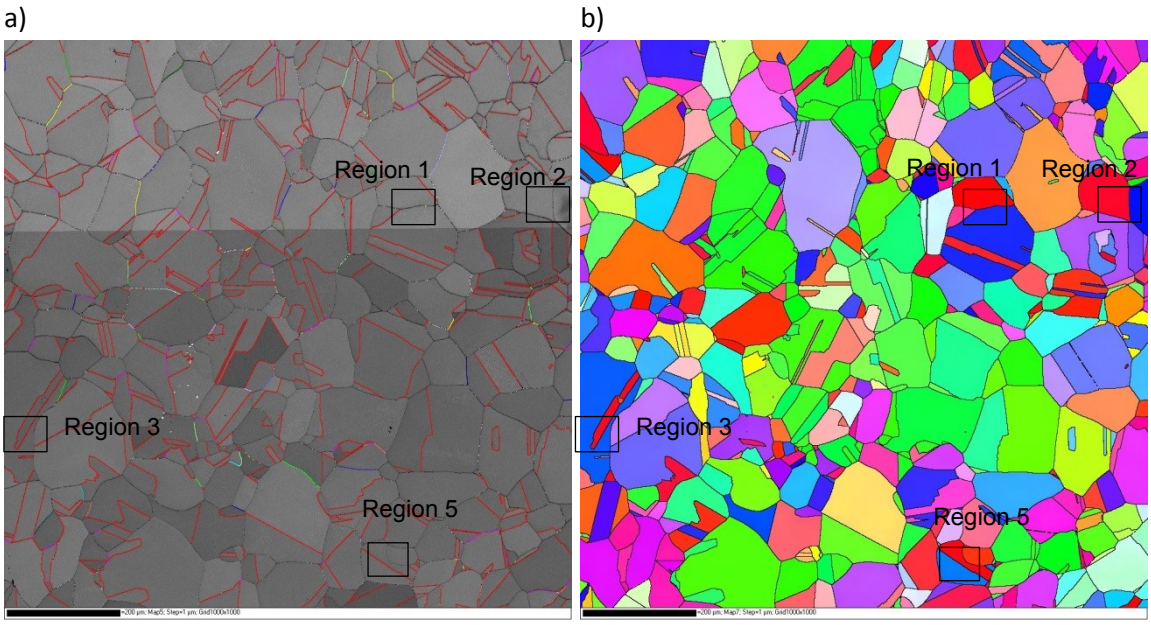

Figure 140. EBSD maps of Sample 56 with a) band contrast image and b) the IPF map of the same area, with regions 1,2,3 and 5 indicated on both maps. Note regions 4 and 6 were measured off the EBSD mapped area.

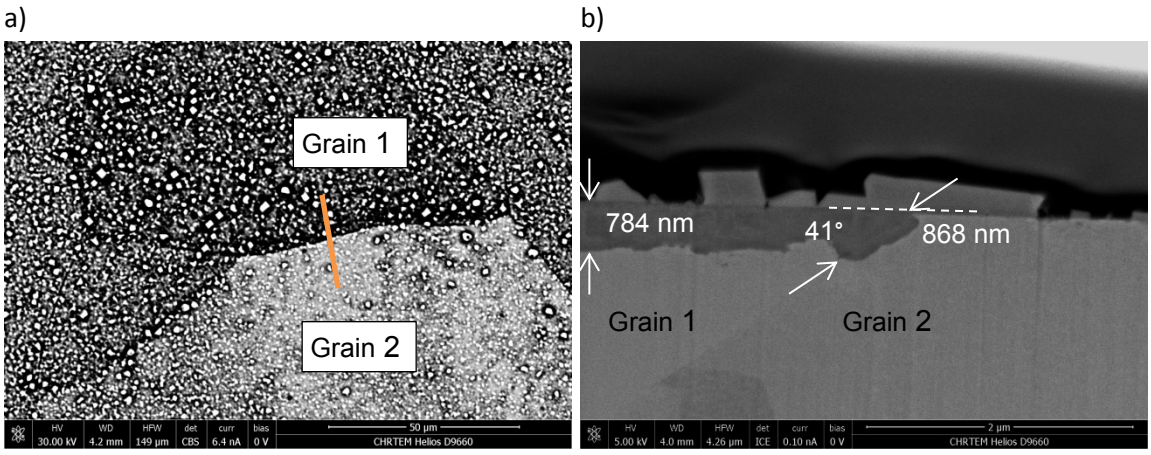

Figure 141. Sample 56 region 1 with a) BSE SEM image at 30 kV with approximate location of the FIB section, and a SEM image of the FIB cross section through the grain boundary.

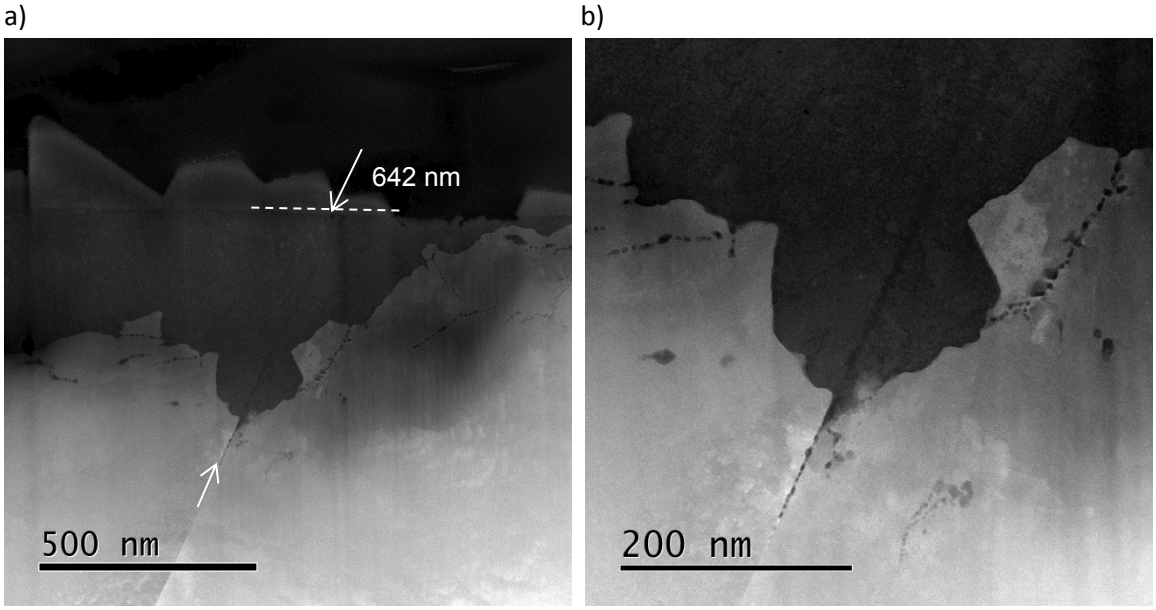

Figure 142. Sample 56 region 1b, which is a separate slice through the same grain boundary as region1, with a) HAAF TEM image of the intergranular oxidation measurement, and b) magnified view of the intergranular oxide front.

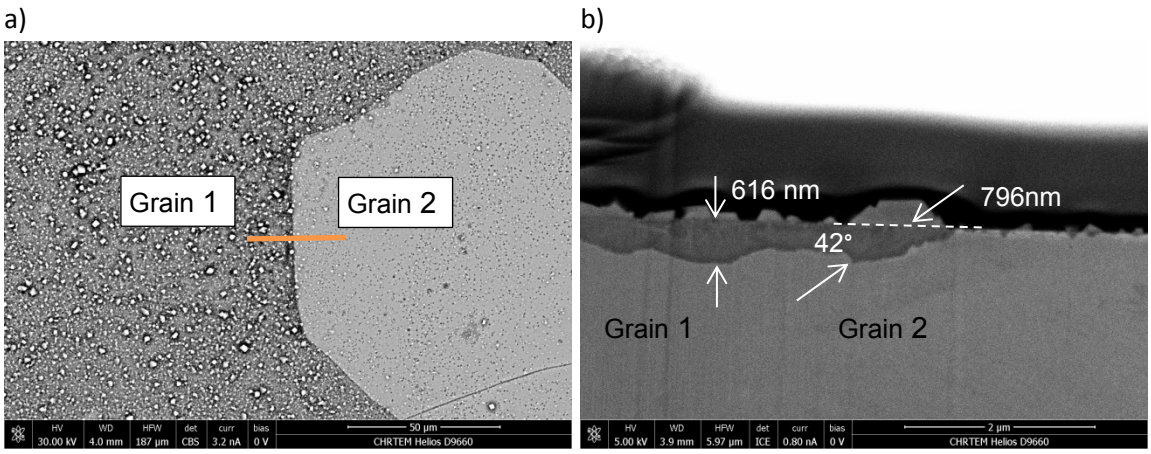

Figure 143. Sample 56 region 2 with a) BSE SEM image at 30 kV with approximate location of the FIB section, and a SEM image of the FIB cross section through the grain boundary.

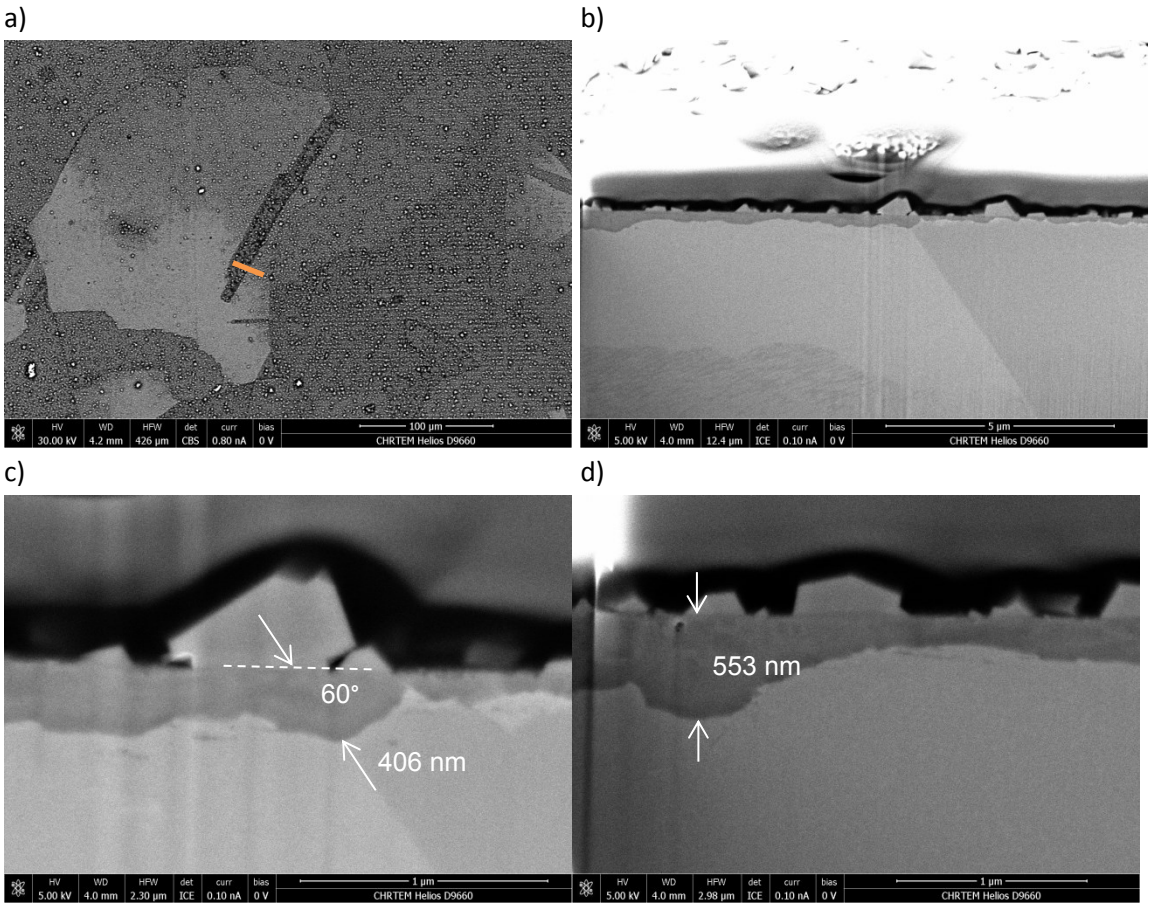

Figure 144. Sample 56 region 3 with a) BSE SEM image at 30 kV with approximate location of the FIB section, and b) a SEM image of the FIB cross section through the grain boundary, c) a magnified SEM image of the intergranular oxidation and d) a magnified SEM image of the maximum surface oxidation.

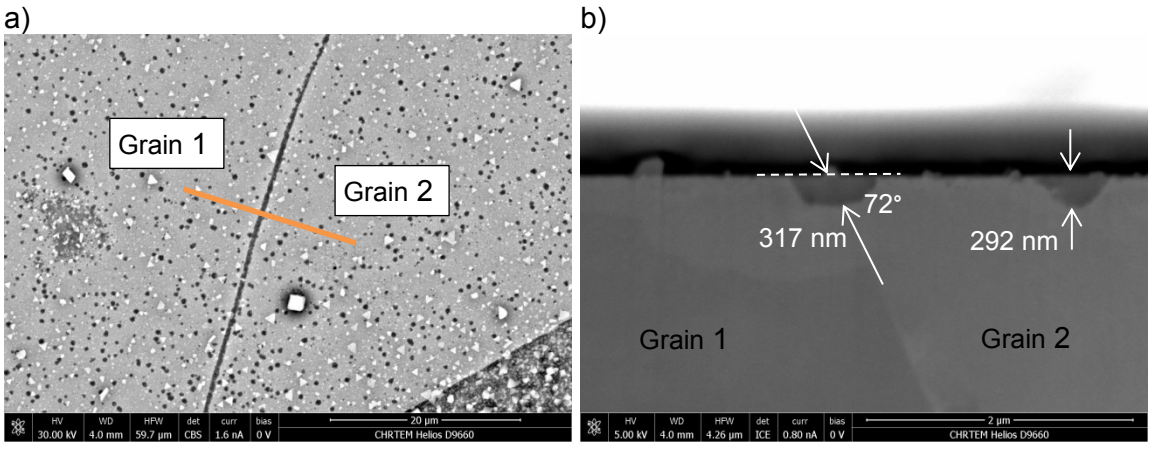

Figure 145. Sample 56 region 4, off the EBSD map, with a) BSE SEM image at 30 kV with approximate location of the FIB section, and b) a SEM image of the FIB cross section through the grain boundary.

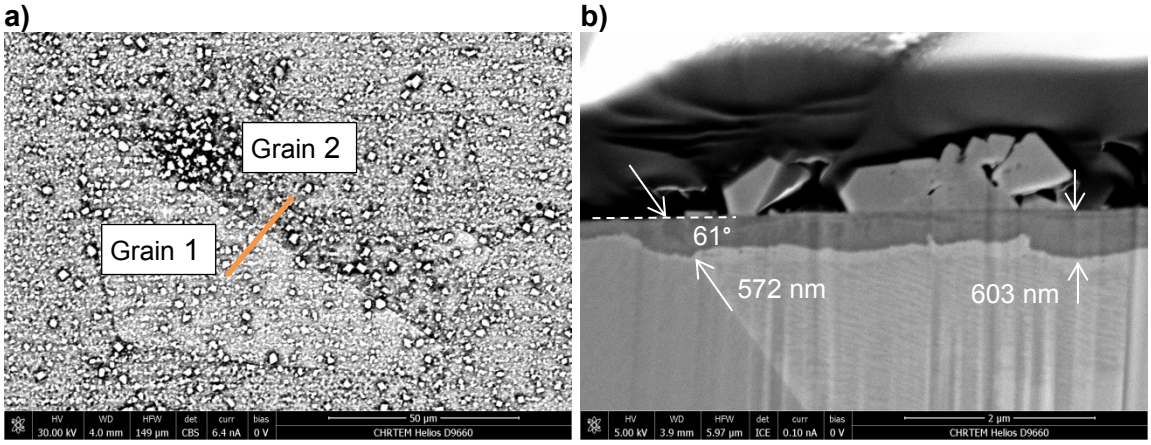

Figure 146. Sample 56 region 5 with a) BSE SEM image at 30 kV with approximate location of the FIB section, and b) a SEM image of the FIB cross section through the grain boundary.

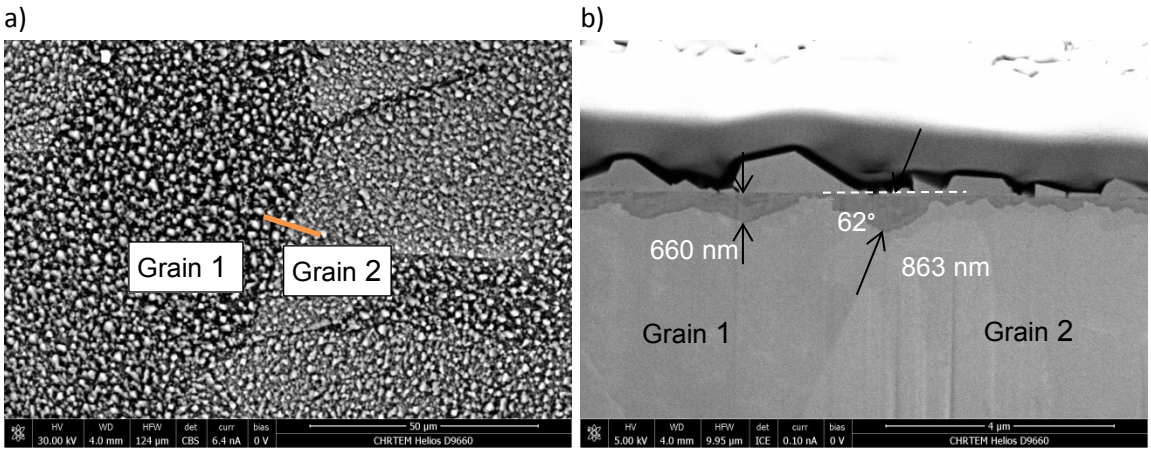

Figure 147. Sample 56 region 6, off the EBSD map, with a) BSE SEM image at 30 kV with approximate location of the FIB section, and b) a SEM image of the FIB cross section through the grain boundary.

Sample 57 – Annealed material exposed at 360°C for 4000 hours

a) b)

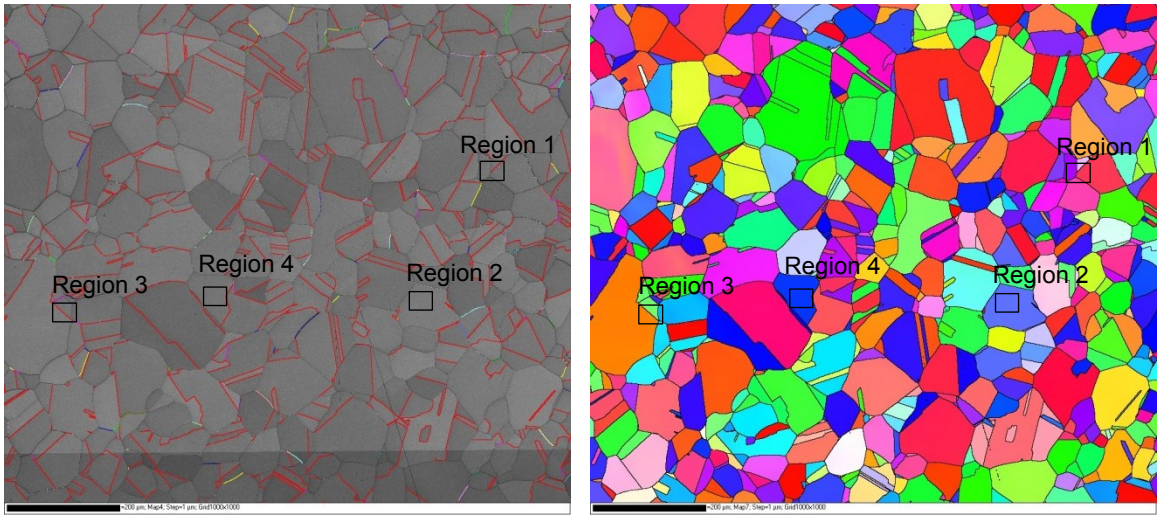

Figure 148. EBSD maps of Sample 57 with a) band contrast image and b) the IPF map of the same area, with regions 1,2,3 and 4 indicated on both maps.

a) **b)**

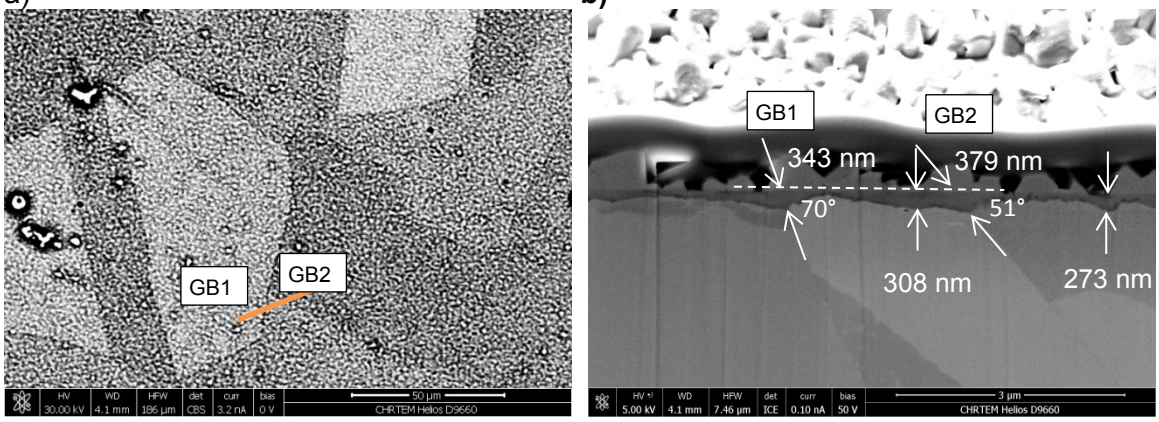

Figure 149. Sample 57 region 1 with a) BSE SEM image at 30 kV with approximate location of the FIB section, and a SEM image of the FIB cross section through both grain boundaries.

a) **b)**

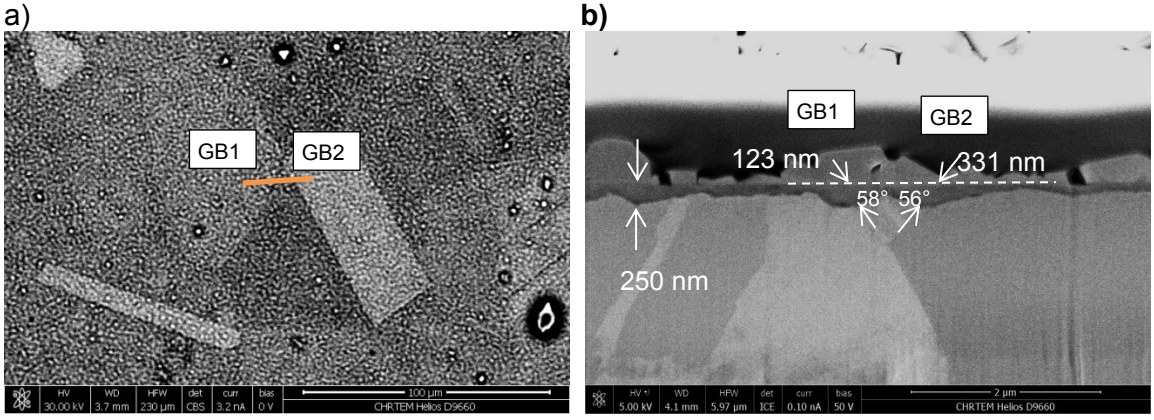

Figure 150. Sample 57 region 2 with a) BSE SEM image at 30 kV with approximate location of the FIB section, and a SEM image of the FIB cross section through both grain boundaries.

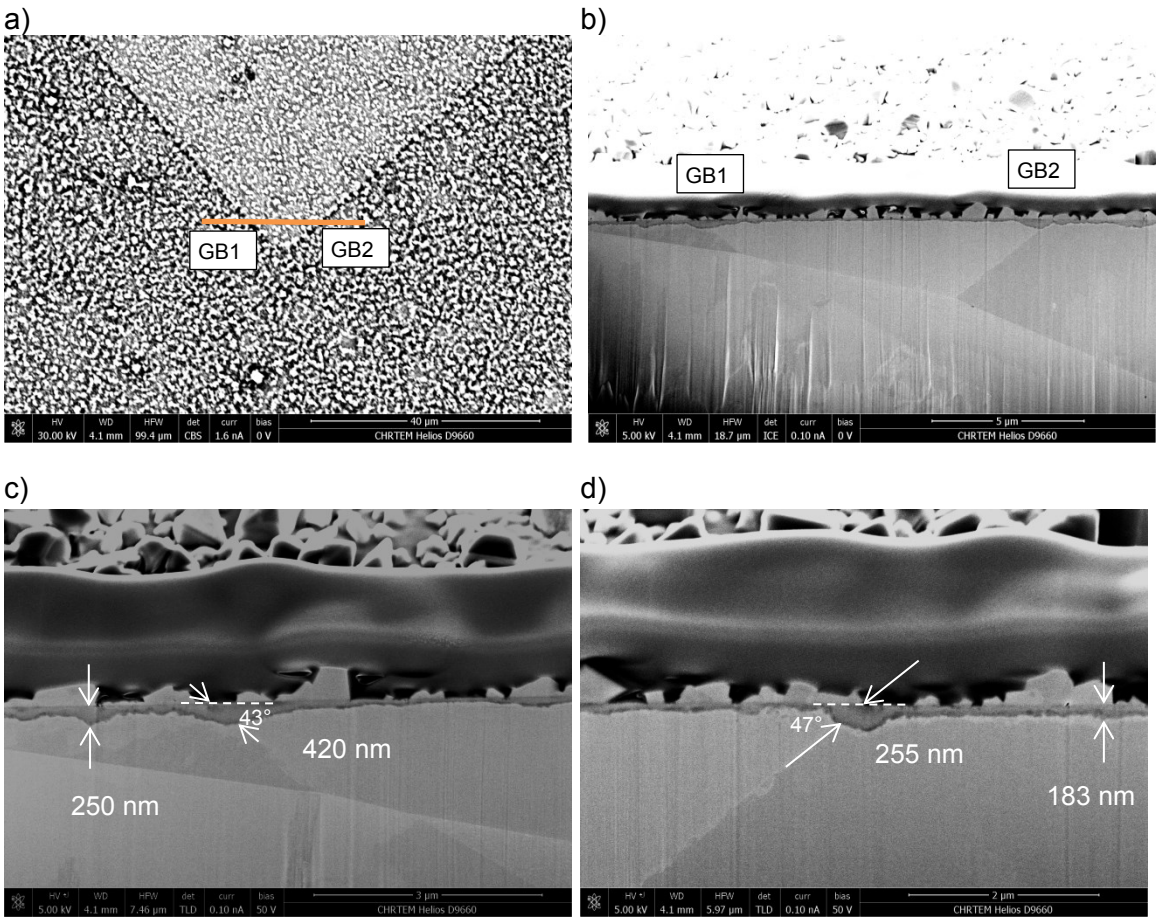

Figure 151. Sample 57 region 3 with a) BSE SEM image at 30 kV with approximate location of the FIB section, b) SEM image of the FIB cross section through both grain boundaries, c) a magnified SEM view of GB1, and d) a magnified SEM view of GB2.

a)

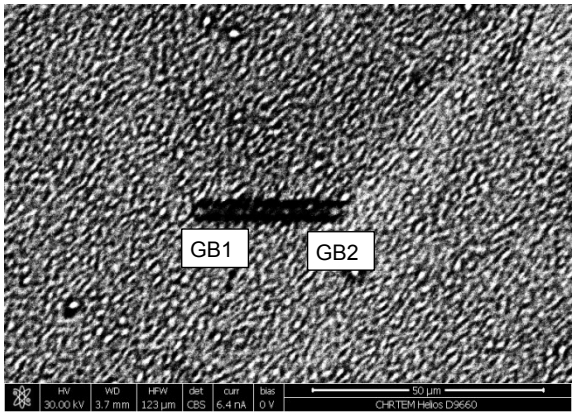

b)

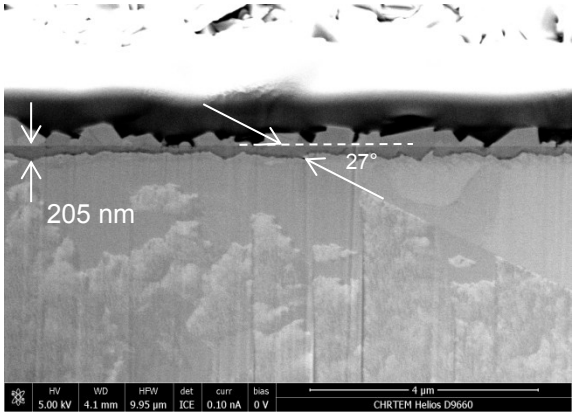

c)

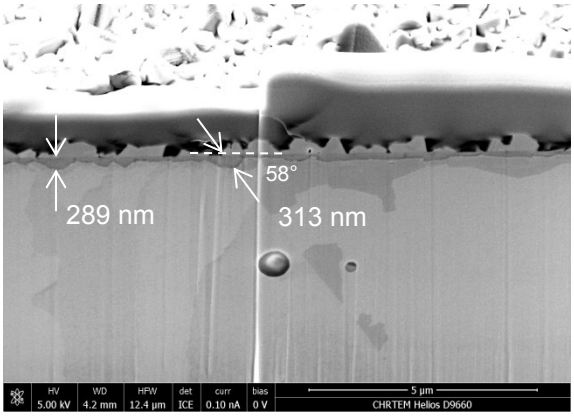

Figure 152. Sample 57 region 4 with a) BSE SEM image at 30 kV with location of the FIB section given by the carbon deposition location, b) SEM image of the FIB cross section through GB1 which was too acute to the surface to measure, and d) SEM image of GB2.

Sample 50 – 20% Cold rolled exposed at 290°C for 5000 hours.

The oxide growth on this sample was too thick to locate the regions of interest on the associated EBSD map.

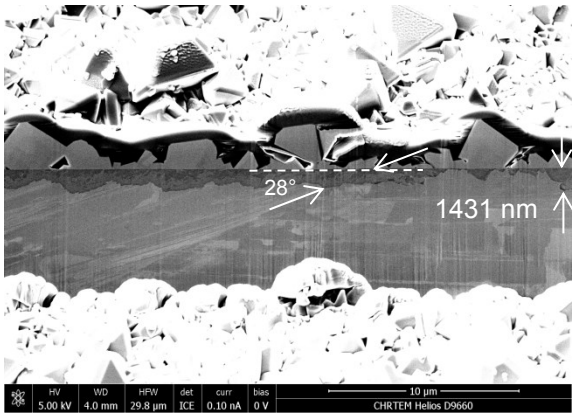

Figure 153. Sample 50 with a SEM image of the FIB cross-section at region 1. The grain boundary included in this section was too acute with the surface to have a valid measurement.

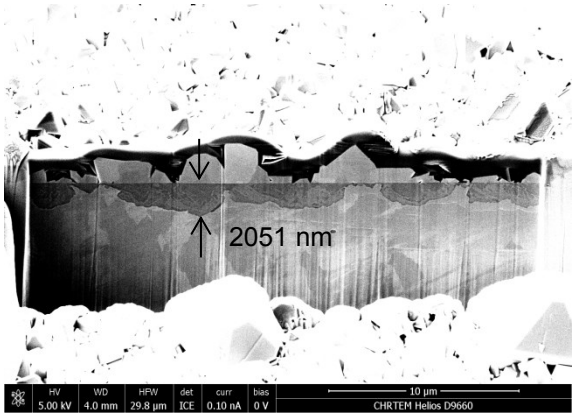

Figure 154. Sample 50 with a SEM image of the FIB cross section at region 2. No grain boundary was included in this cross section.

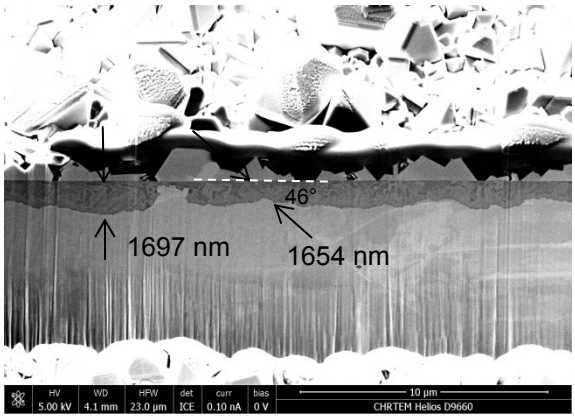

Figure 155. Sample 50 with a SEM image of the FIB cross section at region 3, which included a grain boundary.

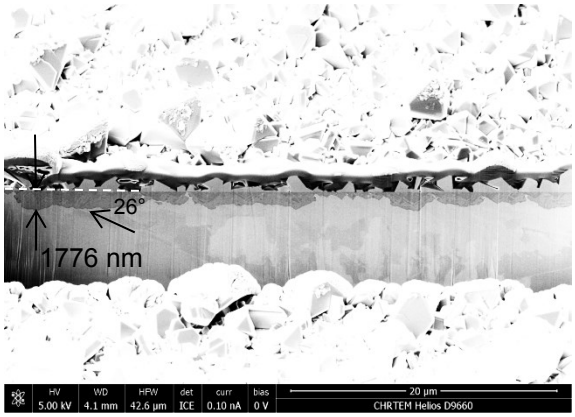

Figure 156. Sample 50 with a SEM image of the FIB cross section at region 4. No grain boundary was included in this cross section.

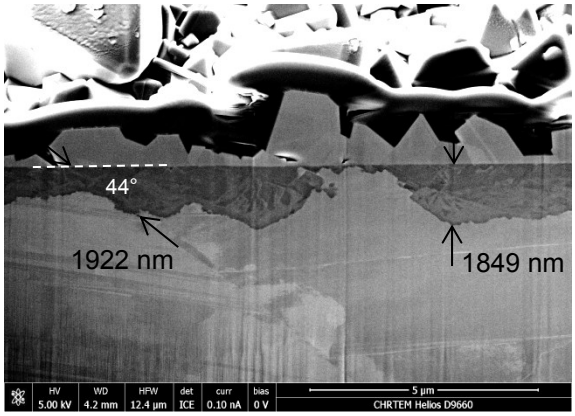

Figure 157. Sample 50 with a SEM image of the FIB cross section at region 5, which included a grain boundary.

Sample 49 – 20% Cold rolled exposed at 320°C for 7000 hours

a) b)

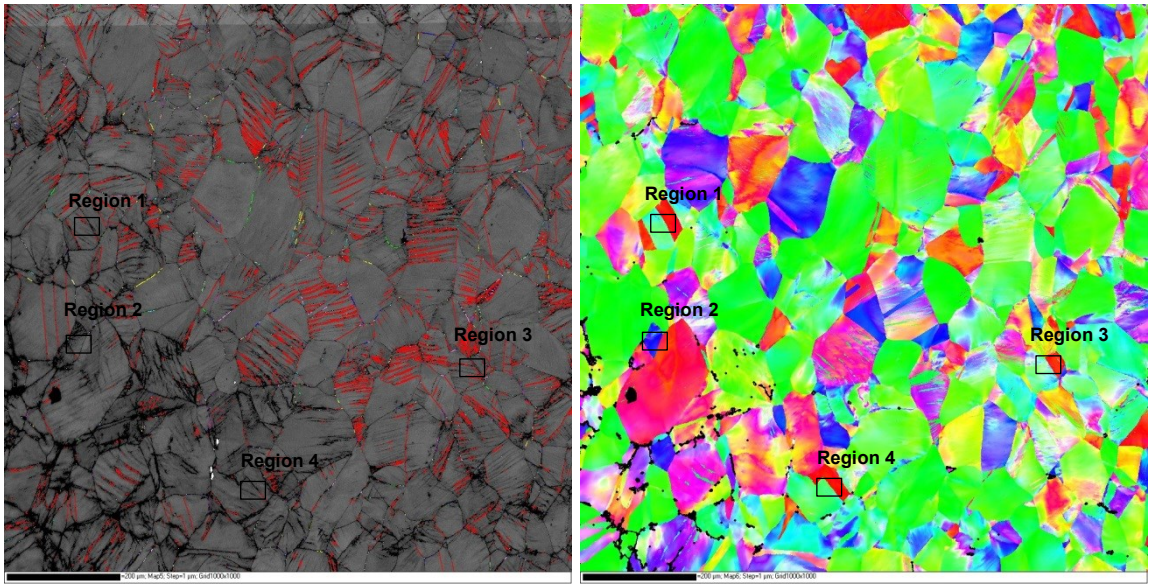

Figure 158. EBSD maps of Sample 49 with a) band contrast image and b) the IPF map of the same area, with regions 1,2,3 and 4 indicated on both maps.

a) b)

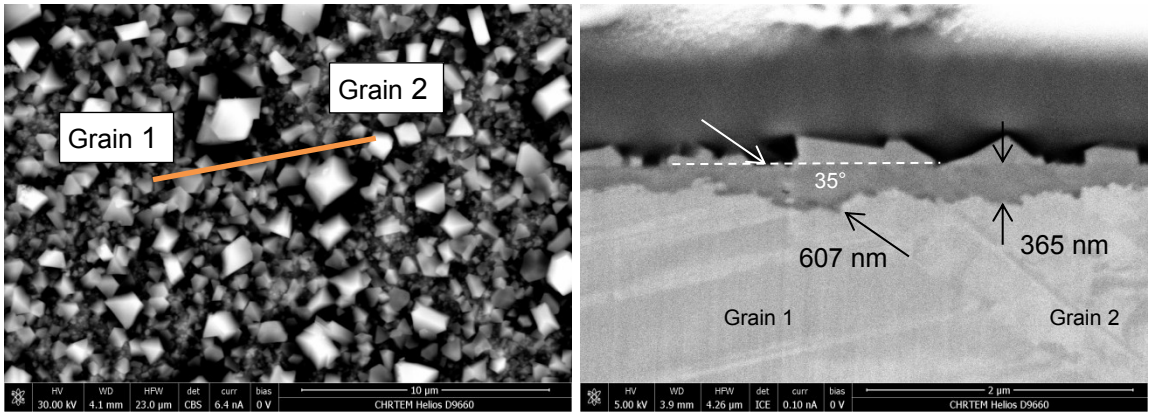

Figure 159. Sample 49 region 1 with a) BSE SEM image at 30 kV with approximate location of the FIB section, and a SEM image of the FIB cross section through the grain boundary.

a) b)

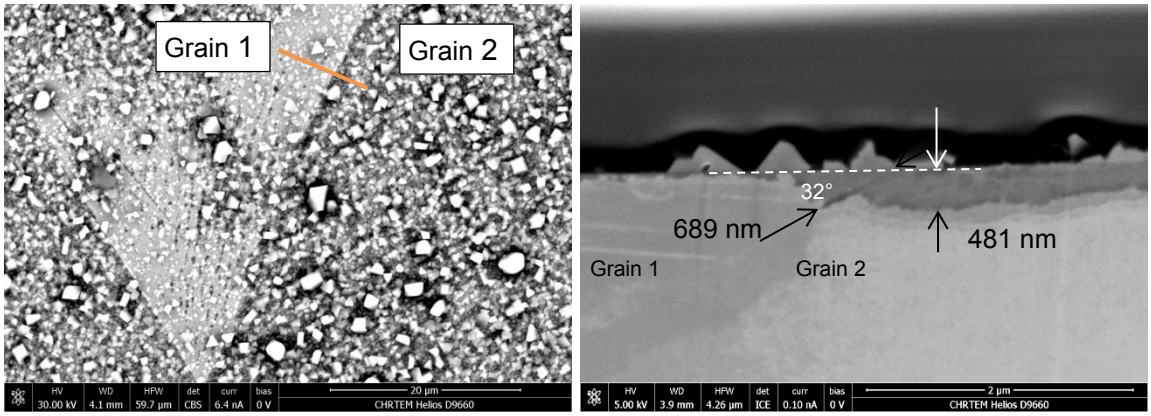

Figure 160. Sample 49 region 2 with a) BSE SEM image at 30 kV with approximate location of the FIB section, and a SEM image of the FIB cross section through the grain boundary.

a) b)

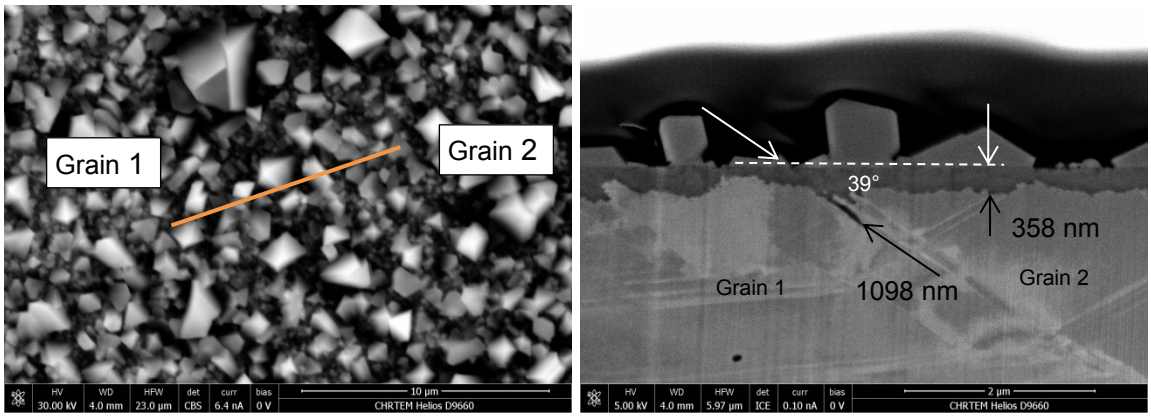

Figure 161. Sample 49 region 3 with a) BSE SEM image at 30 kV with approximate location of the FIB section, and a SEM image of the FIB cross section through the grain boundary.

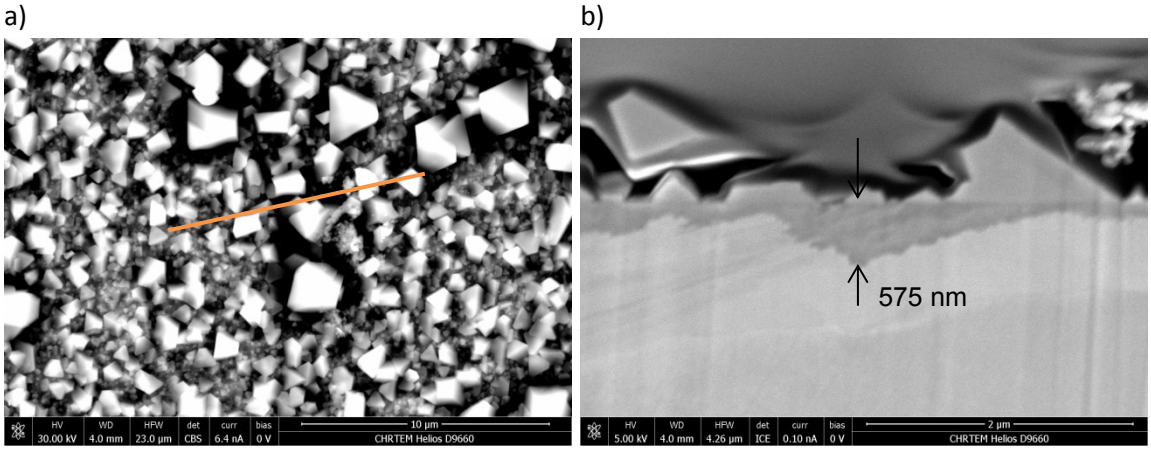

Figure 162. Sample 49 region 3 with a) BSE SEM image at 30 kV with approximate location of the FIB section, and b) a SEM image of the FIB cross section, which did not include a grain boundary.

Sample 51 – 20% Cold rolled exposed at 360°C for 4000 hours

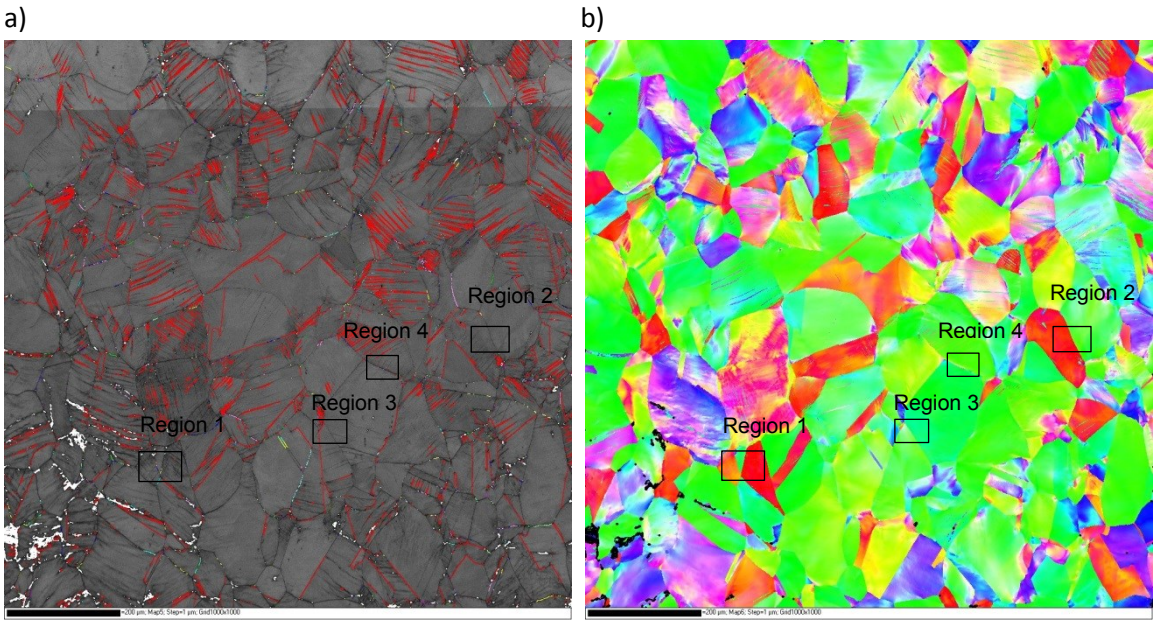

Figure 163. EBSD maps of Sample 51 with a) band contrast image and b) the IPF map of the same area, with regions 1,2,3 and 4 indicated on both maps.

a) b)

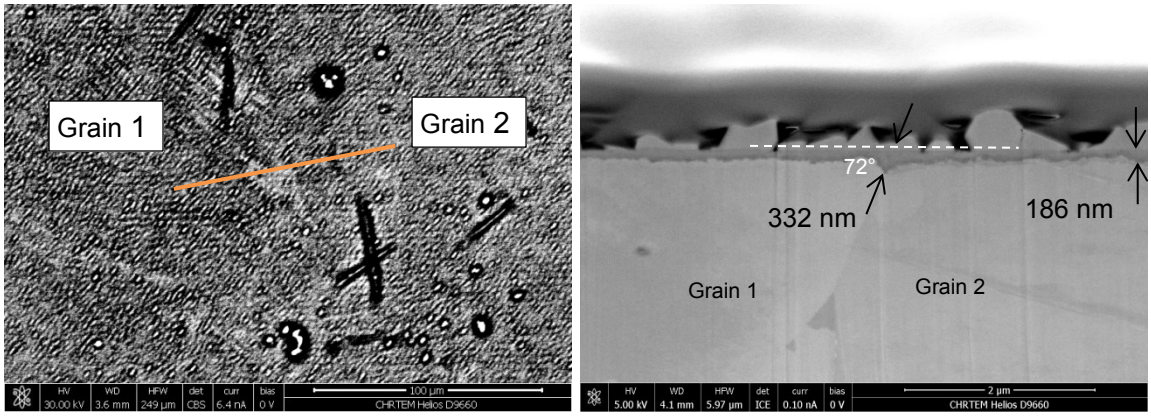

Figure 164. Sample 51 region 1 with a) BSE SEM image at 30 kV with approximate location of the FIB section, and a SEM image of the FIB cross section through the grain boundary.

a) b)

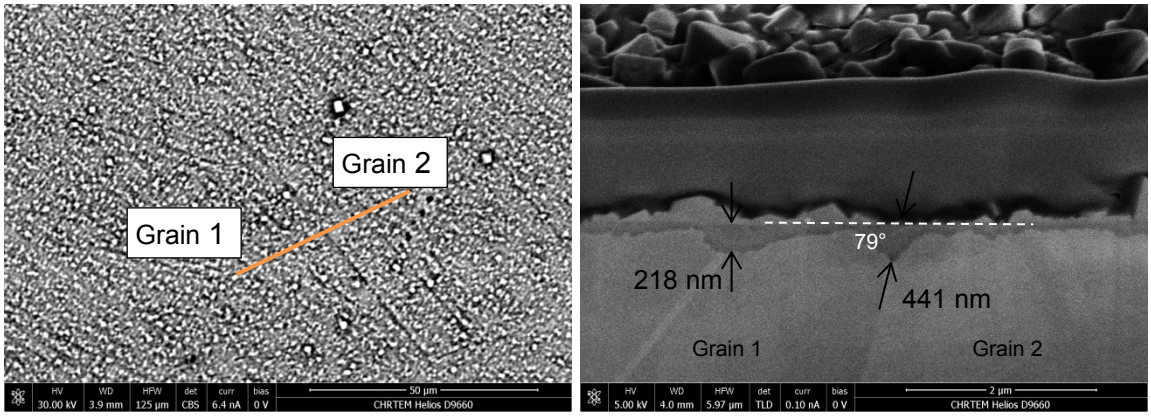

Figure 165. Sample 51 region 2 with a) BSE SEM image at 30 kV with approximate location of the FIB section, and a SEM image of the FIB cross section through the grain boundary.

a) b)

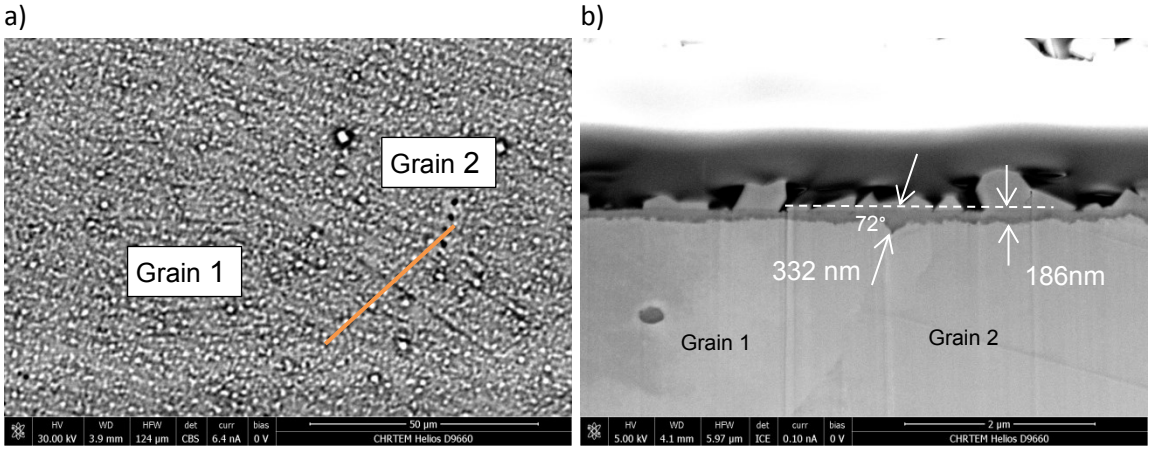

Figure 166. Sample 51 region 3 with a) BSE SEM image at 30 kV with approximate location of the FIB section, and a SEM image of the FIB cross section through the grain boundary.

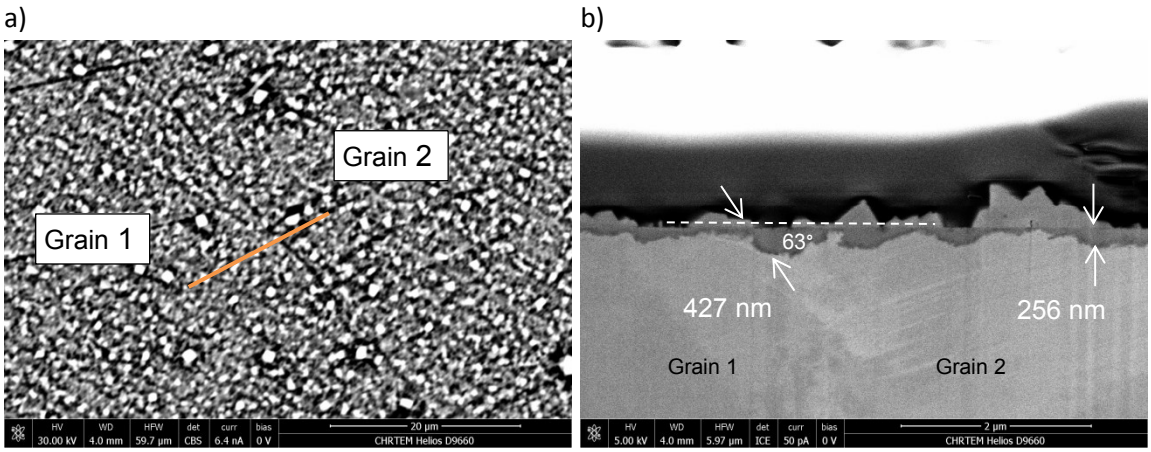

Figure 167. Sample 51 region 4 with a) BSE SEM image at 30 kV with approximate location of the FIB section, and a SEM image of the FIB cross section through the grain boundary.